

# **Dissertation**

submitted to the

Combined Faculty of Natural Sciences and Mathematics

of the Ruperto Carola University Heidelberg, Germany

for the degree of

Doctor of Natural Sciences

Presented by:

Anniek Stokkermans (M.Sc.)

Born in: Rheden, the Netherlands

Oral examination: 18 February 2022



Linking organismal behavior and morphogenesis during  
larva-polyp transition in *Nematostella vectensis*

Referees: Jun.-Prof. Dr. Steffen Lemke

Dr. Takashi Hiiragi





This thesis was carried out at the European Molecular Biology Laboratory in Heidelberg from October 2017 to November 2021 under the supervision of Dr. Aissam Ikmi.



# Summary

While it is known that animal behavior depends on morphology, it remains poorly understood whether and how organismal behavior impacts morphogenesis. During development, behavior emerges at different scales when cells differentiate and form specialized tissues and organs. Such emerging behaviors may include movement or electrical activity taking place on scales ranging from the cellular to the organismal level. Since development is a continuous process, these emerging behaviors have the potential to feed back on development. Indeed, some behaviors that emerge at the tissue and organ scale, in particular contractile behaviors, such as the beating of the developing heart, have been shown to generate mechanical forces that contribute to morphogenesis. Thus, morphology and behavior develop together, and may impact one another. However, this potential two-way relationship has not received much attention at the organismal scale. This is largely because simultaneously studying behavior and morphogenesis is complicated by the different spatiotemporal scales at which these processes take place. Furthermore, while in most species morphogenesis largely takes place during embryonic development, most organismal behaviors are expressed post-embryonically, when they primarily serve animal survival through interaction with the external environment. For these reasons, studying the link between organismal behavior and morphogenesis requires a system in which both processes take place at the same time, and at spatiotemporal scales that are not too far apart. In this thesis, I use the sea anemone *Nematostella vectensis* as a model organism to study the link between organismal behavior and morphogenesis. During a process called larva-polyp transition, *Nematostella* undergoes a simple morphogenetic change from a roughly ellipsoidal larva to a cylindrical polyp with oral tentacles, while simultaneously expressing distinct organismal behaviors such as cilia-based swimming, settlement, and muscle-driven body contractions. Using an imaging setup that allows tracking and monitoring of morphogenetic and behavioral changes at the organismal scale, I characterize the dynamics of larva-polyp transition in wild-type animals. Here, I find that the animals can change their size and shape both separately and simultaneously, and that animal settlement behavior correlates with elongation dynamics. While increase of organismal size largely depends on body cavity inflation by water uptake, change of animal shape requires tissue remodeling during which cells change shape and rearrange. Furthermore, pharmacological, mechanical, and genetic perturbations suggest an important role for muscular-hydraulics in both animal behavior and development. These findings suggest a mechanism in which short-term behavioral contractions generate mechanical forces that induce tissue remodeling on long time scales, thus indicating a potential role for animal behavior in driving morphogenesis.

# Zusammenfassung

Obwohl bekannt ist, dass das Verhalten von Tieren von ihrer Morphologie abhängt, ist es ungeklärt ob und wie sich das Verhalten von Organismen auf deren Morphogenese auswirkt. Während des Entwicklungsprozesses von Organismen tritt Verhalten auf verschiedenen Ebenen auf, wenn sich Zellen differenzieren und spezialisierte Gewebe und Organe bilden. Solche aufkommenden Verhaltensweisen können Bewegungen oder elektrische Aktivitäten auf den verschiedenen Ebenen von Zellen, Geweben, und Organen umfassen. Da Entwicklung ein kontinuierlicher Prozess ist, haben diese aufkommenden Verhaltensweisen das Potenzial, auf die Entwicklung zurückzuwirken. Tatsächlich hat sich gezeigt, dass einige Verhaltensweisen, die auf der Ebene von Gewebe und Organen auftreten, insbesondere kontraktile Verhaltensweisen, wie das Schlagen des sich entwickelnden Herzens, mechanische Kräfte erzeugen, die zur Morphogenese beitragen. So entwickeln sich Morphologie und Verhalten gemeinsam und können sich gegenseitig beeinflussen. Jedoch wurde diese potenzielle Wechselwirkung mit Gesamtblick auf den Organismus nur wenig erforscht. Dies liegt vor allem daran, dass die gleichzeitige Untersuchung von Verhalten und Morphogenese durch die unterschiedlichen räumlichen und zeitlichen Größenordnungen in denen diese Prozesse stattfinden verkompliziert wird. Während die Morphogenese bei den meisten Arten größtenteils während der Embryonalentwicklung stattfindet, werden die meisten Verhaltensweisen von Organismen postembryonal ausgedrückt, wo diese primär dem Überleben der Tiere durch Interaktion mit der Umwelt dienen. Aus diesen Gründen erfordert die Untersuchung des Zusammenhangs zwischen Verhalten und Morphogenese ein System, in dem beide Prozesse gleichzeitig in räumlichen und zeitlichen Größenordnungen stattfinden. In der vorliegenden Arbeit verwende ich die Seeanemone *Nematostella vectensis* als Modellorganismus um den Zusammenhang zwischen Verhalten und Morphogenese zu untersuchen. Während des Prozesses des Larven-Polypen-Übergangs durchläuft *Nematostella* eine einfache morphogenetische Veränderung von einer annähernd ellipsoiden Larve zu einem zylindrischen Polypen mit oralen Tentakeln, während sie gleichzeitig verschiedene Verhaltensweisen wie zilienbasiertes Schwimmen, Ansiedlung und muskelgetriebene Körperkontraktionen ausdrückt. Mit einem Mikroskopie-Aufbau, der es ermöglicht morphogenetische und Verhaltensänderungen auf Organismenebene zu verfolgen und zu überwachen, charakterisiere ich die Dynamik des Larven-Polypen-Übergangs bei Wildtyptieren. Meine Experimente zeigen, dass die Tiere ihre Größe und Form sowohl getrennt als auch gleichzeitig ändern können und dass das Siedlungsverhalten der Tiere mit der Dehndynamik korreliert. Während die Zunahme der Organismengröße weitgehend vom Aufpumpen der Körperhöhle durch Wasseraufnahme abhängt, erfordert die Veränderung der Tierform eine Gewebeumgestaltung, bei der die Zellen ihre Form ändern und interkalieren. Darüber hinaus legen pharmakologische, mechanische und genetische Perturbationen nahe, dass die Muskelhydraulik sowohl im Verhalten

als auch in der Entwicklung der Tiere eine wichtige Rolle spielt. Diese Ergebnisse legen einen Mechanismus nahe, bei dem kurzfristiges Kontraktionsverhalten mechanische Kräfte generiert, die über eine langfristige Zeitspanne eine Gewebeumbildung induzieren. Dies deutet auf eine potenzielle Rolle des Tierverhaltens bei der Steuerung der Morphogenese hin.



# Acknowledgements

I am very grateful to many people who have contributed to making my PhD at EMBL an inspirational and joyful time, during which I have learned a lot.

First of all, many thanks to **Aissam Ikmi** for great supervision, inspiring discussions, and for always bringing a lot of enthusiasm and positive energy into the project. Many thanks to all past and present members of the Ikmi lab: **Peter Steenbergen** (we would be absolutely nowhere without you), **Stephanie Cheung** (it has been great to share the EMBL PhD adventure together with you from the start), **Marie Anzo**, **Soham Basu**, **Kaushikaram Subramanian**, **Richard Bailleul**, **Melodie Doute**, **Sophie Tran**, **Giulia Bergamini**, **Omar Matar**, **Julia Hagauer**, **Paolo Cucurachi**, **Pauline Hansen** and **Florian Gabler**. I have learned from each and every one of you and you have really made me feel at home.

Many thanks to all people who collaborated on the project: **Ling Wang** and **Kaushik** for making OCM imaging of *Nematostella* a reality, **Prachiti Moghe** and **Chii Jou Chan** for finding ways to measure pressure in a challenging model organism and for your helpful discussions, **Gregor Mönke** for valuable input on the data analysis and teaching me how to use the HPC cluster, and **Aditi Chakrabarti** and **Lakshminarayanan Mahadevan** for biophysical modeling and inspirational discussions.

A big thank you for the amazing support from the EMBL core facilities, in particular to **Stefan Terjung**, **Aliaksandr Halavaty**, **Sabine Reither**, **Faba Neumann**, and **Lucas Schütz** from the Advanced Light Microscopy Facility, and **David Will** from Chemical Biology Core Facility. Your input has been very valuable and is very much appreciated. Thank you **Kresimir Crnokic**, for animal husbandry, and **Alexandre Paix**, for genome editing support. Many thanks as well to the people from Bio-IT, in particular **Toby Hodges**, for providing excellent training resources. Also, special thanks to **Christian Tischer**, **Jonas Hartmann** and **Virginie Uhlmann** for advice on image analysis and inspiring me to develop as an image analyst myself.

Next, I would like to thank **Takashi Hiiragi**, **Steffen Lemke** and **Lars Hufnagel** for your valuable input and support during the TAC meetings. Thanks also to **Robert Prevedel** for helpful input during OCM discussion meetings and for serving on my thesis defense committee. Thanks as well to **Lazaro Centanin** for agreeing to serve on my thesis defense committee.

Thank you to all members of the **Aulehla** and **Hiiragi labs** for the discussions in the joint lab meetings, and to all members of the **DB unit** in general for the nice working environment.

Finally, I thank **Christine Ho**, **Naomi Stierle**, **Carina Vibe**, **Branislava Rankovic**, and **Nobuko Tsuchida** for all our hiking, biking, and camping adventures in and around Heidelberg, I had

a great time with you! Special thanks to my family for their unconditional support, and to my partner, **Patrick van Nierop**, for always being there for me.



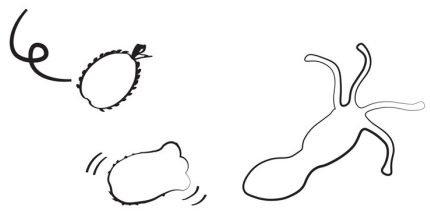
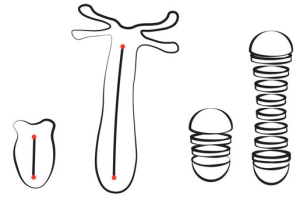
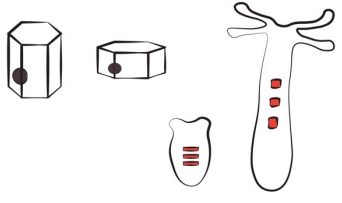
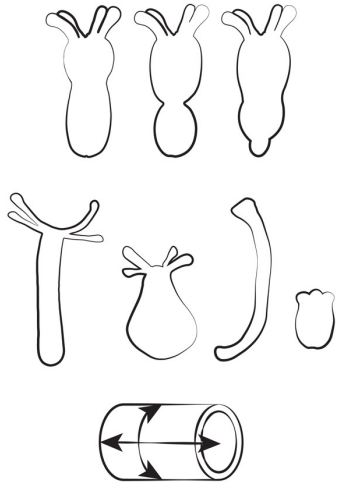
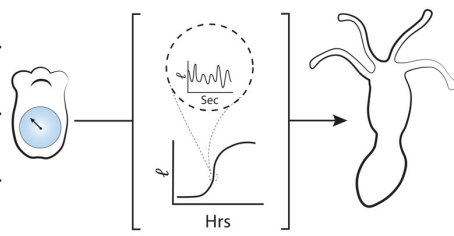
# Contents

<b>Summary</b> .....	<b>vii</b>
<b>Zusammenfassung</b> .....	<b>viii</b>
<b>Acknowledgements</b> .....	<b>xi</b>
<b>Contents</b> .....	<b>xiii</b>
<b>Graphical contents</b> .....	<b>xvi</b>
<b>Morphogenesis and behavior in biological systems</b> .....	<b>1</b>
1.1. Animal development in space and time.....	1
1.2. What classifies as behavior? .....	2
1.3. Morphogenetic feedback mechanisms induced by behavior .....	3
1.4. Studying morphogenesis and behavior at the organismal level .....	4
<b>2. Mechanisms of morphogenesis across scales</b> .....	<b>5</b>
2.1. Biochemical and mechanical signals guide morphogenesis.....	7
2.2. Cell and tissue mechanical mechanisms execute morphogenetic processes .....	8
2.2.1. Generation of active forces .....	8
2.2.2. Passive forces contributing to morphogenesis .....	12
2.2.3. Tissue architecture, material properties, and extracellular environment .....	12
2.3. Axial elongation in different developing systems .....	15
2.3.1. Germband elongation in <i>Drosophila</i> .....	15
2.3.2. Anteroposterior axis formation in vertebrate embryos .....	17
2.3.3. Axial elongation in <i>C. elegans</i> .....	19
<b>3. Cnidarian development</b> .....	<b>23</b>
3.1. Evolution, life cycle and morphology .....	23
3.2. Metamorphosis in cnidarians.....	23
3.3. Cnidarian muscles consist mostly of myoepithelial cells. ....	24
3.4. <i>Nematostella vectensis</i> as a model for studying organismal behavior and morphogenesis ...	25
3.4.1. Genome and genomic tools .....	25
3.4.2. Life cycle and anatomy .....	25
3.4.3. Embryonic patterning.....	26
3.4.4. The nervous system in <i>Nematostella</i> .....	27
3.4.5. <i>Nematostella</i> has a muscle system consisting of longitudinal and circular muscles .....	28
3.4.6. Using <i>Nematostella</i> to study the link between organismal behavior and morphogenesis..	29
<b>4. Aims of the thesis</b> .....	<b>31</b>
1. Development of an experimental workflow and image analysis pipeline to monitor animal behavior and morphogenetic changes in a high-throughput manner. ....	31
2. Characterization of animal behavior and morphogenetic changes during larva-polyp transition in wild-type animals. ....	31
3. Define the role of the gastric cavity and muscle contractions during larva-polyp transition. ....	31
<b>5. Dynamics of larva-polyp transition in <i>Nematostella</i></b> .....	<b>33</b>
5.1. A high throughput imaging approach for quantifying body shape change and organismal behavior .....	33
5.2. Image analysis strategy for extracting shape and size features from 2D images of developing <i>Nematostella</i> larvae .....	34
5.2.1. Preprocessing .....	34
5.2.2. Image segmentation into animal and background.....	34
5.2.3. Extracting shape features.....	35
5.2.4. Data analysis.....	37
5.2.5. Validation of the image analysis pipeline.....	38
5.3. Defining the start of larva-polyp transition based on animal shape circularity .....	39
5.4. Larva-polyp transition in <i>Nematostella</i> is asynchronous and variable in duration.....	40
5.5. Animals explore a morphospace by separately or simultaneously changing body column size and shape .....	42
5.6. Animal settlement behavior correlates with axial elongation dynamics.....	44
5.7. Sessile and motile animals show different morphodynamics during larva-polyp transition ...	47

5.8.	Morphogenesis and animal behavior act on different time scales.....	49
5.9.	Developing <i>Nematostella</i> show two main types of body contractions .....	49
5.10.	Different types of contractile behavior may contribute to specific morphodynamics .....	51
5.11.	Summary and conclusions .....	55
<b>6.</b>	<b>Tissue morphogenesis during larva-polyp transition .....</b>	<b>57</b>
6.1.	Cavity inflation is a main driver of organismal size increase.....	57
6.2.	Cell proliferation plays a minor role during larva-polyp transition.....	60
6.3.	Cell shape changes and cellular rearrangements contribute to redistribution of tissue mass during larva-polyp transition.....	61
6.4.	Cellular rearrangements contribute to axial elongation.....	64
6.5.	Summary and conclusions .....	65
<b>7.</b>	<b>The role of muscular hydraulics during larva-polyp morphogenesis .....</b>	<b>67</b>
7.1.	Muscular hydraulics are responsible for short-term shape and size regulation.....	67
7.2.	Cavity inflation is required for axial elongation .....	68
7.3.	Muscle function is essential for larva-polyp morphogenesis.....	69
7.4.	Development of the muscle system in the body column.....	73
7.5.	Targeted perturbation of muscular hydraulics through RNA interference.....	75
7.6.	Knockdown of <i>Tbx20</i> and <i>BMP2/4</i> decouples size and shape development.....	75
7.7.	<i>Tbx20</i> and <i>BMP2/4</i> KD animals show different morphodynamics and contraction behavior .....	77
7.8.	Tissue remodeling mirrors direction of organismal expansion.....	81
7.9.	Biophysical modelling of larva-polyp transformation .....	87
7.10.	Summary and conclusions .....	90
<b>8.</b>	<b>Animal-environment interactions during larva-polyp transition .....</b>	<b>91</b>
8.1.	Impact of environmental factors on larva-polyp transition.....	91
8.2.	Effects of sea water salinity on larva-polyp transition.....	91
8.3.	Increasing sea water viscosity affects animal shape.....	92
8.4.	Perturbation of settlement affects timing of larva-polyp transition .....	95
8.5.	Effect of light exposure on settlement behavior .....	97
8.6.	Summary and conclusions .....	98
<b>9.</b>	<b>Discussion .....</b>	<b>101</b>
9.1.	Advantages and limitations of the experimental setup.....	101
9.2.	Causes and potential function of inter-organism behavioral variation .....	102
9.3.	How are settlement behavior and muscular hydraulics connected?.....	103
9.4.	Knockdown of homologs of transcription factors involved in cardiogenesis cause muscle function defects in <i>Nematostella</i> .....	104
9.5.	How are muscular hydraulics and tissue morphogenesis connected? .....	105
9.6.	Outlook .....	106
<b>10.</b>	<b>Materials and Methods .....</b>	<b>109</b>
10.1.	Animal husbandry .....	109
10.2.	High-throughput live imaging .....	109
10.3.	Data analysis of live animals .....	109
10.4.	Optical coherence microscopy and data processing.....	111
10.5.	Pressure measurements .....	111
10.6.	Pharmacological treatments .....	111
10.7.	Fixation and immunostaining.....	112
10.8.	Confocal imaging.....	113
10.9.	Quantification of cellular properties.....	113
10.10.	shRNA design and synthesis .....	114
10.11.	Microinjection of shRNAs .....	115
10.12.	CRISPR/Cas9 .....	115
10.13.	Photo-conversion of Kaede .....	115
10.14.	Biophysical manipulation .....	116
10.15.	Data analysis.....	116
10.16.	Biophysical model and balloon experiments.....	116
10.17.	Studying environmental impact on larva-polyp transition.....	116
<b>11.</b>	<b>Appendix.....</b>	<b>117</b>

11.1.	Dynamics of larva-polyp transition in <i>Nematostella</i> .....	117
11.2.	Effect of pharmacological inhibition of muscle function on loss of apical tuft.....	121
11.3.	shRNA knockdown screening experiments.....	122
11.3.1.	Knockdown of Nkx2.5 and Isl-1 affects elongation dynamics and settlement behavior .	124
11.4.	Development of tentacle muscles .....	128
11.5.	FGFRb signaling is involved in patterning of longitudinal tentacle muscles .....	129
<b>Bibliography.....</b>		<b>132</b>

# Graphical contents

<b>1</b>	Animal development in space and time	
<b>2</b>	Mechanisms of morphogenesis across scales	
<b>3</b>	Cnidarian development	
<b>4</b>	Aims	
<b>5</b>	Experimental approach and image analysis pipeline  Dynamics of larva-polyp morphogenesis	
<b>6</b>	Morphogenetic changes at the tissue level	
<b>7</b>	Functioning of the hydrostatic skeleton at short and long timescales  Analysis of alternative morphologies  Biophysical modeling	
<b>8</b>	Environmental factors	
<b>9</b>	Discussion	
<b>10</b>	Materials and methods	
<b>11</b>	Appendix	

# Morphogenesis and behavior in biological systems

## 1.1. Animal development in space and time

Organisms acquire their form in a process called morphogenesis, which is derived from the Greek word 'μορφή' (morphê), which means 'shape', and 'γένεσις' (genesis), which means 'creation'. In most animals, morphogenesis takes place predominantly during embryogenesis, but in some species, such as metamorphosing insects, major morphogenetic changes occur in later life. During embryogenesis, most animals develop in a relatively confined, protected space, such as gelatinous substances (for example frog embryos), egg shells, or the uterus. During this time, animals express limited organismal behaviors, but may be seen twitching or responding to sound or touch. In contrast, postembryonic development takes place in a large open space where the animal is in direct contact with its environment. Here, animal behavior is often directly required for survival, since animals need to actively interact with their environment in order to find food, escape from predators, and find a suitable territory to live and reproduce. An animal's morphology is optimized to express these species-specific behaviors, and behavior is thus heavily dependent on morphology. However, whether behavior also impacts morphology is less well understood. From an evolutionary point of view, such a connection between behavior and morphology is recognized. Selection pressure is determined by the environment together with the way an animal interacts with the environment through behavior. An environmental change (e.g. different prey availability) may induce a behavioral shift (e.g. hunting style), exposing new selection pressures while others may disappear (e.g. it may be more advantageous to run fast on short distances, versus endurance on long distances) (Duckworth, 2009). Through such a mechanism, behavior can drive evolutionary change, such that the animal's morphology becomes optimized for new conditions. However, from a developmental biology perspective, it remains poorly understood whether and how organismal behaviors also feed back on (morphology) development within the same organism. There are a few examples where behavior influences development, but none of these behaviors induces major restructuring of the body. For example, it is generally known that regular exercise can increase the ratio of body muscle to fat, and that the type of exercise and physical loading can lead to certain parts of the body to grow larger muscles than others. A slightly more extreme example is that of a goat born without forelegs, which adopted an upright walking position, resulting in altered morphology of its bones and musculature compared to normal goats (Bertossa, 2011; Slijper, 1942). Furthermore, a relationship has been found between seeing and eye development: visual deprivation by sewing eyelids shut for several months has been demonstrated to lead to myopia (near-sightedness) in monkeys, where the strength of the refractive error was dependent on the duration of the treatment (Hubel et al., 1976;

Wiesel and Raviola, 1977). Thus, while organismal behavior is recognized as a potential regulator of morphology, there is still only limited knowledge about its functional role during development.

## **1.2. What classifies as behavior?**

While the meaning of the word behavior may seem intuitive, a clear definition for the term 'behavior' is lacking, and often contradictory meanings are used (Calhoun and Hady, 2021; Levitis et al., 2009). For example, in the English dictionary, behavior is defined as "the way in which an animal or person behaves in response to a particular situation or stimulus", which automatically excludes non-animal organisms from being able to behave. However, in other contexts one might consider bacteria swimming towards light as behavior. Furthermore, one might ask whether behavior always requires movement. Are reflexes behavior? Can groups of animals behave collectively, or does behavior always refer to the actions of individuals? Can the absence of action also be behavior? Restricting behavior to whole organisms appears to be problematic. If unicellular organisms can behave, should that not also mean that isolated cells belonging to a multicellular organism can behave? Furthermore, in animals such as cephalopods, the nervous system is not centralized the same way as in vertebrates, and the different arms are not entirely under the control of the cephalopod brain. A detached octopus arm has its own neurons with which it can respond to stimuli, such as withdrawal and contraction in response to pinching (Hague et al., 2013). Thus, in an alternative view, one might say that behavior occurs at all levels and scales where form and function are connected (Bertossa, 2011). For instance, while 'running' could be an example of organismal behavior, achieving displacement (function) by using legs (form), the power-stroke of molecular motors such as myosin could be an example of behavior achieving a similar function at a completely different scale. Similarly, collective or collaborative movements in social animals, for example in flocks of birds or ant colonies, could be seen as examples of collective behavior, which show conceptual similarities with collective tissue behaviors in which cells are coupled and respond to each other (**Figure 1**). Thus, although the definition of behavior can be debatable, here I consider behavior as the integrator between form and function, which arises as an emergent property at different scales during development.

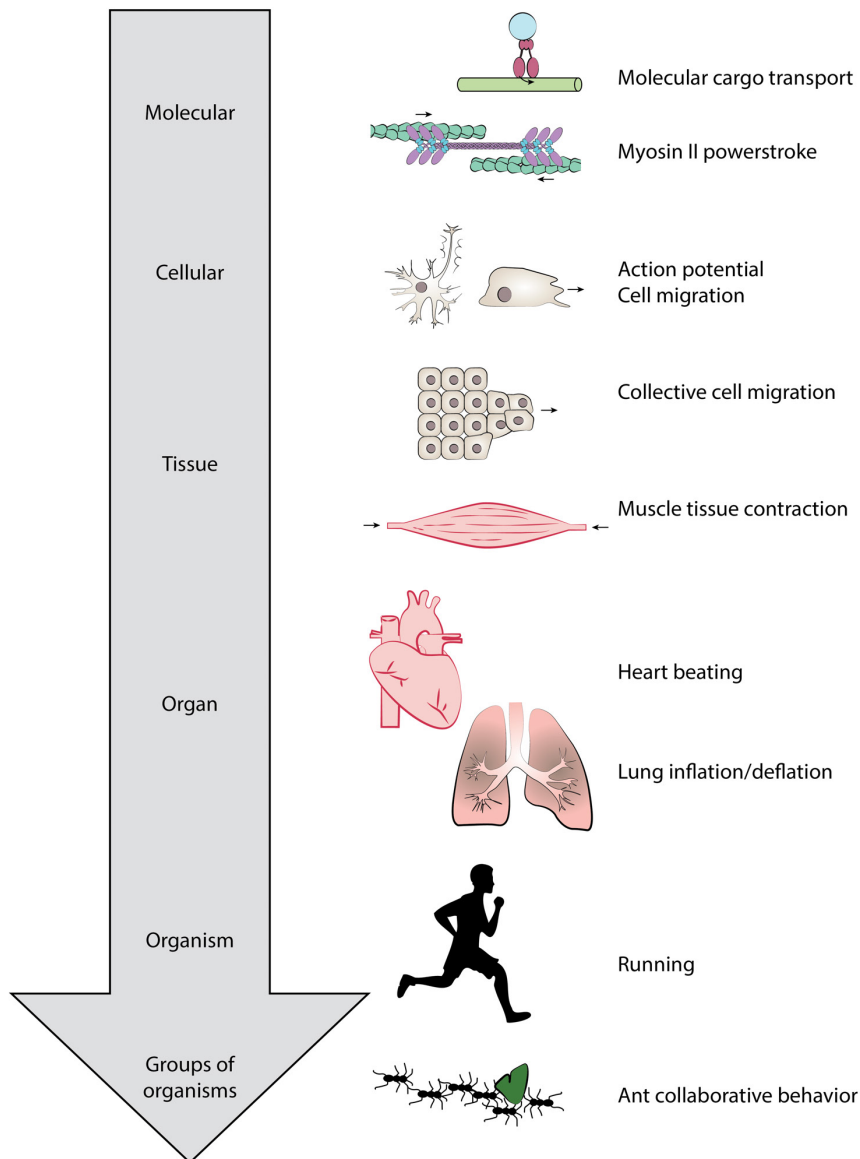


**Figure 1. Examples of biological behaviors at different scales.**

### **1.3. Morphogenetic feedback mechanisms induced by behavior**

Since morphogenesis is a continuous process, new functional properties emerge at different levels in the organism as a result of tissue differentiation and organization: e.g. beating of the developing heart, waves of neuronal activity in the developing brain, or fetal breathing movements. Many of such emerging properties could be classified as cell, tissue, organ, or organismal behaviors. While these behaviors achieve a clear function in the fully developed ‘finished’ organism, they can in some cases also play a role during development and morphogenesis. For example, the development of heart and vasculature requires stresses produced by the fluid flow resulting from heart beating (Andrés-Delgado and Mercader, 2016; Fukui et al., 2021; Lucitti et al., 2007). Similarly, correct neural wiring in the brain requires neural activity, and differentiation of lung cells depends on mechanical forces produced by fetal breathing movements (Li et al., 2018; Penn and Shatz, 1999). As will be

explained in more detail in Chapter 2, emerging contractile behavior has been found to contribute to morphogenesis in multiple settings. For example, muscle alignment in the chick midgut and mouse esophagus depends on contractions generated by neighboring muscle cells (Huycke et al., 2019). Furthermore, embryo elongation in *Caenorhabditis elegans* is dependent on tension generated by muscle contractions (Lardennois et al., 2019; Zhang et al., 2011), and muscle contractions are also involved in lung branching in mouse embryos (Kim et al., 2015). Thus, mechanical forces generated by emerging contractile behaviors at the tissue-to-organ scale can feed back on morphogenetic processes.

#### **1.4. Studying morphogenesis and behavior at the organismal level**

While several behavioral feedback mechanisms have been reported at the tissue-to-organ scale during embryonic morphogenesis, the relationship between behavior and morphogenesis is relatively poorly understood at the organismal level. Traditionally, organismal development and behavior are studied as separate fields. The reason for this is that for most organisms, development and behavior take place at different spatiotemporal scales. Ethology is the science of animal behavior in its ecological system, and mainly focuses on identifying and studying behavioral patterns during post-embryogenesis by for example tracking of body movements and responses while the animal is directly interacting with its surroundings (Escobedo et al., 2020; Wittemyer et al., 2019). In contrast, in developmental biology, organismal morphogenesis is studied mostly in the embryo, at much finer spatial scales but concerning processes that often take hours or days to complete. Studying the potential role of organismal behavior in development thus requires bridging these different spatiotemporal scales. Additional complications arise from the fact that most animals express organismal behaviors mainly post-embryonically, after a complex body plan has already developed. Here, most organismal behaviors involve interaction with the environment, and the presence of different environmental cues can make it difficult to unravel whether a morphological change is a response to an environmental stimulus, or a direct result of animal behavior. Thus, a system to study the potential link between behavior and morphogenesis is ideally a system that shows a simple but clear morphogenetic change, while simultaneously showing organismal behaviors in a non-complex environment.

In this work, I aimed to study the link between organismal behavior and morphogenesis by using larva-polyp transition in the sea anemone *Nematostella vectensis* as a model system. In the next chapters I will first discuss basic concepts of morphogenesis, and then provide background on the biology of cnidarian species and elaborate on why *Nematostella* is a suitable organism to study behavior and morphogenesis.



## 2. Mechanisms of morphogenesis across scales

During morphogenesis, an organism develops its size and shape in a continuous process over time. Here, different parts are not independently formed and assembled, but develop together in the same organism. A set of cellular behaviors consisting of cell growth, cell proliferation, cell death, cell shape changes and cell movements, underlies the morphogenetic changes that occur at higher spatial scales (**Figure 2A**). These behaviors need to be tightly controlled in space and time in order to generate the characteristic shape and size of the developing embryo and produce a functional, living organism. Here, I will discuss concepts of signaling and regulation involved in morphogenesis (**Figure 2B**), and mechanical mechanisms that underlie the execution of morphogenetic processes (**Figure 2C**). Since my project focuses on axial elongation during larva-polyp transition in *Nematostella vectensis*, I will further explain these concepts by discussing how they are employed during axial elongation in other species, namely fruit fly, vertebrate, and nematode embryos.

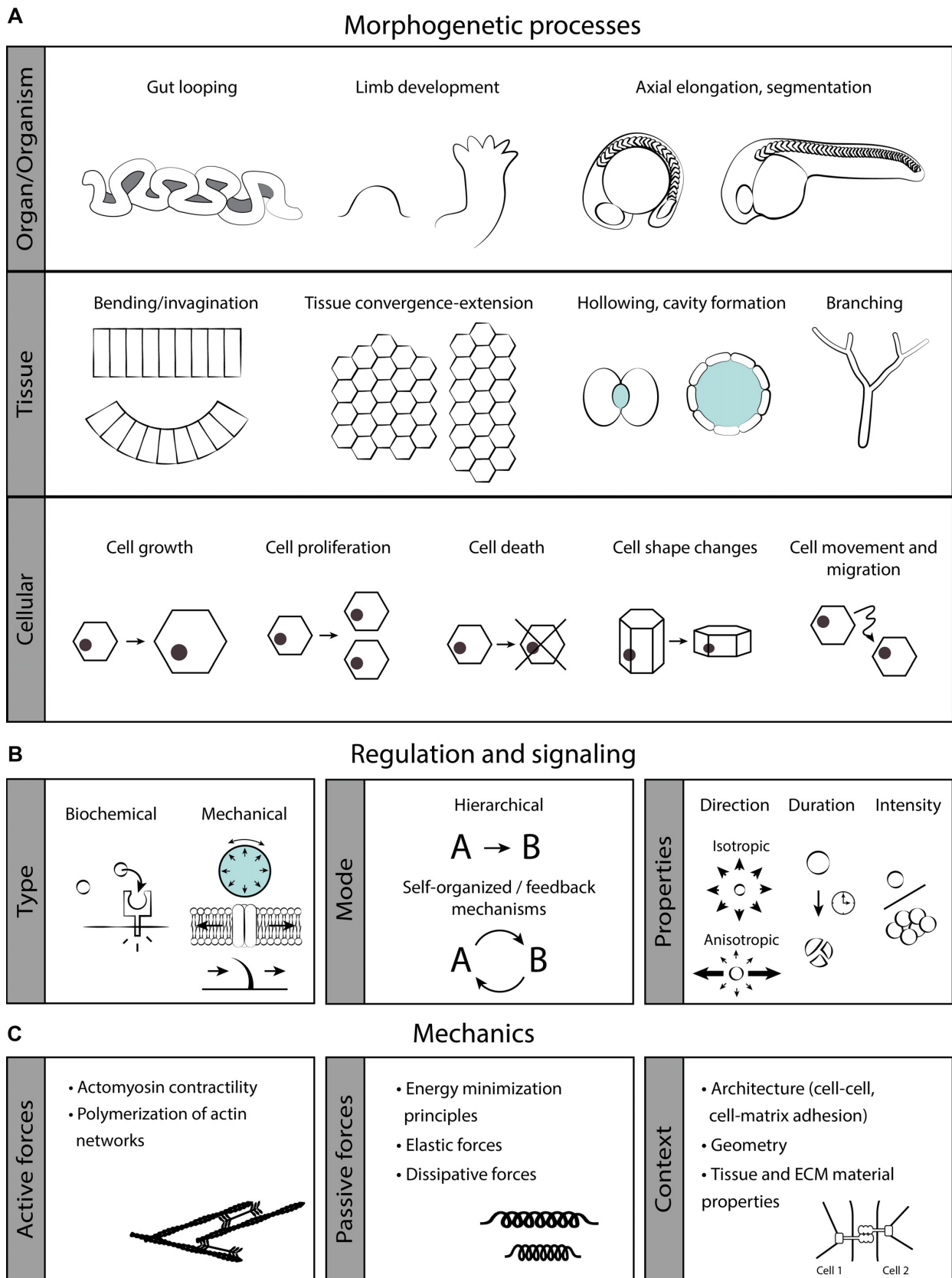


**Figure 2. Morphogenetic processes, their regulation, and mechanical framework.** **A.** Examples of morphogenetic processes at different scales. **B.** Concepts of regulatory mechanisms in morphogenesis. **C.** Mechanical framework underlying morphogenesis, composed of the machinery required for active and passive forces, as well as (material) properties of the tissue and its environment.

## 2.1. Biochemical and mechanical signals guide morphogenesis

Cells can receive and respond to different types of instructive signals (**Figure 2B**). Biochemical signals are frequently used and can act at different ranges. On short distances, neighboring cells can directly communicate with each other through ligands and receptors on the membrane, for example during the establishment of planar cell polarity (PCP) in a tissue (Devenport, 2014). Biochemical communication across a tissue often relies on morphogens, signaling molecules that can induce or regulate morphogenetic processes, such as fibroblast growth factors (FGF) and retinoic acid in the vertebrate presomitic mesoderm (Aulehla and Pourquié, 2010). Morphogen gradients can be established as a result of local production coupled to diffusion and time-dependent degradation. This way, cells at different spatial distances sense different concentrations of the morphogen, which can encode information to induce different cellular responses (Collinet and Lecuit, 2021). Hormones often act over longer distances, and some types can induce morphogenetic changes, for example in metamorphosing insects (Gilbert, 2000).

In addition to biochemical signaling, cells can also respond to mechanical signals. These signals include direct stresses acting on the cell, such as tension, pressure, or shear stress, but can also originate from sensing changes in the stiffness of the surroundings of the cell (Tsata and Beis, 2020). At the molecular level, mechanical forces can be sensed by molecules that unfold or stretch upon mechanical stresses, such as mechanically-gated ion channels, and components of cell-cell and cell-matrix junctions (Hoffman et al., 2011). The process in which a mechanical signal is sensed and translated to a biochemical response is termed mechanotransduction, and it has been found to play a role in numerous processes, including morphogenetic processes, but also cell fate specification and differentiation (Petridou et al., 2017).

Apart from the different nature of the signal (biochemical versus mechanical), there are also different ways in which signals flow (**Figure 2B**) (Collinet and Lecuit, 2021). A signal can follow a simple hierarchical structure, in which one particular cell or tissue sends a signal that is received and responded to by another cell or tissue. In contrast, signaling can also involve feedback loops and/or self-organizing and self-propagating mechanisms. Turing patterns are classic examples where patterns arise without a strict pre-programmed plan, but as the result of a reaction-diffusion mechanism that involves a local activator and a long-range inhibitor (Collinet and Lecuit, 2021). The pattern of follicles forming on the avian skin has been proposed to follow similar Turing pattern principles (Shyer et al., 2017).

Finally, morphogenetic processes can be guided by other properties of the signal, such as direction, duration, frequency and/or intensity of a signal (**Figure 2B**). For example, a stress can be applied equally on the tissue (isotropically), or along a specific axis (anisotropically). In the

*Drosophila* imaginal wing disc, a tension pattern across the tissue regulated by different rates of cell proliferation is thought to control the orientation of cell division (Mao et al., 2013). Also, focal adhesions appear to respond differently to short-term forces than to moderate but sustained forces (Hoffman et al., 2011). Furthermore, embryonic patterning has been shown to scale with a signaling phase gradient during segmentation of the PSM (Lauschke et al., 2013). Here, the phase shift between neighboring PSM cells expressing molecular oscillators depends on the size of the PSM, such that segments form that have a size proportional to the PSM size (Lauschke et al., 2013).

## **2.2. Cell and tissue mechanical mechanisms execute morphogenetic processes**

In response to signals, cells can activate downstream signaling cascades in order to initialize growth, proliferation, apoptosis, cell shape changes, or migration. Cells are the basic building blocks from which organisms are formed, and since these are physical entities, morphogenesis is ultimately a physical process that requires mechanical forces and depends on physical properties of cells and tissue (**Figure 2C**). These forces can be active (generated by cells by hydrolyzing ATP) or passive (e.g. following energy minimization principles). Furthermore, the internal (e.g. tissue architecture and material properties) and external (e.g. extracellular matrix) environment can determine the effect of these forces, as they can provide physical constraints.

### **2.2.1. Generation of active forces**

Active mechanical forces are mostly generated by the actomyosin cytoskeleton at the cellular scale, and by muscles, which also depend on actomyosin contractility at the cellular level, at higher spatial scales. Furthermore, cells can increase their internal osmotic pressure by actively pumping ions (Ellis et al., 2013), and have been proposed to exert pressure on other tissues through random movements along a motility gradient (Bénazéraf et al., 2010).

#### **Force generation through the actomyosin cytoskeleton**

The actomyosin cytoskeleton consists of actin filaments (also called microfilaments) cross-linked by oligomers formed by the myosin II motor protein. Actin filaments consist of actin molecules which can polymerize spontaneously in vitro when the actin monomers (termed G-actin) are sufficiently concentrated. Actin filaments show dynamic assembly/disassembly behavior due to hydrolysis of bound ATP, allowing them to remodel quickly. Before a filament can grow, actin has to form a dimer and then a trimer in a process called nucleation. This process has a low probability of occurring spontaneously, due to the instability of the dimer. However, once a nucleus or trimer is formed, the filament can grow rapidly (Alberts et al., 2015) (**Figure 3A**). Actin filaments are polarized, since the different actin subunits in a filament all point in the same direction. The different ends grow at different rates: the ‘barbed’ or ‘plus’ side grows up to ten times faster than the ‘pointed’ or ‘minus’ end. Since spontaneous nucleation is rare, assembly of new filaments depends on protein

complexes such as Arp2/3 and formin proteins to facilitate nucleation of actin trimers. This way, new filaments can be assembled at specific locations. Arp2/3 bind on the side of other actin filaments and facilitate assembly of a new filament at this location, such that a tree-like network forms. Formin dimers facilitate nucleation of straight, unbranched filaments. These can be bundled together through cross-linking by other proteins. Accessory proteins cross-link and bundle fibers together, creating large and more rigid actin structures. This occurs mostly in the cell cortex, playing an important role in determining cell shape and stiffness (Alberts et al., 2015).

Actin can be organized in contractile structures through the action of myosin motor proteins, which can act both as cross-linkers and as motors that induce sliding of actin filaments. Myosin is a hexameric protein that consists of two heavy chains and two copies of two types of light chains. The head contains the actin binding domain and force generating structure, whereas the long tail mediates dimerization (**Figure 3B**). Myosin II is activated upon phosphorylation of the regulatory light chains by myosin light chain kinase (MLCK). This allows unfolding of the myosin tail and exposure of the actin binding domains in the head region. The tails of different myosin proteins can spontaneously bundle with each other such that bipolar filaments develop, which consist of eight up to several hundreds of myosin proteins, with the heads sticking outwards (**Figure 3C**). Through ATP hydrolysis, myosin heads can perform a 'power stroke', which is a cyclic conformational change that allows myosin heads to push the actin filament in the (-) direction, release it, and bind it again at a new point along the filament, causing the filament to slide. Myosin II minifilaments and actin fibers form networks of distinct organizations, with different contractile properties: for example, highly structured sarcomere-like organization with antiparallel filaments, versus cables with mixed polarity, or branched actomyosin networks (**Figure 3D**) (Alberts et al., 2015).

Myosin II in nonmuscle cells is regulated through phosphorylation of myosin light chain, which can be performed by ROCK or MLCK. ROCK also inactivates myosin light chain phosphatase, which inactivates myosin through dephosphorylation. ROCK is activated through the small GTPase RhoA, which is tethered to the cell membrane. RhoGEFs activate RhoA by exchanging its bound GDP with GTP, whereas RhoGAPs deactivate RhoA by facilitating the opposite reaction. Activation of MLCK is Ca<sup>2+</sup> dependent. Phosphorylation of the myosin regulatory light chain allows actin binding, minifilament assembly, and enables force generation through ATPase activity (Alberts et al., 2015; Craig et al., 1983; Jung et al., 2008).

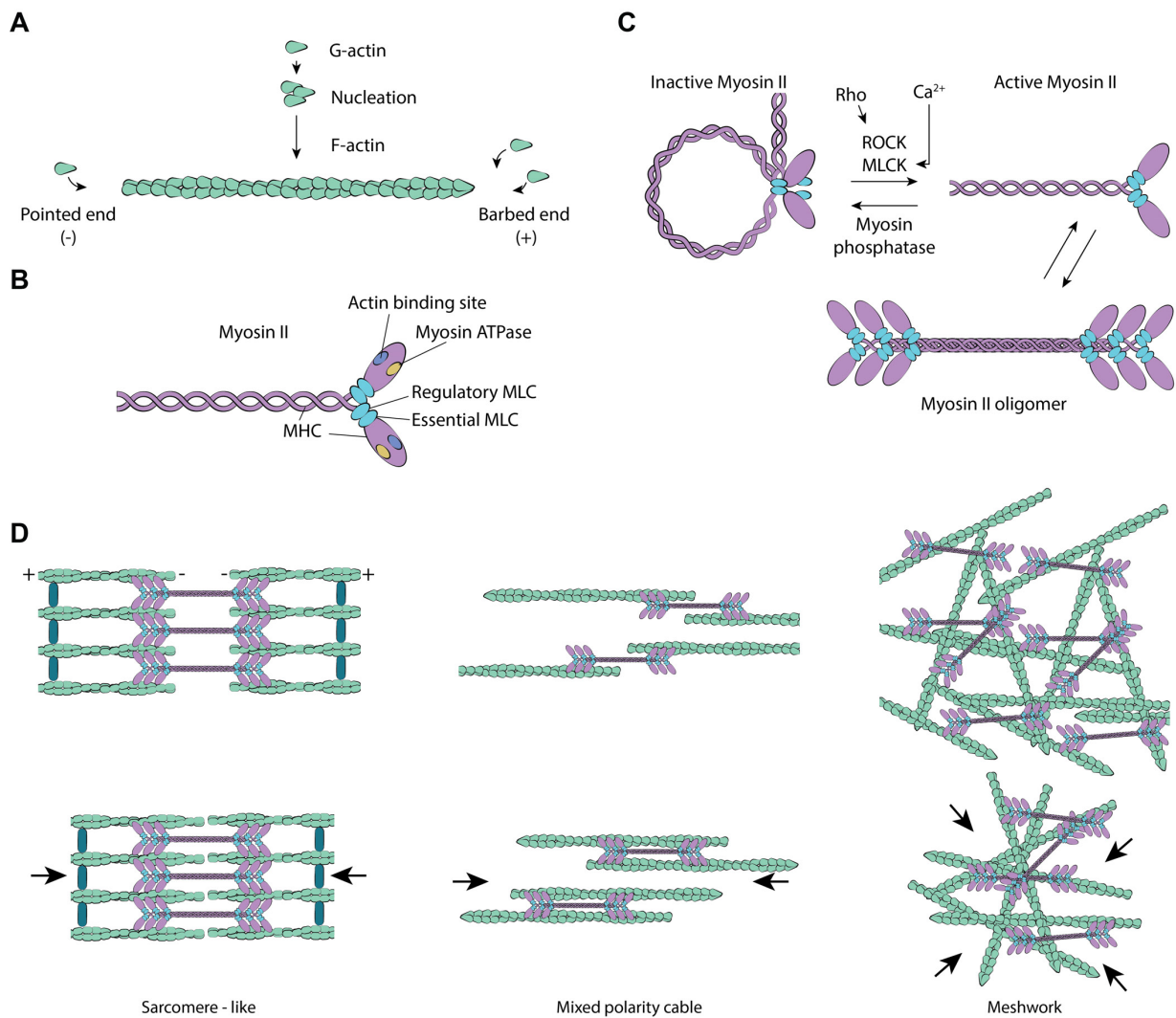


**Figure 3. The actomyosin system.** **A.** Schematic representation of actin polymerization. **B.** Schematic representation of myosin hexamer. **C.** Regulation and minifilament assembly of myosin II. **D.** Different organizations of actomyosin. MHC: myosin heavy chain, MLC: myosin light chain. Schematics are based on drawings from (Alberts et al., 2015; Martin, 2010).

### Force generation by muscles

Muscles are a unique innovation of animals and are well-known for their contractile ability, which is essential for various functions including locomotion, defense, feeding, and digestion. Many bilaterian animals have specialized muscle systems that are mainly derived from the mesoderm. In these animals, the muscle system consists mainly of myocytes, individual muscle cells with a specialized function that can fuse to form multinucleated muscle fibers or stay in a mononucleated form (Susic-Jung et al., 2012). A second type of muscle cells are myoepithelial cells, which, unlike myocytes, have a dual identity and are integrated in epithelial layers and are anchored to extracellular matrix (ECM) (Leclère and Röttinger, 2017). In bilaterians, these cells are mostly found in glandular epithelia (Redman, 1994). Muscle cells can be further categorized in smooth and striated muscles, in which the latter has aligned rows of alternating parallel actin and myosin myofilaments,

spaced by supporting Z-disks. Smooth muscles do not have these alignments but have irregularly spaced myofilaments.

All forms of muscle contraction rely on myosin-induced sliding of actin filaments. Skeletal muscle fibers form through fusion of separate cells. The nuclei of these original cells lay just beneath the cell membrane. The cytoplasm consists mainly of myofibrils, cylindrical structures of chained small contractile units, called sarcomeres. Sarcomeres have a special organization of actin and myosin filaments: actin filaments and myosin thick filaments form interleaved arrays in which the actin filaments point their minus end towards the myosin filaments. The plus end of actin filaments is attached to a Z-disk, a structure built from CapZ and  $\alpha$ -actinin, which protects the filaments from depolymerization. Skeletal muscle can contract rapidly upon stimulation by the associated nerve. When this happens, all sarcomeres contract simultaneously, through ATP hydrolysis of the myosin heads, facilitating many powerstrokes at once. This is possible through a specialized membrane system around the myofibrils, which allows influx of  $\text{Ca}^{2+}$  into the cytosol. Skeletal muscle cells can respond so rapidly to  $\text{Ca}^{2+}$  influx because they express the accessory proteins tropomyosin and troponin, which lock the system such that the myosin heads cannot push on the actin fibers in the absence of  $\text{Ca}^{2+}$ , but release it as soon as the  $\text{Ca}^{2+}$  signal enters the cell. Smooth muscles do not express troponins, but in these cells  $\text{Ca}^{2+}$  influx triggers contraction through binding of calmodulin, which activates MLCK. MLCK phosphorylates myosin light chain, allowing myosin to interact with actin filaments. Phosphorylation-mediated contraction is slow compared to the troponin mechanism (Alberts et al., 2015).

### **Long-range mechanical input during morphogenesis**

Tissue-scale active mechanical forces can originate from local forces in the tissue, or from processes taking place in connected tissues elsewhere. Fluid flow and pressure are other sources of mechanical signals and forces that can have relatively long-range effects in morphogenesis. At the early organismal scale in mouse embryos, luminal pressure has been shown to play a role in controlling embryo size (Chan et al., 2019), and leftward flow of extraembryonic fluid, referred to as nodal flow, is crucial for normal left-right patterning in vertebrate embryos (Nonaka et al., 1998). At the level of organogenesis, fluid flow and associated shear stress have been shown to be important regulators in for example lung, heart, and lymphatic vasculature development (Alcorn et al., 1977; Desmond and Jacobson, 1977; Planas-Paz et al., 2012). When fluid flow is not generated by cilia, it is often driven by muscle contractions, such as is the case for blood flow driven by heart muscle contraction, and airway peristalsis in the developing lung (Bokka et al., 2015; Fukui et al., 2021). Muscles can also directly and indirectly regulate morphogenetic processes without producing fluid flow. For example, the short-term mechanical deformations resulting from embryonic gut peristaltic contractions have been shown to result in long-term elongation of the gut (Khalipina et al., 2019).

Also, muscle organization in the gut has been shown to depend on muscle contraction: longitudinal alignment of the gut muscles in the outer layer depends on cyclic contractions of the inner layer of circular muscles (Huycke et al., 2019). These findings indicate that muscle contractions can play important roles at the tissue-to-organismal scale during morphogenesis, either by generating fluid flows that produce mechanical stresses, or by directly acting on (neighboring) tissues, generating mechanical signals that trigger mechanotransduction pathways or that directly ‘self-squeeze’ the tissue.

### **2.2.2. Passive forces contributing to morphogenesis**

Passive forces during morphogenesis can arise from multiple sources, such as elasticity of tissues, dissipation forces such as friction, or from energy minimization principles. For example, friction between different tissues has been shown to be involved in formation of the chevron shape in the zebrafish myotome (Tlili et al., 2019). A simple, non-biological example of energy minimization is a soap bubble that adopts a spherical shape because this minimizes its surface area. When multiple bubbles are put together in a foam, they form organizations that minimize the total combined surface area. As described in famous work by D’Arcy Thompson, these principles can, to some extent, also be applied to cells and tissues (Thompson, 1942). However, it is important to note that in cells additional forces are at play, and cell shapes in tissues are generally balanced by a combination of adhesive forces, e.g. due to cell-cell adhesion via cadherins, and cortical tension, regulated by the cytoskeleton (Graner and Rivelino, 2017).

Another example that involves energy minimization is illustrated by the looping of the gut. The gut and the dorsal mesenteric sheet are attached to each other, and grow at different rates during development. This results in in-plane stretching and shearing deformations, and out-of-plane bending deformations. The looping occurs passively in order to find a more stable configuration, i.e. minimizing the energy associated with these deformations (Savin et al., 2011). Also, gut villi in chick are thought to form due to restriction of space by growth of circular muscles followed by longitudinal muscles, which creates compression forces that push the inner gut epithelium outwards, and thereby produce ridges, zigzags, and eventually villi (Shyer et al., 2013). Thus, active processes in one tissue can induce morphogenesis through passive forces in another.

### **2.2.3. Tissue architecture, material properties, and extracellular environment**

Apart from the forces required to shape an organism, the extracellular environment and the way cells are organized with respect to each other (i.e. the ‘context’) play a major role in different ways. The characteristic folding, bending, and invagination processes occurring in epithelial sheets of tissue can only take place because of the way epithelia are organized: cells are polarized and are attached to each other through cell-cell junctions, and to the ECM through cell-matrix junctions. This



way, forces can be sensed and can act throughout the tissue, inducing specific deformations. Furthermore, the effect of an applied force on a tissue depends on the material properties of that tissue, i.e. its stiffness, elasticity, and viscosity, and the material properties and geometry of the surroundings can determine in which directions and to which extent a tissue can deform (Collinet and Lecuit, 2021; Petridou et al., 2021; Stooke-Vaughan and Campàs, 2018; Tsata and Beis, 2020). The importance of the relative stiffness between a deforming tissue and its surroundings is for example illustrated in gastrulation in *Xenopus laevis*. This involves convergence-extension movements in the notochord that can only take place correctly if the notochord are sufficiently stiff to resist buckling by surrounding tissues (Adams and Koehu, 1990; Keller et al., 1989).

### **Epithelial architecture**

In epithelial tissues, cells are tightly adhered to one another to form an almost impermeable sheet, that can separate the inside from the outside of multicellular organisms, or subdivide it in different compartments. Epithelia can be organized in different ways. Simple epithelia consist of a single cell layer attached to a thin layer of ECM, called the basal lamina. In contrast, stratified epithelia consist of multiple layers of cells, in which only the bottom cells are adhered to the basal lamina. In pseudo-stratified epithelia all cells are adhered to the basal lamina, but they are arranged such that not all of them reach the top. The coherent nature of epithelia has implications for morphogenetic processes that can take place in epithelia, which can undergo changes such as folding and invagination that are not possible in other tissues that do not have such a strong interconnection between cells. Stresses generated by or sensed by other cells are communicated through the tissue, and therefore the tissue functions as a whole (Davies, 2013).

### **Cell-cell adhesion**

Linkage of cells allows coordinated use of the cytoskeletons across cells. In epithelia, cells are connected to each other through cell-cell junctions and connected to the basal lamina through cell-matrix junctions. Cytoskeletal filaments attach to these junctions, allowing transmission of stresses across different cells. Different types of junctions exist and are arranged differently in the cell. Most apically are tight junctions, which seal the space between different cells and thereby prevent diffusion of molecules into the intercellular space. Non-chordates do not have tight junctions, but have septate junctions instead, which have a different composition but are thought to serve similar functions (Magie and Martindale, 2008). Below the tight junctions are the adherens junctions that form a belt around the cell. Adherens junctions link cells via the transmembrane protein (E-)cadherin and are connected to actin filaments through catenins and other adaptor proteins (**Figure 4**). Through this organization, actomyosin contraction-generated tension can be transmitted to neighboring cells, which can trigger signaling cascades. Adherens junctions can form an adhesion belt (zonula adherens) below the apical surface of the cell, thereby connecting all cells in a sheet.

Constriction in a selected part of the epithelium can then result in invagination of the sheet, and pinching off from the overlaying cells (Davies, 2013). Below the adherens junctions are the desmosomes, which use different types of cadherins, and, similar to adherens junctions, are linked to the cytoskeleton, but to intermediate filaments instead of actin. They provide mechanical strength and allow mechanical loads to be shared by all cells in the epithelium. Gap junctions are structures that form small channels between cells through which small molecules, such as certain signaling molecules, can pass. Cells are connected at the basal side to the basal lamina through focal adhesions, which are linked to the actin cytoskeleton, and hemidesmosomes, which are linked to intermediate filaments. Both focal adhesions and hemidesmosomes use (different types of) integrins to bind to the extracellular matrix components (**Figure 4**) (Alberts et al., 2015). Pulling forces at junctions are important for junction assembly, maintenance, and maturation. Junctions linked to the cytoskeleton are often mechanosensitive, and respond directly to mechanical signals by strengthening the bonds between cells. More specifically, the interaction between E-cadherin, catenins and actin in adherens junctions is tension-dependent. Tension is thought to be sensed by  $\alpha$ -catenin, which undergoes a conformational change in response to tension, revealing a binding site for other junction components (Yonemura et al., 2010).

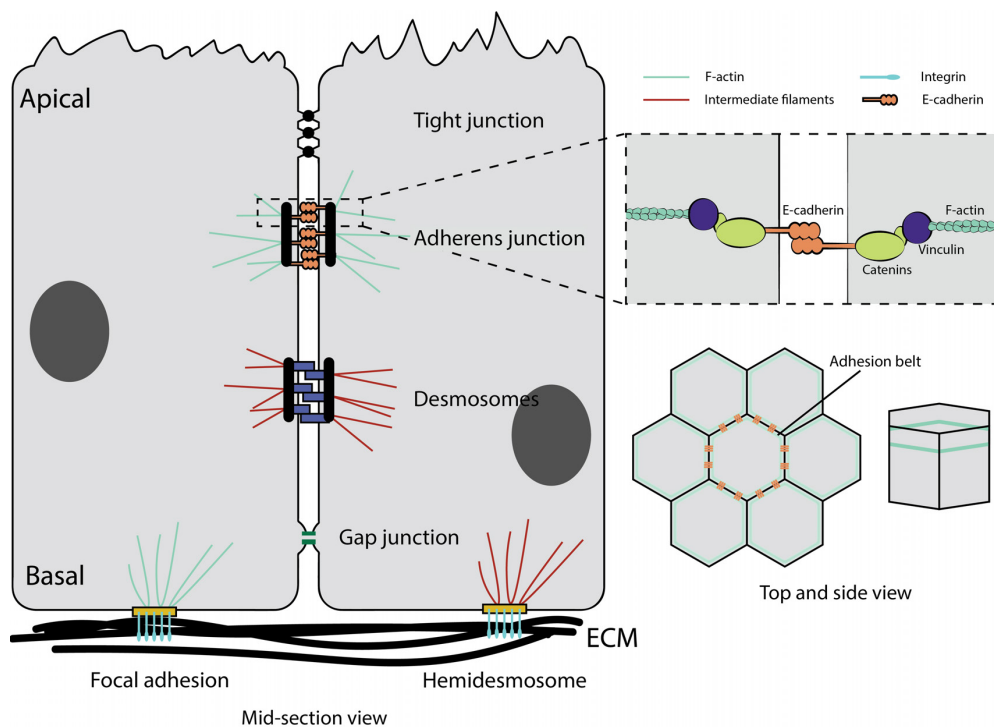


**Figure 4. Different types of junctions in cell-cell and cell-matrix contacts.** Schematic is based on drawings from (Alberts et al., 2015; Davies, 2013)

### The cytoskeleton determines tissue properties

Tissue morphogenesis presents specific requirements to tissue material properties. On one hand, a tissue has to be sufficiently stable such as to not break down under sudden stresses. On the

other hand, tissues need to be sufficiently plastic or ‘fluid’ in order for morphogenetic processes to occur. The cytoskeleton is an important regulator of material properties of cells and tissues. On short timescales (below one to five minutes), tissues show elastic behavior to sudden applied stresses, meaning that they revert back to their original shape as soon as the stress is removed. This is because on short time scales, macromolecular structures cannot rearrange fast enough to remodel in response to stress. In contrast, at longer timescales, tissues often show viscous behavior, meaning that they can slowly flow and acquire a new shape in response to applied stresses. This is due to turnover of crosslinkers in the actomyosin network and actin remodeling and sliding. This so-called viscoelastic behavior is an important characteristic: elasticity can stabilize cell shape and prevent accidental permanent deformation, whereas long timescale fluidity provides plasticity to the system, allowing it to undergo morphogenetic changes (Clément et al., 2017; Collinet and Lecuit, 2021). In some cases, a tissue will behave as a fluid only when a certain level of stress is reached, the so-called yield stress (Mongera et al., 2018), whereas it has also been reported that some tissues can maintain solid properties over longer periods of time (Luu et al., 2011).

Another important material property is tissue stiffness, i.e. the degree of resistance to deformation. Cells can increase their stiffness by increasing actomyosin contractility. At the tissue scale, cell-cell adhesion-dependent connectivity is an important predictor of tissue stiffness, as has been shown during tissue phase-transition in the zebrafish embryo (Petridou et al., 2021). The stiffness of the ECM depends on the composition and organization of the different matrix components. The relative stiffness between different tissues and between tissue and the surroundings is an important factor in determining how movements and shape changes will take place.

### **2.3. Axial elongation in different developing systems**

As discussed, morphogenesis requires control and coordination of cellular behaviors in time and space to drive changes at higher scales. One major morphogenetic change taking place at the organismal level is axial elongation, which is a common process during morphogenesis of many different species. Here, I will briefly discuss some of the mechanisms underlying axial elongation in embryos of the fruit fly *Drosophila melanogaster*, vertebrate species, and the nematode *Caenorhabditis elegans*.

#### **2.3.1. Germband elongation in *Drosophila***

Body axis elongation during embryogenesis in *Drosophila* is a well-studied morphogenetic process. Shortly after the onset of gastrulation, the region that will form the segmented trunk of the larva, the germband, extends and thins and bends around itself. Cells from the sides converge to the middle and insert themselves between other cells, such that the tissue elongates as a whole and

increases around two-fold in length (Bertet et al., 2004; Irvine and Wieschaus, 1994). Three different processes, taking place at different times and locations, have been described to contribute to germband elongation: cell intercalation, cell shape change, and oriented cell division (**Figure 5**).

Cell intercalation has been extensively studied in *Drosophila* germband elongation. During this process, cells exchange neighbors while remaining integrated in the epithelium, which requires junction remodeling. Mechanistically, this can occur through T1 transitions, or via rosette formation (Bertet et al., 2004; Blankenship et al., 2006). In order for the tissue to elongate, junction shrinkage must be restricted to boundaries perpendicular to the direction of extension. This is established through planar polarity in the tissue, which via Rho-1 leads to activation of actomyosin on dorsal-ventral (D/V) junctions and subsequent junction shortening, while Bazooka/PAR-3 maintains junction integrity along anterior-posterior (A/P) junctions (Blankenship et al., 2006; Simões et al., 2010; Zallen and Wieschaus, 2004). Which pathways are involved in establishing planar polarity during gastrulation is still subject to ongoing debate (Kong et al., 2017). *Toll-2,6,8*, members of the Toll receptor family, are expressed in stripes along the anterior-posterior axis. In *Toll-2,6,8* triple mutants, the distinct distribution of myosin II at D/V junctions and Bazooka/PAR-3 at A/P junctions is weakened, and germband elongation is reduced (Paré et al., 2014), indicating that these proteins contribute, but may not completely explain, establishment of polarity. In many tissues, establishment of planar cell polarity (PCP) involves the Frizzled-dependent signaling pathway, but germband extension occurs normally in embryos that lack *dishevelled* or Frizzled and Frizzled2 receptors (Zallen and Wieschaus, 2004), suggesting that Frizzled-dependent planar cell polarity may not play a major role in germband elongation. In addition to accumulation of myosin II at D/V junctions, junction collapse also involves dynamic behavior of actomyosin (Rauzi et al., 2010). Clusters of actomyosin at the cortex show pulsatile behavior and flow to vertical junctions where they are thought to generate forces to gradually shorten junctions (Rauzi et al., 2010). Subsequently, contraction of medial myosin II in the anterior and posterior cells is thought to drive junction extension (Collinet et al., 2015) (**Figure 5**).

Recently, it has been shown that in addition to local stresses driving junction remodeling, tissue-scale pulling forces produced by the invaginating posterior midgut also play a role in tissue extension, by stretching cells and orienting junction growth (Collinet et al., 2015; Lye et al., 2015) (**Figure 5**). Also, oriented cell division have been found to contribute to germband elongation, but is restricted to the posterior part of the germband during the early, fast phase of germband elongation (da Silva and Vincent, 2007) (**Figure 5**).

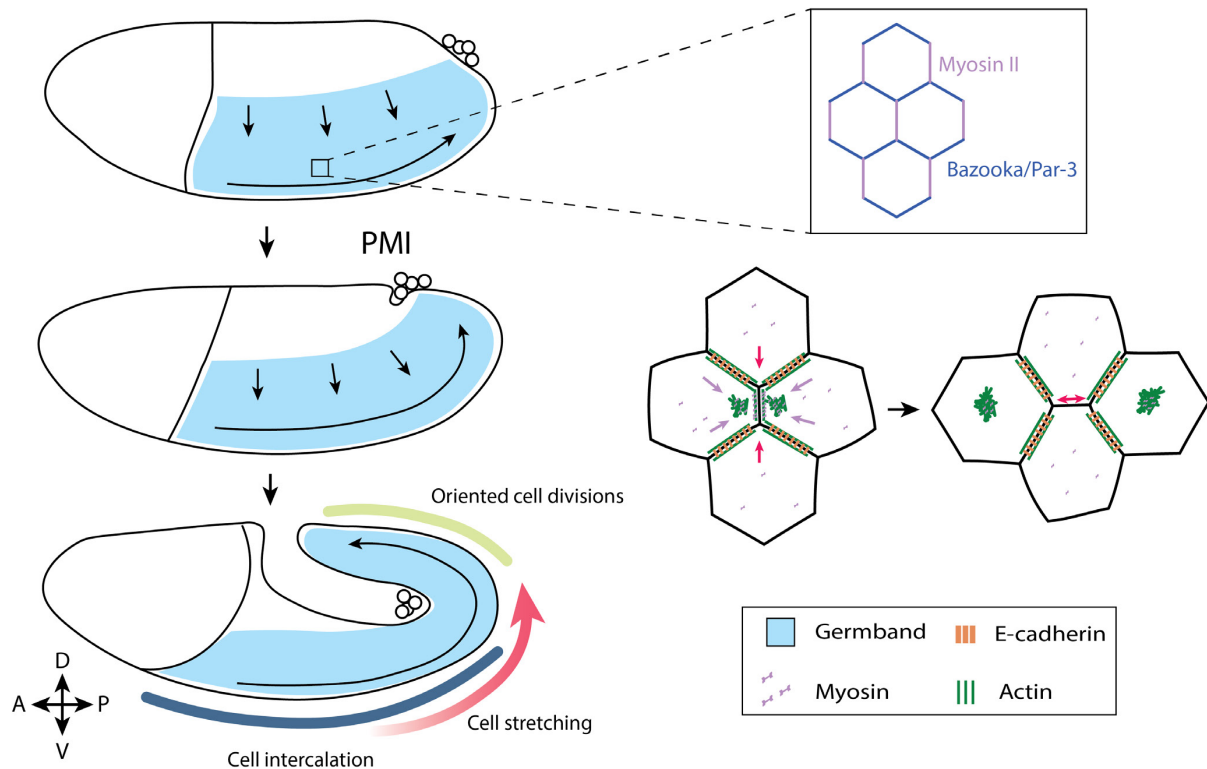


**Figure 5. Schematics of germband elongation in *Drosophila*.** On the left: three stages of germband (light blue) elongation. Black arrows in the embryo indicate tissue flow. Colors in the bottom schematic roughly indicate regions where three different cellular morphogenetic motifs have been observed: cell intercalation (dark blue) takes place in the anterior and middle part of the germband, whereas oriented cell divisions (green) have been shown to contribute to elongation in the posterior part that bends around the embryo (da Silva and Vincent, 2007). Pulling forces exerted by the invaginating posterior midgut (PMI) (pink) have been shown to stretch cells and help orienting newly forming junctions (Collinet et al., 2015; Lye et al., 2015). On the right: planar polarized distribution of myosin II and Bazooka/PAR-3, and a schematic representation of a T1 transition involving myosin II flow towards the junction to shorten it, and contraction of medial myosin II to help formation of a new junction (Collinet et al., 2015; Rauzi et al., 2010). Schematic is based on drawings from (Kong et al., 2017).

### 2.3.2. Anteroposterior axis formation in vertebrate embryos

Formation of the anteroposterior axis in vertebrate embryos involves elongation of multiple tissues, and takes place across multiple stages of embryonic development, from gastrulation to the formation of the last segments during somitogenesis (Bénazéraf, 2019; Bénazéraf and Pourquie, 2013; Mongera et al., 2019). This process involves both rearrangement of existing cells through cell intercalation and cell migration, as well as volumetric growth through proliferation, cell growth and matrix deposition. While cell intercalation and cell migration take place predominantly during early axial elongation and happen on short time scales, volumetric growth accounts for later elongation in the posterior part of the embryo and is slow compared to cell rearrangements, as it is limited by the duration of the cell cycle (Mongera et al., 2019). The relative duration of cell rearrangements and volumetric growth differ between vertebrate species. In zebrafish and *Xenopus*, cell rearrangements during axial elongation span over a longer period of time relative to amniotes, such as chick and mouse embryos, while volumetric growth is smaller (Mongera et al., 2019; Steventon et al., 2016).

Furthermore, several mechanical factors have been found important for elongation in vertebrate embryos, including the ATP-dependent inflation of vacuoles in the notochord of zebrafish, which results in stiffening important for elongation (Ellis et al., 2013), friction forces at the interface between different tissues (Smutny et al., 2017), and cell-matrix adhesion, since loss of stable adhesion results in tissue buckling in zebrafish (Dray et al., 2013).

Vertebrate embryos develop from head to tail, and elongation is initiated by the formation of the primitive streak (formation of the blastopore in anamniotes) and continues by subsequent primitive streak elongation. Elongation of the anterior part of the body takes place during early gastrulation, and occurs mainly through tissue convergence and extension. This can take place through two distinct processes: collective cell migration and cell-cell intercalation, which have both been shown to contribute to elongation in different species, including chicken, zebrafish, and *Xenopus* (Bénaïzeraf and Pourqu  , 2013; Lawson and Schoenwolf, 2001; Sepich et al., 2005; Tada and Heisenberg, 2012). Mesenchymal cells typically intercalate through a mechanism called mediolateral cell intercalation, which involves formation of actomyosin-dependent cell protrusions, rather than remodeling of cell junctions as described earlier in *Drosophila* germband elongation (Shindo, 2018). Mediolateral cell intercalation depends on the PCP pathway and was first described in *Xenopus*, where mesodermal and neural plate cells move towards the midline and induce elongation of the notochord, neural tube, and paraxial mesoderm, but this process also been reported in other species (B  n  zeraf and Pourqu  , 2013; Goto et al., 2005; Shih and Keller, 1992; Yen et al., 2009; Yin et al., 2008).

Later, when the posterior streak has fully regressed in birds and mammals, further elongation occurs in the posterior region and takes place mainly through supply of new cells and volumetric growth (B  n  zeraf and Pourqu  , 2013; Catala et al., 1995; Mongera et al., 2019). During this time, axis elongation takes place in concert with axis segmentation. In a process called somitogenesis, a posterior region of paraxial mesoderm, called the presomitic mesoderm (PSM), periodically segments into somites, which are epithelial structures that give rise to the vertebrae, ribs, muscle and dermis of the back. This process is regulated by the segmentation clock, together with signaling gradients of FGF and retinoic acid (Resende et al., 2014). Cell proliferation takes place in a progenitor region in the tailbud, which continuously supplies new cells to the PSM. Tailbud cells contribute to both mesodermal and neuroectodermal lineages, sustaining elongation of all tissues (Cambray and Wilson, 2002; Tzouanacou et al., 2009). The continuous supply of new cells from the tail bud region has been proposed to drive a self-sustaining mechanical mechanism in chick embryos (Xiong et al., 2020). Cells migrating out of the tail bud have high cell motility, which is regulated by a posterior-to-anterior gradient of FGF signaling in the PSM (B  n  zeraf et al., 2010). This gradient is opposed by a cell rigidity gradient towards the anterior of the embryo, which is thought to play a role

in maintaining a straight and extended axis. This active cell behavior is thought to generate pressure on the neural tube and notochord, which compress laterally and extend posteriorly, driving elongation (Mongera et al., 2018; Xiong et al., 2020) (**Figure 6**).

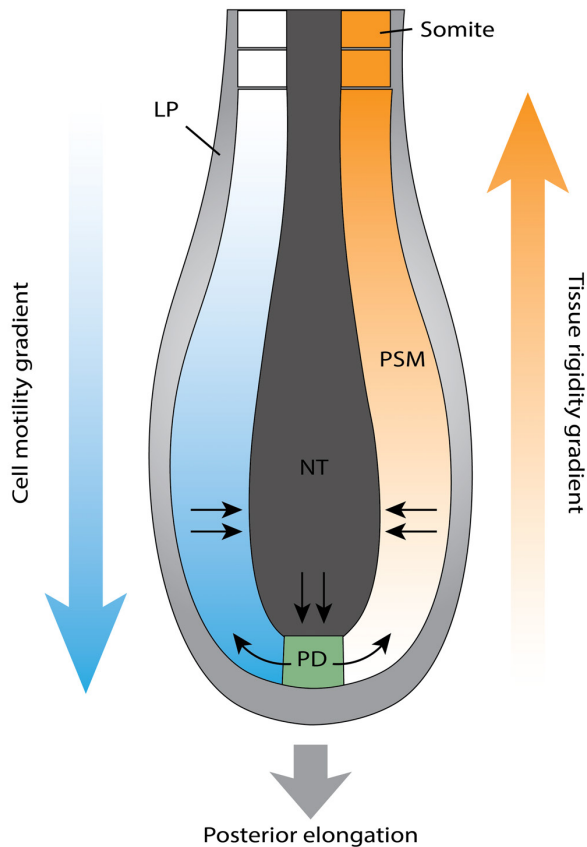


**Figure 6. Model of a mechanical feedback loop driving posterior elongation in the chick embryo.** A random motility gradient in the PSM is opposed by a tissue rigidity gradient. In addition, movement of PSM cells is limited by the presence of the lateral plate (LP). Due to this confinements, the pushing forces exerted by the moving PSM cells have been proposed to drive elongation posteriorly (Bénazéraf et al., 2010; Regev et al., 2017). Xiong et al. (2018), propose that these motile cells compress axial tissues, which then drive elongation. In turn, the neural tube (NT) and notochord push on the progenitor domain (PD) in the tailbud, which promotes release of new cells from the tailbud which replenish both the PSM and supply cells to the axial tissues (Xiong et al., 2020). Schematic based on drawings and data from (Mongera et al., 2019; Xiong et al., 2020).

### 2.3.3. Axial elongation in *C. elegans*

After the initial stages of embryogenesis, *C. elegans* embryos undergo an elongation of about four-fold from the ‘bean’ stage (corresponding to one-fold) to the ‘pretzel’ stage (corresponding to four-fold) (Priess and Hirsh, 1986) (**Figure 7**). Similar to axial elongation in vertebrate species, elongation in *C. elegans* also involves coordination between multiple tissues, in this case the dorsal/ventral epidermis, the lateral epidermis, and muscles. The epidermis in the *C. elegans* embryo consists of six strips of cells that run from head to tail. The strips on the two sides of the embryo are called the seam cells, or lateral epidermis, and have short and disorganized actin filaments together with high levels of non-muscle myosin II, promoting actomyosin contractility. In contrast, the total

of four strips of dorsal and ventral cells have parallel circumferential actin bundles (Priess and Hirsh, 1986). In contrast to axial elongation in vertebrate embryos, elongation in the nematode *C. elegans* does not involve cell proliferation or migration (Sulston et al., 1983). Instead, epidermal cell shape changes underlie axial elongation. Initially, the longest axis of epidermal cells is oriented along the dorsal-ventral axis, but during embryo elongation the cell angles rotate by 90 °. Initial elongation is thought to depend on actomyosin activity in the seam cells but not in dorsal and ventral cells. The RhoGEF RHGF-2 is a positive regulator of ROCK activity and is expressed in the seam cells, whereas the RhoGAP RGA2 negatively regulates ROCK activity in the dorsal and ventral cells, resulting in high tension in the seam cells compared to the dorsal and ventral cells (Chan et al., 2015; Diogon et al., 2007). During early elongation, actomyosin contractions in the seam cells are thought to squeeze the embryo, increasing internal hydrostatic pressure to drive elongation. The rigid actin bundles in the dorsal and ventral cells confer stiffness to the system, such that elongation occurs along the anterior-posterior axis (Vuong-Brender et al., 2017).

Muscle contraction occurs from the 1.7-fold stage onwards and is required for late elongation, as muscle defective embryos (Pat-phenotype) arrest at the two-fold stage (Williams and Waterston, 1994). A mechanotransduction pathway that links muscle tension to hemidesmosome maturation in the dorsal and ventral cells has been shown to promote morphogenesis during this stage (Zhang et al., 2011). While hemidesmosomes are thought to relay the signal from the muscle to the dorsal and ventral cells, adherens junctions are proposed to communicate the signal between the dorsal/ventral cells and the seam cells (Gillard et al., 2019). Here, muscle contraction has been shown to induce planar polarization of the PAR module in the seam cells, which promotes dorsal-ventral organization of actin. Absence of muscle contraction or PAR polarization leads to actin misorientation, and cells do not reorient themselves from dorsal-ventral to anterior-posterior orientation (Gillard et al., 2019). In addition to promoting dorsal-ventral actin organization in seam cells, muscle contraction is also thought to impact the organization of actin bundles in the dorsal and ventral cells (Lardennois et al., 2019). Since the embryo volume remains constant during elongation, an increase in length must be accompanied with a reduction in diameter. This means that the actin bundles in the dorsal and ventral cells need to shorten. Since the muscles and the epidermis are tightly connected through hemidesmosomes, muscle contractions can displace and stretch epidermal cells. Through elastic behavior, the cell would revert back to its original shape as soon as the stress is removed, unless the new cell shape is somehow stabilized. It is thought that a mechanical visco-plastic deformation process facilitates this: while stretching of cells induces actin severing, capping or bundling of the severed actin filaments can ‘repair’ them while at the same time induce shortening of the actin cables. This stabilizes the new cell shape in a ratchet-like mechanism (Lardennois et al., 2019). Thus, axial elongation in *C. elegans* involves coordination between the



muscles and the different epidermal cells, in which muscle contraction is thought to 1) promote dorsal-ventral actin organization in the contractile seam cells to promote cell elongation along the anterior-posterior axis, and 2) stretch dorsal and ventral cells while triggering actin severing, which, followed by capping or bundling stabilizes cell shape by shortening actin cables (Gillard et al., 2019; Lardennois et al., 2019; Vuong-Brender et al., 2017) (Figure 7).

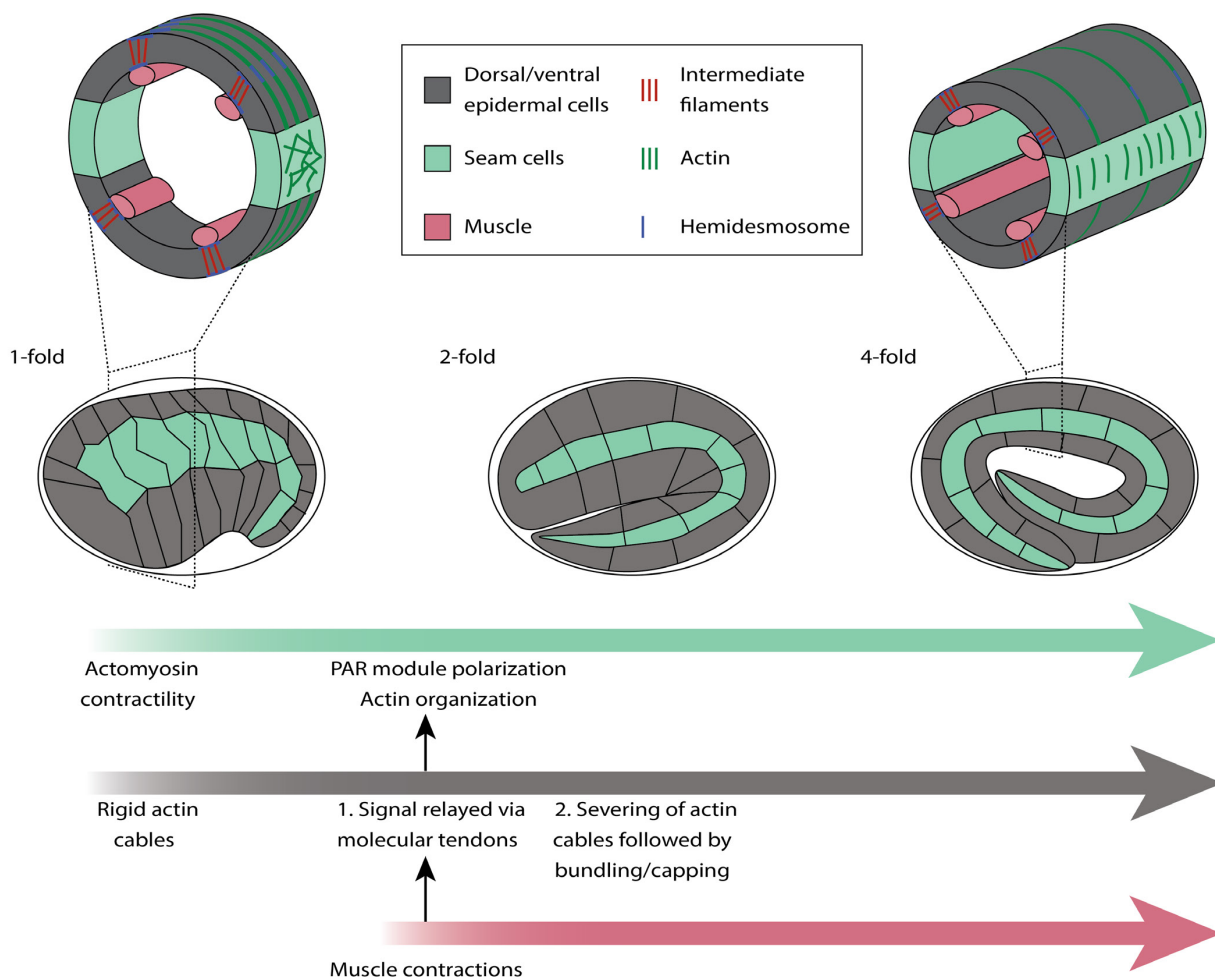


**Figure 7. Schematic representation of axial elongation in *C. elegans*.** This process is thought to involve interaction between three different tissues: contractile seam cells (green), passive dorsal and ventral cells (grey), and muscles (pink). Muscle contraction starts around the 1.7-fold stage, and is thought to induce a mechanotransduction pathway in the epidermis that promotes morphogenesis (Gillard et al., 2019; Zhang et al., 2011). Furthermore, muscle contraction is thought to stretch epidermal cells and induce actin severing, which can promote shortening of the actin bundles in the dorsal and ventral cells, stabilizing cell shape (Lardennois et al., 2019). Schematics are based on data and drawings from (Gillard et al., 2019; Lardennois et al., 2019; Zhang et al., 2011).



## 3. Cnidarian development

### 3.1. Evolution, life cycle and morphology

Cnidarians (corals, sea anemones, hydroids and jellyfish) are a diverse group of mainly marine organisms. They are divided into anthozoans (sea anemones and corals) and medusozoans (jellyfish and hydroids). Anthozoans are mostly sessile and form polyps, whereas medusozoans often have both a polyp and a free swimming medusa stage. Cnidarians are diploblastic animals, meaning that they develop from two germ layers: ectoderm and endoderm, and lack a mesoderm. They have a non-centralized nerve net and typically have a single gut opening. From the outside, they appear radially symmetric, but many species have internal asymmetries. The characteristic trait of the phylum is the stinging cell, or nematocyte, which is used for catching prey and defense. The phylogenetic position of cnidarians as the sister group of bilaterians makes them interesting for studying evolution of bilaterians, but cnidarians are also used for studying other fields, such as ecology, regeneration and morphogenesis (Abrams et al., 2015; Fritz et al., 2013; Ikmi et al., 2020; Levy et al., 2021; Livshits et al., 2017; Martindale et al., 2004; Pukhlyakova et al., 2019; Ryan et al., 2007; Steinmetz et al., 2017; Watanabe et al., 2009).

### 3.2. Metamorphosis in cnidarians

The life cycle of cnidarian species typically involves multiple phenotypes. Gastrulation first yields two-layered, free-swimming planula larvae, which subsequently settle and undergo metamorphosis to become benthic polyps with oral tentacles. Whereas the polyp stage is the final form in anthozoans, medusozoan species from the classes Scyphozoa and Cubozoa generate another free-swimming, sexually mature form known as a medusa or jellyfish that is generated through asexual propagation by the benthic polyp form. In Hydrozoa, the medusa stage is absent, but polyps can both sexually and asexually reproduce, in the latter case via lateral budding. The mechanisms that induce metamorphosis differ between cnidarian species, but typically rely on external stimuli, unlike the intrinsic elevation of hormones that trigger metamorphosis in insects and amphibians (Leitz, 1997). These external stimuli are often derived from chemicals from bacteria or algae, that live on the substrate to which the larva attaches (Leitz, 1997; Müller and Leitz, 2002). For many species, however, the exact natural inducers of metamorphosis are unknown (Leitz, 1997; Müller and Leitz, 2002). Also, not all species require such signals, whereas others require highly specific signals. Possibly, the specificity of the required signal correlates with the ability of the juvenile form to move to a more suitable environment post-metamorphosis (Müller and Leitz, 2002). Whereas the sea anemone *Nematostella vectensis*, which typically digs itself in soft sediments but remains mobile after metamorphosis, does not appear to rely on any external cues to induce metamorphosis, species

that settle permanently on hard substrates, such as the coral *Acropora millepora*, the jellyfish *Cassiopeia andromeda*, and the hydroid *Hydractinia* are dependent on specific signals that are indicative of a suitable niche (Hand and Uhlinger, 1992; Hofmann and Brand, 1987; Muller, 1969; Müller and Leitz, 2002; Negri et al., 2001). In these species, larvae sink and often explore the substrate, and when a suitable substrate is found, they adhere themselves permanently before metamorphosis is initiated (Müller and Leitz, 2002).

It is thought that the nervous system plays a role in signaling downstream of the sensory cells, as several ions, neurotransmitters, such as serotonin and catecholamine, as well as neuron-derived peptides (neuropeptides) have been found capable of artificially inducing metamorphosis in *Hydractinia* and other species (Leitz, 1997; Müller and Leitz, 2002). Neuropeptides of the LWamide and RFamide families have been found to induce both behavioral and developmental biological processes in cnidarian species (Grimmelikhuijzen and Westfall, 1995; Leitz, 1997). For example, the myoactive neuropeptide Hym-176 has been shown to induce muscle contraction in *Hydra* (Yum et al., 1998) and several neuropeptides derived from *Anthopleura* and *Hydra* have been shown to induce metamorphosis in *Hydractinia* (Gajewski et al., 1996; Takahashi et al., 1997). In *Nematostella*, CRISPR knockouts of the GLWamide precursor gene have recently shown that GLWamide is not required for the induction of metamorphosis, but acts as an accelerator (Nakanishi and Martindale, 2018).

### **3.3. Cnidarian muscles consist mostly of myoepithelial cells.**

Cnidarian cell types can be broadly classified in (myo)epithelial cells, gland cells, neurons, germ cells, and nematocytes (Buzgariu et al., 2015; Sebé-Pedrós et al., 2018; Steinmetz et al., 2017). In contrast to bilaterians, the muscle system in cnidarian species consists mostly of myoepithelial cells instead of myocytes. In these cells the basal myofilaments are anchored to the ECM while the apical side is integrated in the epithelium. Myoepithelial cells are important components of the epidermis and gastrodermis, the two body layers in cnidarians, which are derived from ectoderm and endoderm, respectively. Typically, myoepithelial cells are multifunctional and can play roles in for example digestion, attachment, as support for nematocytes and to host symbionts (Buzgariu et al., 2015; Campbell, 1987; McAuley and Smith, 1982). Interestingly, cnidarians can possess myocytes and myoepithelial cells of both the smooth and striated type. Comparative genomics studies have shown that it is likely that striated muscles have evolved convergently in cnidarians and bilaterians, as cnidarians have striated muscle myosin heavy chain orthologues, but lack several other crucial components present in bilaterian striated muscles, including the troponin complex and titin (Steinmetz et al., 2012).

### **3.4. *Nematostella vectensis* as a model for studying organismal behavior and morphogenesis**

The starlet sea anemone *Nematostella vectensis* is an anthozoan cnidarian species that lives in brackish sea water and can be found along coastal regions of North America and England (Hand and Uhlinger, 1992). *Nematostella* is easy to culture under laboratory conditions and can be kept throughout their entire life cycle (Hand and Uhlinger, 1992). Over the last few decades, *Nematostella* has emerged as a powerful model organism for studying evolution, regeneration and adaptation to changing environmental conditions (Amiel et al., 2015; Layden et al., 2016; Steinmetz et al., 2017).

#### **3.4.1. Genome and genomic tools**

*Nematostella* has a genome estimated to be 244 Mb in size, divided over 15 pairs of chromosomes (Zimmermann et al., 2020). Sequencing of the genome has revealed remarkable similarity to that of vertebrates in terms of gene content and organization (Putnam et al., 2007; Zimmermann et al., 2020). Members of many key molecular pathways involved in development are encoded in the genome of *Nematostella*, including Wnts (Kusserow et al., 2005), Homeobox members (Chourrout et al., 2006), FGFs (Matus et al., 2007), bone morphogenetic proteins (BMPs), Notch pathway members (Marlow et al., 2012), Hedgehog (Hh) proteins (Matus et al., 2008), and T-box family members (Yamada et al., 2007). Over the years, several methods and genetic tools have been applied and optimized for use in *Nematostella*, including morpholino-mediated and short-hairpin (shRNA) mediated gene knockdown (He et al., 2018; Rentzsch et al., 2008), injection of messenger RNA (mRNA), I-SceI meganuclease-mediated transgenesis (Renfer et al., 2010), and gene editing using transcription activator-like effector nucleases (TALENs) and clustered regulatory interspaced short palindromic repeats/associated endonuclease Cas9 (CRISPR/Cas9) (Ikmi et al., 2014), which have greatly advanced *Nematostella* as a model organism.

#### **3.4.2. Life cycle and anatomy**

Like other cnidarians, *Nematostella* develops from two germ layers: ectoderm and endoderm, which are separated by a layer of extracellular matrix, called the mesoglea. The life cycle of *Nematostella* can be subdivided in an embryonic stage, transition from larva to primary polyp, and development from juvenile to adult animal (**Figure 8**). During these different stages, the animal faces different environments. During embryonic development, fertilized eggs develop inside a gelatinous substance called egg jelly, which is secreted by the mother animal. During this stage, they first form a hollow blastula, undergo gastrulation through invagination, and finally develop into planula larvae (Hand and Uhlinger, 1992; Marlow et al., 2013; Sinigaglia et al., 2015). Once the larvae are formed, they emerge from the egg jelly and enter a free-swimming phase, in which they propel themselves through ciliary beating. Eventually, the larva settles down and undergoes a transition from a free-swimming (pelagic) larva to a benthic (settled), tubular-shaped primary polyp with four tentacles

(Fritz et al., 2013; Hand and Uhlinger, 1992; Reitzel et al., 2007). This process is referred to as larva-polyp transition, or metamorphosis. Primary polyps subsequently proceed to the last, feeding dependent stage of development. During this time, they are referred to as juvenile polyps, and they grow in size, develop additional tentacles, and become sexually mature (Hand and Uhlinger, 1992; Ikmi et al., 2020). In its adult form, *Nematostella* has a tubular shape that is normally closed at the aboral end and has a mouth and pharynx with 16 tentacles on the oral side. Eight mesenteries, sheet-like tissue that runs in the oral-aboral direction, divide the region around the pharynx in eight sectors. The mesenteries start to develop from the endoderm during the planula stage, and harbor digestive and reproductive cells, as well as longitudinal myoepithelial cells (Moiseeva et al., 2017).

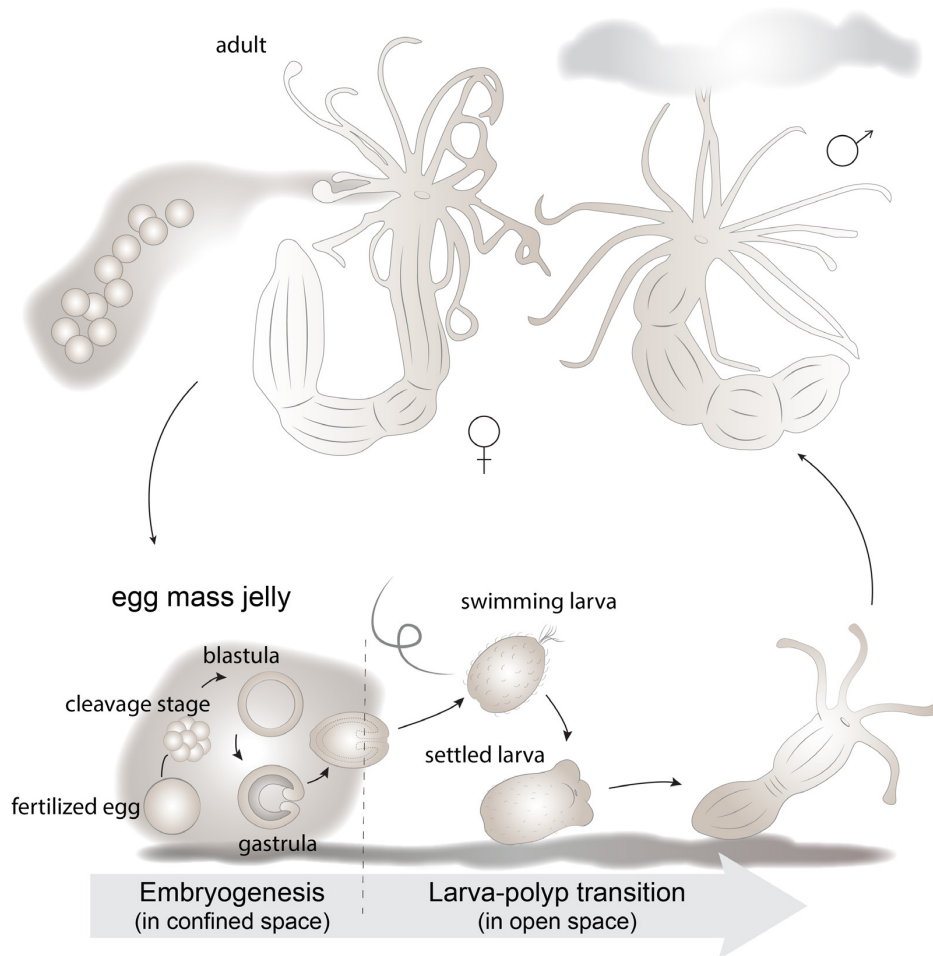


**Figure 8. Schematic depiction of the life cycle of *Nematostella vectensis*.**

### 3.4.3. Embryonic patterning

Although from the outside *Nematostella* appears radially symmetric, the body plan contains two axes: the primary axis, which runs from the oral to aboral pole, and the directive axis, which is visible in subtle asymmetries in the mesenteries and the syphonoglyph, a ciliated groove in the mouth. Wnt/ $\beta$ -catenin signaling is crucial for establishment of the oral-aboral axis (Marlow et al.,

2013; Röttinger et al., 2012). From the mid-blastula stage onwards, different Wnt genes are expressed, and mark distinct domains in both the ectoderm and endoderm of the oral half of the embryo (Kusserow et al., 2005). In contrast, the aboral territory is marked by expression of *NvSix3/6* and *NvFoxQ2*, which is involved in head patterning in bilaterians, and is found to be crucial for development of the aboral region (Sinigaglia et al., 2013). Pharmacological overactivation of Wnt/ $\beta$ -catenin signaling results in an expansion of the oral domain (Marlow et al., 2013; Röttinger et al., 2012), whereas inhibition of Wnt signaling leads to an expansion of the aboral domain (Marlow et al., 2013).  $\beta$ -catenin has been found essential for initiating patterning of both the oral and aboral region by stimulating *NvSix3/6* expression aborally, and inhibiting Wnt receptor *NvFrizzled5/8* orally (Leclère et al., 2016a).

Development of the secondary body axis, or directive axis, depends on signaling of the BMP pathway. In bilaterians, BMP signaling is important for establishment of the dorsal-ventral axis, but the pathway is employed in a different manner than in cnidarians. In *Nematostella*, BMP ligands and antagonist chordin are originally radially expressed around the blastopore at gastrula stage, but become asymmetrically expressed on one side of the embryo by the mid-gastrula stage (Finnerty et al., 2004; Rentzsch et al., 2006; Saina et al., 2009). In contrast, in bilaterians chordin and BMP do not overlap, and chordin is thought to concentrate BMPs at the production site (Rentzsch and Technau, 2016). Interestingly, knockdown of BMPs or *NvChd* results in loss of asymmetric expression, and increased radial expression, indicating self-inhibition of BMP signaling (Saina et al., 2009). While knockdown of BMP or *NvChd* does not prevent gastrulation or the establishment of an oral-aboral axis, patterning of the directive axis is abolished, leading to animals that are completely radially symmetric, and loss of expression of several endoderm markers (Leclère and Rentzsch, 2014; Saina et al., 2009). BMP signaling is required for expression of Hox genes and formation of mesenteries (Genikhovich et al., 2015), and recently it has been shown that an axial Hox code is involved in radial segmentation of the endoderm in eight distinct sectors, thereby showing how gene expression downstream of BMP signaling is involved in patterning of the directive axis (He et al., 2018).

#### **3.4.4. The nervous system in *Nematostella***

*Nematostella* does not possess a centralized nervous system, but develops a nerve net from both the ectoderm and endoderm. The nervous system in *Nematostella* consists of epithelial sensory and sensory-motor cells and basally located ganglion cells, which are morphologically similar to interneurons in bilaterians. Both sensory cells and ganglion cells can connect to other neurons and to myoepithelial cells (Nakanishi et al., 2012). Some regions are denser in neurites than others, for example, tracts of neurites have been found along the mesenteries (Marlow et al., 2009). A third cell type, the mechanosensitive nematocyte, is considered to be a highly specialized neural cell type unique to cnidarians. Neurons are thought to be derived from a neural progenitor population that

expresses *NvSoxB2* (Richards et al., 2014). Much is still unknown about the functioning of the nerve net and how transmitted signals translate to animal behavior (Rentzsch and Technau, 2016).

### **3.4.5. *Nematostella* has a muscle system consisting of longitudinal and circular muscles**

The muscle system of *Nematostella* consists of longitudinal and circular muscles, which are distinct in morphology, localization, and gene expression (Jahnel et al., 2014; Sebé-Pedrós et al., 2018). The longitudinal muscles of the body column are located in the mesenteries and can be subdivided into parietal muscles, located towards the distal part of the mesenteries, and more proximally located retractor muscles (Jahnel et al., 2014). The circular muscles are organized perpendicular to the longitudinal muscles and bridge the space between the different mesenteries. Both the longitudinal and circular muscles of the body column consist of myoepithelial cells (Jahnel et al., 2014). As the animal grows and develops as into a juvenile polyp, the parietal and retractor muscles become folded (**Figure 9**), and only remain connected to the epithelium via thin cytoplasmic bridges. In contrast, the circular muscle cells maintain a shorter and wider connection between the basal myofilaments and the apical epithelial component of the cell (**Figure 9**) (Jahnel et al., 2014). Together, the longitudinal and circular body column muscles enable contractions that result in peristaltic movements. The muscle system in the tentacles is also composed of circular and longitudinal muscles, but with the difference that the longitudinal tentacle muscles are localized on the ectodermal side of the mesoglea. The difference can be explained by the different origin of the longitudinal muscles of the body column and the tentacles. Whereas the longitudinal body column muscles, as well as the circular muscles in both tentacles and body column are derived from the endoderm, the longitudinal muscles present in the tentacles develop from the ectoderm during metamorphosis. This involves detachment and migration of epithelial longitudinal muscle precursor cells from the ectoderm to the site of tentacle budding. The now mesenchymal cells become localized at the base of the epithelium, where they extend into the tentacles (Jahnel et al., 2014).



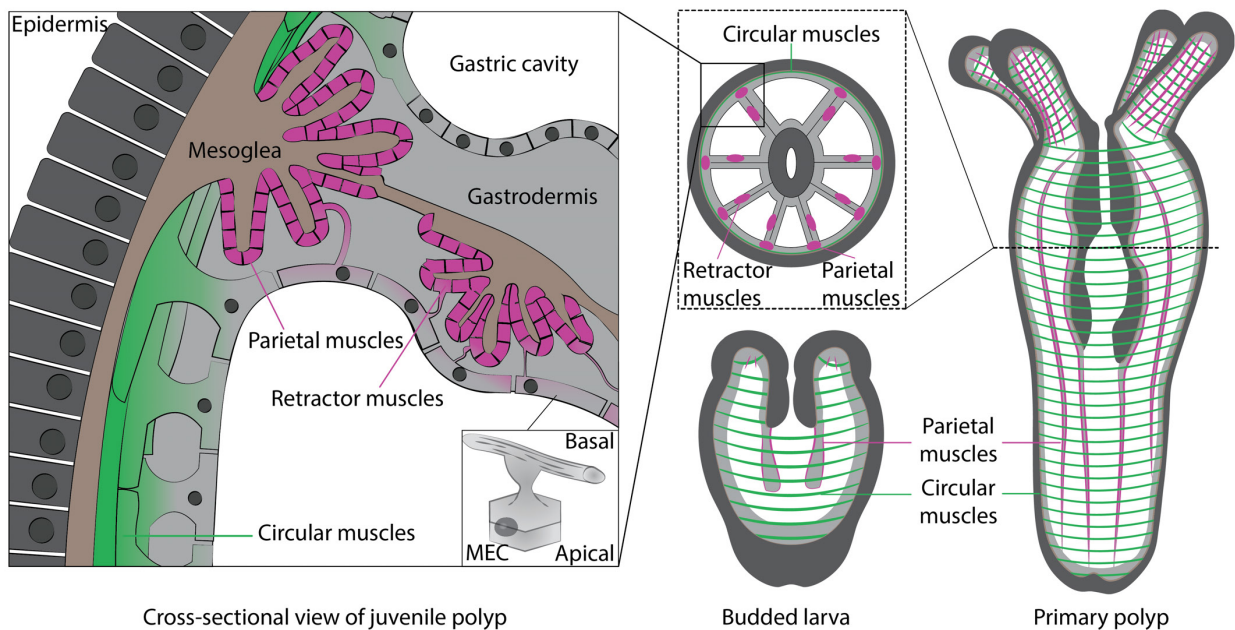


**Figure 9. Schematic representation of muscle organization in *Nematostella* larva and polyp.** Longitudinal muscles are colored in magenta, circular muscles in green. Myoepithelial cells (MEC, inset) have a dual identity: they are part of both the muscle system and the epithelium. At juvenile stage, the longitudinal parietal and retractor muscles become folded, and the muscle part of the longitudinal myoepithelial cells only remains attached to the cell body via thin cytoplasmic bridges (Jahnel et al., 2014).

Like other sea anemones, *Nematostella*'s tubular shaped body column forms a hydrostatic skeleton, a cylindrical-like structure supported by internal fluid pressure (Batham & Pantin, 1950; Kier, 2012). The shape of the body column can be regulated through muscle contractions. Assuming a constant volume, a contraction on one side automatically has to result in an expansion elsewhere. Muscles in hydrostatic skeletons are typically organized such that both the diameter and the length of the tube can be regulated (Kier, 2012). Following this principle, a relatively small change in diameter can result in a large increase in tube length (Kier, 2012). In the case of *Nematostella*, the diameter can be regulated through contraction of the circular muscles, whereas the longitudinal muscles can change the length of the body column (Jahnel et al., 2014). Two types of muscle contractions can be distinguished: isotonic muscle contractions, which generate force by changing the length of the muscle, and isometric contractions, which generate force without changing muscle length and can be used to maintain a certain conformation. The combination of these two types of muscle contractions and the two different types of muscles, circular and longitudinal, together maintain and regulate the shape of the body column of *Nematostella*.

### 3.4.6. Using *Nematostella* to study the link between organismal behavior and morphogenesis

As described previously, organismal behavior and morphogenesis are generally studied as separate fields, and little is known about how morphogenetic processes are coordinated with active

organismal behaviors. Studying this relationship requires a system in which both processes can be studied simultaneously, with minimal environmental complexity. In this regard, *Nematostella* offers several advantages. *Nematostella* has a simple body plan consisting of only two layers, and undergoes a relatively simple morphogenetic change from an ellipsoid larva to a tubular polyp, while showing distinct behaviors such as swimming, settling and contracting. Although *Nematostella* larvae develop in an open aquatic space, they require minimal input from their environment while undergoing larva-polyp transition. For example, they are not dependent on uptake of external nutrients, and do not seem dependent on specific settlement-inducing environmental cues. This absence of environmental complexity makes it easier to study the link between animal morphogenesis and behavior. Furthermore, *Nematostella* is compatible with microscopy due to its small size and optical accessibility, and offers the advantage that several genetic tools can be applied in this organism. Together, these features make *Nematostella* an attractive model for studying how organismal behavior is coordinated with morphogenesis.

## 4. Aims of the thesis

In order to study the relationship between organismal behavior and morphogenesis during *Nematostella* larva-polyp transition, this work has been divided in three sections with separate goals.

### **1. Development of an experimental workflow and image analysis pipeline to monitor animal behavior and morphogenetic changes in a high-throughput manner.**

Studying behavior and morphogenesis during larva-polyp transition requires a setup that allows recording of both animal behavior and morphogenetic changes during the entire developmental process. Such a setup requires not only identifying an imaging setup that allows recording of such data under conditions that are tolerable for the animal, but also requires an image analysis pipeline that tracks behavioral and morphogenetic developments for individual animals. Furthermore, in order to study variation between animals and the effect of different experimental conditions, the setup needs to be executable in a sufficiently high-throughput manner. Therefore, the first aim of this work is to establish an experimental workflow with an image analysis pipeline that tracks animal development at the organismal scale. This will be discussed in the first half of Chapter 5.

### **2. Characterization of animal behavior and morphogenetic changes during larva-polyp transition in wild-type animals.**

The second aim of the thesis is to provide a descriptive analysis of the behavioral and morphogenetic changes that take place in wild-type animals. Organismal-scale behavioral and morphogenetic changes can be analyzed for a large population of wild-type animals using the setup described under Aim 1, and this will be the focus of the second part of Chapter 5. Furthermore, volumetric imaging of live animals and high-resolution images of fixed animals can help gain understanding of the underlying morphogenetic changes that take place at the tissue level. This will be the focus of Chapter 6.

### **3. Define the role of the gastric cavity and muscle contractions during larva-polyp transition.**

During the larval stage, animals develop a hydrostatic skeleton, which is formed by the muscle system surrounding the fluid-filled gastric cavity. This system allows the animal to change shape on short timescales, i.e. during animal behavior. However, the role of the hydrostatic skeleton during larva-polyp transition and the connection to animal behavior, are poorly understood. Therefore, the third aim is to gain mechanistic understanding of the functioning and role of the hydrostatic skeleton during larva-polyp transition, which could be achieved through

pharmacological, mechanical and genetic perturbations of the muscle system and the cavity. This will be the focus of Chapter 7. Furthermore, testing of different environmental conditions might reveal changes in animal behavior and could help gain understanding about the conditions that allow the system to function. This aspect will be discussed in Chapter 8.

## 5. Dynamics of larva-polyp transition in *Nematostella*

### 5.1. A high throughput imaging approach for quantifying body shape change and organismal behavior

As discussed in the introduction, *Nematostella* larvae undergo a process called larva-polyp transition, during which they elongate their body column, expand their body cavity, and grow four primary tentacles. During this time, they also show several distinct organismal behaviors, including swimming, settlement behavior, and muscle-driven contractions. Physically constrained larvae fail to develop into elongated polyps, which suggests that organismal behaviors might be important for normal development. To study how organismal behaviors are integrated in larva-polyp transition, a high-throughput setup is needed that allows monitoring of both behavior and morphological changes in freely developing animals. To achieve this, an Acquirer screening microscope was used, with which a large number of isolated larvae can be imaged throughout the entire larva-polyp transition (**Figure 10**). For this, single animals are placed in the wells of a 384-well plate, and imaged with brightfield illumination. A good balance between animal number and time resolution was empirically found at 200 animals and a five-minute time interval. To track morphogenetic and behavioral changes throughout larva-polyp transition, I wrote a FIJI Jython script to automatically extract morphogenetic and behavioral information from these large amounts of image data. In this chapter, I will first outline the image analysis strategy, and then discuss how it was applied to study developmental and behavioral dynamics in a large population of developing *Nematostella* larvae.

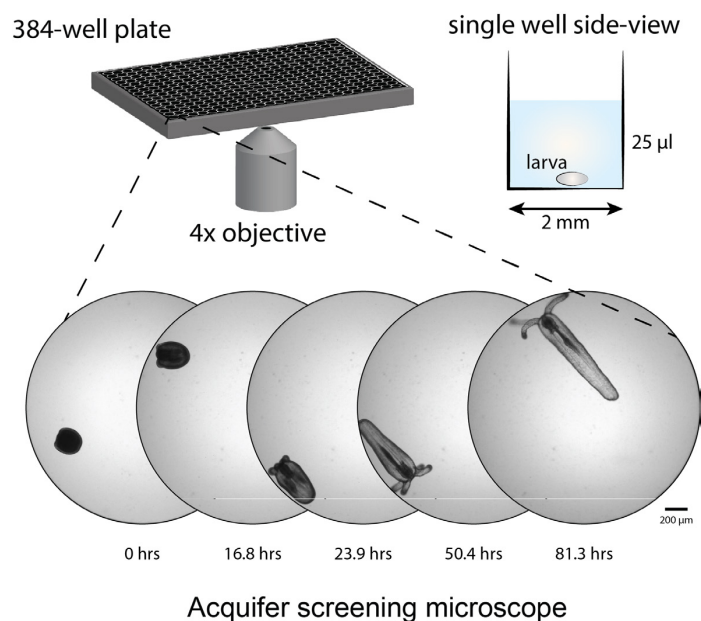


**Figure 10. Experimental setup.** Schematic of imaging setup using the Acquirer screening microscope, showing example images of the same animal in a single well at various points in time. Scale bar: 200 µm.

## 5.2. Image analysis strategy for extracting shape and size features from 2D images of developing *Nematostella* larvae

FIJI offers the possibility to automate image analysis by designing and writing custom analysis pipelines. Moreover, it is possible to run code without a graphical user interface (GUI), called 'headless mode', allowing processing on a high performance computing (HPC) cluster. This way, the processing of data can easily be parallelized, thereby strongly reducing the duration of the analysis. For example, with the code developed here, a typical experiment with 200 animals and ~1500 measured time points per animal, can be processed in less than one hour. The image analysis pipeline consists of several steps: preprocessing, segmentation of the image into animal and background, and extraction of shape features from the animal (**Figure 11**), as will be outlined below.

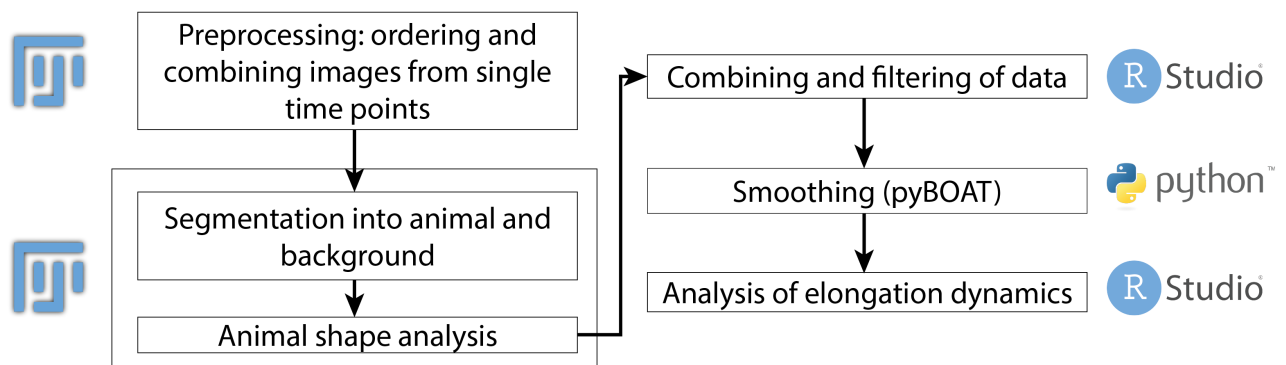


**Figure 11. Schematic overview of image analysis pipeline, consisting of preprocessing, image analysis using FIJI, and subsequent data analysis using Python and RStudio.**

### 5.2.1. Preprocessing

The preprocessing step serves to concatenate the images from single time points into time series for individual animals. The images are ordered by time, illumination channel and z-height (where applicable), and subsequently concatenated and cropped to the size of the well. This way, a single file with the ordered time points is created for each animal. Processing of individual animals can then be parallelized by creating a so-called job script for each animal, which is submitted to the HPC cluster.

### 5.2.2. Image segmentation into animal and background

Segmentation of the image into foreground (animal) and background (the well and its surroundings) starts with background subtraction. For this, an estimation has to be made of what the background roughly looks like. Since the animal is a moving dark object on a light background, a maximum intensity projection of the entire time sequence can be used to essentially mimic an empty well. This projection thus contains everything that is static, including non-moving shadows and dirt, and can therefore serve well for background subtraction. In some cases, segmentation into foreground and background is complicated by the presence of debris excreted by the animal or by

changing shadows that arise from condensation of water on the lid of the plate. To filter this out, a more dynamic background subtraction is required. For this, a correction background image can be created for each time frame. This is a modified image of the previous time point, in which an enlarged version of the region that was defined as animal is filled in with background pixel values (**Figure 12A**, second image, dotted lines). All other pixel values, including those of the shadows or dirt, remain intact and can therefore be subtracted from the next time frame. The background pixel values used to fill in the animal are estimated by applying a large morphological dilation followed by erosion (MorpholibJ package (Legland et al., 2016)). Since the animal area is relatively small compared to the surrounding area, morphological dilation results in the disappearance of the animal while roughly maintaining the pixel values of the empty regions. Subtraction of this correction background image from the original image ensures that the animal stands out clearly, as all background is removed (**Figure 12A**, middle image).

After background subtraction, a small Gaussian blur is applied and the image is segmented by using a threshold based on an offset from the median pixel value inside the well (**Figure 12A**, 4<sup>th</sup> image). Objects within the range of expected sizes and circularities are selected from the masked image using the particle analyzer function. Only a single object is allowed per time point. To ensure that the presumed animal is in focus, a modified image is calculated that is the result of the subtraction of a blurred image from the original image. This highlights the edges of the objects in the image (**Figure 12A**, 5<sup>th</sup> image). An in-focus score is then calculated based on the standard deviation at the boundaries of the object. Out-of-focus objects will have little contrast at the edges and will therefore have a low score, allowing them to be filtered out. This step is important, as the animal might rotate out of plane and therefore be in an unfavorable orientation for shape and size measurements. If the animal is tilted in the z-dimension, part of it will be out of focus, enabling rejection of that image based on the in-focus score. However, if the animal is in a completely vertical position, it will again be entirely in focus and in such cases it is not possible to easily filter out the animal. Here, outlier detection combined with manual proofreading is still required.

### 5.2.3. Extracting shape features

Morphogenetic changes during larva-polyp transition involve changes in organismal size and shape. The binary image (**Figure 12A**, 4<sup>th</sup> image, **Figure 12B**, 1<sup>st</sup> image) containing a single foreground object serves as the basis for extracting such features. Two important features can directly be derived from the binary image: object circularity and object location. Object circularity is determined by the relationship between the area and the perimeter of the object. Perfect circles have a circularity of 1, as they have the maximum possible area relative to their perimeter. Spiky objects, on the other hand, have a low area relative to the perimeter, and therefore have a low circularity. Circularity is a particularly useful feature for studying developing *Nematostella*, as larvae tend to

have a round shape that gradually transforms into a spikier shape with low circularity, due to the development of tentacles and elongation of body column (**Figure 12B**, top). Object location is determined by the centroid location of the object, and can be used to track animal movement inside the well (**Figure 12B**, top).

Additional processing of the binary image is required to measure body column length and diameters along the body column. The 'skeletonize' function in FIJI removes pixels at the boundaries of the object until it is reduced to a 'skeleton' that is one pixel wide all around (**Figure 12B**, middle). This makes it possible to detect and segment the different 'branches' belonging to body column and tentacles, and also provides an easy way to define the length of 'banana-shaped' objects, which can be extracted using the AnalyzeSkeleton function (Arganda-Carreras et al., 2010). Since the skeleton branch only contains the internal skeleton pixels and does not extend to the boundaries of the object, the skeleton branch length underestimates the actual length of the body column. To correct for the missing pixels at the two extremities of the body column branch, the distances to the boundary at the two extremities of the branch are added to the total branch length.

To correctly assign the oral and aboral poles, a second threshold is applied to detect the pharynx region, which is located orally and can be distinguished by its darker appearance due to high tissue density. For cases in which the pharynx could be reliably detected, the skeleton pixel closest to the centroid of the pharynx is assigned as the oral pole. Conversely, the other extremity belonging to the body column branch is labeled aboral pole. When the pharynx cannot be detected, the presence of tentacle branches is used to determine animal polarity. In these cases, the pixels at the junction between body column branch and tentacle branches are used to assign the oral pole. When no tentacle branches are present, or branches were present at both ends, the oral and aboral poles could not be reliably detected and are denoted 'NA' in the output file.

In addition to the skeleton, a distance map is calculated using the Euclidean Distance Map function in FIJI (**Figure 12B**, bottom). In a distance map, each pixel value indicates the distance of that pixel to the nearest boundary of the object. The combination of the skeleton with the distance map makes it possible to estimate the width of an object at any given point along its skeleton branch, since the object width at that point is equal to the distance to the boundary, multiplied by two. From these measurements, the body column branch can be identified as the branch that has the longest length and largest average width. Furthermore, these measurements provide a vector containing the body column diameter along every point of the skeleton branch. From this, total body column volume (tissue and cavity combined) is estimated by summing the volumes of 1-pixel tall cylinders for every location along the body column main axis, where the diameter of the cylinder is determined by the width of the column at that particular position. Two half-spheres with a radius determined by the body column width at the extremities are added to account for the two poles.



In summary, the following features are extracted from the binary image, skeleton and distance map (**Figure 12B**):

- Animal area
- Animal circularity, which is defined as  $4\pi \frac{Area}{Perimeter^2}$
- Body column length, defined as body column branch length plus correction at the extremities
- Average body column diameter
- Body column diameters along the oral-aboral axis
- Animal location from centroid coordinates
- Oral and aboral pole coordinates
- Estimated body column volume

#### **5.2.4. Data analysis**

The output of the script consists of a zip folder that contains all the regions of interest (ROIs), as well as a text file with all the measurements for every time point for one animal (**Figure 12B**, right). The ROIs that are saved include the ROI for the entire animal, the labeled body column branch and tentacle branches, and the labeled oral and aboral poles. All text files can then be combined and processed further using RStudio and Python scripts.

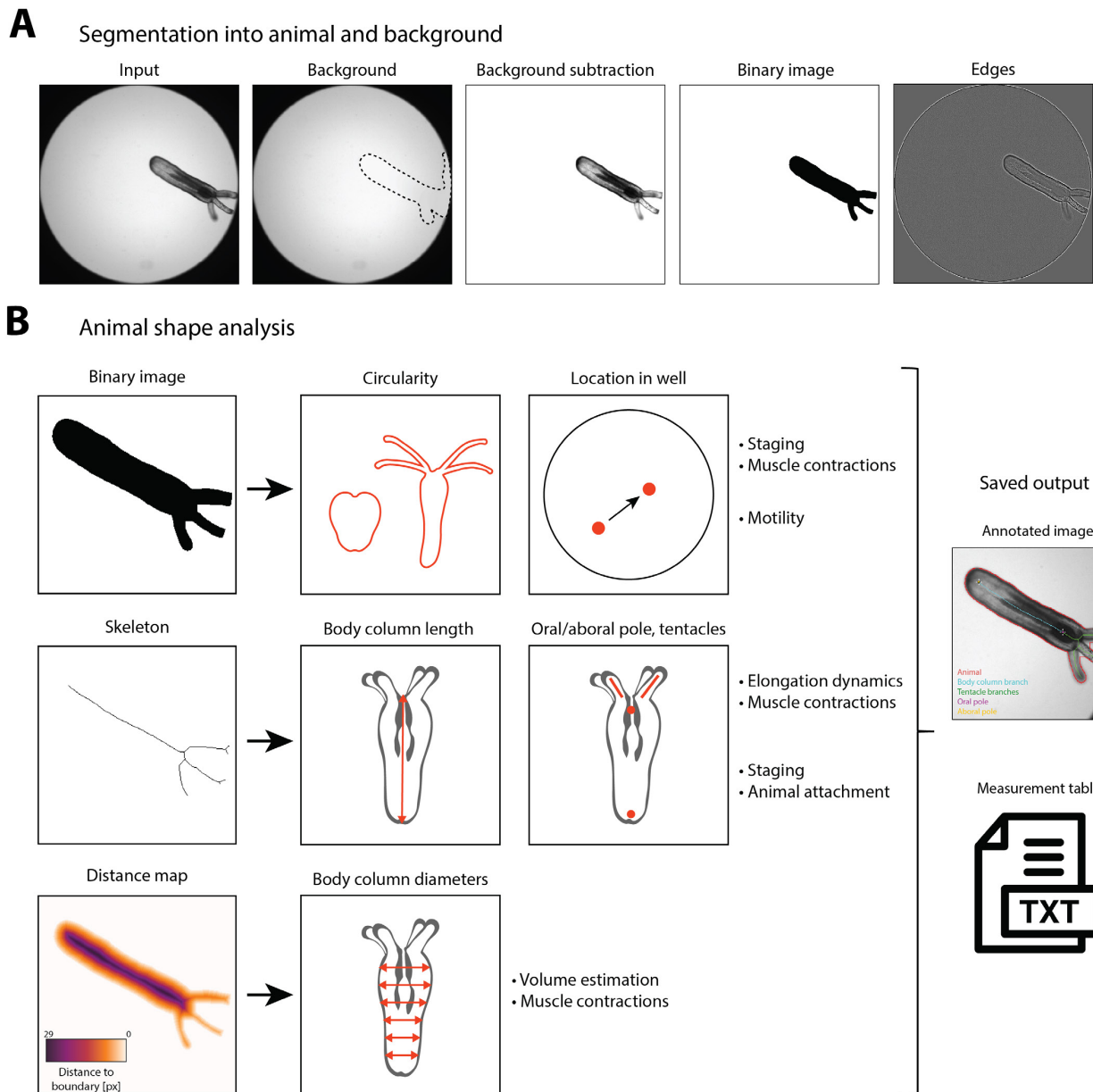


**Figure 12. Image analysis strategy for monitoring morphogenesis and animal behavior in freely developing *Nematostella* larvae. A.** Strategy for image segmentation using background subtraction and edge detection. **B.** Strategy for animal shape analysis, using the FIJI's skeletonize and distance map functions in order to extract features such as animal outline circularity, body column length, and body column diameters.

### 5.2.5. Validation of the image analysis pipeline

Since the image analysis pipeline has to work under variable conditions (e.g. differences in background, differences in animal stage, and related opacity), validation of the method was done mostly by visually checking the output in the annotated images of different animals (**Figure 12B**, right). From this, I found that the best results are obtained with transition-stage animals that have good contrast with respect to the background. In such cases, the annotation is mostly correct. However, problems may arise under several conditions. For example, during the larval stage, animals are small and round and rotate frequently. This makes the quantification of body length and diameter

along the oral-aboral axis less accurate, as an animal that is rotated in  $Z$  will appear shorter. The same problem may occur during later development, as animals sometimes rotate and stick to the side of the well in a vertical orientation. When the tentacles become very long, segmentation of the tentacles is often incorrect, as they have too little contrast to accurately distinguish them from the background. However, as the focus in this project is mainly on the body column, these errors can mostly safely be ignored. Changes in contrast due to shadows or dirt in the well are largely filtered out, but occasionally can still result in errors, especially when they are very dynamic over time. After many rounds of optimization, the method described here was found to be sufficiently efficient and accurate. However, manual checking is still advisable, because of artefacts that may arise from certain animal appearances or contaminations, such as debris and air bubbles.

### 5.3. Defining the start of larva-polyp transition based on animal shape circularity

Using the Acquirer microscope and the described image analysis pipeline, I recorded and tracked the development of wild-type animals from five separate experiments. The resulting combined dataset consisted of measurements for 669 individuals, excluding animals that died, showed clear signs of misdevelopment, or had too few reliable data points (e.g. because the animal moved out of focus, was stuck to the side of the well, or due to presence of large dirt, etc.). To explore elongation dynamics in this large dataset, I first focused on global animal shape change, as this could serve as a good indicator of animal developmental stage. Here, I aimed to determine the time of initiation of larva-polyp transition, and classify each animal at any given time point as 'larva', 'transition' or 'polyp', depending on how far it has progressed in larva-polyp transition. Since animals start off with a mostly round shape but acquire an elongated shape with tentacle appendages as they develop into polyps, animal shape circularity seemed to be a good feature to estimate animal stage. Indeed, the measurements show that before larva-polyp transition is initiated, circularity fluctuates around 0.85, but as soon as the animal starts to elongate and grow tentacles, circularity decreases strongly and then levels off around 0.2 (**Figure 13A**). Circularity is also subject to animal behavior: a contracted animal has a much rounder shape than an extended one. Therefore, animal stage should be determined based on the global trend of circularity in time, not on individual raw measurements. Therefore, smoothing was applied using the sinc-smooth function from the pyBOAT package (Mönke et al., 2020) (see Materials and Methods for details). Based on the smoothed trajectory, the three stages were distinguished as follows: larva (circularity  $> 0.8$ ), transition (circularity  $0.8 - 0.3$ ), and polyp (circularity  $< 0.3$ ) (**Figure 13A**). This definition of the transition stage overlaps well with major changes in body length, average body column width, and the detection of newly formed tentacles (**Figure 13B-D**), a sign that the animal has initiated larva-polyp transition. The boundaries of 0.8 and 0.3 for circularity define a relatively strict regime that captures the major changes from larva to early polyp, but not the slower changes in polyps that occur later (e.g. after 60 hours in the animal in **Figure**

13A). The reason that this later development is not included in the transition stage, is that not all polyps reach the same end-circularity, and therefore the end of the transition stage is less-well defined on the population level.

#### **5.4. Larva-polyp transition in *Nematostella* is asynchronous and variable in duration**

Combining the smoothed trajectories for circularity for multiple animals from the same experiment reveals that animals start larva-polyp transition at different time points, even though they have the same age (date of fertilization) and develop under the same conditions (**Figure 13E**, left). In order to compare elongation dynamics within a large population of animals and across different experiments, the different trajectories were time-shifted to align them to the start of the transition stage, denoted as  $t_0$  (**Figure 13E**, right). Analyzing the data in this 'pseudotime' allows direct comparison of different shape features irrespective of the difference in start time of the transition stage. After time-shifting the trajectories, it became clear that animals not only vary widely in the onset of larva-polyp transition and in final morphology, but also in the total time needed to complete larva-polyp transition (**Figure 13E**, F). The duration of the transition stage shows a wide distribution, with an average of  $26.7 \pm 14.1$  hours (**Figure 13G**). Animals thus elongate at different rates, and this appears to be largely independent of animal length (**Figure 13H**). These results suggest that larva-polyp morphogenesis relies on a plastic developmental program that may be influenced by multiple factors.

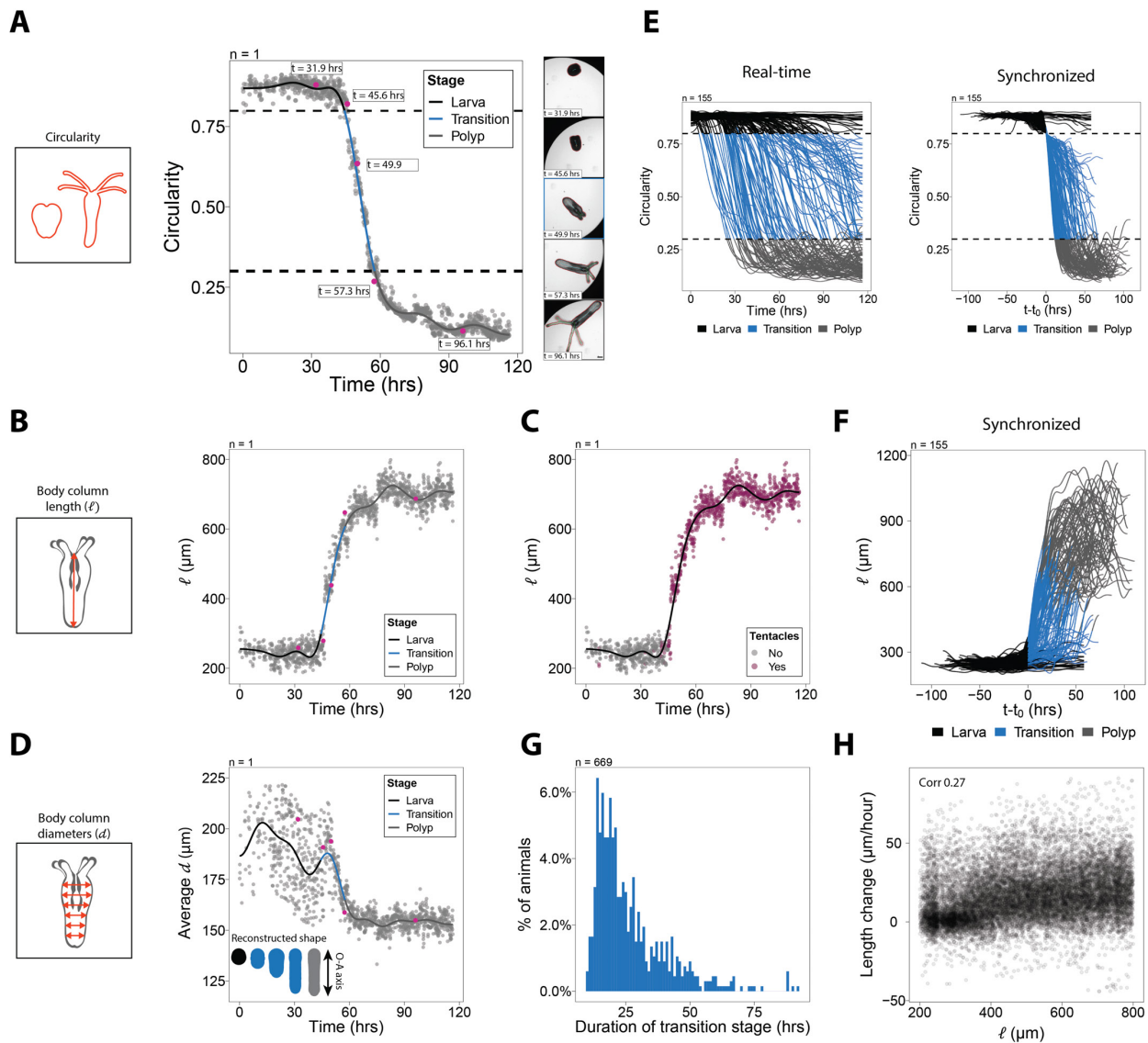


**Figure 13. Variable elongation dynamics in a population of developing *Nematostella* larvae.** A-D. Raw measurements (dots) and smoothed curve for circularity (A), body column length (B, C), and average body column diameter (D) over time. Thresholds set at a circularity of 0.8 and 0.3 mark distinct stages in development: larva (black), transition (blue), and polyp (gray). Snapshots at different time points (pink dots) are shown on the right in (A). Inset in (D) shows the reconstructed body column shape based on the collection of body column diameters along the oral-aboral (O-A) axis. Due to the short body axis, average body column diameter can only be reliably measured after larva-polyp transition is initiated. E. Left: smoothed curves for circularity over time for 155 animals from the same experiment, color-coded for developmental stage. Right: the same measurements, but synchronized in pseudotime, where  $t_0$  marks the start of the transition stage. Animals that never entered the transition stage (completely black lines) are centered above  $t_0$  for visualization purposes only. F. Smoothed curves for body column length in pseudotime, color-coded for developmental stage. G. Distribution showing the duration of the transition stage, obtained from data from 6 experiments with 669 polyps in total. H. Body column length is weakly correlated (0.27) with body column length change. Figure panels shown here also partially appear in (Stokkermans et al., 2021) and were made by me. Scale bar: 100  $\mu\text{m}$ .

## 5.5. Animals explore a morphospace by separately or simultaneously changing body column size and shape

Multiple changes occur during larva-polyp transition, including a transformation of the body from ellipsoidal to cylindrical, expansion of the internal cavity, and development of secondary structures in the form of tentacles on the outside and mesenteries inside the body column. In this study, I focused mainly on the changes with respect to the body column, as this provides a clear but relatively simple morphogenetic change. Essentially, the morphological change of the body column consists of two components: 1) an increase in size, and 2) a shape change from ellipsoidal to cylindrical. To study these two changes during larva-polyp transition, body column volume was used as a proxy for size, and body column length-over-width aspect ratio as a proxy for shape (**Figure 14A, Appendix Table 1**). Using these two features, the size-shape relationship can be mapped as a scatterplot, revealing a 2D ‘morphospace’, with all the combinations of body column volumes and aspect ratios an animal has explored during its development. The direction of change in morphospace, here termed ‘morphodynamics’, indicates whether the animal is changing predominantly in size, shape, or both, at a given point in time (**Figure 14B**).

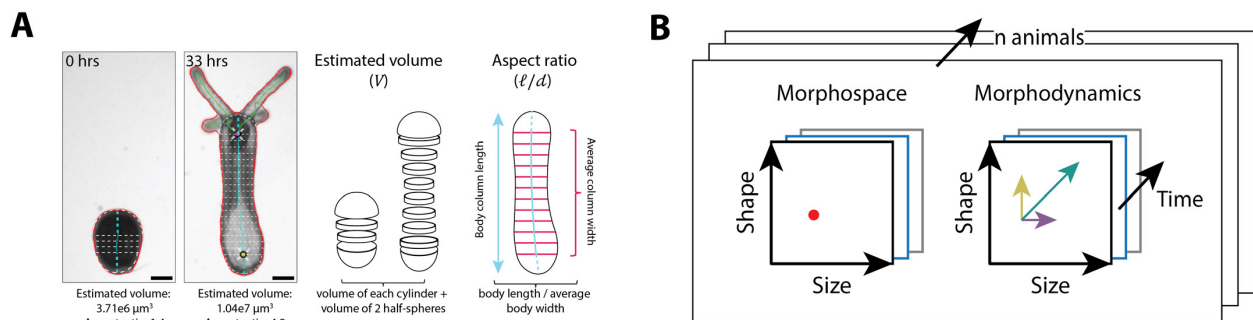


**Figure 14. Body column changes can be decomposed in a change in size and a change in shape. A.** A larva (left) and corresponding polyp (right), showing an increase in total body column volume, and a shape change from ellipsoidal to cylindrical. Body column volume ( $V$ ), calculated by the sum of the volumes of all cylinders along the body column and two half-spheres at the poles, is used as a proxy for size, and length-over-width aspect ratio ( $\ell/d$ ) is used as proxy for shape. **B.** Schematic representations of the dimensionality of the data. Thick arrows indicate dimensions. Morphology is described in two dimensions: size and shape, here termed ‘morphospace’. The red dot marks the size-shape relationship for a single time point. The respective change in size and shape can be visualized as a vector with a direction and amplitude, here termed ‘morphodynamics’. Measurements are taken over time and each individual animal can be seen as its own dimension. Figure panels shown here also appear in (Stokkermans et al., 2021) and were made by me.

Figure 15A and B illustrate this approach by showing size and shape measurements of a single animal, over time, and in morphospace, respectively. Upon close inspection, it can be seen that although both volume and aspect ratio increase over time, they are not necessarily increasing at the same time throughout development. In this particular example, the animal increases mainly in volume between  $t = 16.3$  hours to  $t = 20.7$  hours, but mainly in aspect ratio from 20.7 hours to 28.3 hours. From 28.3 hours to 34.2 hours, the animal increases in both volume and aspect ratio. Thus,

this animal follows a zig-zag-like pattern in morphospace, rather than a straight line in which volume and aspect ratio always increase simultaneously and proportionally.

To better understand the relation and contribution of changes in size and shape to the final morphology, I classified morphodynamics in four different categories (**Figure 15C, D**). Here, I use the term ‘inflating’ to indicate a predominant increase in body column volume, resulting in mostly isotropic expansion (purple color in Figure 15). The term ‘stretching’ is used to indicate a predominant increase in aspect ratio, resulting in elongation of the animal without volume increase (yellow). When the animal simultaneously increases both body column volume and aspect ratio, resulting in anisotropic expansion, it is denoted as ‘combined inflating and stretching’ (green), and when the animal neither increases in body column volume nor aspect ratio, it is labeled as ‘no elongation’ (gray). In case of the last category, the animal either did not substantially change at all, or it changed its size and/or shape back to a smaller or more spherical shape (**Figure 15D**, see Materials and Methods for details). Color-coding the smoothed trajectory in morphospace visualizes the type of change (i.e. the type of morphodynamics) the animal is undergoing at a particular time point (**Figure 15C, D**). Mapping the data points for all animals combined reveals a wide range of different volumes and aspect ratios that are explored during larva-polyp transition (**Figure 15E**). Here, animals can take different trajectories, varying the duration and order of morphodynamics that lead to their final shape (**Figure 15F**). The pattern ‘*combined inflating and stretching*’ – ‘*stretching*’ – ‘*combined inflating and stretching*’ appears to be common (**Figure 15F**). However, other patterns are also observed and produce polyps of similar end-morphology (**Figure 15F**, rightmost column). Combined, I found that most of the total body length increase is due to ‘combined stretching and inflating’ (**Appendix Figure 2A**), followed by ‘stretching’. ‘Combined stretching and inflating’ also shows the highest elongation rate (**Appendix Figure 2B**). Animals spend relatively little time ‘inflating’, indicating that volume increase mostly co-occurs with aspect ratio increase (**Appendix Figure 2C, Appendix Table 2**).

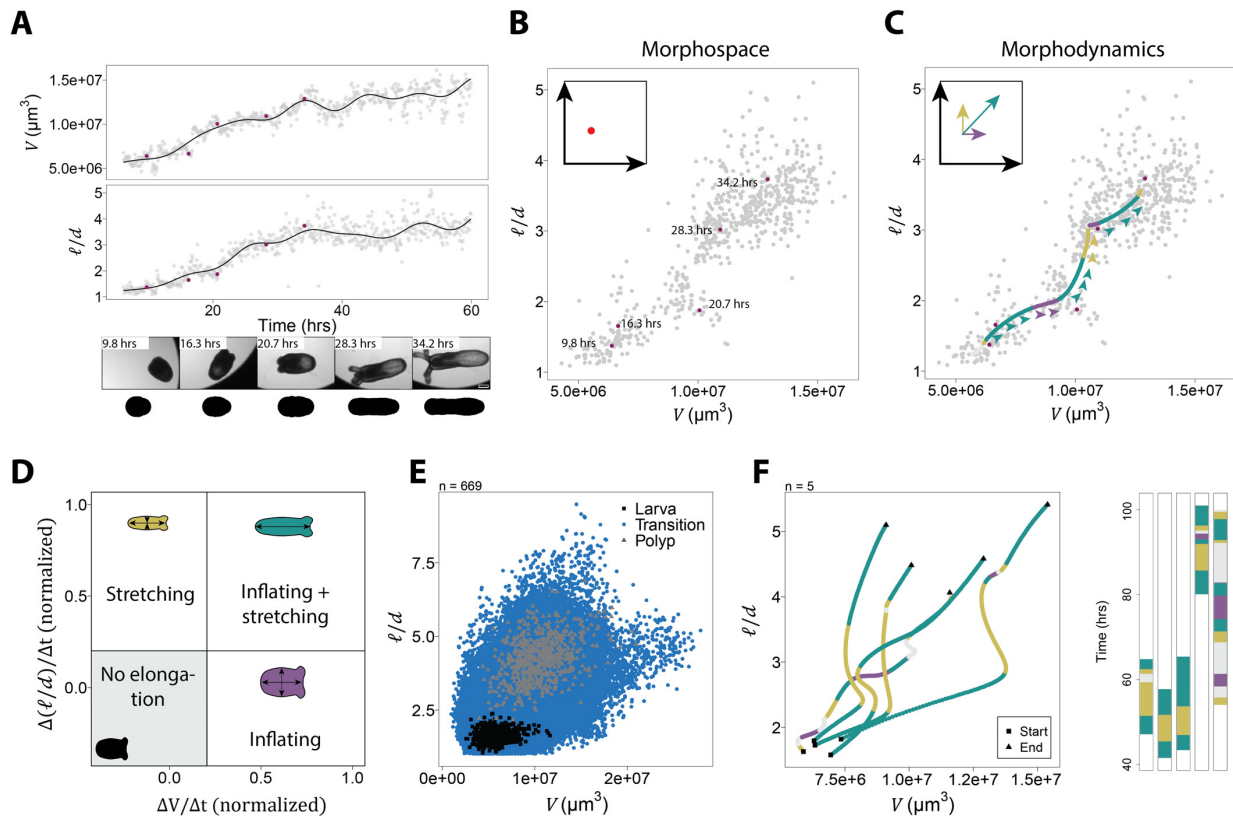


**Figure 15. Developing larvae explore a morphospace by respectively changing their size and/or shape during larva-polyp transition.** **A.** Example of a single individual showing body volume and aspect ratio over time. Pink dots correspond to snapshots in time, of which images and reconstructed shapes are shown below. **B.** Morphospace plot for the individual shown in A, with corresponding labeled pink dots. **C.** Morphospace plot with smoothed trajectory of volume and aspect ratio in morphospace, color-coded for morphodynamics (see D) to indicate the type of change the animal is undergoing at a particular time point. Arrowheads show direction in time. **D.** Schematic representation of the different morphodynamics and used terminology. Morphodynamics are calculated per time point, based on the normalized change in volume and aspect ratio. **E.** Morphospace plot showing the averaged locations of larvae (black squares), and polyps (gray triangles). Blue dots show measurements taken during the transition stage. **F.** Trajectories in morphospace for five individual animals during the transition stage, color-coded for the corresponding morphodynamics at each time point. Bars indicate the duration of the different morphodynamics. Figure panels shown here also partially appear in (Stokkermans et al., 2021) and were made by me. Scale bars: 100  $\mu\text{m}$ .

## 5.6. Animal settlement behavior correlates with axial elongation dynamics

Since the duration of the transition stage (Figure 13G), end-morphology (Figure 15E) and morphodynamics (Figure 15F, Appendix Figure 1, Appendix Table 2) all showed a high variability, I next asked how this variability could be explained. The size an animal acquires as a primary polyp may depend on the variation in egg size, as the egg is the only source of nutrients until the animal reaches the polyp stage and acquires the ability to catch prey. Splitting the embryo in two at the four-cell stage has been shown to yield primary polyps of reduced size (Ikmi et al., 2020). The origin of variation in elongation dynamics is less clear. Genetic and environmental factors may play a role, but may not explain all of the observed variation, as even the offspring from the same parents show



variation in onset of elongation and elongation rate within the same experimental conditions (**Appendix Figure 2**).

Another possibility is that elongation dynamics are influenced by (stochastic) animal behavior. Many species of marine invertebrates know a free-swimming, pelagic form as larvae, and a settled, benthic form as juveniles and adults. In these species, larvae that are about to start metamorphosis often settle and adhere to a substrate (Jackson et al., 2002; Leitz, 1997), so in these cases the switch from swimming to settlement behavior overlaps with morphological changes. To study swimming/settling behavior in developing *Nematostella* and its potential relationship with elongation dynamics, the distance animals moved between time points was calculated throughout their development. Combining the measurements from all transition-stage time points from multiple experiments reveals an elbow-distribution where displacement below 130  $\mu\text{m}$  between time points occurs at high frequency, and displacement above 130  $\mu\text{m}$  is widely distributed but occurs at low frequencies (**Figure 16A**). This reflects the swimming/settling behavior of the animal: non-swimming animals show low displacement, whereas swimming animals show random displacement within the well, as the speed of swimming is much higher than the rate of image acquisition. In order to further analyze these different states of swimming/settling behavior and compare them to elongation dynamics, a displacement below 130  $\mu\text{m}$  was classified as 'low motility' and a displacement of 130  $\mu\text{m}$  or more as 'high motility' (**Figure 16A**). Measuring motility over pseudotime for all animals combined reveals that high-motility dominates before the start of larva-polyp transition, and is surpassed by low-motility behavior after about four hours since the exit from the larval stage, consistent with a switch from a pelagic to a benthic form (**Figure 16B**). In *Nematostella*, this switch appears to occur during early larva-polyp transition, rather than before or at the start of metamorphosis, as has been reported for other species (Leitz, 1997; Müller & Leitz, 2002).

As settlement behavior is associated with attachment to a substrate in most cnidarian species, including *Hydractinia*, *Acropora*, and *Cassiopeia* (Hofmann and Brand, 1987; Leitz, 1997; Muller, 1969; Müller and Leitz, 2002), the next question was whether the decrease in motility is the result of active attachment of the animal to the surface. Indeed, while transferring animals by mouth pipet, I noticed that early polyps often stick their lower body column to the bottom of glass and plastic dishes. Because attachment could not be measured directly in microscopy experiments, I instead measured the displacement of the oral and aboral pole separately during larva-polyp transition. Here, I found that the oral pole moves significantly more than the aboral pole during low motility but not during high motility behavior, suggesting that the animal indeed adheres itself to the bottom of the plate using the aboral part of the body column, whereas the oral end remains free (**Figure 16C**). This behavior persists throughout the transition stage, but most animals regain some motility as

polyps, and appear to displace themselves at the bottom of the plate at irregular intervals by gliding and contracting.

To investigate whether the variability in elongation dynamics (**Figure 13F, G**) correlates with differences in swimming/settlement behavior, the elongation rate was measured separately for low and high motility states. This revealed that the increase in body length is significantly higher during low motility compared to high motility (**Figure 16D**). Moreover, animals appear to be able to switch between a state of high motility with slow elongation and a state of low motility and fast elongation (**Figure 16D**, colored dots). A state of both high motility and high elongation rate was also observed, as is visible in the upper part of the ‘high motility’ violin plot (**Figure 16D**). This state of high motility and fast elongation occurs predominantly at the start of the transition stage (**Figure 16E**), suggesting that the first part of larva-polyp transition is distinct from later development, and that larva-polyp transition is initiated prior to animal settlement.

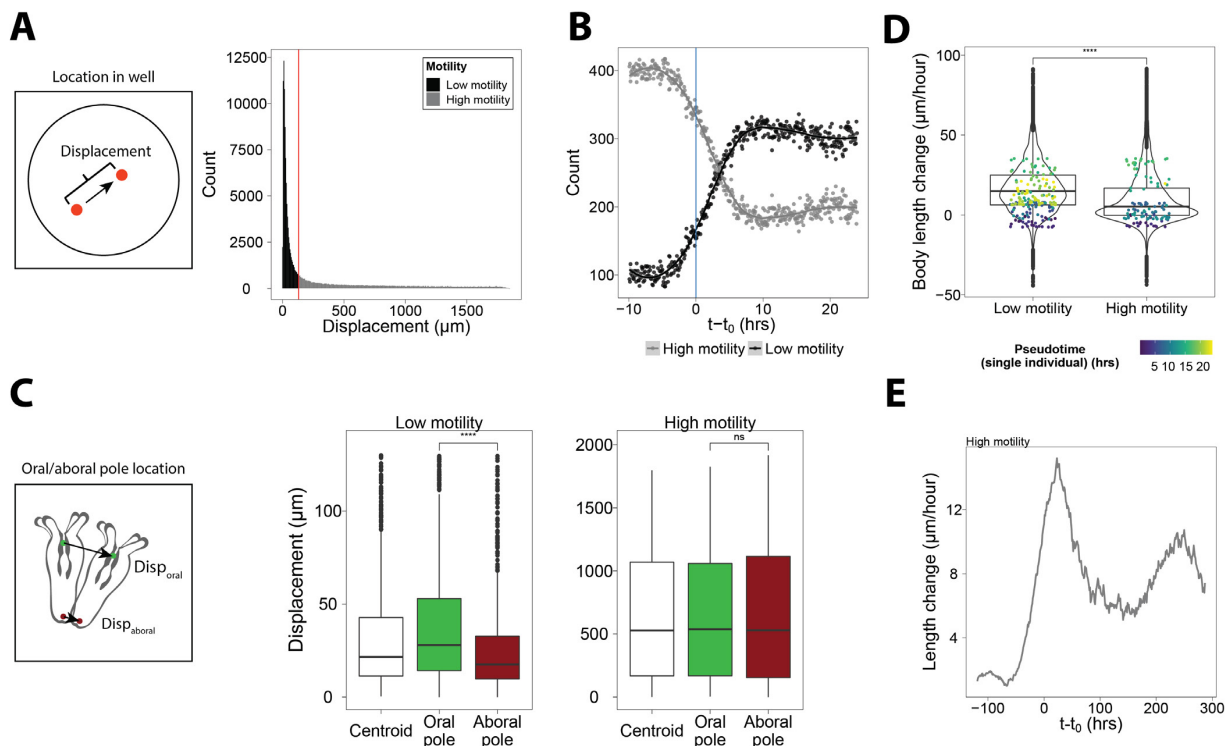


**Figure 16. Correlation between settlement behavior and elongation rate.** **A.** Quantification of animal displacement per five-minute time interval. A cutoff at 130  $\mu\text{m}$  displacement is used to distinguish low (black) and high (grey) motility. Counts are based on combined data ( $n = 669$  animals, with a total of 143934 measured transition-stage time points). **B.** Occurrence of high and low motility in pseudotime. **C.** Quantification of displacement of the oral (green) and aboral pole (red) during high and low motility. **D.** Violin plots showing the distribution of body length change for time frames with low and high motility, respectively. Colored dots indicate measurements for a single individual, showing that the same animal can switch between both states. Pseudotime is indicated by color. **E.** Average body length change over pseudotime for time frames that show high motility. The first peak indicates that animals increase their body column length while showing high motility mainly in the first hours of the transition stage. Figure panels shown here also partially appear in (Stokkermans et al., 2021) and were made by me.

## 5.7. Sessile and motile animals show different morphodynamics during larva-polyp transition

The relationship between elongation rate and settlement behavior can be further analyzed at the level of individual animals. Figure 17 shows three examples of animals with different elongation dynamics and swimming/settling behavior. Animal 1 settles soon after the start of larva-polyp transition, and shows rapid elongation with a clear period of attachment as judged by the oral and aboral pole displacement. In contrast, animal 2 remains motile throughout most of the transition stage, and elongates at a slower rate. Animal 3 starts to undergo larva-polyp transition, but then pauses and only elongates further upon settlement. Although elongation dynamics and settlement behavior are very different among these three examples, all produce healthy-looking polyps.

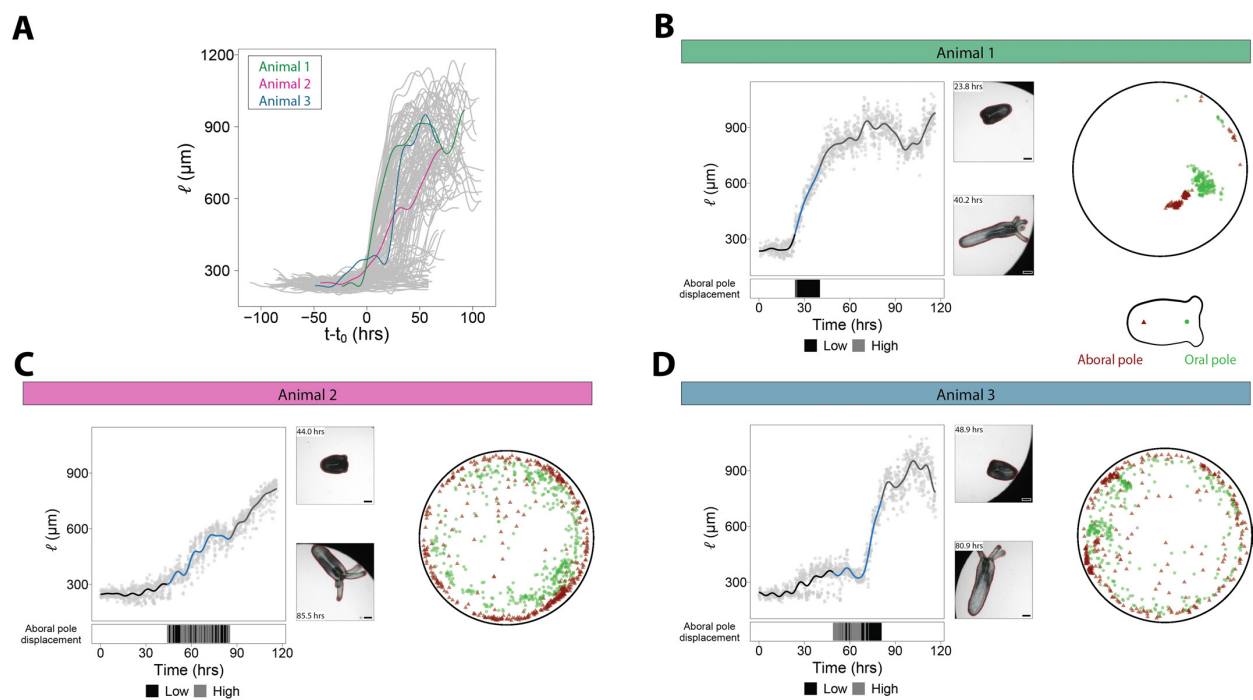


**Figure 17. Elongation dynamics and settlement behavior and three individuals.** **A.** Smoothed curves for body length as shown in Figure 13F, highlighting three individuals. **B-D.** Measurements for the animals highlighted in (A). On the left: body length over time, color-coded for developmental stage (black: larva, blue: transition, grey: polyp). The bar below indicates displacement of the aboral pole during the transition stage. On the right: location of the oral (green dot) and aboral (red triangle) poles in the well during the transition stage. Figure panels shown here also appear in (Stokkermans et al., 2021) and were made by me. Scale bars: 100  $\mu\text{m}$ .

To further compare elongation dynamics between animals showing different swimming/settling behavior, animals were classified either as ‘sessile’ or ‘motile’ based on the median motility during the transition stage, using a cut-off of 130  $\mu\text{m}$  (Figure 18A). The majority of animals (494/669) become sessile during the transition stage, whereas the remaining 175 animals show high motility throughout most of the transition stage. As expected, sessile animals show a higher average elongation rate (Figure 18B), and spend less time in the transition stage (Figure

18C). Comparing morphodynamics, it appears that motile animals switch more often between different morphodynamics than sessile animals (**Figure 18D**). Furthermore, larvae that become sessile often exhibited a stereotyped pattern composed of ‘combined stretching and inflating’ with relatively high motility behavior, followed by ‘stretching’ with a marked phase of low motility (**Figure 18E, F**). Such stereotypic pattern was absent in animals that maintain high motility throughout larva-polyp transition, which on average increase their body column volume and aspect ratio in a more linear fashion (**Figure 18E, F**). Sessile and motile animals thus not only differ in elongation rate, but have a slightly different size-shape relationship during larva-polyp transition. This is also reflected in the summary statistics of morphodynamics: whereas sessile animals increase their length through both ‘stretching’ and ‘combined stretching and inflating’, motile animals rely mostly on ‘combined stretching and inflating’ for length increase (**Appendix Figure 3, Appendix Table 3**). Together, these results suggest that larva-polyp transition is guided by a relatively plastic developmental program, in which the axial elongation dynamics correlate with patterns in settlement behavior.

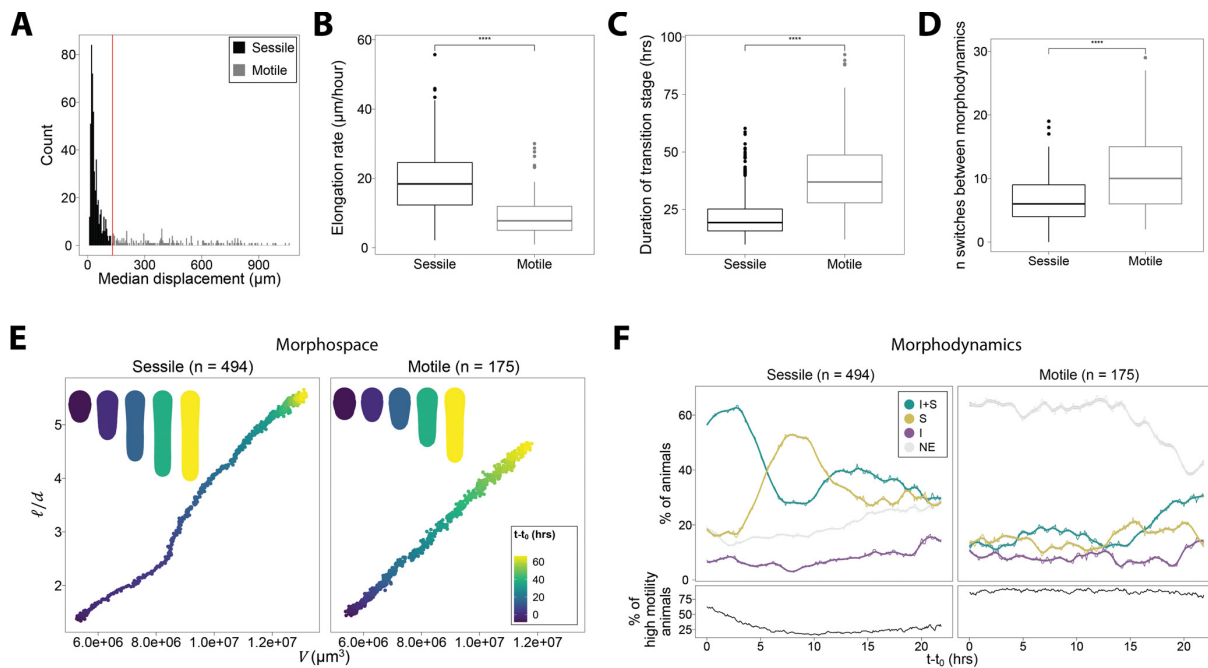


**Figure 18. Sessile and motile animals differ in morphology and pattern of morphodynamics.** **A.** Histogram of the median of displacement for the entire transition stage for individual animals. Animals that show a median displacement below 130  $\mu\text{m}$  are classified as sessile (black,  $n = 494$ ), whereas animals with a median displacement above 130  $\mu\text{m}$  are classified as motile (gray,  $n = 175$ ). **B-D.** Elongation rate (B), duration of transition stage (C), and number of times an animal switches between different morphodynamics (D) in sessile and motile animals. **E.** Average location in morphospace per pseudo-time point for sessile and motile animals. Insets show the reconstructed shape at five different time points. **F.** Distribution of morphodynamics in pseudotime in sessile and motile animals. The bar below shows the percentage of animals showing ‘high motility’ at a given pseudotime point. Note that sessile animals show high motility in the first few hours of the transition stage, whereas motile animals show high motility throughout most of their entire transition stage. Morphodynamics are abbreviated as follows: ‘I+S’: combined stretching and inflating, ‘S’: stretching, ‘I’: ‘inflating’, ‘NE’: no elongation. Figure panels shown here also partially appear in (Stokkermans et al., 2021) and were made by me.

## 5.8. Morphogenesis and animal behavior act on different time scales.

Recordings of developing *Nematostella* larvae at five-minute resolution revealed dynamic changes in animal size and shape as they undergo larva-polyp transition. However, the size and shape of an animal at a given time are not only dependent on the developmental state, but are also subject to the effects of animal behavior. For example, at one time point an animal can have a greatly reduced length due to a body contraction, while appearing completely extended again at the next time point (**Figure 19A**). In such a case it is unlikely that the animal has undergone major morphogenetic changes, rather, it has only temporarily changed its conformation as a result of behavior. Morphogenesis and behavior in *Nematostella* act on time scales that are relatively far apart (**Figure 19A**). Whereas morphogenesis takes place over hours to days and is considered mostly as a one-way, irreversible change, behavior acts on the scale of seconds to minutes and the change in body shape and size is reversible. While these two processes act on different time scales, they also co-occur at the same time. This raised the question whether this short-lived animal (contraction) behavior and long-term morphogenesis are linked, i.e. does behavior impact morphogenesis? In order to study animal contraction behavior during larva-polyp transition in more detail, the same imaging strategy was applied, but instead of recording an entire population of animals, single individuals were recorded at five-second resolution. Such high time resolution recordings reveal 'spiky' patterns in body length over time, visualizing overall length increase, combined with the effects of animal contractile behavior (**Figure 19B**).

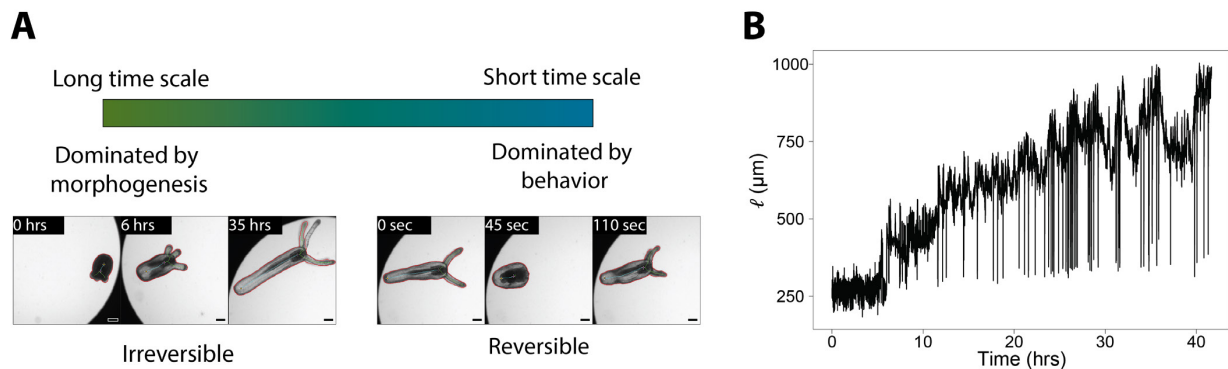


**Figure 19. Morphogenesis and animal behavior act on different time scales.** **A.** Schematic illustrating irreversible morphogenetic changes that take place on long time scales, and short-lived behavioral morphological (conformational) changes that are reversible. **B.** Recording of a single individual at five-second time resolution, revealing co-occurrence of morphogenesis (total body column length increase) and animal behavior (sudden, short-lived decreases and increases in length due to body contractions).

## 5.9. Developing *Nematostella* show two main types of body contractions

Recordings of complete larva-polyp transition at five-second time resolution yield large and dense datasets that can be interpreted at different levels. While developmental changes are visible at the hour-to-day time scale, zooming in to the second-to-minute time scale shows how animals

undergo large but reversible shape changes (**Figure 20A**). This makes analysis of the data complicated: the 'true', developmental size and shape of an animal at a given moment in time are not well-known, as they are influenced by the behavioral state of the animal. So how can one distinguish between a change that is the result of development, and a change resulting from animal behavior? Since the two processes take place on different time scales, I tried to separate them by distinguishing the global trend (long time scale) from the short time scale fluctuations. Here, I used animal circularity to look at both long and short-term shape changes, as it worked well to detect both overall morphological change (as used in the staging method) as well as changes in shape due to contractions (**Figure 20A, B**). Heavy smoothing by applying a sinc filter with a large cut-off period of 167 minutes or longer (see Materials and Methods), leaves only the trend of the data intact, estimating morphological change as a result of development (**Figure 20B**, middle left). Subtracting this trend from the original five-second resolution data sequence leaves only the high-frequency, behavioral components, without the long-term effects. From this I extracted a 'contraction score' (or C-score for short, see Materials and Methods for details) that detects short-lived changes in circularity, as a proxy for contractile activity.

Based on the contraction score together with the profile of body column diameters from oral to aboral pole, two major types of contractions can be distinguished. First, when the longitudinal retractor muscles contract, animals retract their tentacles and shorten dramatically, while increasing their body column diameter. These contractions take place in a matter of seconds, and the animals generally recover their original shape within a minute (**Figure 20C**, left). This defensive behavior can be triggered by pinching the animal or by creating vibrations in the water, but is also observed in developing animals without the occurrence of a clear disturbance. Such contractions have a large impact on animal circularity, and show up as clear peaks in the contraction-score profile (**Figure 20C**, bottom right). Second, one can observe circular muscle-driven peristaltic contractions that propagate through the body column and take around 30-60 seconds to complete, depending on the length of the body column (**Figure 20C**, right). These contractions have less impact on overall circularity, and show up as a moderate but continuous elevation in the contraction-score profile (**Figure 20C**, bottom right). Both types of contractions are observed frequently, but at irregular intervals. During the time in between these two major types of contractions, smaller contractions can be observed, that appear as 'wiggling' and small stretching and retracting movements. As reported by (Batham and Pantin, 1950a; Kier, 2012), the longitudinal and circular muscles in sea anemones act similarly to muscle antagonists in vertebrates. In agreement with this, the measurements of body column length and average body column width over time in the experiments performed show an anti-correlation with a Pearson correlation coefficient of -0.62.



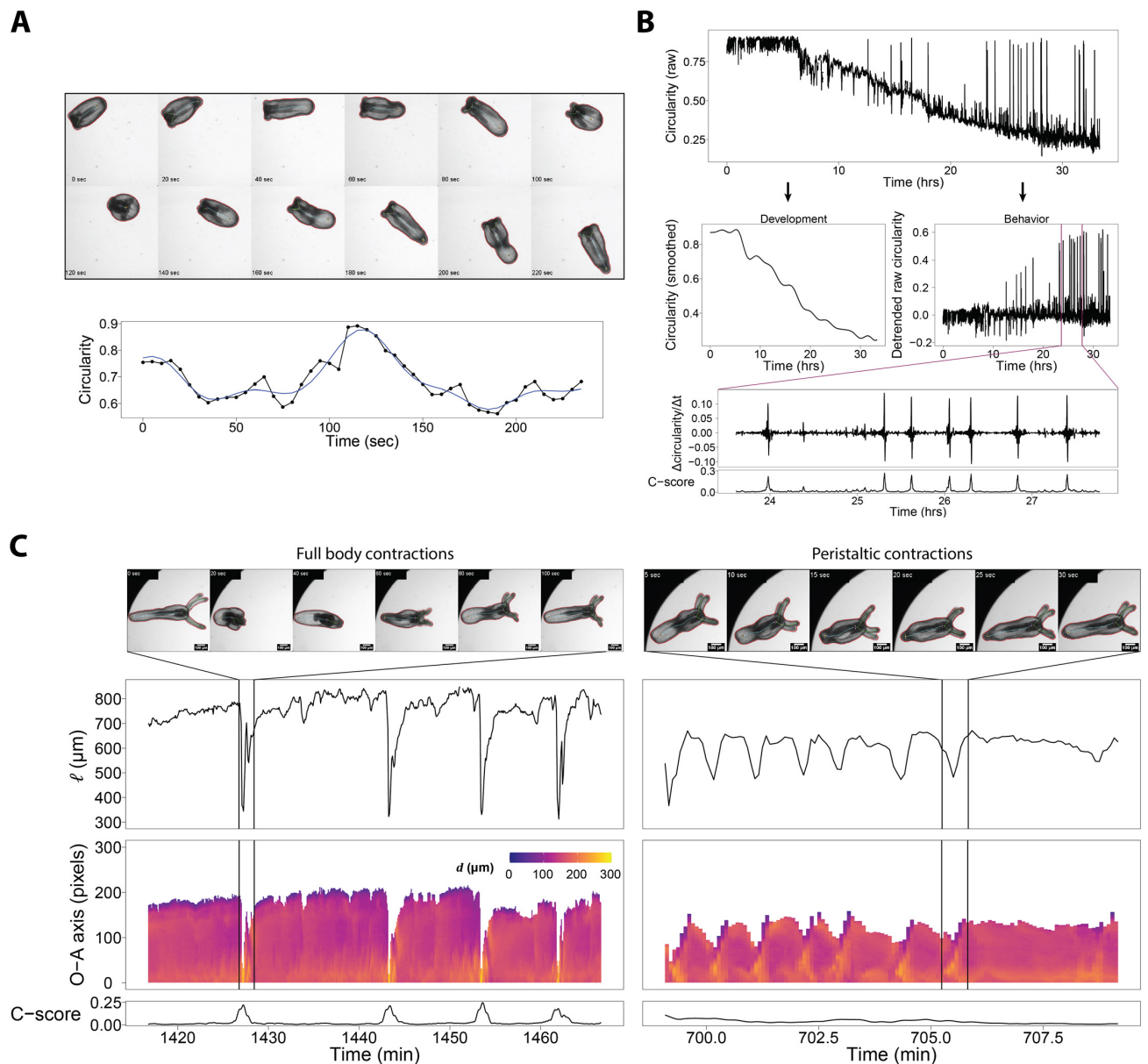


**Figure 20. Circularity-based detection of body contractions during larva-polyp transition.** **A.** Recording of animal contractions at 5-second interval and corresponding measurements of circularity during a time window of 220 seconds. **B.** Method to detect and score contractile activity based on changes in circularity on short time scales. **C.** Measurements of animal length, body column diameter along the (non-calibrated) oral-aboral (O-A) axis, and contraction score ( $5 \text{ sec}^{-1}$ ) during full-body contractions and peristaltic contractions. Scale bars:  $100 \mu\text{m}$ .

### 5.10. Different types of contractile behavior may contribute to specific morphodynamics

The question remained whether contractile behavior correlates with elongation dynamics. In order to search for patterns, the data can be analyzed at different levels, e.g. by looking at individual animals (**Figure 21A**), by averaging behavior in multiple animals (**Figure 21B**), by looking at individual sequences of morphodynamics (**Figure 22**), or by averaging different morphodynamics among animals (**Appendix Table 4**).

Unfortunately, the high variability that is present in high time resolution data due to different animal behaviors makes it difficult to distinguish strong 1-1 relationships between morphogenesis and contraction behavior. Nevertheless, some recurring patterns were observed that may provide some hints about the mechanistic function of the hydrostatic skeleton during larva-polyp transition. During early larva-polyp transition, animals are often motile and show active contractions, while showing isotropic ('inflating') or anisotropic ('combined inflating and stretching') expansion (**Figure 21** and **Figure 22A**). The image recordings reveal that during this time the animal shows contractions that look like a pumping mechanism, suggesting that peristaltic contractions may be involved in increasing body column volume. Animals are not attached to the plate, as indicated by (slowed) swimming behavior and in-place spinning. Following body column inflation, most animals settle and appear to stick to the plate. In the following hours, relatively few major short-term body deformations occur, and animals use 'stretching' to elongate their body column (**Figure 22B**). In the recordings, small body contractions can be observed during this time, and it appears as if the animal is literally stretching and squeezing itself, suggesting that in this case the muscle forces may act directly on the body wall to drive elongation. Late larva-polyp transition is often dominated by 'combined stretching and inflating' with increased contractility (**Figure 21** and **Figure 22C**). During this time, animals increase both animal body column volume and aspect ratio while showing a combination of full-body contractions followed by peristaltic contractions (**Figure 22C**). In contrast, during sequences labeled 'no elongation' the animal often shows high motility, sometimes combined with active contractions (**Figure 22D**). In these cases, the animal appears to move using a combination of swimming or gliding together with contraction behavior that pushes the animal forward.



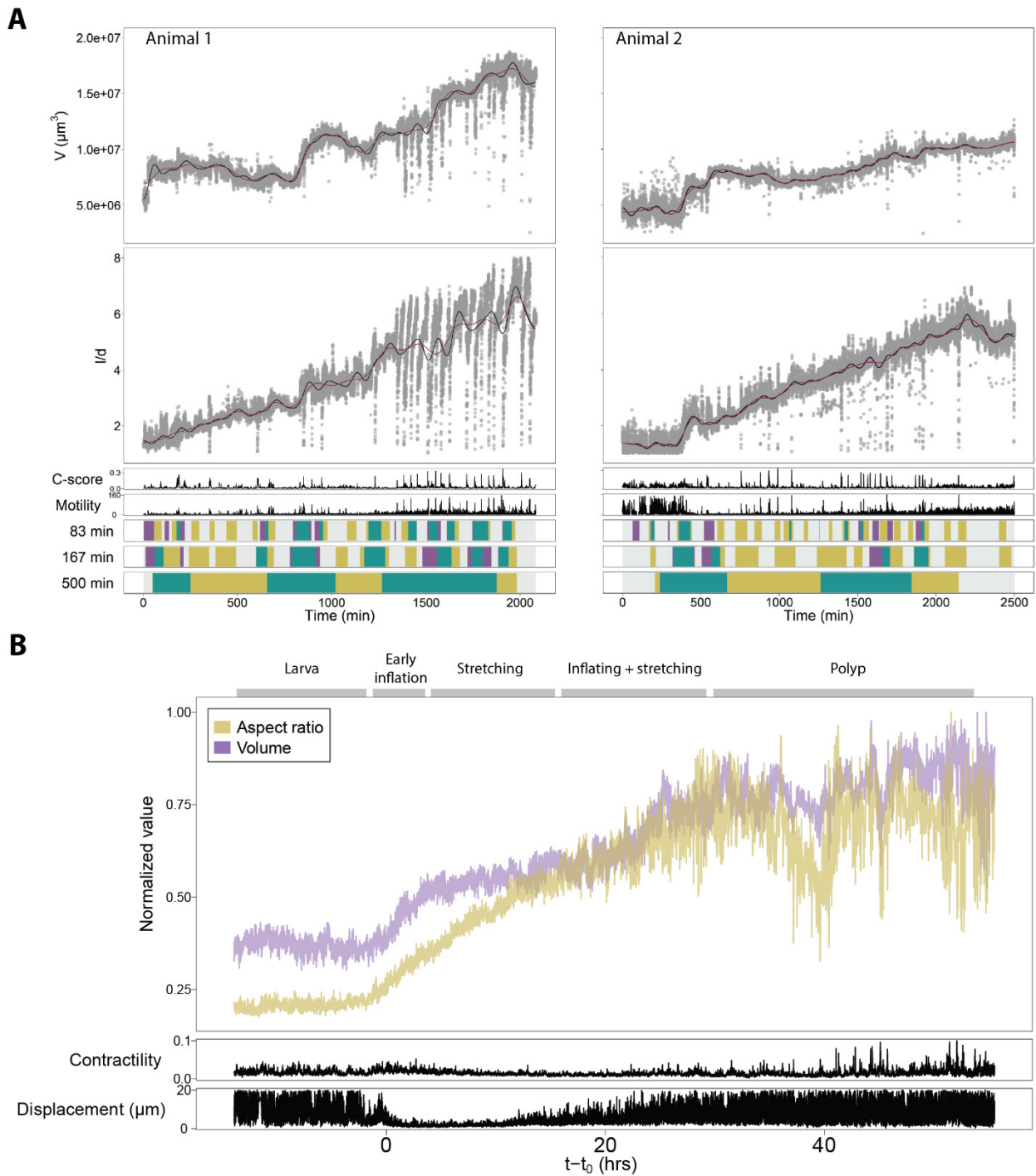


**Figure 21. Animal behavior and elongation dynamics in individual animals and averaged among individuals.** **A.** Profile of animal body column volume, aspect ratio, contraction-score, motility, and morphodynamics over time for two individuals. **B.** Averaged and normalized body column volume and aspect ratio, as well as contraction score and displacement per 5-second interval for 23 wild type animals. Values for displacement are truncated at  $20 \mu\text{m}/5 \text{ sec}$ , for visualization purposes.

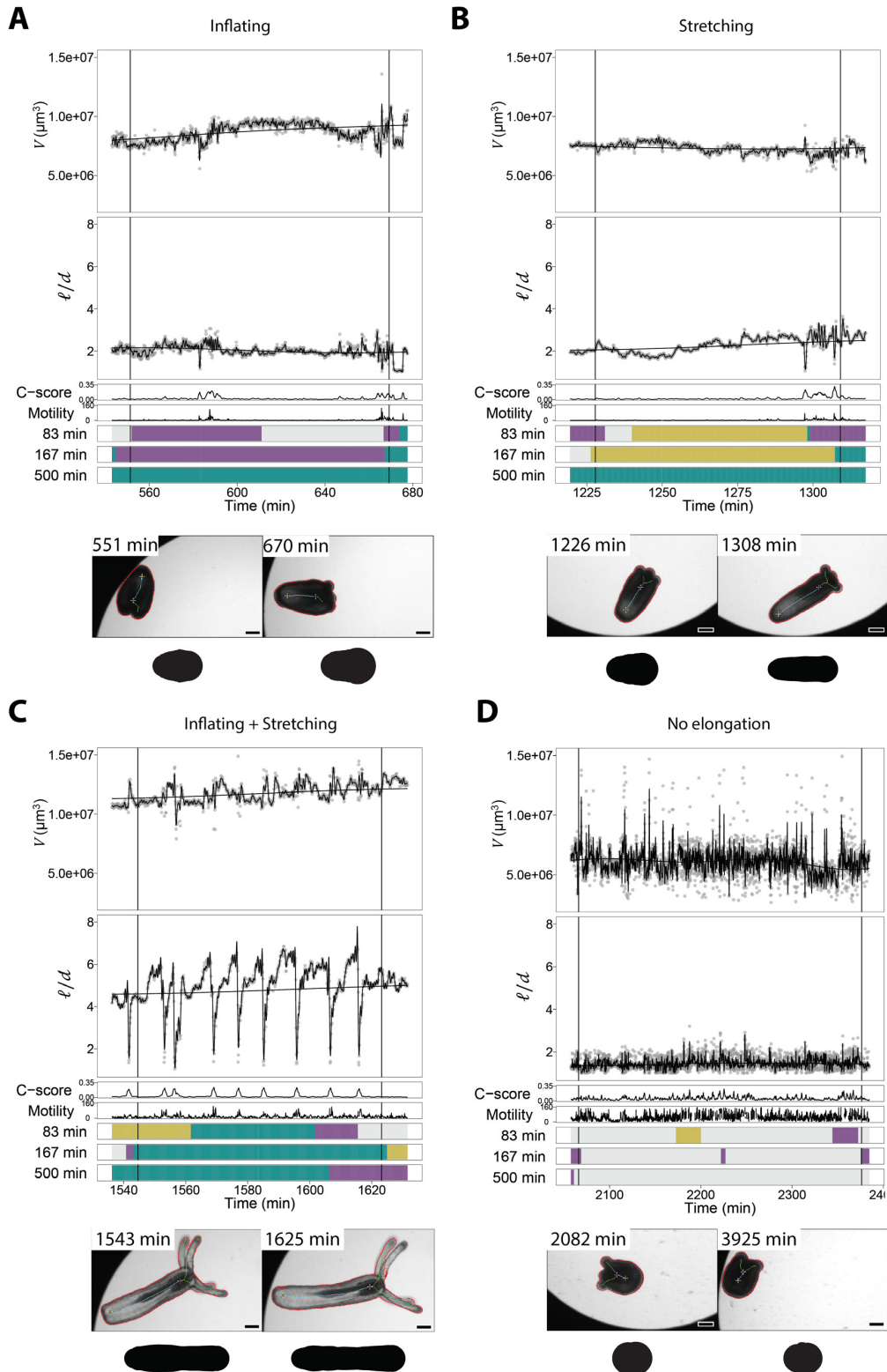


**Figure 22. Time sequences showing different types of morphodynamics recorded at high time resolution.** A-D. Profile of animal body column volume, aspect ratio, contraction score, and motility for different morphodynamics: ‘inflating’ (A), ‘stretching’ (B), ‘combined stretching and inflating’ (C), no elongation (D). Morphodynamics are calculated from smoothed data with different cut-off periods (83, 167, and 500 minutes). Smoothed line corresponds to smoothing with a cut-off period of 167 minutes. Images corresponding to start and end time points are shown below, together with reconstructed shapes (black). Measurements in (D) are noisier because quantification is complicated by active movements and rotations in the early stage animals.

## 5.11. Summary and conclusions

*Nematostella* larvae undergo a major but simple morphogenetic change while expressing dynamic organismal behaviors as they develop into polyps. By establishing an experimental setup with an image analysis pipeline, these morphogenetic and behavioral changes could be recorded in a high-throughput manner. From these data, I found that larva-polyp transition in *Nematostella* is a dynamic process with high inter-organism variation. At the end of the transition stage animals have increased in size and adopted a cylindrical body column shape, although the final morphologies still include a range of long and short, large and small animals. The polyp stage morphology is reached through changing body column volume and aspect ratio, sometimes separately and sometimes simultaneously. These changes were further investigated by classifying them into distinct morphodynamics: 'inflating', 'stretching', 'combined stretching and inflating', and 'no elongation'. Interestingly, animal swimming/settling behavior was found to correlate with elongation dynamics, and sessile animals were found to show a stereotypic pattern composed of an initial inflation through isotropic (inflating) or anisotropic (combined stretching and inflating) expansion, that is followed by a period of stretching during which the animal appears to be attached to plate bottom. Animals that remain motile throughout the transition stage do not show such a pattern. Contraction behavior was studied by recording animals at five-second resolution and measuring the change in circularity at short time scales. From this analysis, it was difficult to find direct relationships between animal contractile behavior and elongation dynamics. However, through manual observation and averaging of data from multiple animals, subtle patterns could be found. 'Pumping' peristaltic contractions overlap with inflation of the body column, whereas small 'squeezing' contractions with occasional full body and peristaltic contractions appear to induce stretching in attached animals with minimal volume change. The following chapters will focus on understanding the functioning of the hydrostatic skeleton and its impact on the tissue. Chapter 6 focuses on tissue level changes underlying size and shape change during larva-polyp transition. Chapter 7 focuses on the mechanisms behind size and shape changes through perturbation studies. Finally, Chapter 8 discusses ongoing work investigating some of the environmental factors that may influence larva-polyp morphogenesis.



## 6. Tissue morphogenesis during larva-polyp transition

### 6.1. Cavity inflation is a main driver of organismal size increase

As described in Chapter 5, *Nematostella* larvae change both in size and shape during larva-polyp transition. Since larvae do not feed until they have acquired tentacles required for prey capture, it seems likely that the increase in organismal size is due to fluid uptake from the environment. Measuring the area of the body cavity in mid-section images of fixed animals reveals an expansion of the cavity during larva-polyp transition (**Figure 23A**). However, it is not easily possible to reliably extract information about the relative contribution of cavity inflation to the total animal volume from 2D images of fixed samples, in part because of the asymmetry of the internal (mesentery) tissue. To reliably measure the volume of tissue and body cavity, a method is required that can capture the volume of an entire, living animal at a fast rate. In practice, this means that the entire animal volume has to be captured within a few seconds, in order to minimize the effects of animal movement and contraction. Standard confocal microscopy techniques generally do not allow such fast imaging. Moreover, they require fluorescent labeling to visualize the animal, but the limited penetration depth in thick, dense specimens makes it impossible to capture the entire animal with this approach. To overcome these issues, the use of a new microscopy technique called optical coherence microscopy (OCM) was explored in collaboration with the laboratory of Robert Prevedel at EMBL Heidelberg. This technique is derived from optical coherence tomography (OCT), which is frequently used for medical purposes, historically most notably for imaging of the retina (Aumann et al., 2019; Fujimoto and Swanson, 2016). In a nutshell, this technique relies on the way light waves echo back from the scanned tissue. The delay of the back-reflected waves contains information about the tissue depth at which the reflection occurred. This information can be revealed by an interferometer, wherein one part of the light probes the sample, and another part is sent to a reference arm of well-known length with a mirror at its end. The light that is passed on to the sample echoes back with a delay compared to the light that is reflected from the mirror in the reference arm. The interferometer then combines the light coming back from the two paths. Due to the difference in time, the two light waves can be shifted in phase relative to each other, causing constructive or destructive interference. Therefore, the resulting change in light intensity in the interferometer output is informative of how much shift has occurred, which is a function of the difference in optical path lengths. The time (and hence the distance) from a light source at which interference can occur depends on the light coherence: the property that tells how similar a wave is, and hence how well it can interfere with itself at different times. Monochromatic lasers have a high coherence, as they consist of light waves of very similar wavelength. In OCM, light sources of low coherence are used. This means that interference of the wave with itself can only occur if the difference in optical path

lengths falls within the short coherence length of the light source. Therefore, the lower the coherence length, the higher is the theoretical z-resolution of the OCM setup. Thus, in OCM the axial resolution depends on the light source, instead of on the focusing optics (Aumann et al., 2019).

In order to use this principle to scan a sample, three main methods have been used so far. The first method, called time-domain OCT (TD-OCT) scans the reference mirror in Z while recording the light intensity, generating a so-called A-scan. By scanning the sample beam laterally, a cross-sectional image or B-scan is created. The second and third technique both make use of spectral information to generate A-scans and do not need to mechanically scan the optical path length. These are called Fourier-domain OCT (FD-OCT). They either use a broad-band light source with a spectrometer to separate the different wavelengths, or a light source that sweeps across wavelengths in time. Both techniques record an interference spectrum from which the tissue depth can be extracted through inverse Fourier transformation, generating an A-scan presenting the reflected light intensity over Z. Contrast within the resulting image arises from the differences in reflectivity between different media within the specimen. Hence, OCM makes use of the modulation frequencies in the interference spectrum to extract depth information, and the amplitude of interference modulation to distinguish heterogeneities between different layers of the specimen (Aumann et al., 2019).

OCM is a label-free method and often uses near-infrared light that has a high penetration depth, which is essential for capturing relatively thick and dense samples, such as *Nematostella* larvae. Although this technique already allowed us to capture a much larger part of the animal than was possible with confocal microscopy, it was still challenging to capture complete larvae due to high light scattering effects at this developmental stage. To overcome this problem, a dual-view FD-OCM setup with broad-band light source was established by Ling Wang (Prevedel lab, EMBL Heidelberg) (**Figure 23B**). With this setup, the same animal can be simultaneously imaged from two complementary views, which, after reconstruction, yields the full volume of the animal in all three dimensions (**Figure 23C-D**). With this approach, the same animal could be imaged at the larval and polyp stage, in order to measure the change in cavity and tissue volume. From this data, acquired by Kaushikaram Subramanian (Ikmi and Prevedel groups, EMBL Heidelberg), we found an approximately 9-fold increase in cavity volume, and 1.5-fold increase in tissue volume (**Figure 23E**). We found that the cavity sizes varied from one animal to another, and also appeared to be variable within the same animal at different time points, indicating that animals can regulate their size by inflating or deflating their body cavity. Although animals are unable to eat during larva-polyp transition, we also observed an increase in tissue volume. This could potentially be explained by an uptake of water by the cells, thereby expanding the tissue. However, also the possibility of tissue overestimation has to be considered, as a small dilation of the tissue boundaries can have a large

accumulative effect in long and thin shapes, such as the *Nematostella* body column and tentacles. Therefore, the current OCM-based method for tissue and cavity quantification is currently being further optimized by Ling and Kaushikaram, in order to measure such potential overestimation. This overestimation factor could then be incorporated in the image analysis pipeline in order to more accurately define the tissue boundaries. Finally, the dual-view OCM setup also allowed us to compare the volumes measured from 3D OCM acquisitions with the estimated volumes from 2D images, such as those acquired on the Acquirer screening microscope. We found that both measurements are in similar order of magnitudes, but on average, the estimation from 2D images is slightly lower than from 3D images (**Figure 23F**). This is expected, as an animal with a tilt in the oral-aboral-axis with respect to Z shows up slightly smaller when viewed in the XY-dimensions only. Therefore, the volume is most accurately estimated when the animal is lying perfectly flat in XY with its oral-aboral axis perpendicular to the Z dimension. In the image analysis pipeline applied to live imaging data from the Acquirer screening microscope, the problem of animal tilt is to some extent solved by rejecting images of animals that are partially out of focus, as this is indicative of a tilt in the Z dimension. However, animals with a small tilt are not rejected, which might explain why the volume is slightly underestimated in 2D images. In conclusion, we noted that dual-view OCM is a useful method for capturing thick and fast-moving developing *Nematostella*, and that this technique can be further explored for recording both animal development and behavior in the future. This technique allowed us to quantify the change in volume of cavity and tissue during development, and to confirm that cavity inflation is indeed a major contributor to organismal size. Moreover, it allowed us to validate that size increase as measured from 2D images falls in the same range as when measured from 3D images that contain the full information.

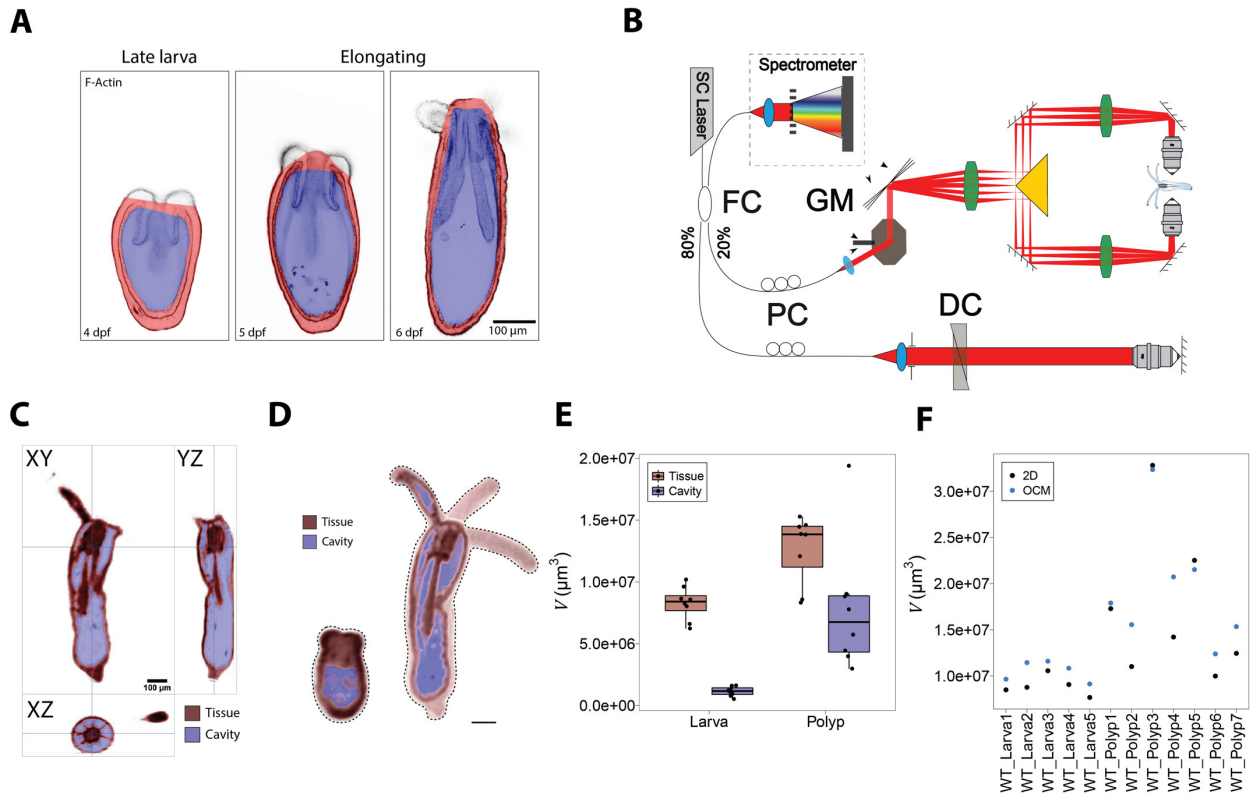


**Figure 23. Cavity expansion is a major driver of organismal size.** **A.** Mid-sections of fixed *Nemastostella* larvae at different stages, stained for F-actin. Body wall tissue is manually labeled in red, and cavity and internal tissue are labeled blue. **B.** Schematic diagram of dual-side view spectral-domain OCM setup. FC: fiber coupler; GM: galvo mirror; DC: dispersion compensator; PC: polarization controller; SC Laser: supercontinuum laser. Diagram and OCM setup are produced by Ling Wang (Prevedel lab, EMBL Heidelberg). **C.** Orthogonal views of the same animal, imaged with dual-view OCM and labeled for tissue (red) and cavity (blue). **D.** Opened 3D view of a larva and corresponding polyp, imaged with dual-view OCM and labeled for tissue (red) and cavity (blue). **E.** Quantification of tissue and cavity volume at larva and polyp stage, based on OCM data. **F.** Comparison of estimated total animal volume (cavity and tissue combined) as obtained from 3D OCM images and 2D flattened images derived thereof. All shown OCM data was produced by Kaushikaram Subramanian (Ikmi and Prevedel groups, EMBL Heidelberg). Figure panel B, D-F also appear in (Stokkermans et al., 2021). Scale bars: 100  $\mu\text{m}$ .

## 6.2. Cell proliferation plays a minor role during larva-polyp transition

I next focused on the changes that take place at the tissue level during larva-polyp transition that could explain how the animal undergoes such a drastic change in shape. As described in Chapter 2, well-known mechanisms known to play a role in tissue morphogenesis include oriented cell division, cell shape changes, and cellular rearrangements (**Figure 24A**). Cell divisions with an orientation bias have been shown to occur during early larval development (Fritz et al., 2013). To investigate whether (oriented) cell division is also important during larva-polyp transition, budding larvae at the start of larva-polyp transition were treated with 5 mM hydroxyurea (HU). This treatment significantly reduced the number of proliferating cells, as quantified by the number of phosphorylated histone 3 (pH3) positive cells, which marks cells that are in M phase (**Figure 24B**). After 24 hours of treatment with 5 mM HU, the effect was still present. Remarkably, animals still



elongated and produced normal looking polyps (**Figure 24C, D**), suggesting that cell proliferation is not critical at this stage of development.

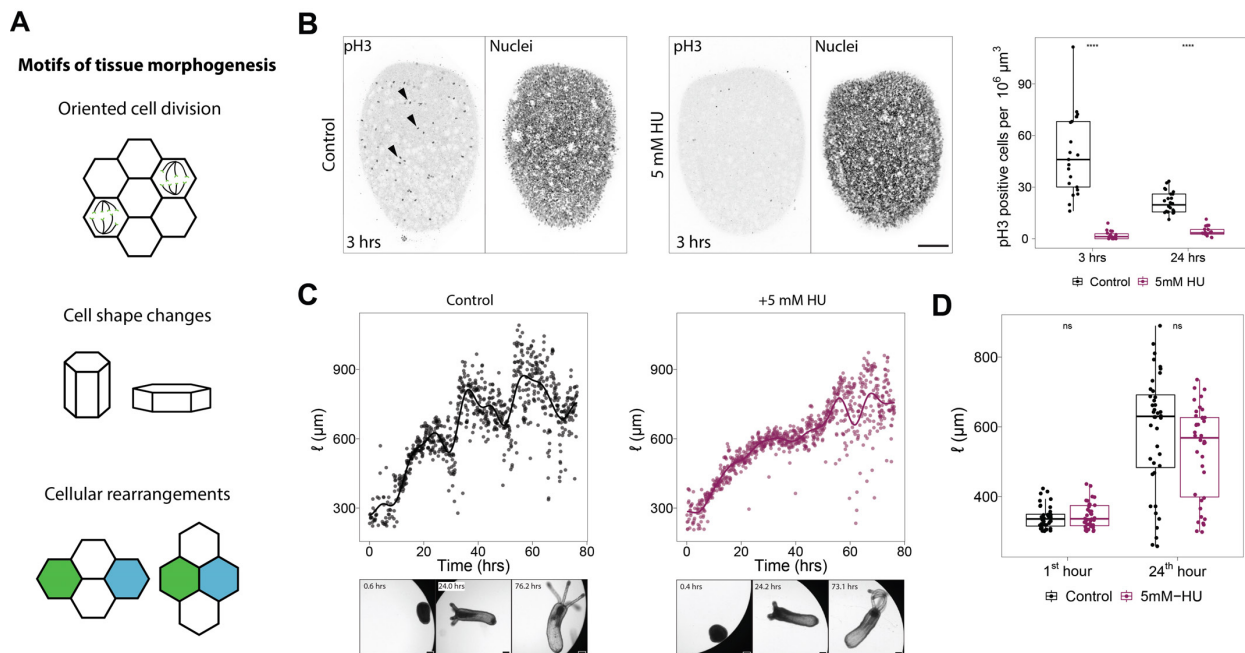


**Figure 24. Blocking cell proliferation does not prevent larva-polyp transition.** **A.** Common motifs in tissue morphogenesis include oriented cell division, cell shape changes, and cellular rearrangements such as cell-cell intercalation. **B.** Effect of 5 mM HU on the number of phosphorylated histone 3 (pH3) positive nuclei (two-sided unpaired Wilcoxon rank sum test; \*\*\*\* $p < 0.0001$ , control:  $n = 21$  (3 hrs),  $n = 24$  (24 hrs), 5 mM HU:  $n = 19$  (3 hrs),  $n = 20$  (24 hrs). Images show confocal maximum intensity projections of a control and a treated larva after 3 hours, stained with an antibody targeting pH3 (left) and with Hoechst to label nuclei. Arrowheads indicate examples of pH3 positive cells. **C.** Quantification of body length for a control animal and an animal treated with 5 mM HU. **D.** Quantification of body length of developing larvae after 1 hour and after 24 hours of treatment with 5mM HU or control sea water (two-sided unpaired Wilcoxon rank sum test; n.s.  $p > 0.05$ , control:  $n = 40$ , 5mM HU:  $n = 38$ ). Scale bars: 100 µm. Figure panel B-D also appear in (Stokkermans et al., 2021) and were made by me.

### 6.3. Cell shape changes and cellular rearrangements contribute to redistribution of tissue mass during larva-polyp transition

Since cell proliferation was found to play a minor role in tissue morphogenesis during larva-polyp transition, and animals cannot take up any nutrients during larva-polyp transition, a redistribution of tissue mass through cell shape changes and/or cellular rearrangements could provide an explanation for the observed organismal shape change. Previously, it has been shown that ectodermal and endodermal tissue undergo thinning during larva-polyp transition (Fritz et al., 2013). Since the ectoderm and endoderm are pseudostratified epithelia (Fritz et al., 2013), this thinning indicates a decrease in cell height. In order to further investigate cellular shape changes during larva-polyp transition, animals were fixed at different stages and stained with fluorescently labelled phalloidin or with an antibody targeting Cadherin3 (Pukhlyakova et al., 2019). I found that the ectoderm becomes progressively thinner as the animal elongates, in agreement with what has been published before (Fritz et al., 2013), and that it remains slightly thicker at the two poles

compared to the middle region of the body column (**Figure 25A-C**). If cells were to change shape without loss of volume, a decrease in cell height would have to coincide with an increase in cell diameter, i.e. cells become shorter and wider (**Figure 25D**). To investigate whether this is the case, I quantified the ectoderm apical surface area of cells at different developmental stages. Indeed, ectodermal cells increase their apical surface area substantially during larva-polyp transition, but estimated cell volume remains similar (**Figure 25E-G**). Endodermal cells appear to undergo a similar shape change as ectodermal cells (**Figure 25A, E**), but the high curvature and dense tissue at the larval stage prevented accurate quantifications of cell apical surface area at this stage.

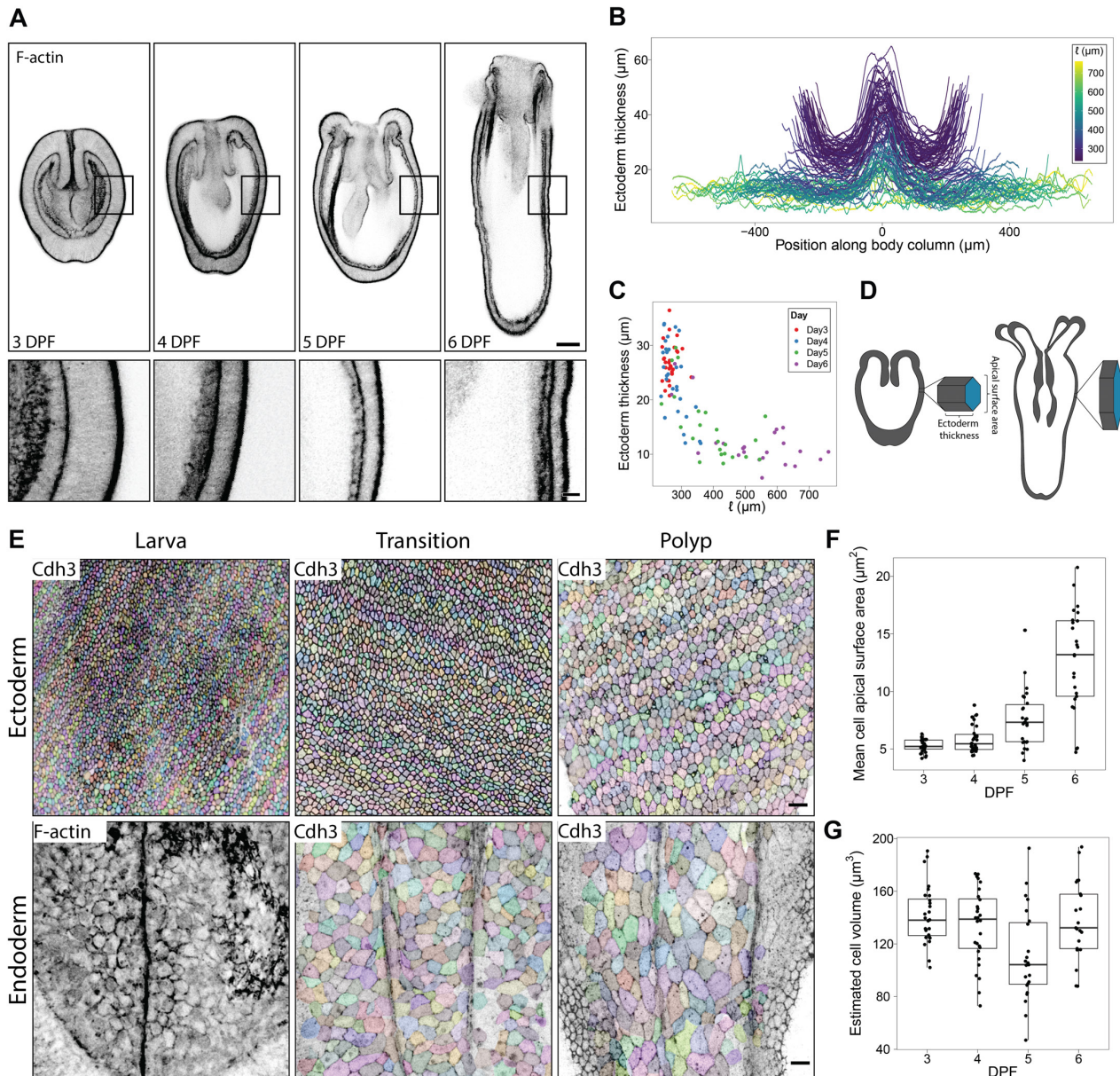


**Figure 25. Ectodermal and endodermal cells flatten and widen during larva-polyp transition.** **A.** Confocal mid-plane sections of fixed animals stained for F-actin at different days post fertilization (DPF), showing thinning of both the ectodermal and endodermal tissue layer. **B.** Quantification of ectodermal thickness along the body column, color-coded for animal length. A position of 0 corresponds to the aboral pole. Negative and positive numbers on the x-axis refer the measurements from the left and right side of the animal, respectively. **C.** Quantification of animal body column length versus average mid-body column ectoderm thickness. **D.** Cartoon showing how a change from tall columnar cells to short and wide cells can expand the total animal surface area. **E.** Confocal images of ectoderm and endoderm at different stages, corrected for animal curvature, showing increase of cell apical surface area in both layers. For the larva, two different individuals are shown; the images for transition-stage and polyp show the two tissue layers in the same individual. Colors indicate cell segmentation. Curvature-correction of the endoderm was insufficient to obtain flat images suitable for cell segmentation at the larval stage (bottom left). **F-G.** Quantification of ectodermal cell apical surface area (**F**) and estimated cellular volume (**G**) at different DPF. Cell volume was estimated by multiplying tissue thickness (i.e. cell height) with the estimated apical surface area. Scale bars: 50  $\mu\text{m}$  (**A**, top), 10  $\mu\text{m}$  (**A**, bottom, and **E**).

#### 6.4. Cellular rearrangements contribute to axial elongation

While cell shape changes flatten the epithelial layers and thereby increase the surface area of the animal, cell shape changes alone can only explain an organismal length increase of around 1.5 to two-fold. However, animals generally increase their length by three to four-fold. Previously, it has been shown that cellular rearrangements also contribute to tissue morphogenesis during larva-polyp transition (Fritz et al., 2013). This was shown by injecting a plasmid encoding eGFP under the control of the ubiquitin promoter at the single cell stage. This results in mosaic expression of eGFP, visible as random patches of fluorescently labeled cells (**Figure 26A**). Polyps have more elongated patches compared to larvae, suggesting that cells have intercalated along the oral-aboral axis (Fritz et al., 2013). However, cellular rearrangements have not been studied in the same animal over time so far. To try to achieve this, developing larvae expressing eGFP labeled patches were imaged on a NikonA1 confocal microscope with resonance scanner. This allowed faster imaging, which made it possible to record the development from larva to polyp in 3D and for two channels simultaneously (eGFP and dextran-red background stain) (**Figure 26B**). This revealed elongation of the same patch of cells over time (**Figure 26**), and could in principle also provide information about the speed of local tissue elongation. However, the frequent rotations and contractions of the animal combined with the lack of control over the amount and location of eGFP positive patches made it difficult to perform any standardized quantifications. In order to overcome these issues, a second approach was investigated, in which embryos were injected with shRNA encoding the photo-convertible protein Kaede (Ando et al., 2002). This enabled targeted photo-conversion of a specific region of the animal (**Figure 26C, D**). After larva-polyp transition, the photo-converted patches had increased length/width aspect ratios, indicative of cellular rearrangements along the oral-aboral axis. Photo-converted patches are easier to trace back than random eGFP labeled patches, but (long-term) imaging at cellular resolution in living samples remains challenging, so that at this stage no quantifications could be performed at the cellular level (for quantifications of the stripe aspect ratio, please see **Figure 40** in Chapter 7).

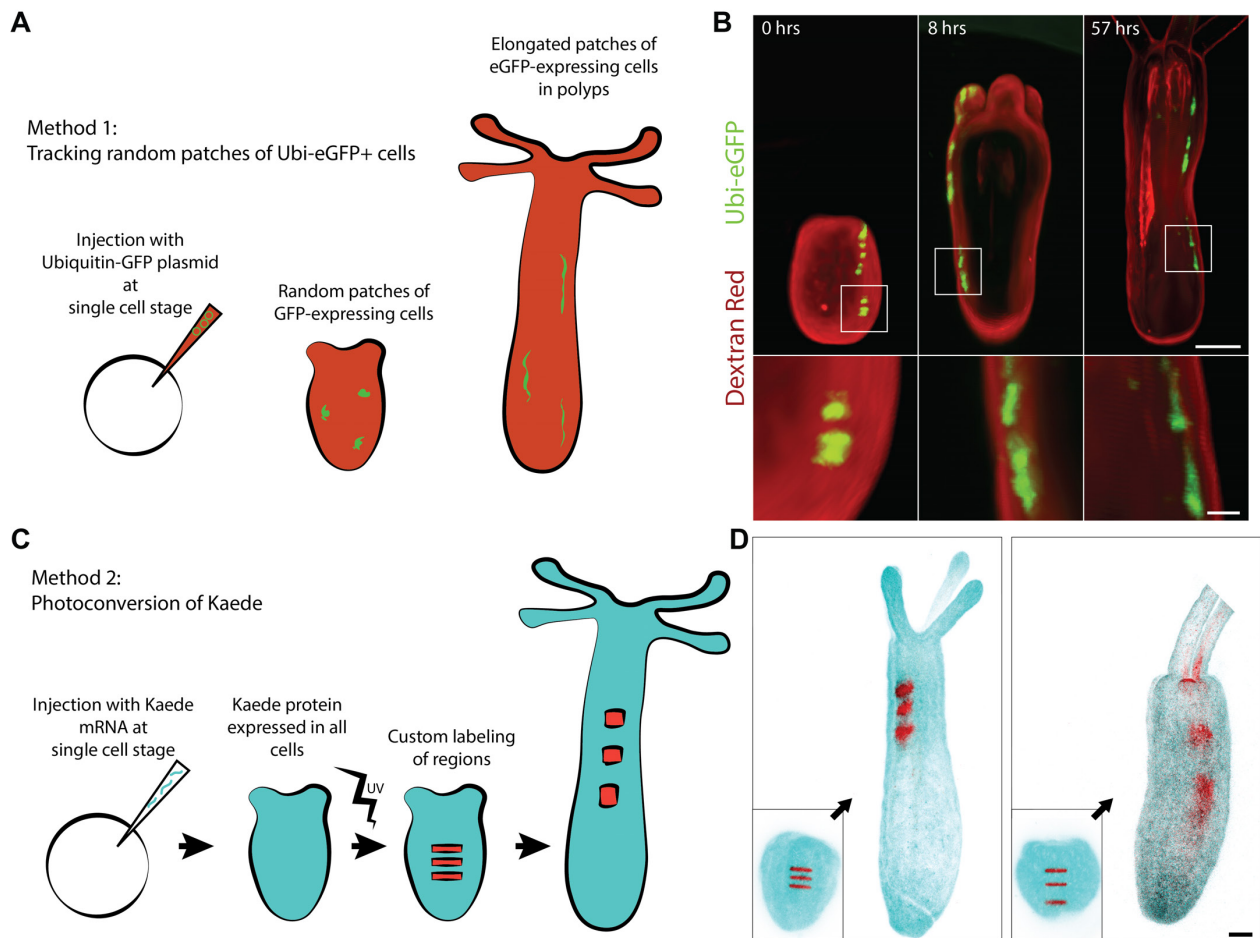


**Figure 26. Cellular rearrangements contribute to axial elongation.** **A.** Strategy to study cellular rearrangements through mosaic expression of eGFP. **B.** Confocal maximum intensity projections of the same animal at different time points, showing shape changes of the eGFP labeled cell patches. **C.** Strategy to study cellular rearrangements by photo-converting specific regions of the body at the larval stage. **D.** Two examples of photo-converted animals, before and after axial elongation. Scale bars: 100  $\mu\text{m}$  (B, full-view), 20  $\mu\text{m}$  (B, zoom), 50  $\mu\text{m}$  (D).

## 6.5. Summary and conclusions

During larva-polyp transition, *Nematostella* undergoes major changes in size and shape. In order to investigate how animals increase their size, we used a new optical coherence microscopy setup, developed in the Prevedel lab by Ling Wang. This enabled us to measure tissue and cavity volume of the entire animal before and after elongation. From these data, we found that the increase in size can largely be attributed to inflation of the body cavity. We also observed an increase in tissue volume, which could potentially be explained through uptake of water into certain tissues, although we cannot exclude tissue overestimation in the quantification method at this stage.

In order to investigate the changes occurring at the tissue level during animal shape change, I studied the individual contributions from cell proliferation, cellular shape changes, and cellular rearrangements. Cell proliferation appears to play a minor role during larva-polyp transition, as blocking cell proliferation with HU had only a small, non-significant effect on animal elongation. In

contrast, cell shape changes were found to increase animal surface area, as ectodermal and endodermal cells undergo a shape change from tall, columnar cells, to flat and wide cells. Cellular volume appears to remain relatively constant in ectodermal cells, but it was not possible to measure this accurately in endodermal cells of the body. In addition to cell shape changes, cellular rearrangements take place in order to facilitate a polarized organismal shape change through redistribution of cellular mass. Measuring tissue rearrangements at cellular resolution in an actively behaving animal remains challenging. However, photo-conversion in animals expressing Kaede could provide a useful future strategy to investigate cellular rearrangements at the tissue level.



## 7. The role of muscular hydraulics during larva-polyp morphogenesis

### 7.1. Muscular hydraulics facilitate short-term shape and size regulation

As described previously, the body column of *Nematostella*, as well as many other cnidarian species of sea anemone, is hollow and filled with fluid. A muscular body wall surrounding a fluid-filled cavity is characteristic of a hydrostatic skeleton, a system in which muscular forces are transmitted via internal fluid (Kier, 2012) (**Figure 27A**). When the animal's mouth is closed, a contraction on one side of the body column automatically leads to an expansion elsewhere, in order to accommodate the same amount of liquid inside. In *Nematostella*, peristaltic contraction waves can push the liquid through the body column, and thereby locally stretch the animal and help to circulate the fluid inside (**Figure 27A**). Direct pressure measurements obtained by inserting a probe inside a contracting animal, performed by Prachiti Moghe (Hiiragi group, EMBL Heidelberg), showed that muscle contractions can increase luminal pressure, thereby allowing the fluid pressure to act as a long range force on the tissue, locally deforming the tissue on short time scales (**Figure 27B**). Moreover, the muscular action of the hydrostatic skeleton is important for animal movement and shape maintenance. This is supported by the finding that when extended animals are treated with the muscle relaxant linalool (Goel et al., 2019), they appear unable to maintain their elongated shape and rapidly revert back to a shorter and wider shape (**Figure 27C**). This suggests that tonic muscle contractions are important to maintain polyp shape, even in the absence of visible contractions when the animal is seemingly at rest. Furthermore, animals treated with linalool often deflate upon prolonged exposure, after which they remain in a state showing no or little body contractions (**Figure 27D**). However, animals can recover from this state by re-inflating their body column, which coincides with active body contractions (**Figure 27D**). Thus, the combination of regulating luminal pressure and (local) muscle contractions allows the animal to regulate both its size and shape during short (minute) time scales and homeostatic conditions.

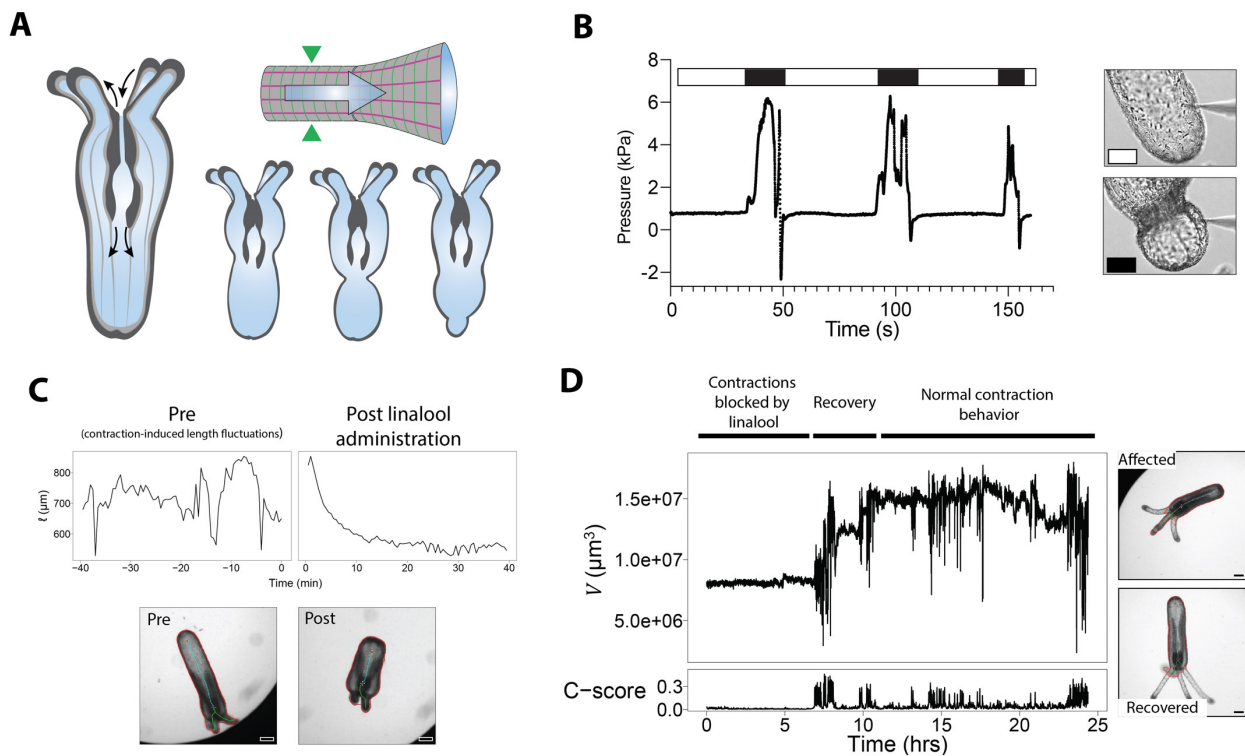


**Figure 27. Muscular hydraulics regulate organismal size and shape at short time scales.** **A.** Schematic of the hydrostatic skeleton in action. When the animal's mouth is open (left) water can go in or out, increasing or decreasing animal size. When the mouth is closed (right), muscle contraction can induce fluid flow inside the animal to modulate (local) animal shape. In *Nematostella*, muscle contractions often appear as peristaltic contractions that travel through the body column. **B.** Cavity pressure increases locally as a result of contractile activity. Experiment and quantification by Prachiti Moghe (Hiiragi lab, EMBL Heidelberg). **C.** Effect of linalool treatment, which induces a dramatic decrease in length and results in a shorter and wider animal shape. **D.** Quantification of animal body column volume before and after recovery from linalool treatment, showing re-inflation coinciding with organismal contractions. Figure panel B and C also appear in (Stokkermans et al., 2021). Scale bars: 100 μm.

## 7.2. Cavity inflation is required for axial elongation

As described in Chapter 6, cavity inflation during larva-polyp transition is a major contributor to organismal size. To investigate whether it is also essential for larva-polyp morphogenesis, Aissam performed a mechanical perturbation experiment in which larvae were pierced either on normal, closed capillaries, or on 'open' capillaries that have holes (**Figure 28A**). Since such open capillaries allow water exchange between the cavity and the outer environment, they prevent any buildup of luminal pressure. While control animals inflated their cavity successfully, animals pierced on open capillaries failed to inflate their cavity (**Figure 28A**). Interestingly, these animals also did not elongate their body column, suggesting that cavity inflation and hydrostatic associated pressure are required for axial elongation (**Figure 28A**). Forced mechanical inflation of larvae can dramatically increase their size at timescales at the order of minutes (**Figure 28B**). However, the shape change is largely isotropic, with minimal body column aspect ratio increase, suggesting that although cavity pressure is important for elongation, a directional force that acts on longer timescales is needed to



permanently elongate the shape of the animal and reach the high aspect ratios typically seen in the body columns of polyps.

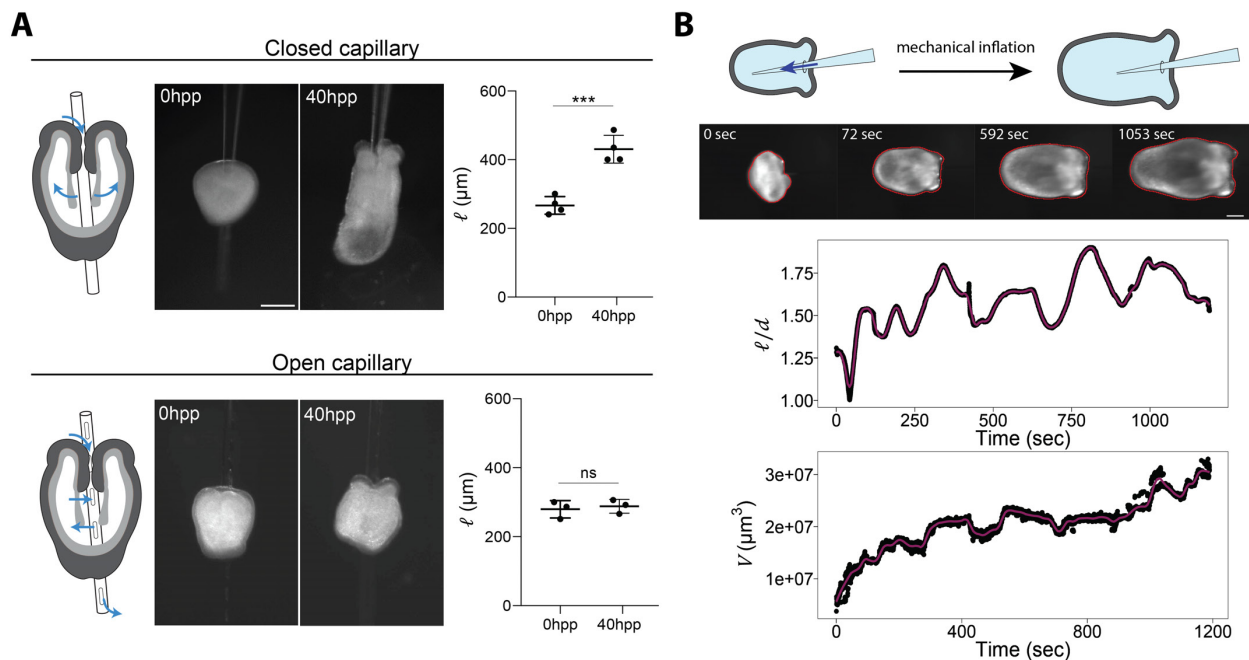


**Figure 28. Cavity inflation is essential for larva-polyp transition.** **A.** Mechanical perturbation of cavity hydrostatic pressure by insertion of a closed capillary (control), or an open capillary that has holes, preventing build-up of pressure (two-tailed unpaired t-test, \*\*\* $p < 0.001$ ; n.s.  $p > 0.05$ ). hpp: hours post perforation. Experiment and quantification by Aissam Ikmi (EMBL Heidelberg). Stefan Terjung (Advanced Light Microscope Facility, EMBL Heidelberg) helped with producing open capillaries. **B.** Forced inflation of a wild-type larva, showing that although volume can be strongly increased, animal aspect ratio increase is limited at short time scales. Figure panel A also appears in (Stokkermans et al., 2021) and was made by Aissam Ikmi. Scale bars: 100  $\mu\text{m}$ .

### 7.3. Muscle function is essential for larva-polyp morphogenesis

Since muscle contractions can induce short-lived increases in luminal pressure (**Figure 27B**), the next step was to test the role of muscle function during the much longer process of larva-polyp transition. To do this, I tested the effect of different muscle inhibiting drugs:  $\text{MgCl}_2$  (Batham and Pantin, 1950b), linalool (Goel et al., 2019), menthol (Abrams et al., 2015; Batham and Pantin, 1950b), and rocuronium bromide (Khuenl-Brady and Sparr, 1996). Treatment with these drugs indeed decreased contractile activity in developing animals (**Figure 29A, B**). Long-term exposure to 0.5%  $\text{MgCl}_2$  or 0.5mM rocuronium bromide during development resulted in animals that are much smaller and less elongated than controls (**Figure 29C, D**), suggesting that active muscle function is required for larva-polyp morphogenesis.

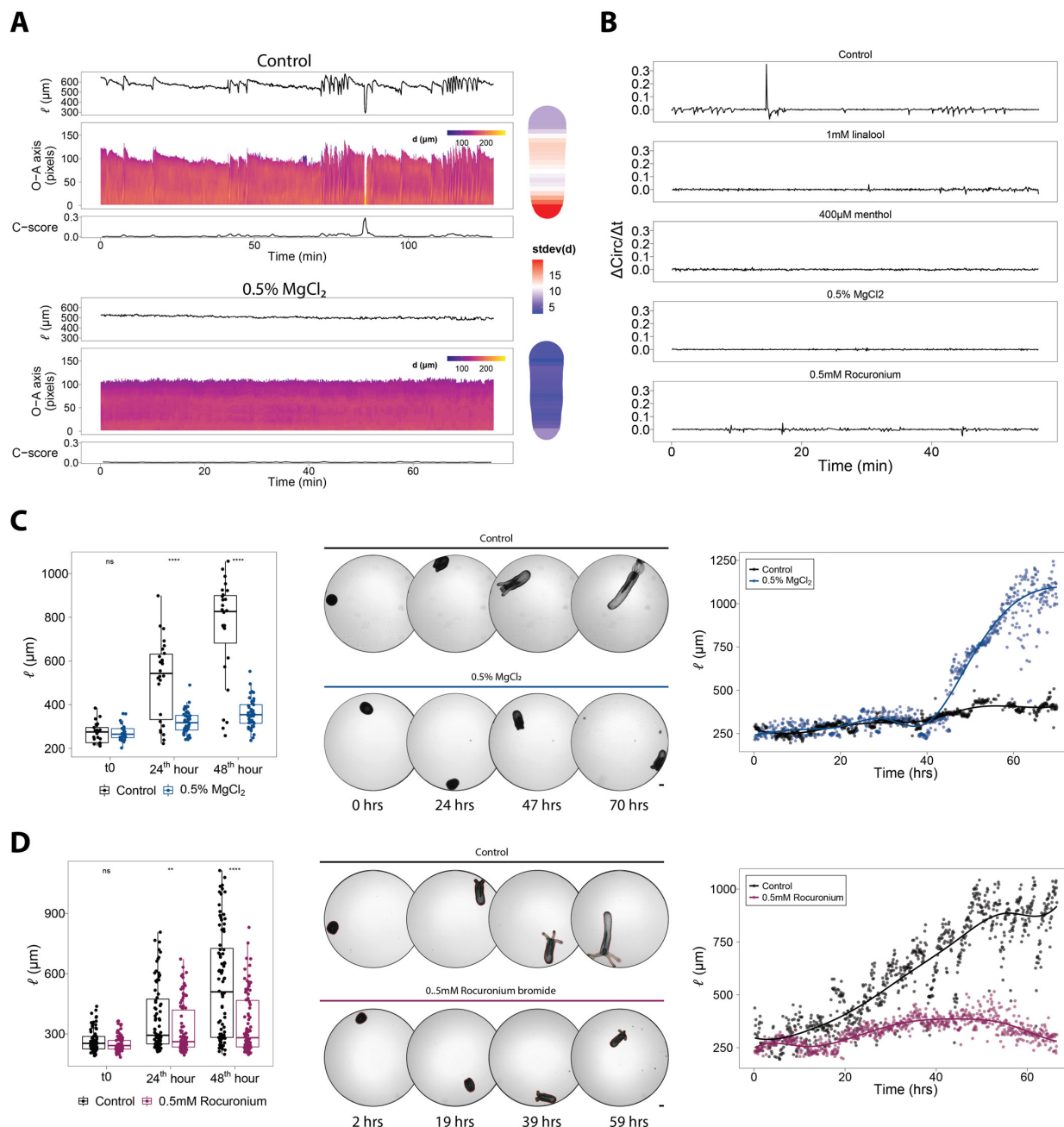


**Figure 29. Effect of muscle inhibiting drugs on animal contractility and development.** **A.** Quantification of body column length, diameter along the oral-aboral (O-A) axis, and contractility score for a control animal and an animal in 0.5%  $\text{MgCl}_2$ , showing that 0.5%  $\text{MgCl}_2$  reduces contractile activity. Shapes on the right show average animal shape, color-coded for local standard deviation of body column diameter (in  $\mu\text{m}$ ), as a proxy for deformation at different body column regions (blue = low deformation, red = high deformation). **B.** Quantification of short-term change in animal circularity in drug-treated animals and a control animal. Data for control and 0.5%  $\text{MgCl}_2$  also appears in (A) and is reprinted for comparison. **C-D.** Quantification of animal length in control animals and those treated with 0.5%  $\text{MgCl}_2$  (C) or 0.5mM rocuronium bromide (D) (left panels) (two-sided unpaired Wilcoxon rank sum test; \*\*\*\* $p < 0.0001$ , \*\* $p < 0.01$ , n.s.  $p > 0.05$ ).  $n = 27$  (C, control),  $n = 46$  (C, 0.5%  $\text{MgCl}_2$ ),  $n = 93$  (D, control),  $n = 99$  (D, 0.5mM rocuronium bromide). Images and body length quantification of individual control animals and drug-treated animals are shown in the middle and right panels. Scale bar: 100  $\mu\text{m}$ .

Menthol and linalool could not be tested under the same conditions using the Acquirer microscope, because they are volatile and do not remain stable in solution in small volumes in plate

wells. Therefore, to study the effect of muscle inhibition on tissue morphogenesis, late larvae at 5 days post fertilization were kept in large (6 cm) glass dishes with the different drugs and fixed at 8 days post fertilization, the time at which control animals had typically developed into primary polyps. Although most animals developed tentacle buds, they did not inflate their cavity or elongate their body column to the same extent as control animals (**Figure 30A-C**). Furthermore, the ectoderm of drug-treated animals did not undergo the same extensive thinning that happens under control conditions (**Figure 25A-C** and **Figure 30A, D**), and animals did not develop the characteristic small hole at the aboral pole, called the aboral pore, which is normally present at the polyp stage (**Figure 30E**). In line with decreased ectoderm thinning, ectoderm cell apical surface area did not increase to the same extent as in controls, and most cells did not acquire the characteristic actin-rich rings in the middle of the cells (Momose et al., 2012), as a sign of lack of tissue differentiation and maturation (**Figure 30F, G**). Of the tested conditions, treatment with 0.5 mM rocuronium bromide had the smallest effect, with some tissue thinning and development of actin-rings, but animals did not reach normal size and shape (**Figure 30A-G**). Animals treated with linalool and menthol often maintained the apical tuft, a characteristic feature of the larval stage, suggesting that animals grown under these conditions were more severely affected and arrested at an earlier stage (**Appendix Figure 4**). Together, these and earlier described results suggest that muscle function acts both at the short time scale, modulating and maintaining organismal size and shape, and at a much longer, developmental time scale, involved in organismal morphogenesis during larva-polyp transition.

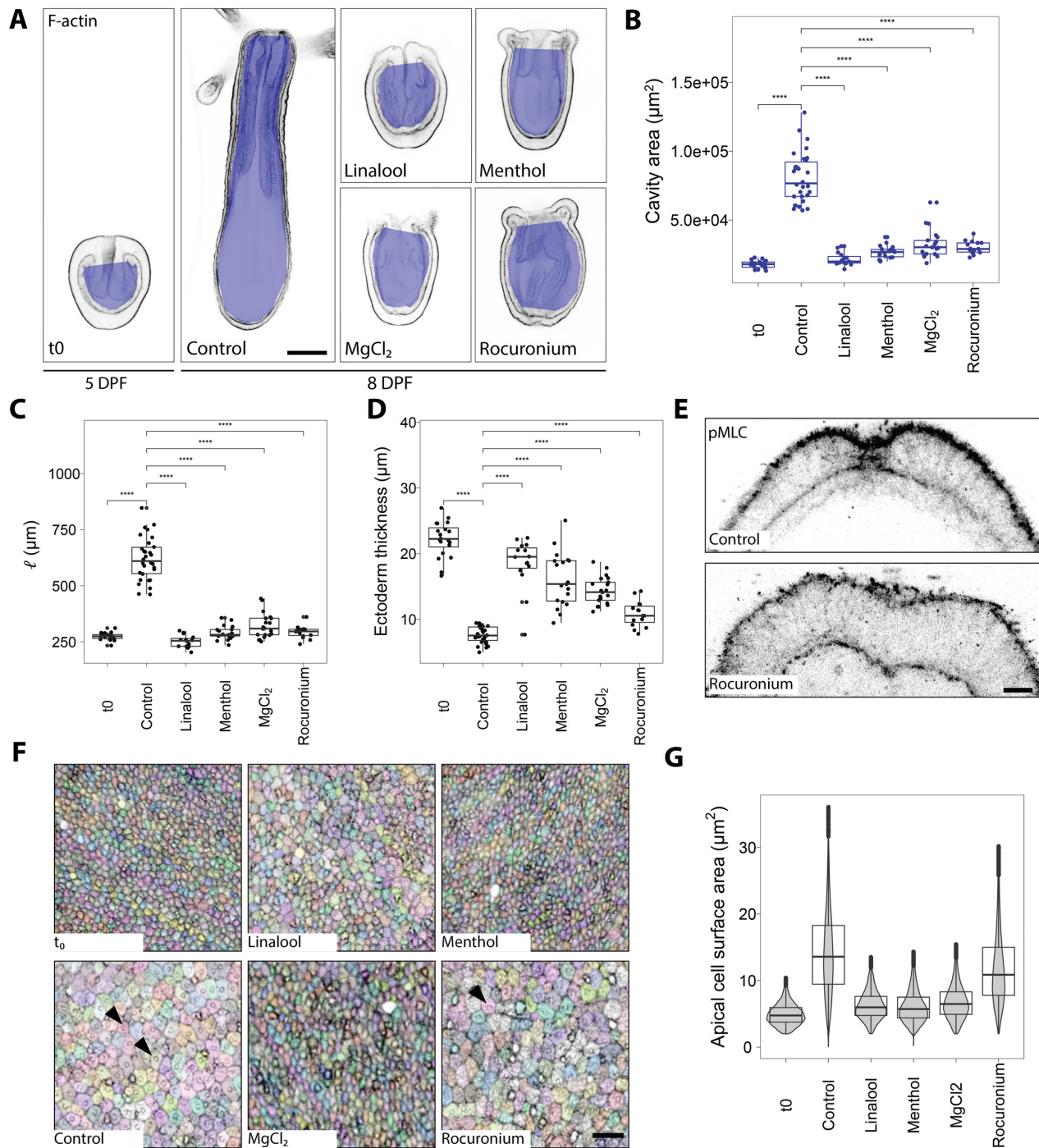


**Figure 30. Effect of muscle inhibiting drugs on tissue morphogenesis and maturation.** **A.** Midsection views of fixed animals stained for F-actin with phalloidin and fixed at 5 DPF (t0) or 8 DPF (drug-treated and control). The area of the cavity and internal tissue is shown in blue, and quantified in **B**. **B-D.** Quantification of cavity midsection area (**B**), animal length (**C**) and ectoderm thickness (**D**) in controls and drug-treated animals after fixation (two-sided unpaired Wilcoxon rank sum test; \*\*\*\* $p < 0.0001$ ). t0:  $n = 20$ , control:  $n = 30$ , 1 mM linalool:  $n = 15$ , 400  $\mu\text{M}$  menthol:  $n = 19$ , 0.5%  $\text{MgCl}_2$ :  $n = 21$ , 0.5mM rocuronium bromide:  $n = 15$ . **E.** Confocal mid-section image of the aboral pole of a control and rocuronium bromide-treated animal, stained with an antibody targeting pMLC. The control animal has developed an almost complete opening at the aboral pole, which is enriched for pMLC. The animal treated with rocuronium has not formed any aboral pore structure. **F-G.** Images of segmented ectodermal cells (**F**) and quantification of ectoderm cell apical surface area (**G**) for the drug-treated animals and controls quantified in **B-D**. Arrowheads indicate examples of actin-rich rings in differentiated tissue. Figure panels A-C also appear in (Stokkermans et al., 2021) and were made by me. Scale bars: 100  $\mu\text{m}$  (**A**), 10  $\mu\text{m}$  (**E**, **F**).



#### 7.4. Development of the muscle system in the body column

Since muscle activity appears to be important for larva-polyp transition, the development of the muscle system before and during larva-polyp transition was analyzed in more detail. As described in Chapter 3, the muscle system of *Nematostella* consists of longitudinal and circular muscles, which are distinct in morphology, localization, and gene expression (Jahnel et al., 2014; Sebé-Pedrós et al., 2018). Muscles can be visualized using an antibody targeting phosphorylated myosin light chain (pMLC), which stains mostly the longitudinal tentacle and body column muscles, and with phalloidin to stain for F-actin, which strongly stains all muscles (**Figure 31A, B**). Muscle development begins during early larval stage. Around two days post fertilization, the first longitudinal muscle fibers can be observed as thin actin-rich bundles (**Figure 31A**). During the subsequent days, more fibers develop and bundle together into thicker longitudinal muscles. Circular muscles become visible around three days post fertilization, at the mid-planula larval stage (**Figure 31A**). By the budded larval stage, a well-organized muscle system is present, prior to major body elongation (**Figure 31A**).

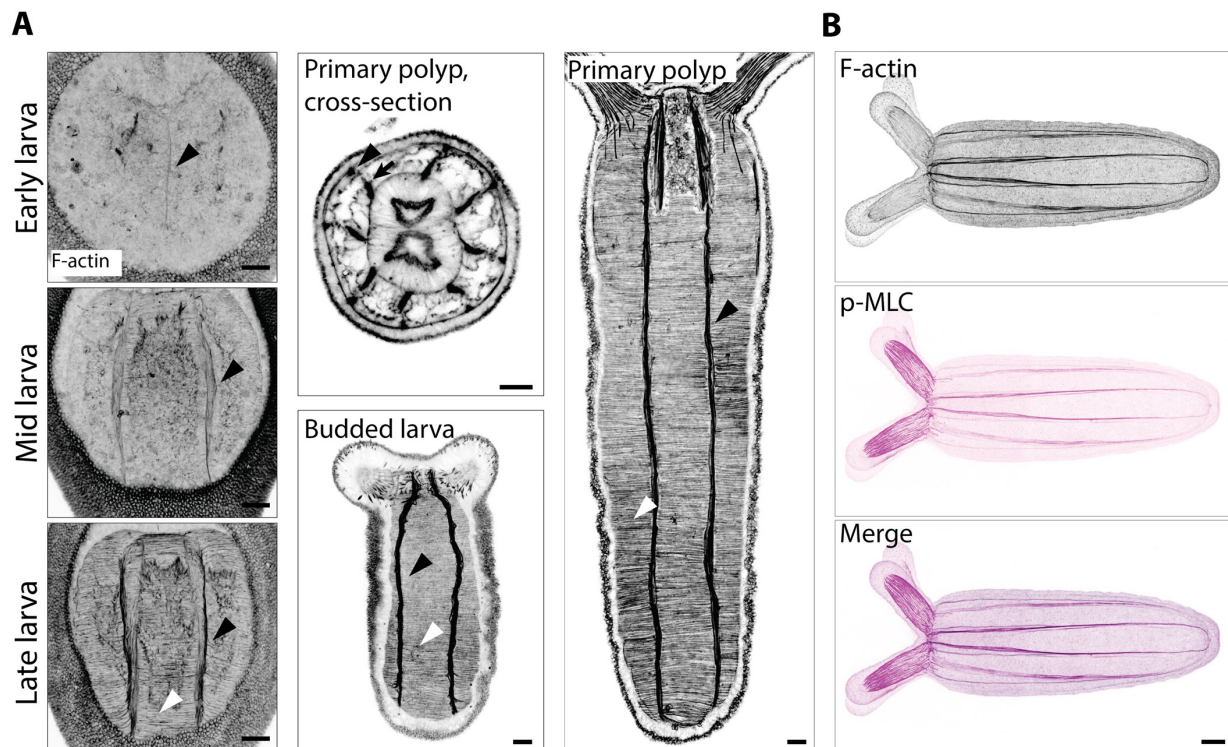


**Figure 31. Development of the muscle system in *Nematostella*.** **A.** Development of body column muscles. Longitudinal muscles (black arrowheads) become visible in early larvae at 2 DPF. Circular muscles (white arrowheads) are thinner and become visible at mid to late planula larval stage. A cross-sectional image (middle subpanel, top) shows two types of longitudinal muscles: parietal muscles, located close to the boundary of the body column (arrowhead), and retractor muscles, located deeper inside the mesenteries (arrow). A well-organized muscle system is present at budded larval stage (middle subpanel, bottom), prior to elongation, and in primary polyps (right subpanel). **B.** Staining for F-actin (phalloidin, in black) and phosphorylated myosin light chain (magenta) in a primary polyp. Budded larva and primary polyp shown in (A) also appear in (Stokkermans et al., 2021) and were produced by me. Scale bars: 20  $\mu\text{m}$  (A), 50  $\mu\text{m}$  (B).

To further investigate muscle fiber arrangement during larva-polyp transition, I analyzed high resolution images of muscle fibers in animals at different developmental stages. Whereas fibers are still thin and largely disorganized at the early and mid-larval stage, clear condensation into thicker, well-organized fibers can be observed at later stages (**Figure 32A-C**). Interestingly, muscle fibers at budded larval stage appear to be thinner but more numerous per unit length along the oral-aboral axis compared to fibers in polyps (**Figure 32B, D**). In budded larvae, fibers appear to overlap slightly, whereas fibers at the polyp stage seem to form a thinner sheet (**Figure 32B**), suggesting that the muscle fibers intercalate vertically and may be pulled apart longitudinally as the animal elongates. Muscle fibers increase in thickness from budded larva to polyp stage, and eventually cover over 60% of the total area in the muscle plane (**Figure 32B, E-F**). However, it was not possible to identify which exact fibers belong to which cell, complicating the precise measurements of fiber thickness, and it is therefore likely that the fiber thickness measurements shown here are an under-estimation of true fiber thickness. In summary, a well-organized muscle system consisting of longitudinal and circular muscles is present at late larval stage, prior to elongation, but further maturation of the muscle system takes place during lava-polyp transition, resulting in a thinner sheet with thicker longitudinal and circular muscle fibers.

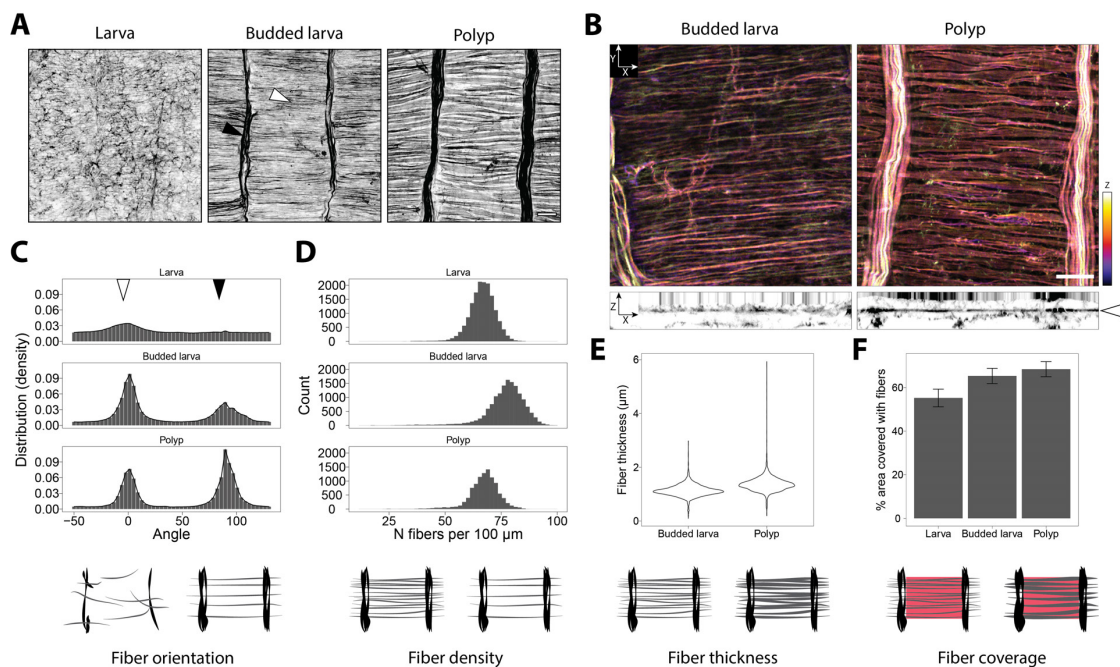


**Figure 32. Development and organization of muscle fibers during larva-polyp transition.** **A.** F-actin staining showing the muscle layer at larval, budded larval, and polyp stage. **B.** Top: XY view of F-actin staining showing muscle fibers at budded larval and polyp stage. The image is corrected for curvature of the body column and colors represent the remaining relative z-depth. Bottom: XZ view showing the curvature-corrected tissue layer. White arrowhead indicates the location of the circular muscle sheet. At polyp stage, this has become thinner and more uniform compared to budded larval stage. **C.** Density plot showing measurements of muscle fiber orientation at larval, budded larval, and polyp stage. **D.** Histogram showing muscle fiber count at larval, budded larval, and polyp stage. **E.** Quantification of fiber thickness at budded larval and polyp stage. **F.** Quantification of the area covered by muscle fibers at larval, budded larval, and polyp stage. Quantifications based on data from  $n = 11$  larvae,  $n = 14$  budded larvae,  $n = 11$  polyps. Scale bars: 10  $\mu\text{m}$ .

## 7.5. Targeted perturbation of muscular hydraulics through RNA interference

While treatment with muscle relaxants had a clear effect on larva-polyp morphogenesis, its disadvantage is that the drugs act globally on the animal and may cause additional toxicity effects. In order to specifically target different components of the hydrostatic skeleton, a list of target genes involved in longitudinal or circular muscle development, neurogenesis, or patterning, was constructed based on published in situ hybridization and single cell transcriptomics data (Seb Pedr s et al., 2018; Steinmetz et al., 2017). For these genes, we designed primers to synthesize short-hairpin RNA (shRNA), using a customized R script to facilitate shRNA design with specific requirements (see Materials and Methods for details). Construction of the gene list, design of shRNA and injection of shRNA were performed together with Aissam. Omar Matar (intern in Ikmi lab, EMBL Heidelberg) helped with shRNA synthesis.

Gene knockdown can be achieved in *Nematostella* by shRNA injection at the single cell stage (He et al., 2018). Appendix Table 5 provides a summary of the shRNA tested, the gene target, and whether or not a phenotype was found. Assessment of the phenotype was initially based on the morphology of the animal at the time point at which control animals had reached the primary polyp stage. When animals injected with shRNA showed an abnormal size or shape, or were delayed in development, the phenotype was studied into more detail by imaging injected animals with the Acquirer screening microscope to screen for altered elongation dynamics or animal behavior. Although multiple interesting phenotypes were found (see Appendix section 3 for more details), I will here focus only on the phenotype of *NvTbx20* KD and *NvBMP2/4* KD.

## 7.6. Knockdown of *Tbx20* and *BMP2/4* decouples size and shape development

*Tbx20* is a T-box transcription factor that is expressed during cardiac muscle development in vertebrate and invertebrate animals (Chen et al., 2021; Qian et al., 2008; Stennard et al., 2003). In *Nematostella*, two paralogs of *Tbx20* exist: *NvTbx20.1* and *NvTbx20.2*. Interestingly, knockdown of *Tbx20* in *Nematostella* resulted in animals that have a relatively short but wide and bulky body column (**Figure 33A**). In contrast, the earlier reported phenotype of *BMP2/4* KD, which leads to loss of the directive axis in *Nematostella*, results in long and thin, ‘noodle’-shaped animals (Lecl re and Rentzsch, 2014; Saina et al., 2009). Measuring animal aspect ratio and estimated body column volume reveals that size and shape development are essentially decoupled in these two knockdown conditions. *Tbx20* KD animals can inflate to volumes that are similar to or even exceed those of wild type animals, but they have lower aspect ratios due to their comparably short and wide body column. In contrast, *BMP2/4* KD animals strongly increase in aspect ratio as they develop, but appear incapable of inflating their body columns (**Figure 33B**).

Interestingly, *Tbx20* KD and *BMP2/4* KD animals show distinct muscle organization. In *Tbx20* KD animals, both longitudinal and circular muscles appear disorganized (**Figure 33A, C**). Instead of tight bundles of longitudinal muscles bridged by neatly organized circular muscles, muscle fibers in *Tbx20* KD animals are organized in loose bundles that frequently mix (**Figure 33A, C**). Generally, the muscles in the aboral half of the animal are more affected than the oral half, and also the shape of the body column is often widest at the aboral end (**Figure 33A**). In contrast, *BMP2/4* KD animals do not form any mesenteries and do not develop any longitudinal parietal or retractor muscles, resulting in a body column with circular muscles only (**Figure 33A, C**).

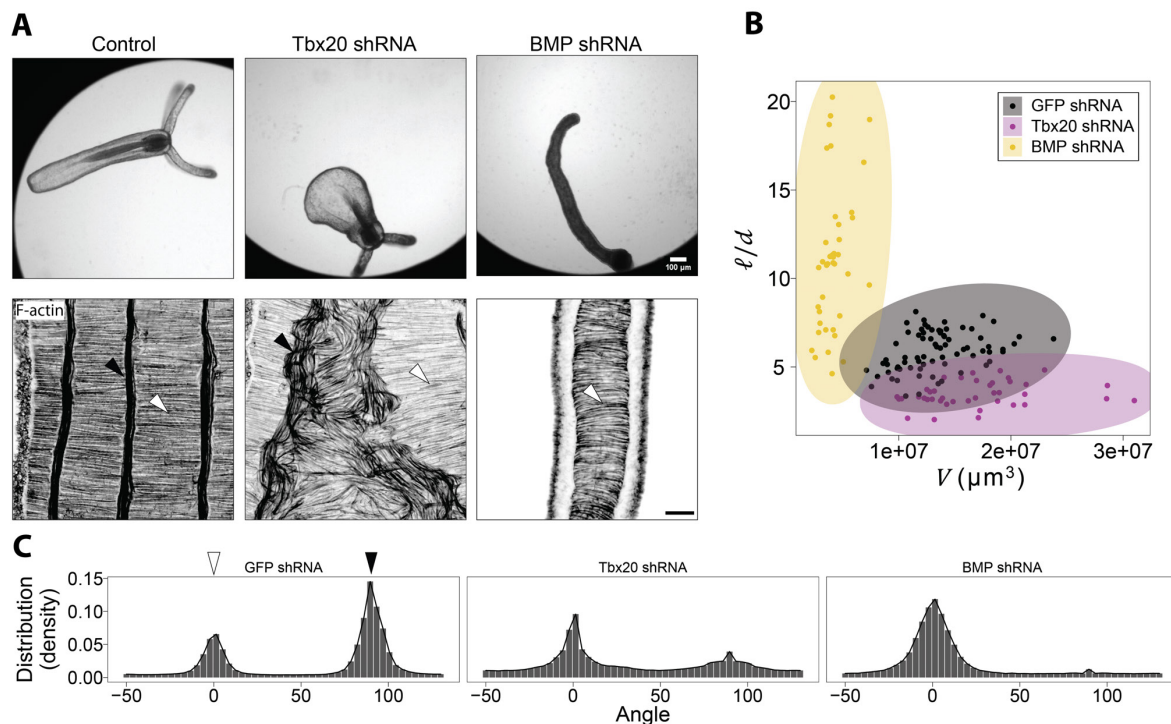


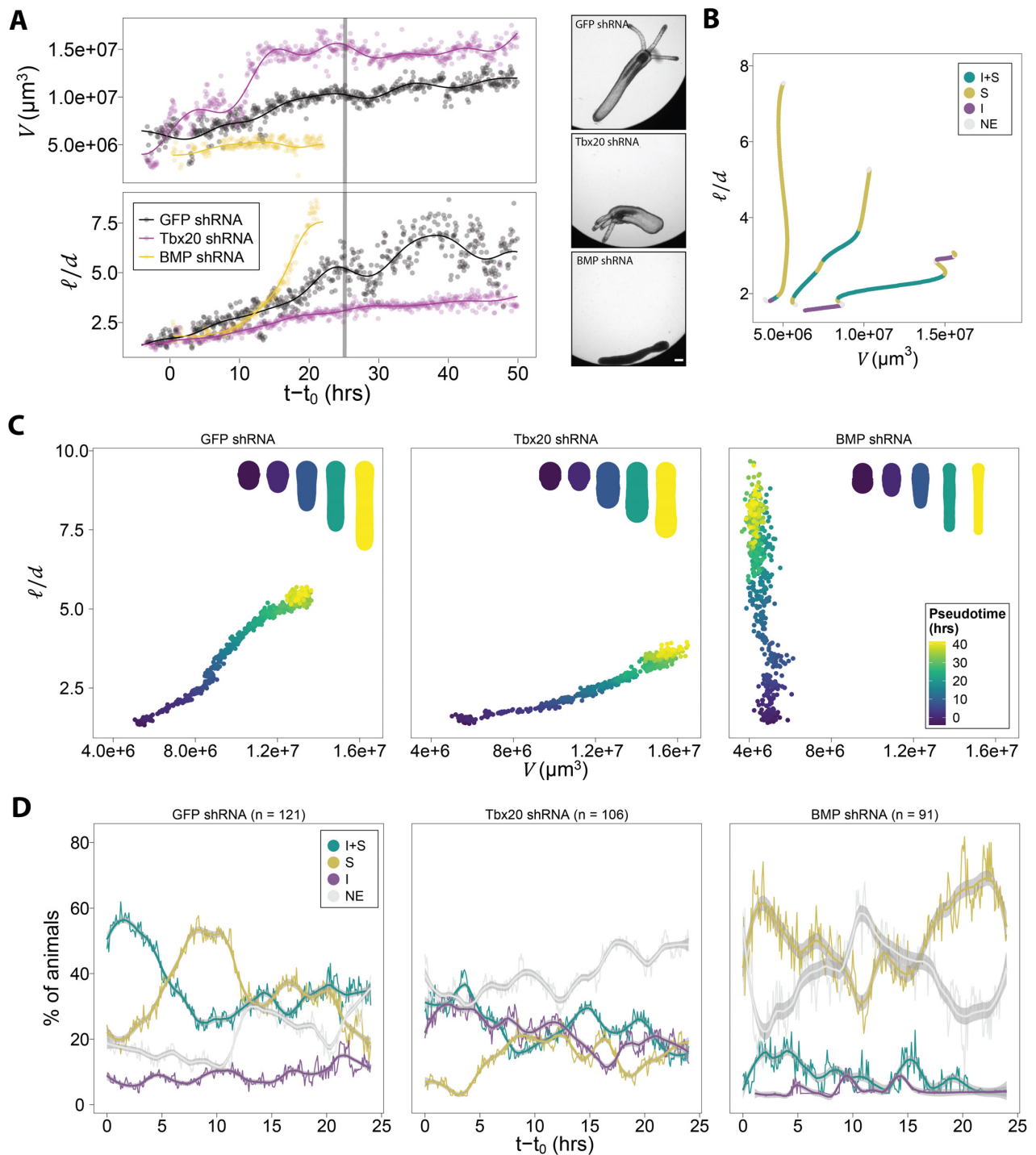
**Figure 33. Knockdown of *Tbx20* and *BMP2/4* decouples size and shape development.** **A.** Brightfield and confocal images of control, *Tbx20* KD and *BMP2/4* KD animals. Confocal images show F-actin staining of the muscle layer, showing disorganized muscles in *Tbx20* KD and absence of longitudinal muscles in *BMP2/4* KD animals. Black and white arrowheads indicate longitudinal and circular muscle, respectively. **B.** Quantification of body column aspect ratio and volume for control ( $n = 74$ ), *Tbx20* KD ( $n = 40$ ) and *BMP2/4* KD ( $n = 37$ ) animals. **C.** Density plot showing measurements of muscle fiber orientation in control (GFP shRNA,  $n = 15$ ), and *Tbx20* ( $n = 9$ ) and *BMP2/4* ( $n = 10$ ) KD animals. Disorganized muscle organization is visible in the reduced bias in muscle fiber angle in *Tbx20* KD animals, and lack of longitudinal muscles in *BMP2/4* KD is visible by the absence of fibers with an angle of 90 degrees. Scale bars: 100  $\mu\text{m}$  (A, top), 20  $\mu\text{m}$  (A, bottom). Figure panel A also appears in (Stokkermans et al., 2021) and was produced by me.

The phenotype of *Tbx20* KD was independently validated by Aissam through generation of *Tbx20* CRISPR KO animals (**Appendix Figure 7**). Strikingly, we found *Tbx20* CRISPR KO animals that had an almost completely round morphology and showed muscle organization defects throughout the entire body column (**Appendix Figure 7C**). This was occasionally also observed in *Tbx20* KD animals, but in general the effect of *Tbx20* KD was more variable and often largely restricted towards the aboral side (**Appendix Figure 7C**).



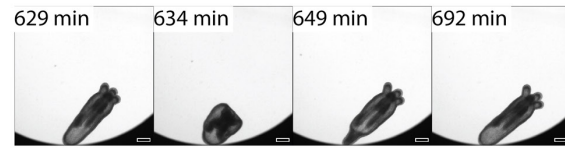
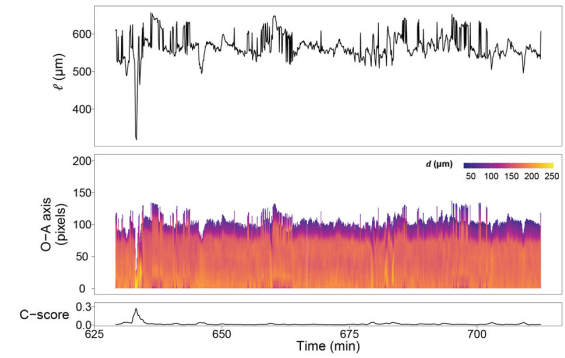
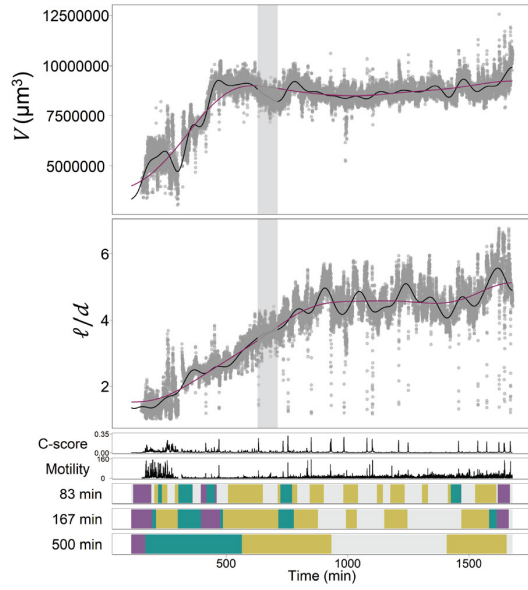
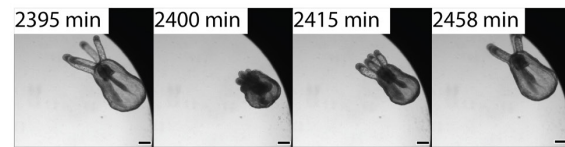
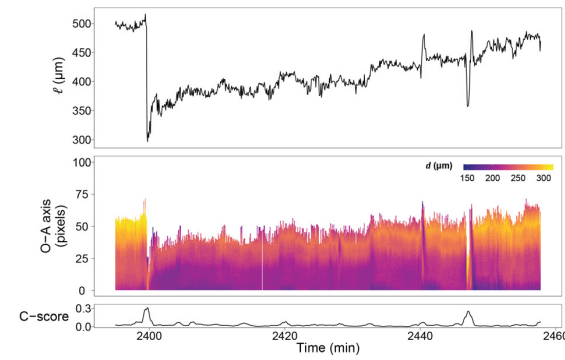
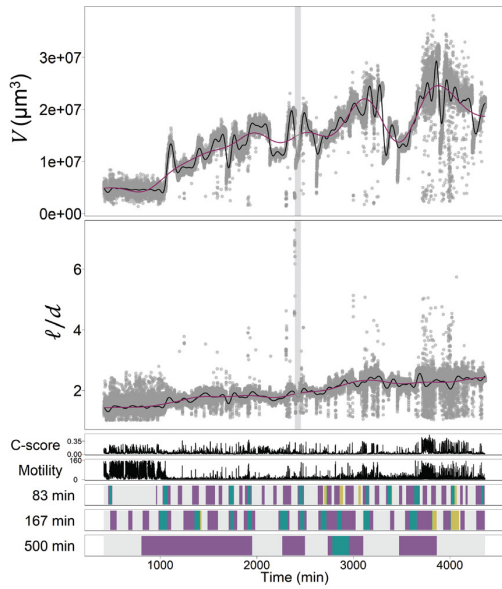
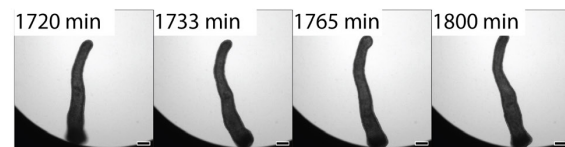
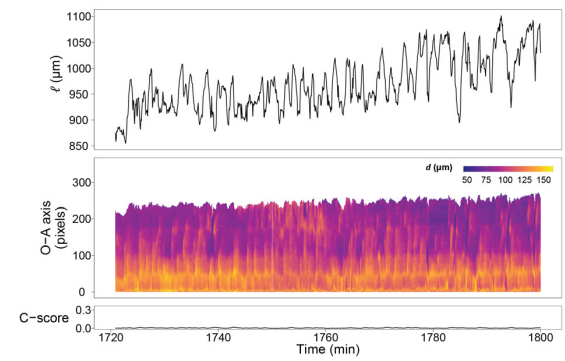
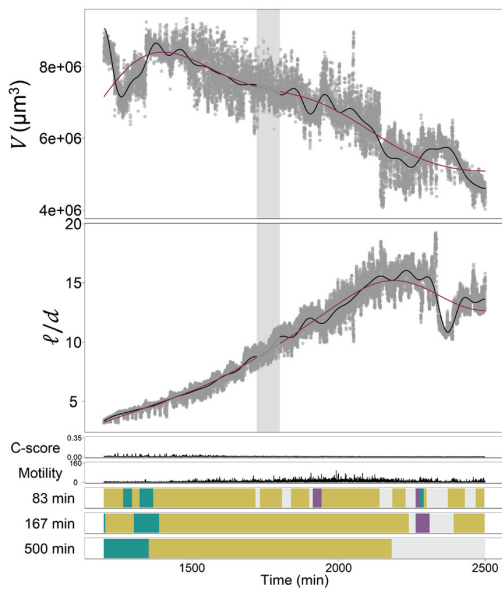
### **7.7. *Tbx20* and *BMP2/4* KD animals show different morphodynamics and contraction behavior**

To compare how control, *Tbx20* KD and *BMP2/4* KD animals change their size and shape over time, their development in morphospace and associated morphodynamics were studied at both the level of individual animals and at the population level. Control animals show net diagonal movement in morphospace, mostly through combinations of 'stretching' and 'combined stretching and inflating'. In contrast, *BMP2/4* KD animals move mostly vertically in morphospace, and show strong enrichment for 'stretching', whereas *Tbx20* KD animals are biased to move more horizontally in morphospace and show enrichment for 'inflation' and 'combined stretching and inflating' (**Figure 34**).



**Figure 34. Trajectories in morphospace and associated morphodynamics in control, *Tbx20* KD and *BMP2/4* KD animals.** **A.** Quantification of body column volume and aspect ratio for a control (GFP shRNA), *Tbx20* KD, and a *BMP2/4* KD animal. End-morphology is shown to the right. **B.** Trajectories in morphospace for the animals shown in (A), color-coded for morphodynamics. Trajectories are truncated at 25 hours since the start of the transition stage, as marked in (A). **C-D.** Averaged trajectories in morphospace, grouped by pseudotime (C), and associated morphodynamics in pseudotime (D) (n Control = 121, n *Tbx20* shRNA = 106, n *BMP2/4* shRNA = 91). Insets in C show average shape at 5 different pseudo-timepoints. Morphodynamics are indicated as follows 'I+S': 'inflating and stretching' (green), 'S': 'stretching' (yellow), 'I': 'inflating' (purple), 'NE': 'no elongation' (gray). Scale bar: 100  $\mu\text{m}$ .

Since muscles are disorganized in *Tbx20* KD animals, and longitudinal muscles are completely absent in *BMP2/4* KD animals, abnormal contractile activity may be expected in these animals. To investigate this, shRNA KD animals and controls were imaged at five-second resolution and their changes with respect to body column diameter and animal circularity were recorded. Despite their disorganized muscles, animals treated with *Tbx20* shRNA show relatively normal contraction behavior (**Figure 35**). However, deflation of the body column is observed at irregular intervals, suggesting that the animal may be less efficient in pushing water down the body column by using the circular muscles and instead releases water through the mouth (**Figure 35B**). Possibly, the widened shape of *Tbx20* KD animals is the result of inefficient squeezing of the circular musculature, as a direct effect of muscle disorganization. The body wall may expand in all directions, as the circular muscles fail to induce a strong polarized force that squeezes the animal and extends it in the oral-aboral axis. In contrast, *BMP2/4* KD animals lack restriction in length that the longitudinal muscles might normally provide, such that contraction of the circular muscles may drive body elongation to an extreme. Indeed, we observe steady elongation with frequent contractions of the circular muscles in *BMP2/4* KD animals, which can occur at multiple locations along the body column at the same time (**Figure 35C**). As expected, full body contractions are completely absent in these animals (**Figure 35C**). To confirm that elongation in *BMP2/4* animals requires active muscle function, *BMP2/4* KD animals were treated with linalool or menthol at the larval stage. This resulted in animals of reduced length compared to controls, suggesting that active muscle contractions are indeed required for elongation (**Figure 36**).

**A****B****C**

**Figure 35. Morphogenesis and animal contractile behavior in control, *Tbx20* KD, and *BMP2/4* KD animals.** A-C. Quantifications of body column volume and aspect ratio, as well as contractility score, motility, and morphodynamics at different time scales for a control animal (A), *Tbx20* KD animal (B), and *BMP2/4* KD animal (C). Note the difference in total time shown. The panel below shows the zoomed-in region of the area marked in gray in the main plot, showing body column length, diameter along the oral-aboral axis, and contractility-score. Images of examples of contractile behavior are shown below. The control animal shows typical sporadic contractions, such as a full-body contraction. The *Tbx20* KD animal shows normal contractions, but also sudden contraction-triggered deflation events, combined with slow re-inflation of the body column. The *BMP2/4* KD animal shows steady elongation with small but frequent contractions at multiple locations of the body column (visible in the kymograph intensity changes). Scale bars: 100  $\mu\text{m}$ .

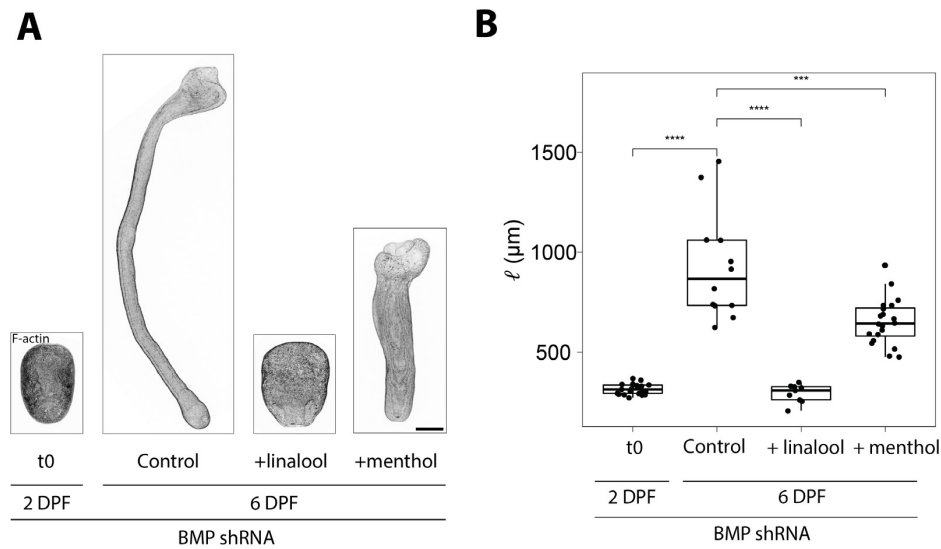


**Figure 36. Treatment with muscle inhibiting drugs prevents elongation in *BMP2/4* KD animals.** A. Maximum intensity projections of confocal images of animals stained for F-actin at t0 (2 DPF) and after 4 additional days of treatment with muscle inhibiting drugs (DMSO control, 1 mM linalool, 400  $\mu\text{M}$  menthol). B. Quantification of body column length for these conditions (two-sided unpaired Wilcoxon rank sum tests; \*\*\* $p < 0.001$ , \*\*\*\* $p < 0.0001$ ). Figure panels also appear in (Stokkermans et al., 2021) and were produced by me.

Remarkably, settlement behavior does not appear to be strongly affected in neither *Tbx20* KD nor *BMP2/4* KD animals, as a population of sessile and motile animals is present for all conditions (**Appendix Figure 8A**). Settlement behavior was more variable for *BMP2/4* KD animals than for controls, but this may in part be explained by the severe phenotype of *BMP2/4* KD animals, which manifests in a high variation of animal morphologies and behaviors in general. Interestingly, *BMP2/4* KD animals still show a similar correlation between elongation rate and settlement behavior as controls: *BMP2/4* KD animals that show settlement with attachment behavior generally elongate faster (**Appendix Figure 8B**).

## 7.8. Tissue remodeling mirrors direction of organismal expansion

To understand how the different organismal morphologies of control, *Tbx20* KD, *BMP2/4* KD, and depressurized animals on open capillaries (**Figure 37A**) are reflected at the tissue scale, I analyzed high resolution images of animals from these different conditions that were fixed and stained for F-actin or Cdh3. *Tbx20* KD animals showed similar ectoderm thinning as controls, while



*BMP2/4* KD animals showed reduced thinning, and animals pierced on open capillaries showed almost no thinning at all (**Figure 37B, C**). In line with this, ectoderm apical surface area strongly increased in controls and *Tbx20* KD animals, but not in animals on open capillaries (**Figure 37D, E**). For *BMP2/4* KD animals, the results were highly variable and strongly depended on animal length; the longer the animal was, the larger the apical surface area (**Figure 37D, E**). On average, however, the cellular shape changes were smaller in *BMP2/4* KD compared to controls and *Tbx20* KD, consistent with the reduced animal surface area in the comparably small *BMP2/4* KD animals.

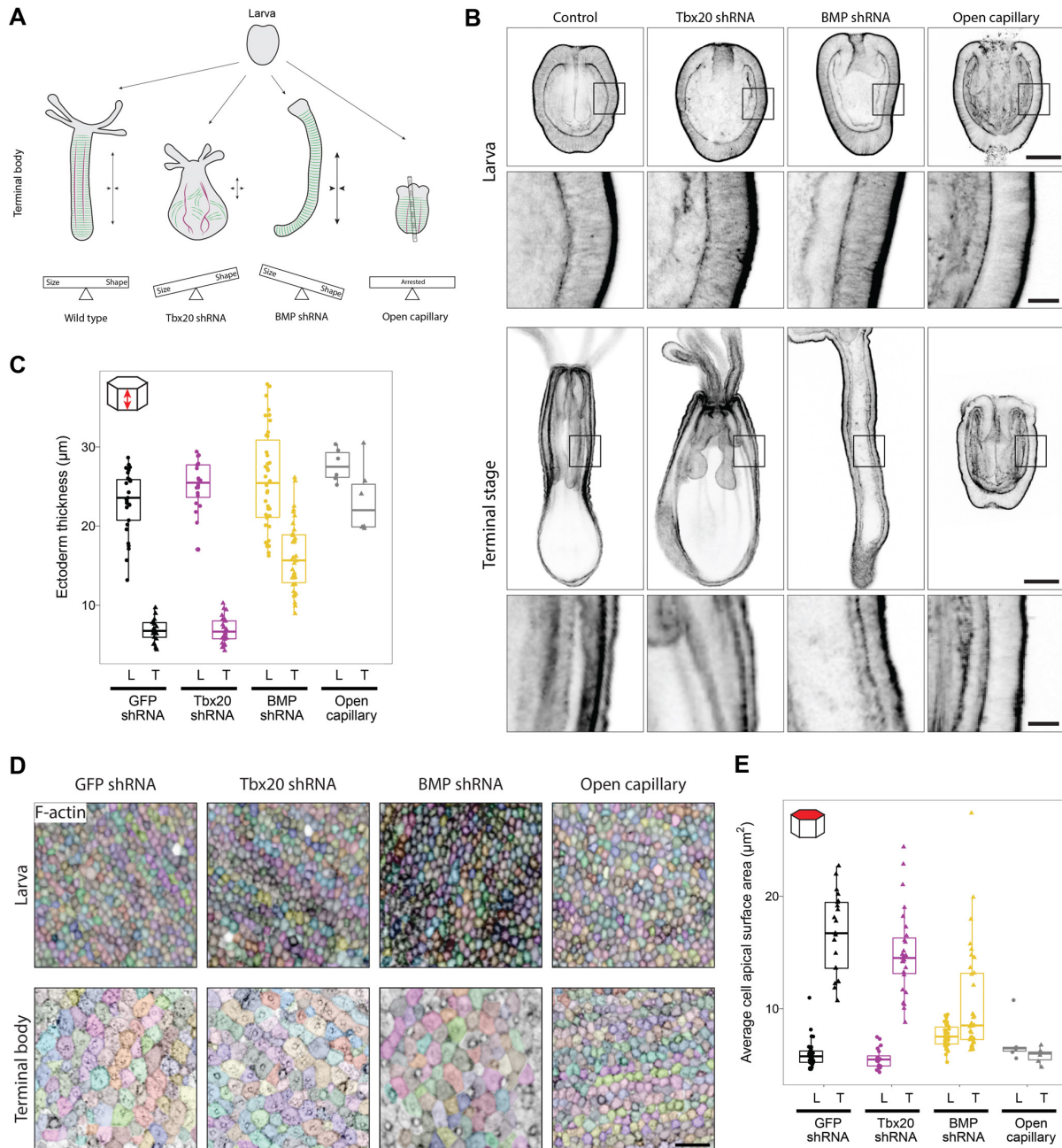


**Figure 37. Cellular shape changes under different perturbation conditions. A.** Schematics of muscle organization and animal size-shape relationship for control, *Tbx20* KD, *BMP2/4* KD, and depressurized animals. **B.** Confocal mid-plane slices of animals stained for F-actin. **C.** Quantification of epidermal thickness for larva (L, control  $n = 29$ , *Tbx20* KD  $n = 20$ , *BMP2/4* KD  $n = 38$ , and open capillary  $n = 6$ ) and terminal stage (T, control  $n =$

21, *Tbx20* KD  $n = 27$ , *BMP2/4* KD  $n = 34$ , and open capillary  $n = 6$ ). **D.** Epidermal apical surface view of animals stained for F-actin. Images are corrected for curvature using the MinCostZSurface FIJI plugin. Colors indicate cell segmentation. **E.** Quantification of average apical cell surface area for larva (L, control  $n = 29$ , *Tbx20* KD  $n = 20$ , *BMP2/4* KD  $n = 38$ , and open capillary  $n = 6$ ) and terminal body (T, control  $n = 21$ , *Tbx20* KD  $n = 27$ , *BMP2/4* KD  $n = 34$ , and open capillary  $n = 6$ ). Scale bars: 100  $\mu\text{m}$  (B, full-view) 20  $\mu\text{m}$  (B, zoom), 10  $\mu\text{m}$  (D). Figure was largely adapted from (Stokkermans et al., 2021) and was originally made by me. The capillary perturbation was performed by Aissam.

At the larval stage, ectodermal cells are mostly aligned with the oral-aboral axis, except at the two poles. In polyps, this bias in cell angle is often maintained, albeit sometimes slightly reduced (**Figure 38**). In contrast, cell angles are more evenly distributed in *Tbx20* KD animals, whereas *BMP2/4* KD animals largely maintain the bias in cell orientation, consistent with organismal shape (**Figure 38**). However, the distribution of cell apical surface areas and cell angles is not even across the body column. Typically, cells have larger areas above the pharynx region and in the lower body column, whereas cells are smaller from the pharynx to middle region of the body column, and at the aboral pole (**Figure 39A, B**). The degree of ectodermal thinning shows the inverse pattern, indicating that cellular shape changes do not occur uniform across the body column (**Figure 39B**). Also cell angles are not evenly distributed: close to the tentacles, cells are often oriented perpendicular to the body axis, while around the pharynx, cells largely maintain the oral-aboral orientation. In the lower body column, cell angles typically become more random, especially in *Tbx20* KD animals, which sometimes also show regions where cell angles are largely perpendicular to the oral-aboral axis (**Figure 38** and **Figure 39A, C**). This uneven distribution in cell areas and angles suggests that cells may have different tissue properties along the body column, or experience different stresses. Possibly, cells sense long range forces acting at the organismal level, and can stretch and/or reorient to different extents and in different directions, depending on the direction of expansion of the animal. The finding that animals treated with muscle inhibiting drugs and depressurized animals on open capillaries do not show extensive tissue remodeling suggests that cell shape changes are guided by muscular-hydraulic forces, rather than through a tissue-autonomous mechanism.

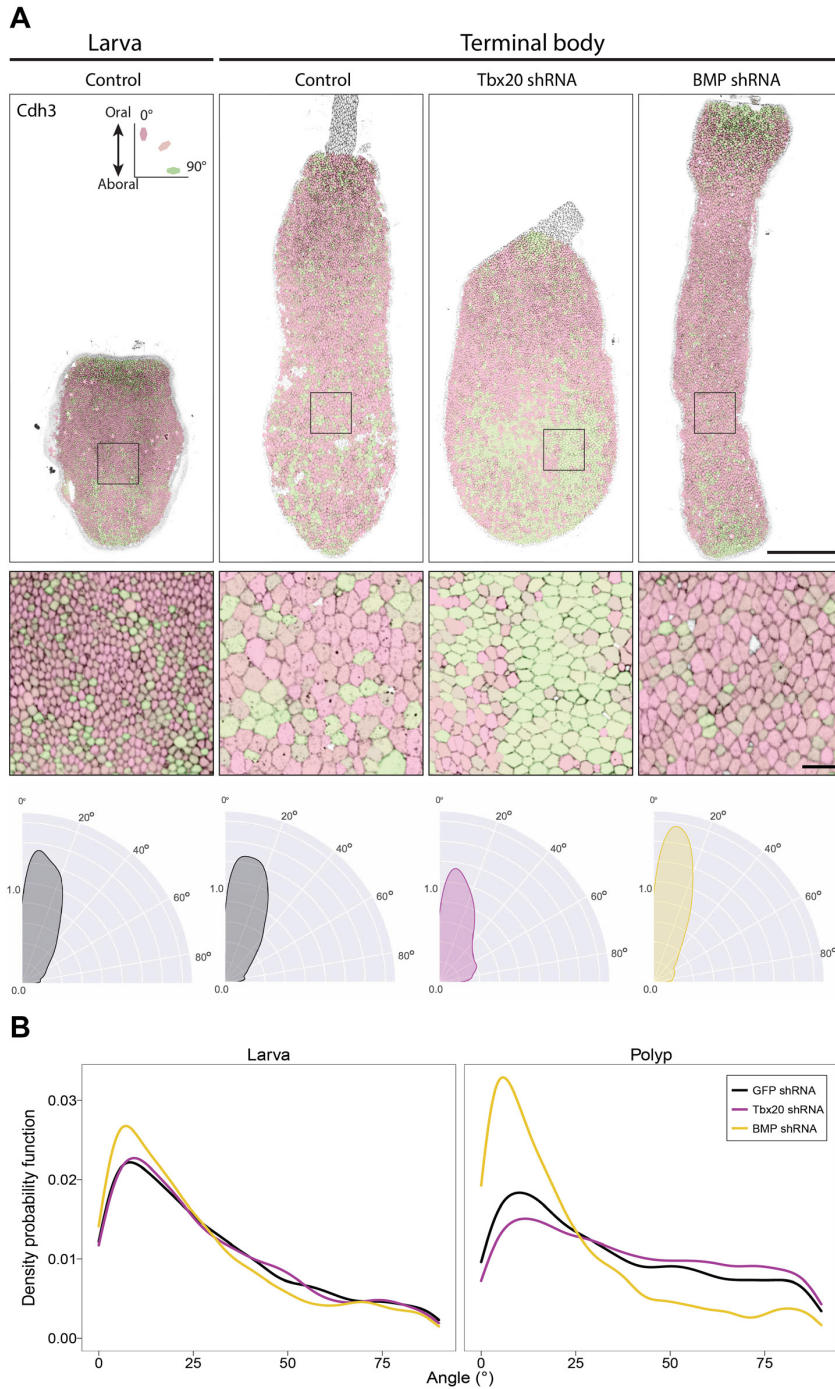


**Figure 38. Ectodermal cell angle correlates with animal shape.** **A.** Confocal images showing the surface of animals stained with Cdh3 antibody (Pukhlyakova et al., 2019), color-coded for cell angle (red: aligned with body oral-aboral axis, green: perpendicular to oral-aboral axis). Images are corrected for surface curvature using the MinCostZSurface plugin in FIJI. Corresponding density distributions for cell angles in the entire visible ectoderm are shown below. **B.** Density plots showing the distribution of cell angles at different stages and perturbations. Scale bars: 100  $\mu\text{m}$  (A, full-view), 10  $\mu\text{m}$  (A, zoom). Figure panels also partially appear in (Stokkermans et al., 2021) and were made by me.



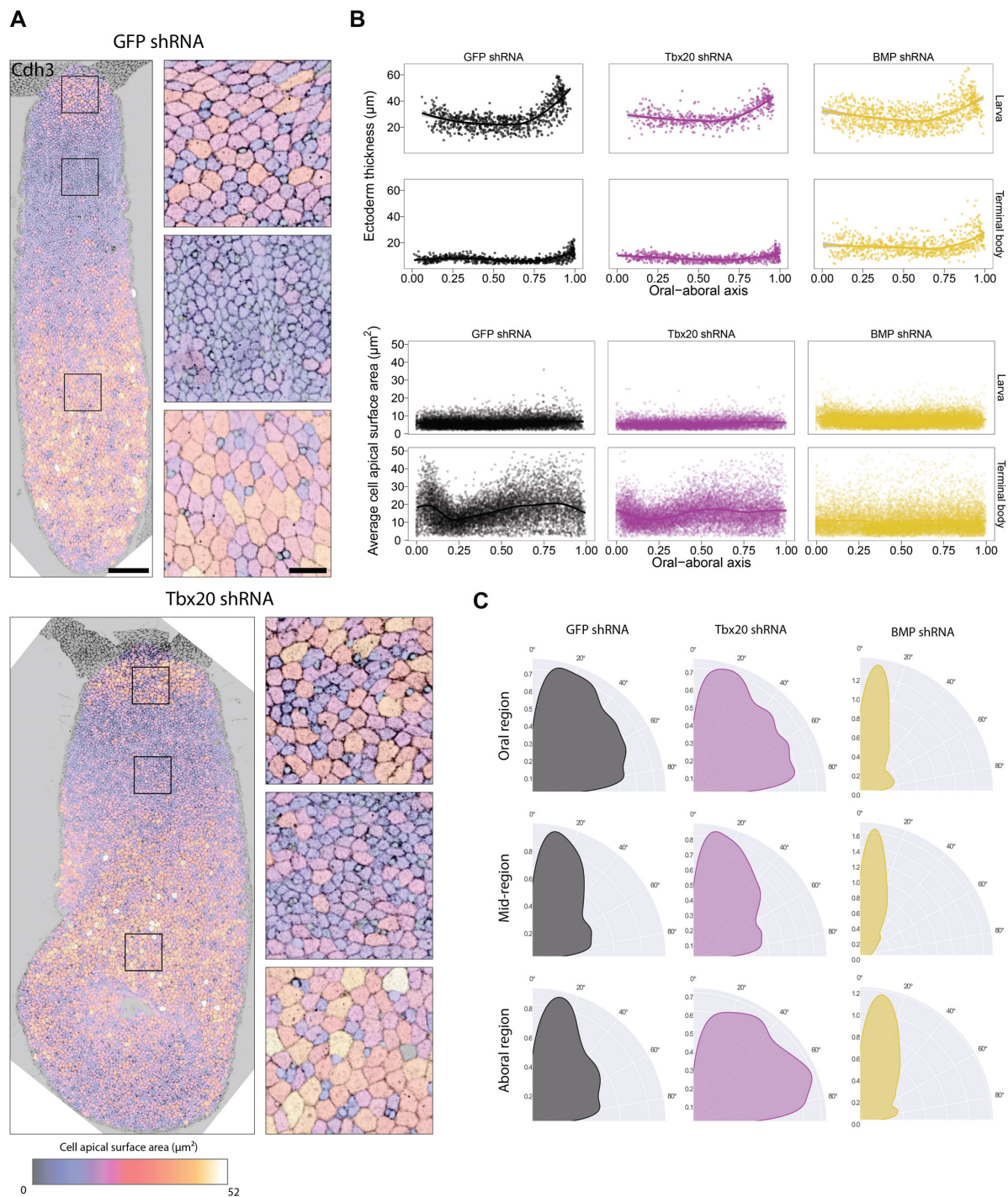


**Figure 39. Local variation in tissue behavior during larva-polyp transition.** **A.** Confocal images showing the ectoderm surface of animals stained with Cdh3 antibody (Pukhlyakova et al., 2019), color-coded for cell apical surface area. Images are corrected for surface curvature using the MinCostZSurface plugin in FIJI. **B.** Quantification of ectoderm thickness and average cell apical surface area along the body column. For average cell apical surface area, 400 cells are randomly sampled per animal. Control:  $n = 29$  (larva),  $n = 21$  (terminal body), *Tbx20* KD:  $n = 20$  (larva),  $n = 27$  (terminal body), *BMP2/4* KD:  $n = 38$  (larva),  $n = 35$  (terminal body). Ectoderm thickness was manually measured at multiple random locations along the body column for each animal. Control:  $n = 32$  (larva),  $n = 28$  (terminal body), *Tbx20* KD:  $n = 20$  (larva),  $n = 29$  (terminal body), *BMP2/4* KD:  $n = 38$  (larva),  $n = 37$  (terminal body). **C.** Polar density plot showing the distribution of cell angles at the oral region (1/3), mid-region (2/3), and aboral region (3/3) of control, *Tbx20* KD, and *BMP2/4* KD animals. Data from the same animals as shown in (B) is used, with 400 randomly sampled cells per animal. Scale bars: 50  $\mu\text{m}$  (A, overview), 10  $\mu\text{m}$  (A, zoom).

Not only cell angles correlate with organismal morphology, also the direction of cellular rearrangements appears to follow the shape of the animal. In control animals, photo-converted stripes typically increase their (length/width) aspect ratio, suggesting that cells rearrange with a bias towards the oral-aboral axis (**Figure 40**). In contrast, in *Tbx20* KD animals, stripes largely maintain a similar aspect ratio as they had in larvae. *BMP2/4* KD animals show extreme stripe elongation, such that occasionally different stripes even fuse together (**Figure 40**). Together, these results show that tissue organization correlates with animal shape, and suggest that global morphogenetic changes may direct tissue morphogenesis.

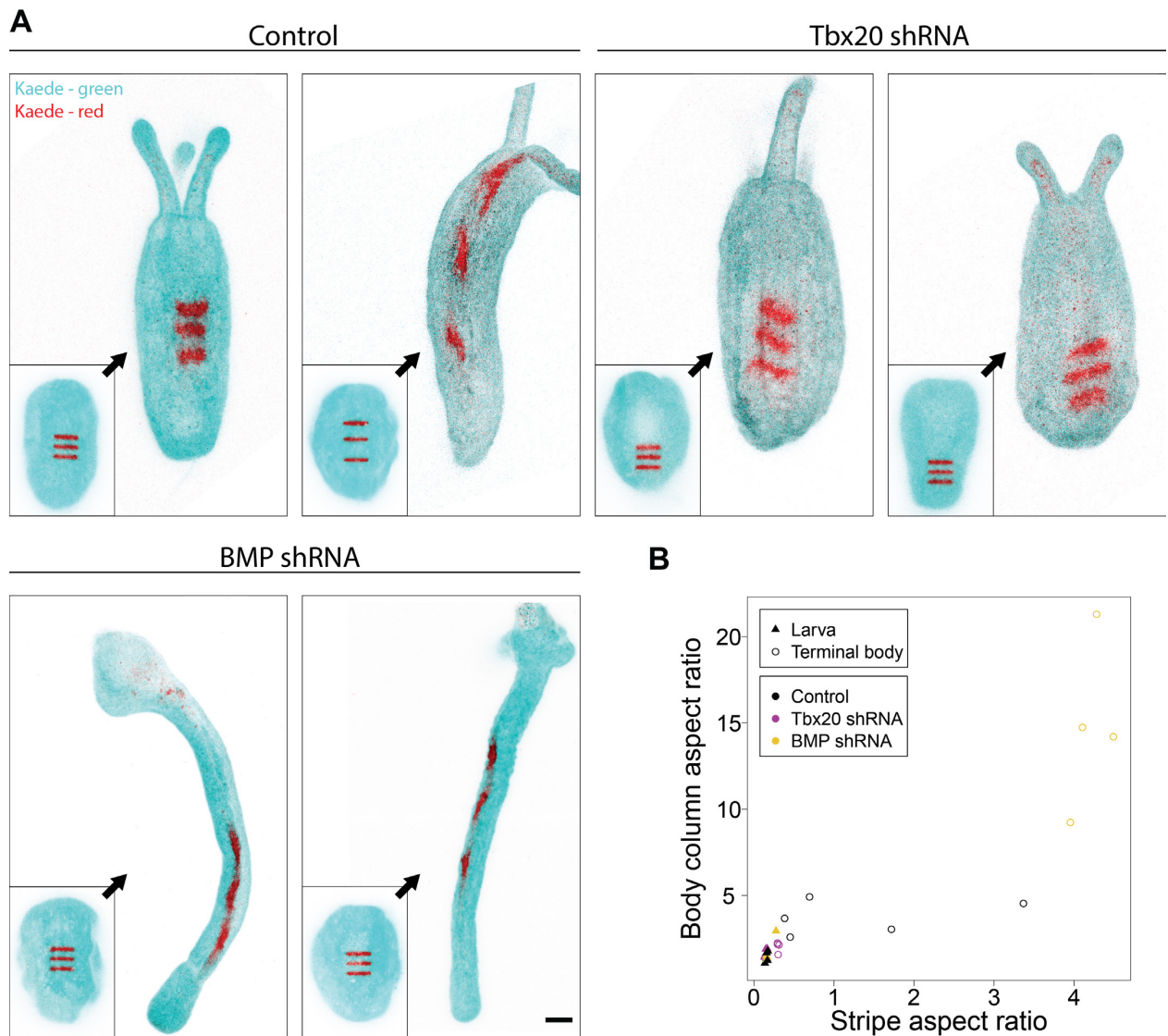


**Figure 40. Cellular rearrangements in controls and *Tbx20* and *BMP2/4* shRNA animals. A.** Examples of photo-converted stripe transformation in control, *Tbx20* KD and *BMP2/4* KD animals. **B.** Quantification of stripe aspect ratio (length/width) versus body column aspect ratio. Control n = 5, *Tbx20* KD n = 4, *BMP2/4* KD n = 4. Panel A partially appears in (Stokkermans et al., 2021) and was made by me. Scale bar: 50  $\mu$ m.

## 7.9. Biophysical modelling of larva-polyp transformation

To biophysically link larva-polyp morphogenesis to muscular hydraulics, we collaborated with Lakshminarayanan Mahadevan and Aditi Chakrabarti (School of Engineering and Applied Sciences, Harvard University). They developed a minimal biophysical model, in which the body column of *Nematostella* is modeled as a cylinder with a closed aboral end and an oral opening that can be either open or closed. Through pressurization, the cylinder with length  $\ell(t)$ , radius  $r(t)$ , and wall thickness  $h(t)$  can change shape. Their model assumes a Kelvin-Voigt model, which consists of an elastic element (with Young's modulus  $E$ ) and a viscous dashpot (with viscosity  $\eta$ ) in parallel, coupled to a muscular spring ( $E_m$ ) in series (**Figure 41A**). Through this organization, the system has both elastic and viscous properties, behaving elastically on short time scales but slowly creeping on long time scales. This is in agreement with the finding that tonic muscle contraction appear to maintain animal shape, and that treatment with linalool can lead to rapid relaxation of the system, resulting in a rounder animal morphology (**Figure 27C**). To understand in which direction the cylinder grows, the stresses are computed for both the axial direction and the azimuthal direction. The axial and azimuthal stresses are described by:  $\sigma_z = Pr/2h$  and  $\sigma_\theta = Pr/h$ , respectively, where  $P(t)$  is the intra-luminal pressure. How the tissue responds to these stresses depends on the tissue material properties, in particular the relative stiffness of the tissue in the axial and azimuthal direction. This can help explain the different phenotypes observed in control, *Tbx20* KD, and *BMP2/4* KD. If the animal is stiffer in the azimuthal direction than in the axial direction, the preferred direction of deformation upon pressurization will be in the axial direction, similar to the observed morphology in control animals and *BMP2/4* KD animals. Here, we speculate that the differential stiffness in the axial and azimuthal direction could be due to different muscle organization. The circular muscle fibers are more numerous than the longitudinal fibers and might thereby make the tissue stiffer in the azimuthal direction, favoring expansion in the axial direction (**Figure 41B**). *BMP2/4* KD animals could be an extreme version of this principle, as the lack of longitudinal fibers might increase this stiffness anisotropy, such that the tissue is much stiffer in the azimuthal direction compared to the axial direction. In contrast, disorganized muscles in *Tbx20* KD may result in similar stiffnesses in both directions. In such a case, the model predicts that the cylinder would grow isotropically in both directions, in line with the observed *Tbx20* KD organismal morphology (**Figure 41B**). To illustrate and support the relationship between differential stiffness and morphology upon pressurization, Aditi performed an experiment in which balloons were inflated with and without taped bands to mimic the passive effects of the muscle fibers (**Figure 41C**). This way, similar morphologies as those observed in wild-type, *Tbx20* KD and *BMP2/4* KD animals could be obtained (**Figure 41C**), supporting the hypothesis that the differential stiffnesses in these animals, potentially through the different muscle organization, are responsible for the different animal shapes.

Measurements of the pressure in the body column upon contraction have led to two observations: first, there is a small positive pressure in the body column, possibly due to basal muscle tone, fluid uptake, or osmotic imbalances while the animal keeps its mouth closed. At times, we also observed cases where the pressure was zero, suggesting that the mouth was open, equalizing the pressure inside and outside. Second, the pressure increased upon contraction (**Figure 27B**). In the model, the pressure  $P(t)$  in the cylinder is described by two parameters: 1) a static component, called the ‘priming pressure’, which could correspond to the small positive pressure when the animal is not contracting but keeps its mouth closed, and 2) a dynamic component, called the ‘pumping pressure’ which could correspond to the increase in pressure upon muscle contraction. In the model, the priming pressure is constant, whereas the pumping pressure is modelled as an oscillator:  $P(t) = p_T + p_0 \cos(\omega t)$ , where  $p_T$  is the static priming pressure and  $p_0$  is the amplitude of the oscillatory pumping pressure term with frequency  $\omega$ . In this relationship, the static priming pressure brings the axial wall stress close to a yield stress, above which plastic deformation can occur, and the dynamic pumping pressure tips it past the yield stress, resulting in a dynamic elongation profile (**Figure 41D, E**). Thus, this combination of “priming and pumping” can cause the body wall to deform irreversibly in a dynamic fashion, directly linking behavior dynamics to larva-polyp morphogenesis. Indeed, simultaneous length increase and body contractions are observed in data of live animals recorded at five-second resolution (**Figure 41F**). However, not every contraction necessarily leads to elongation, possibly because not every contraction increases the pressure above the yield stress. Together with the principles of differential stiffnesses, this model accurately recapitulates the observed dynamics and morphologies, and supports the idea that animal behavior at short time scales can contribute to animal morphogenesis on long time scales (**Figure 41G**) (Stokkermans et al., 2021).



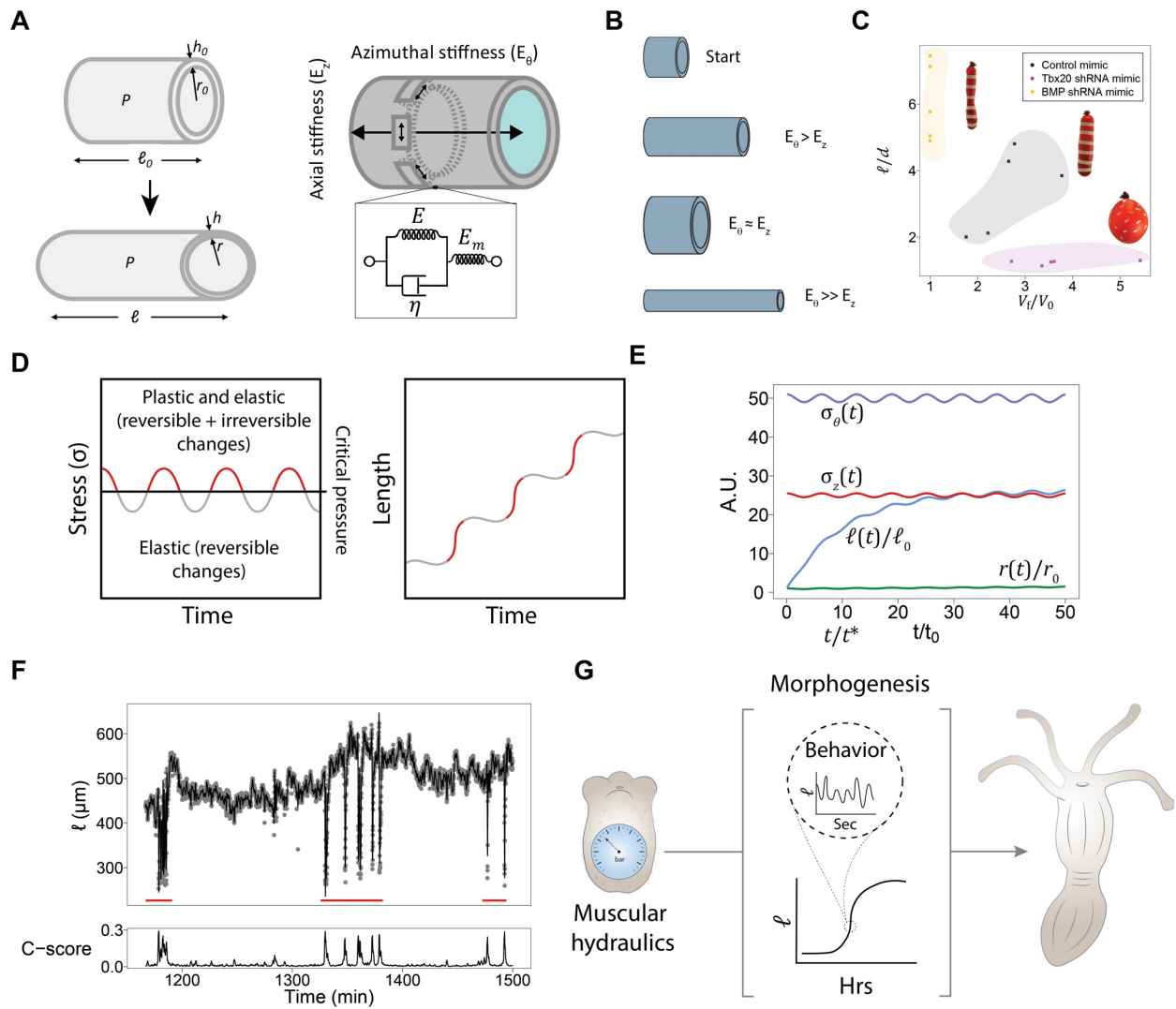


**Figure 41. Biophysical model recapitulates larva-polyp size and shape changes.** **A.** *Nematostella* modeled as a cylindrical shell of thickness  $h(t)$ , length  $l(t)$  and radius  $r(t)$ , with time varying pressure in the cavity  $P(t)$ . A Kelvin Voigt model with a muscular spring in series is used to model tissue properties, which have differential stiffness along the axial ( $E_z$ ) and azimuthal ( $E_\theta$ ) axes. Model is developed by L. Mahadevan and Aditi Chakrabarti. Cartoons are adapted from their work. **B.** Schematic representation of cylinder shapes that would result from pressurizing a starting cylinder (top) for different conditions:  $E_\theta > E_z$  corresponding to wild-type animals,  $E_\theta \approx E_z$ , corresponding to *Tbx20* KD, and  $E_\theta \gg E_z$ , corresponding to *BMP2/4* KD. **C.** Body column aspect ratio ( $l/d$ ) as a function of cavity volume changes ( $V_i/V_0$ ) for balloon experiments shows similar qualitative trends as for control, *Tbx20* KD, and *BMP2/4* KD animals. Representative images of corresponding balloon shapes are shown. Experiment and quantification by Aditi Chakrabarti. **D.** Cartoon explaining how an oscillating force, that occasionally surpasses a critical yield stress can cause irreversible changes, i.e. lengthening of a cylinder. **E.** The dynamic analytical model describing change in length ( $l(t)/l_0$ ) and radius ( $r(t)/r_0$ ), and the axial ( $\sigma_z$ ) and azimuthal ( $\sigma_\theta$ ) stresses applied to the cylindrical shell as a function of dimensionless time ( $t/t^*$ ) at steady state, where  $t^* = \eta/E$ . Model and plot by Aditi Chakrabarti and L. Mahadevan. **F.** Experimentally observed changes in body column length correlate with contractile activity (red lines), consistent with a priming role for the base luminal pressure, and a pumping role for the dynamic muscular-hydraulic pressure generated by contractions. **G.** Summary of how muscular hydraulics drive larva-polyp morphogenesis. Figure and figure legend are adapted from (Stokkermans et al., 2021).

## 7.10. Summary and conclusions

From the late larval stage onwards, *Nematostella* possesses a hydrostatic skeleton through which short-term organismal size and shape changes can be regulated through muscle contractions that regulate cavity pressure. However, muscular hydraulics are also important for long-term larva-polyp transition, since depressurized animals pierced on open capillaries and animals treated with muscle inhibiting drugs do not develop into normal polyps and show limited tissue remodeling. Knockdown of *Tbx20* results in animals with an abnormal round shape, which is in strong contrast to the morphology of *BMP2/4* KD animals, which have a long and thin shape. At the tissue level, cell shape changes and cellular rearrangements correlate with organismal morphology in control, *Tbx20* and *BMP2/4* KD animals. Interestingly, *Tbx20* KD and *BMP2/4* KD animals have different muscle organizations compared to controls: in *Tbx20* KD animals, longitudinal and circular muscles are disorganized, whereas longitudinal muscles are entirely absent in *BMP2/4* KD animals. This suggests that organismal size and shape development are differentially controlled by antagonistic muscles: lack of organized circular muscles in *Tbx20* KD animals may prevent efficient squeezing of the body column along the oral-aboral axis, leading to expansion of the body column in all directions. In contrast, lack of longitudinal muscles in *BMP2/4* KD animals may 'soften' the animal in the oral-aboral axis and may thereby favor elongation to this direction. This idea was supported by modelling the body column of *Nematostella* as a growing cylinder, which shows that differential stiffness in the axial and azimuthal direction can result in different morphologies. These could be recapitulated using balloons with taped bands that mimic muscle organization observed in control, *Tbx20* KD and *BMP2/4* KD animals. Together, these results suggest that muscular hydraulics can induce long long-range forces that drive organismal morphogenesis through cavity inflation and induce stretching and redistribution of the tissue to match to a new shape.

## 8. Animal-environment interactions during larva-polyp transition

### 8.1. Impact of environmental factors on larva-polyp transition

Muscular hydraulics play an important role during larva-polyp transition, as perturbation of the hydrostatic skeleton and associated muscle organization can lead to abnormal shape and size phenotypes. However, the functioning of the hydrostatic skeleton does not only depend on animal intrinsic properties, such as muscle organization, but can also be influenced by environmental factors. For example, sea water salinity, pH, temperature, osmolarity, and viscosity may impact animal physiology and behavior. Although *Nematostella* does not rely on specific environmental cues to induce metamorphosis, the type of substrate may still affect how likely an animal is to settle and adhere during larva-polyp transition. Naturally, *Nematostella* lives in brackish environments, such as salt marshes and saline lagoons, in which conditions such as salinity and temperature can vary rapidly and widely (Hand and Uhlinger, 1992; Sheader et al., 1997). As a mostly sessile species, *Nematostella* has a relatively high tolerance to changing environmental conditions, and for this reason they are also used for studying stress-response genes and the interaction between (epi)genome and bacteria in changing environments (Fraune et al., 2016; Reitzel et al., 2008). From a morphogenetic point of view, it is also interesting to ask how different environmental factors may impact the functioning of the hydrostatic skeleton and associated shape changes. While in this study development in *Nematostella* has so far been studied in the same, minimal environment, this chapter focuses on ongoing work that aims to investigate the impact of environmental factors on larva-polyp transition and animal behavior.

### 8.2. Effects of sea water salinity on larva-polyp transition

Adult *Nematostella* can live in a wide range of different salinities, varying from 2-42 ppt (Sheader et al., 1997). At salinities below 12 ppt or above 40 ppt, animals tend to retract their tentacles and become inactive but slow acclimatization to a different salinity has been shown to slightly shift these boundaries (Sheader et al., 1997). To study the effect of increased and decreased salinity during larva-polyp transition, larvae were moved from 12 ppt artificial seawater (ASW) to 4, 8, or 36 ppt ASW in a large volume (6 cm glass dishes). Whereas an increase from 12 to 36 ppt was well-tolerated and resulted in normal polyp development, a decrease of salinity to 4 or 8 ppt resulted in misdevelopment and death of the majority of animals, which frequently adopted a 'bubble-like' appearance (**Figure 42A**). An immediate and a graded transfer to decreased salinity conditions had similar effects. Analysis of elongation dynamics in animals in 12 ppt ASW versus animals in 36 ppt

revealed only minimal differences in elongation dynamics, where on average animals develop slightly faster in 12 ppt ASW (**Figure 42B-D**). Thus, while animals are sensitive to decreased sea water salinity, they are robust to increasing salt concentrations at the larval stage.

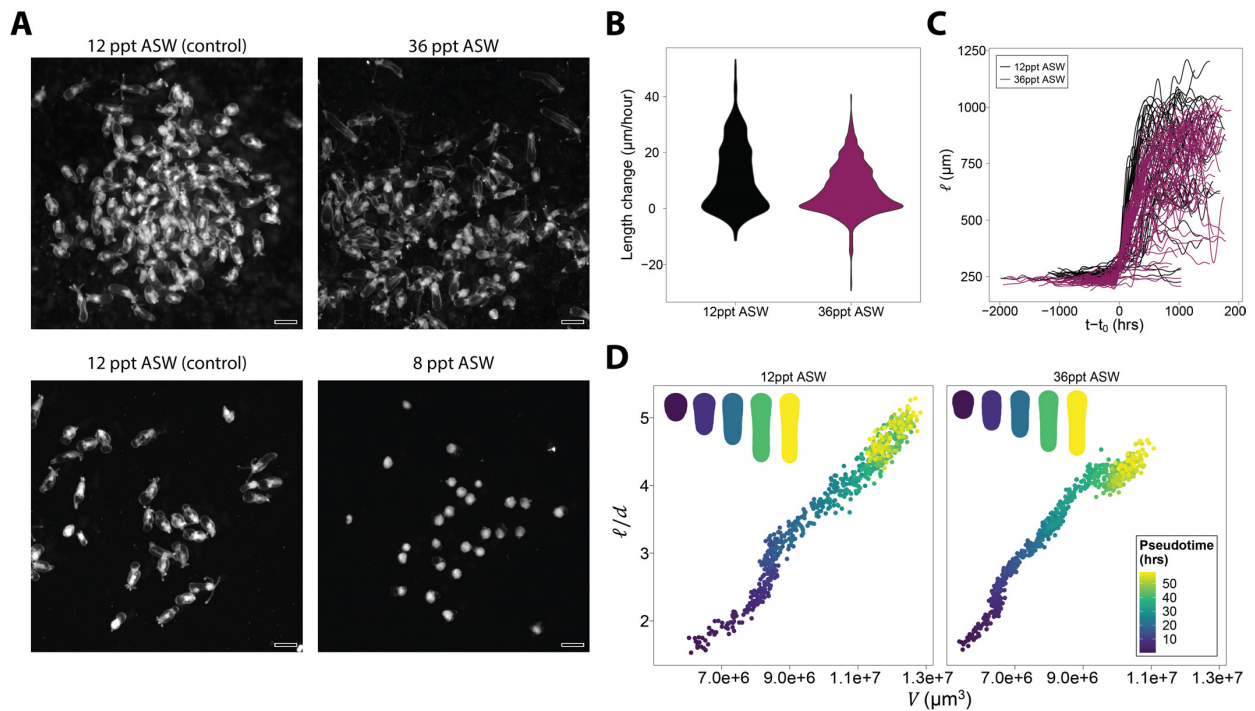


**Figure 42. Larval development under different salinity conditions.** **A.** Pictures of animals incubated in 12 ppt ASW (control), or 36 or 8 ppt ASW. **B.** Violin plot showing body column length change during the transition stage of animals in 12 ppt versus 36 ppt ASW. **C.** Quantification of body column length in pseudotime reveals that animals can develop well in 36 ppt ASW and acquire similar body column lengths as controls. **D.** Quantification of morphospace trajectories, color-coded by pseudotime. Insets show averaged body column shapes. Scale bars: 500  $\mu\text{m}$ .

### 8.3. Increasing sea water viscosity affects animal shape

Since hydrostatic skeletons change shape by pushing liquid through muscular contractions, changing the viscosity of the liquid might affect the functioning of the hydrostatic skeleton. To test this, different solutions were tested to increase the viscosity of seawater. Animals did not survive well in ASW containing gelatin, but they appeared well-tolerant to 1% methylcellulose (MC). Although animals can survive for weeks in 1% MC, larva-polyp transition is affected in multiple ways. Animals that developed in 1% MC from the larval stage onwards were substantially shorter and often wider compared to controls (**Figure 43A-C**). Although larvae initiated elongation, they often shrink or arrest elongation after about 35 hours and remained in a round morphology (**Figure 43C**). Similar morphologies were observed in animals kept in low concentrations of low-melting agarose or xanthan gum. In 1% MC, both animal aspect ratio and animal volume are decreased compared to controls, but overall the effect was largest on animal shape, as animals in 1% MC sometimes can reach similar volumes as controls, but not the same aspect ratio. Placing these animals back in normal 12



ppt ASW resulted in almost complete recovery, taking place over several days (**Figure 43D**). Animals in 1% MC show strongly decreased settlement behavior (**Figure 43E**), possibly because the thicker solution makes it harder for animals to make direct contact with the plate bottom. Furthermore, as 1% MC increases the viscosity of sea water, it may be harder for the animal to contract and exert forces on the tissue. To test the effect of 1% MC on contractility, animals were recorded at five-second resolution and contractions were visualized in kymographs. As is visible from the difference in tilt in the lines of the kymographs in **Figure 43F**, peristaltic contractions propagate at a slower speed in the animal in 1% MC compared to the control, indicating that contractility is not inhibited but slowed down under these conditions. The earlier described shRNA knockdown studies suggest that muscle organization may impact morphology. Interestingly animals in 1% MC were found to have less well-organized muscles compared to controls, and sometimes showed muscle defects similar to those observed in *Tbx20* KD animals (**Figure 43G-I**), suggesting that morphology may also affect muscle organization. One possibility is that a mismatch in the timing of muscle elongation and axial elongation causes the fibers to fan out because they are restricted in space. Whether rescue of animal morphology by placing affected animals back in normal sea water also rescues muscle fiber organization, remains to be investigated. Taken together, increasing the viscosity of the seawater by using 1% MC affects both animal morphology and behavior, possibly because it limits the action of the hydrostatic skeleton and may compress the animal to a rounder shape.

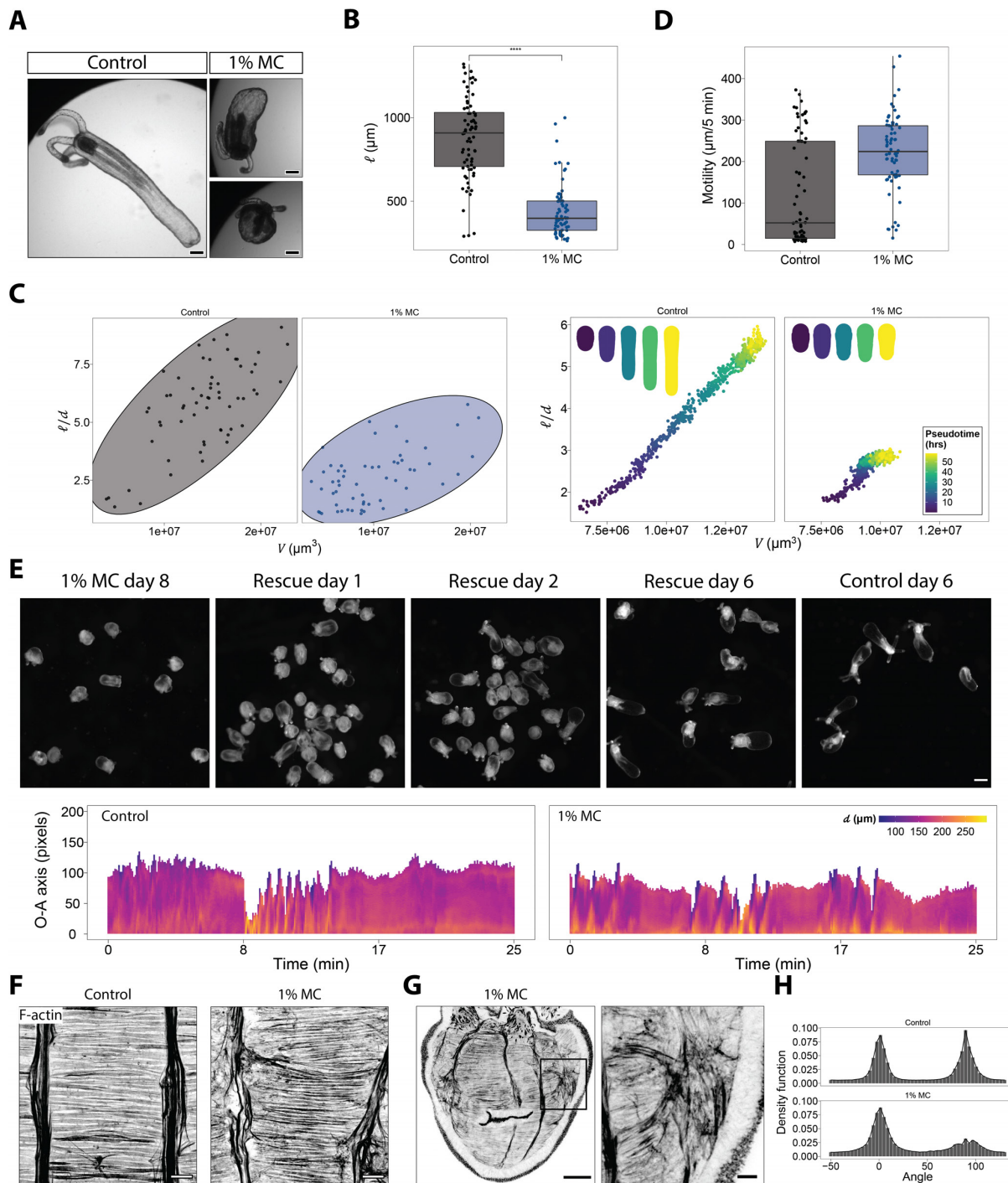


**Figure 43. Effect of increased viscosity on larva-polyp morphogenesis and behavior.** **A.** Brightfield images of a control animal and two animals developed in 1% MC. **B.** Quantification of body column length for controls ( $n = 74$ ) and animals developed in 1% MC ( $n = 70$ ). **C.** Quantification of body column aspect ratio and volume for controls and animals in 1% MC after larva-polyp transition (left) and averaged per group in pseudotime (right). Insets show averaged shapes. **D.** Quantification of median displacement per animal during the transition stage. Animals developing in 1% MC show strongly reduced settlement behavior. Both motile and sessile animals are present in the control group. **E.** Animals developed in 1% MC for 8 days from mid-larval stage onwards show recovery when rescued with normal 12 ppt ASW. **F.** Kymographs of body column diameter along the oral-aboral axis for a control animal and an animal in 1% MC, showing reduced contraction speed, reflected in the difference in tilt of the stripes. **G-I.** Muscle organization (F-actin staining and angle quantification) in controls ( $n = 16$ ) and animals developed in 1% MC ( $n = 6$ ), showing reduced polarity in longitudinal muscle fiber organization. Scale bars: 100  $\mu\text{m}$  (A), 10  $\mu\text{m}$  (F), 50  $\mu\text{m}$  (G, overview), 10  $\mu\text{m}$  (G, zoom).

#### 8.4. Perturbation of settlement affects timing of larva-polyp transition

To better understand the relationship between settlement behavior and elongation dynamics, I asked whether perturbation of adhesive settlement behavior would negatively affect elongation dynamics. Some cnidarian species only undergo metamorphosis when they adhere to a specific substrate, but this does not appear to be the case for *Nematostella* (Bucher et al., 2016; Iwao et al., 2002; Leitz, 1997; Müller and Leitz, 2002). Nevertheless, there might be a preference for adhesion to certain substrates. In the experiments with the Acquirer microscope, plates with plastic bottoms are used. To test if other substrates would enhance or inhibit adhesive settlement behavior, *Nematostella* larvae were incubated in dishes with different substrates: 1) plastic, 2) glass, 3) gelatin coated glass, and 4) teflon film. Although *Nematostella* larvae appear to have a small preference for plastic and glass (**Figure 44A, B**), animals could adhere to all substrates and developed into normal polyps. As none of the different substrates, including the anti-sticky teflon surface, could completely block settlement, I attempted to perturb settlement in different ways. For this, I either applied continuous shaking to the dishes with developing animals, to prevent them from settling and touching the bottom, or mounted animals in hanging droplets, so that they would settle down to the bottom of the droplet without touching the substrate (**Figure 44C**). Animals developed slower in both conditions (**Figure 44D-G**). However, different experiments gave variable results and were complicated by the facts that shaking the dish did not always completely prevent settlement, and that evaporation and flattening of small hanging droplets sometimes allowed animals to stick to substrate while sitting upside-down. Furthermore, these approaches did not allow recording of the dynamics of larva-polyp transition at higher time resolution. I therefore attempted to image animals in hanging and standing drops in the Acquirer screening microscope, but found that the results so far are not reliable, because the droplets could not be kept intact for more than 4 days due to evaporation. Therefore, future experiments to test the role of settlement are still required, and would need solutions to the problem of evaporation of small droplets, for example using a microfluidics set-up.

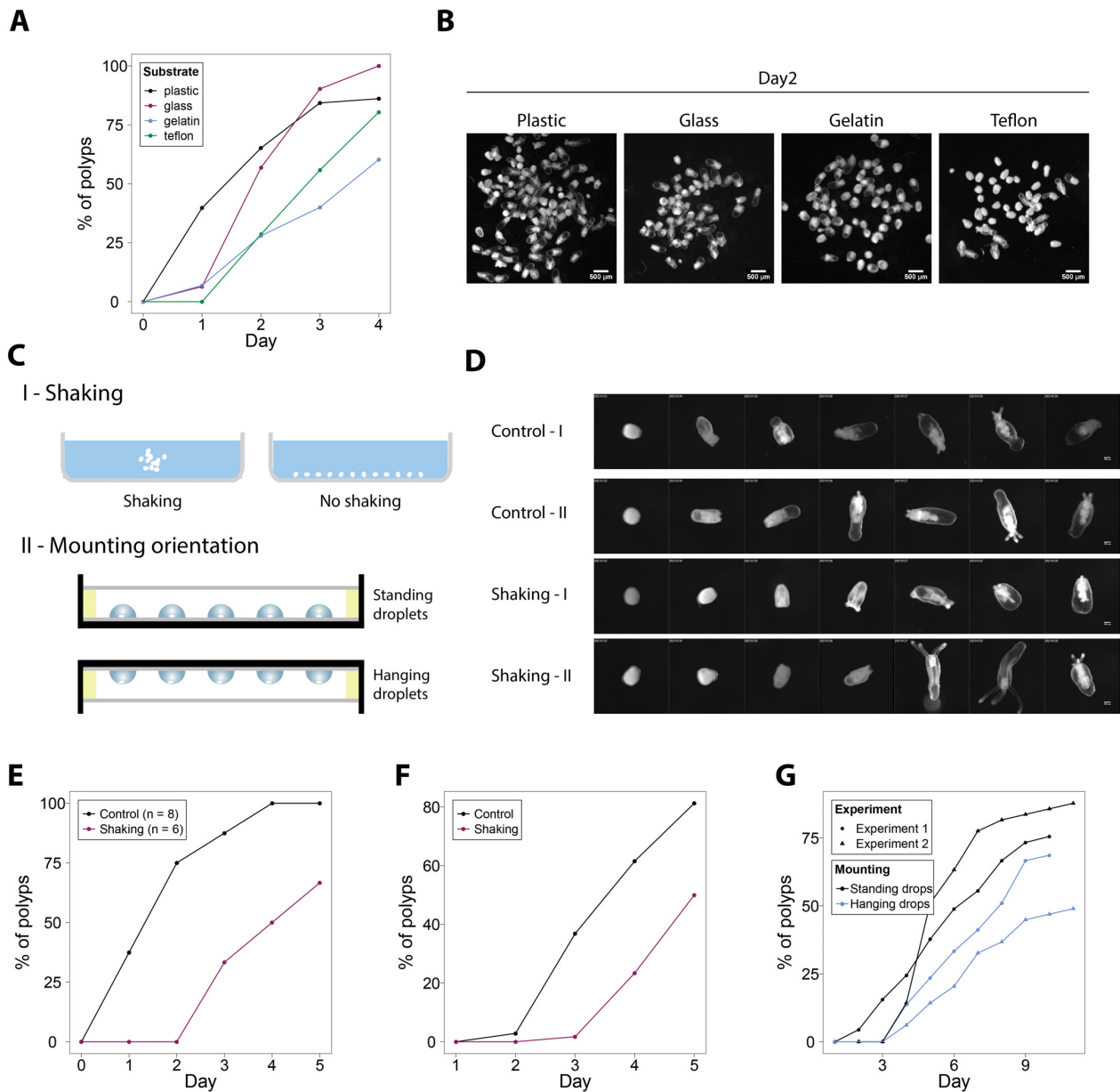


**Figure 44. Perturbation of settlement behavior affects timing of larva-polyp transition.** **A.** Changes in the percentage of animals at the polyp stage for a bulk experiment in which each group of animals is incubated in a dish with a different substrate (plastic dish, glass dish, gelatin-coated glass dish, teflon film). Each group contains 66-113 animals. **B.** Images taken at day 2 of the experiment shown in A. **C.** Two approaches to perturb settlement: 1) applying shaking to do the dish with animals, 2) mounting animals in hanging versus standing droplets. **D.** Pictures of four individuals over time, with and without shaking of the dish. **E.** Percentage of animals at the polyp stage for control (n = 8 animals) and animals to which shaking is applied (n = 6). **F.** Changes in the percentage of animals at the polyp stage for a bulk experiment with and without shaking. Each group contains between 70-85 animals. **G.** Percentage of animals at the polyp stage over time for two experiments in which animals are mounted in standing drops or hanging drops. Each group contains 45-51 animals. Scale bars: 500  $\mu\text{m}$  (B), 100  $\mu\text{m}$  (D).

## 8.5. Effect of light exposure on settlement behavior

Earlier findings have shown that adult *Nematostella* are light-sensitive, and that exposure to blue and green light results in enhanced locomotive behavior compared to red light exposure (Leach and Reitzel, 2020). In the confocal microscope, non-anesthetized animals react to laser light exposure by contracting or moving away. Light exposure could thus potentially serve as another strategy to disrupt settlement. To test whether short-term laser light exposure could trigger a behavioral response in the animal, I imaged animals before, during, and after exposure to 12 seconds of 470 nm light on the Acquirer microscope. Here, I found that many animals show a clear behavioral response. The type of response correlated with animal stage: while larva responded with increased swimming behavior, animals in the transition stage and polyp stage often only contracted (**Figure 45A-C**). In some cases, a previously seemingly attached animal released itself from the substrate by contracting, and also showed increased motility. The effect of light exposure was temporary; most animals did not show prolonged increased swimming behavior after light exposure was terminated. Although these results indicate that light exposure can trigger a behavioral response, that in some cases can disrupt animal settlement, I did not find a clear difference in elongation dynamics and settlement behavior when animals were illuminated with 470 nm light for 3 seconds per five-minute time interval for multiple days (**Figure 45D**), suggesting that these conditions were too mild to have a clear impact on elongation dynamics. However, this strategy could be explored further, for example by combining it with adaptive feedback microscopy, to specifically expose the animal to light when it is about to settle. This might help to find conditions in which animal (settlement) behavior can be specifically disrupted, to study the effect on elongation dynamics during larva-polyp transition.

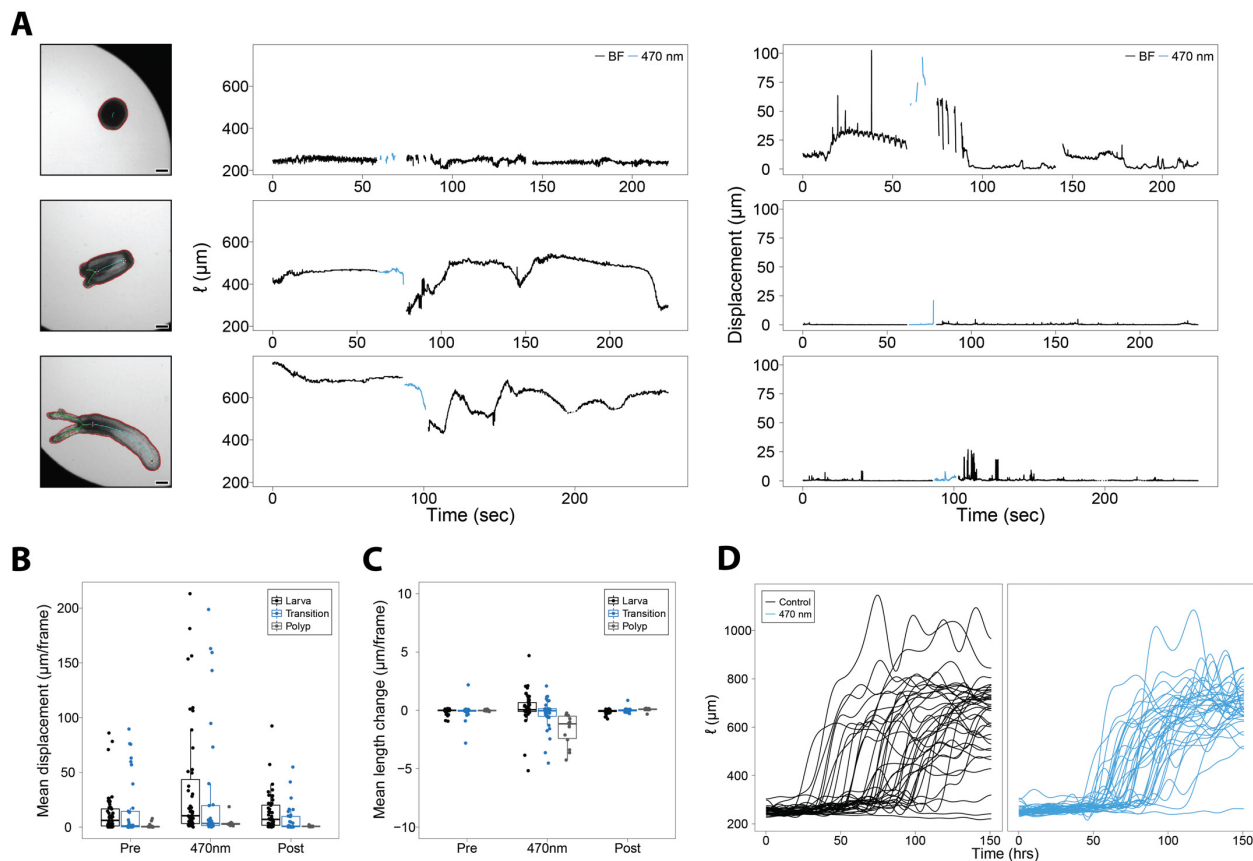


**Figure 45. Effect of light exposure on settlement behavior and elongation.** **A.** Quantification of body length and displacement before, during and after exposure to 470 nm light (light blue) in a larva (top), transition stage animal (middle), and polyp (bottom). **B-C.** Averaged displacement and length change before, during and after exposure to 470 nm laser light. **D.** Quantification of body length in time in control animals and animals exposed to 3 seconds of 470 nm laser light per five-minute time interval. Scale bars: 100  $\mu\text{m}$ .

## 8.6. Summary and conclusions

Although *Nematostella* can tolerate a wide range of different conditions (Shedder et al., 1997), environmental factors can shift the dynamics of larva-polyp transition or change polyp morphology. Such conditions can include changes in seawater salinity, viscosity, or exposure to light. Increasing sea water salinity had a limited effect on larva-polyp transition dynamics. In contrast, larvae appear sensitive to a decrease in salinity to 8 ppt ASW. Increasing viscosity directly influences animal morphology, possibly because it constrains the animal, and because muscular forces are less effective in a viscous liquid. Indeed, peristaltic contractions propagate at a slower rate in 1% MC. In a viscous solution, the muscles may fail to properly squeeze the animal into an elongated shape, such that the animal acquires a rounder morphology instead. However, this morphology does not have to be permanent, since animals released from 1% MC can still acquire a normal polyp morphology within days after being placed back in normal 12 ppt ASW.

Although numerous attempts have been made, it remains challenging to completely abolish settlement behavior. *Nematostella* appears capable of adhering to all substrates tested here, and

different substrates had minimal effects on larval settlement and metamorphosis. However, the efficiency of attachment could be reduced by applying shaking, or by mounting animals in hanging droplets. These animals took longer to develop into polyps. However, it remains difficult to assess whether the observed delay in elongation is directly due to reduced attachment or due to other stresses caused by the perturbation. Mounting animals in hanging droplets may induce the least stress, but a reliable method to keep the hanging drops intact for a longer period of time still has to be developed. Alternatively, disruption of settlement through exposure to specific light sources could be explored further.





## 9. Discussion

In this study, I have used larva-polyp transition in *Nematostella* as a system to study the relationship between organismal behavior and morphogenesis. Using an image analysis pipeline to track behavioral and morphogenetic changes, I found that larva-polyp transition is a dynamic process with high inter-organism variability. While animal settlement behavior correlates with elongation dynamics, perturbation studies showed that a functional hydrostatic skeleton is essential for body cavity inflation and tissue remodeling. On short time scales, animals show body contraction behavior that regulates internal fluid pressure, and that may act as a long-range force that contributes to organismal morphogenesis on long time scales, thereby connecting animal behavior and morphogenesis.

### 9.1. Advantages and limitations of the experimental setup

Using an experimental setup in which animals can freely move while tracking their development proved to be a useful strategy to gain access to both animal behavior and morphogenetic dynamics. Active animal behavior complicates the use of confocal microscopes, because the animal does not stay in the field of view and in the focal plane. While anesthetics and physical confinement of the animal can temporarily overcome these issues, they cannot be applied on the developmental time scale, as they prevent normal larva-polyp morphogenesis. In contrast, imaging animals at low magnification in the brightfield channel is minimally invasive and yields large amounts of image data, tracking development for a large number of animals simultaneously and facilitating comparison of different experimental conditions using drugs and shRNAs. However, this strategy also has some limitations. First, it is limited to use at the organismal scale, and cannot be easily used to track tissue morphogenesis. Second, images are captured in 2D, such that the volume of the animal has to be estimated and cannot be measured directly. This can introduce artifacts, especially when the animal rotates itself to stand vertically in the well. In this study, OCM imaging was explored and found to be a promising strategy to study animal development and behavior in 3D due to its rapid image acquisition and high penetration depth. In future experiments, OCM may provide new ways to study the dynamics and relationship between body contractions, mouth opening, and cavity inflation. Third, while image data is informative, it does not tell the complete story, and therefore has to be interpreted carefully. The staging method used here depends on animal circularity, a visible animal feature that is also influenced by animal behavior and that is variable among individuals. For this reason, I defined the transition stage by boundaries that mark a relatively small window, while in reality the process is more gradual and longer in duration. Furthermore, visible animal deformations are not necessarily indicative of how actively the muscles are working. In a system in which the internal pressure is large, higher muscular forces are needed to induce a

particular body deformation than in a system with low internal pressure, just like it is easier to squeeze a half-inflated balloon compared to a fully inflated balloon. The forces acting on a tissue can thus not be inferred from body deformation measurements directly. Nevertheless, the presence or absence of active contractile behavior can be informative to find patterns that link animal behavior and morphogenesis. While contraction behavior is obvious to see by eye, detecting it based on size and shape measurements is not straightforward. Here, I used the change in circularity to detect when animals contract. Although this works well for detecting high amplitude contractions in polyps, detection of smaller contractions at especially early stage animals is more difficult and complicated by frequent animal rotation and displacement. Although morphogenesis and animal behavior co-occur during larva-polyp transition, they still happen at time scales that are relatively far apart, which is one of the main reasons that make simultaneously studying behavior and development challenging. Recording individual animals at high time resolution can record both short-lived contraction behavior and long-term morphogenesis, but yields large amounts of data of which interpretation is non-trivial. Depending on the time scale (i.e. how much one zooms in on the data), an animal can appear to do different things, e.g. temporarily shrinking due to contraction or deflation on the behavioral time scale, while elongating on the developmental time scale. The difference in time scales and the high variability between animals prevented me from detecting direct relationships between contractions and an increase in body length in these image data sequences. However, more sophisticated computational approaches including machine learning that can take multiple size and shape features into account simultaneously might be able to help identify recurring cross-time scale patterns that might be hidden more deeply in the data.

## **9.2. Causes and potential function of inter-organism behavioral variation**

Measurements of elongation dynamics in a population of wild type animals developing under the same conditions revealed a high variability among individuals in terms of duration of larva-polyp transition, rate of elongation, and final morphology. Furthermore, animals show variability in swimming and settlement behavior, and animals that remain motile were found to elongate at a slower rate compared to stably adhered, settled animals. The underlying cause for this variation is not obvious. While the size of the egg may play a role in influencing the final size a primary polyp may acquire, as this is the only source of nutrients up to this stage, it seems unlikely that egg size has a large effect on animal behavior, as similar-sized larvae can show different behavior and elongation dynamics and still produce polyps of similar size. Reducing genetic variation by comparing offspring from the same parents still revealed a spectrum of different elongation dynamics, suggesting that animal behavior and elongation dynamics are likely to not be solely controlled by genotype either. Another possibility is that differences in animal behavior and elongation dynamics arise from stochasticity or noise within the population. In other systems, it has been shown that genotype and

environment alone can indeed not explain all inter-organismal variation. For example, in *Drosophila*, animals from inbred lines grown under the same environmental conditions have been found to express variation in behavioral dynamics (Werkhoven et al., 2021). The term ‘stochastic individuality’ describes the phenomenon of behavioral variation between animals that cannot be predicted even when all genetic and environmental information are known (Honegger and de Bivort, 2018). Most likely, these differences largely arise at the molecular level by amplification of small, stochastic fluctuations of protein concentrations (Honegger and de Bivort, 2018). An interesting example is provided by a species of pea aphids (*Acyrtosiphon pisum*), which produces clonal offspring that show remarkable individual variation. When the animals are startled during feeding, some let go of the plant they are feeding on, while others stay and continue feeding. The animals that stay on the plant take a higher risk but have a short-term advantage (more food) if they survive. These animals produce the bulk of their offspring during early life. In contrast, animals that show escaping behavior take a smaller risk and therefore have a higher life expectancy, and they spread out their total offspring over a longer period of time (Schuett et al., 2015). This illustrates two different reproductive strategies in genetically identical animals living under the same conditions. A high variation in behavior may provide an advantage to a species under unpredictable environmental conditions, since it increases the chance that some individuals will be well-matched in order to survive (Honegger and de Bivort, 2018). This could possibly also apply to developing *Nematostella* larvae and the decision whether to settle and develop rapidly, or to stay mobile and develop slowly. Under natural conditions, the advantage of early settlement and fast larva-polyp transition would be that the animal gains the ability to feed earlier. However, prolonged motility might be advantageous under conditions where the local environment is sub-optimal for polyp life and a better environment might be found elsewhere.

### **9.3. How are settlement behavior and muscular hydraulics connected?**

Although *Nematostella* does not require a substrate-based cue to undergo larva-polyp transition, adhesive settlement behavior positively correlates with elongation rate, and disruption of attachment through shaking or upside-down mounting delays development. While motile animals show on average mostly linear development in morphospace, corresponding to simultaneous change in size and shape, sessile animals show a zig-zag-like pattern, in which part of their development involves elongation without substantial volume increase (‘stretching’). The timing of the ‘stretching’ phase overlaps with the switch from swimming to adhesive settlement, suggesting that this behavioral switch creates a ‘kink’ in the otherwise linear trajectory in morphospace. High time resolution recordings revealed that animals show irregular contraction behavior throughout larva-polyp transition, where peristaltic and full body contractions appear more frequently during periods of volume increase, while contractions during ‘stretching’ elongation without volume increase

induce mostly small local body deformations and appear to squeeze the animal. Nevertheless, the details of how exactly muscular hydraulics connects to settlement behavior remain to be further investigated. One hypothesis is that motility and elongation rely on the same muscular hydraulic machinery (**Figure 46**). Shortening of cilia during larva-polyp transition (Fritz et al., 2013) likely decreases their effectiveness for swimming and animals that remain mobile during larva-polyp transition appear to move through a combination of swimming or gliding and contraction-mediated crawling behavior. Possibly, muscle contractions in combination with stable settlement favor a more efficient use of muscular hydraulic forces to increase internal pressure and drive tissue remodeling, while contraction in an unattached state would instead push the animal and contribute to movement. An alternative hypothesis is that settlement triggers a separate response in the animal, that increases muscle contraction throughout the entire body column in order to increase luminal pressure and stretch the tissue. Studies of neural activity during swimming, settling, and contraction behavior may provide clues about how different types of animal behavior relate to different short and long-term body deformations. Furthermore, it would be interesting to investigate whether perturbation of the expression of neuropeptides, which are thought to speed up larva-polyp transition (Nakanishi and Martindale, 2018) alters animal behavior.

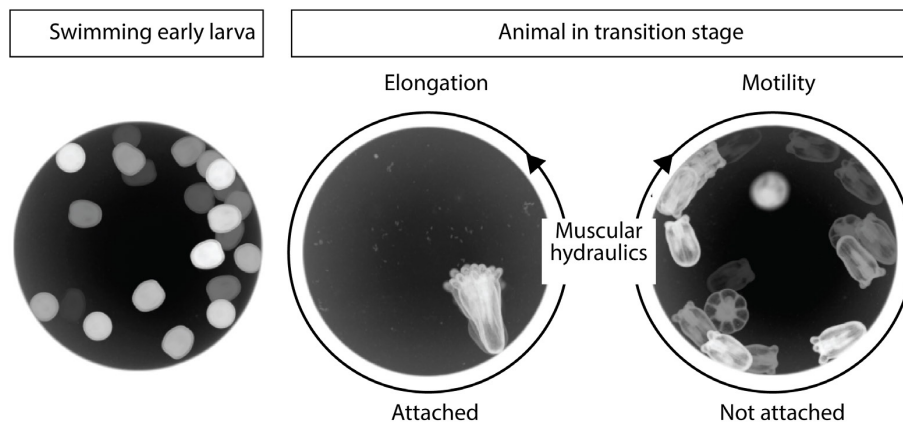


**Figure 46. Schematic model of a potential trade-off between elongation and motility, in which both processes rely on muscular hydraulics.**

#### **9.4. Knockdown of homologs of transcription factors involved in cardiogenesis cause muscle function defects in *Nematostella***

Pharmacological inhibition of muscle contraction inhibited larva-polyp morphogenesis, suggesting that active muscle function is important for development. A shRNA knockdown screen targeting genes involved in muscle and neural development was performed to target the hydrostatic skeleton more specifically. Here, we found several shRNAs that induce a morphological phenotype. The clearest shRNA KD phenotypes all involved knockdown of transcription factors, namely homologs of Nkx2.5, Isl-1, and Tbx20 (Appendix section 11.3), which are known to be involved in

cardiac muscle development in bilaterians (Bodmer, 1993; Chen and Fishman, 2000; Chen et al., 2021; Dorn et al., 2015; Prall et al., 2007; Stennard et al., 2003). Although muscle organization appears normal in *NvNkx2.5* KD animals, peristaltic contractions appear to be reduced and most animals remain as budded larvae or only develop beyond this stage after a strong delay, suggesting a defect in (induction of) muscle function (Appendix 11.3.1). Since shRNA phenotypes can be transient due to time-dependent degradation of shRNA, generation of CRISPR KO animals will make clear whether the 'true' phenotype is a delay in development, or a complete arrest at the budded larval stage (ongoing work by Aissam). In *Hydra*, a homolog of *Nkx2.5* is expressed in the *Hydra* peduncle region, which is associated with body contraction and fluid pumping (Shimizu and Fujisawa, 2003). Although *Nematostella* does not have a heart, it is interesting that knockdown of genes involved in cardiac development in bilaterians appear to induce muscle function defects in *Nematostella* that are also related to contraction and pumping.

### **9.5. How are muscular hydraulics and tissue morphogenesis connected?**

While body cavity inflation is a main driver of organismal size during larva-polyp morphogenesis, organismal shape change depends on cell shape changes and cellular rearrangements. The findings that cavity inflation and tissue morphogenesis are impaired in animals treated with muscle contraction inhibiting drugs and in depressurized animals, suggests that muscular hydraulics are required for these processes. Moreover, perturbation of muscle organization using shRNA KD of *Tbx20* and *BMP2/4* results in two distinct morphological phenotypes: *Tbx20* KD animals have disorganized muscles and inflate their cavity but acquire a rounder morphology than control animals, while *BMP2/4* KD animals lack longitudinal muscles and do not inflate but acquire a long and thin morphology. Cell angles and direction of cellular rearrangements match with the morphology of these animals, suggesting that cellular behaviors are directed by forces that depend on muscle organization and function. These could be forces in the form of hydraulic pressure generated by muscle contractions. As explained by the discussed biophysical model, one possibility is that muscle organization determines tissue stiffness, and that the combination of differential tissue stiffness and pressure generation through priming and pumping by muscular contractions regulate morphogenesis. In this case, similar pressures induce different morphogenetic outcomes due to differential tissue properties. Alternatively, muscle organization might directly determine force anisotropy. Disorganized muscles might be unable to efficiently squeeze the animal, and therefore generate mostly isotropic forces. In contrast, in the absence of longitudinal muscles, the circular muscles may take over entirely and restrict fluid flow to the oral-aboral axis, generating a strong anisotropic force.

A related question to how muscular hydraulic forces may drive tissue elongation, is how termination of elongation is eventually achieved. *BMP2/4* KD animals appear to elongate indefinitely, and continue thinning until they fragment themselves. However, since *BMP2/4* KD results in a very severe phenotype that lacks all inner tissue organization and is not viable, it is unclear if the fragmentation is the result of elongation forces or because the animal is dying. The *BMP2/4* KD phenotype should therefore be interpreted carefully in all aspects. Unfortunately, no shRNA was found that specifically targeted the longitudinal and circular muscles separately. Termination of elongation could be regulated in different ways. One hypothesis is that above a certain limit, tissue resists further thinning and rearrangement, and that the forces generated by the muscular hydraulic machinery are not strong enough to induce any further tissue remodeling. Alternatively, the formation of the aboral pore might create a valve that opens in response to high pressures, essentially depressurizing the animal, such that it cannot generate pressures high enough to induce tissue remodeling any longer. Indeed, at later polyp stage, animals are sometimes observed to suddenly release debris from the aboral end, indicating that they have a functional opening at this stage. Although experimentally challenging, it would be interesting to try to manipulate the timing of aboral pore formation, and see whether this correlates with polyp length.

## 9.6. Outlook

Morphogenesis involves coordination of processes taking place at different scales, guided by local and global forces. Both fluid pressure and muscular forces can act at different scales, and have been shown to be important in many different developing systems, including otic vesicles, cellular cysts and size control in whole embryos (Chan et al., 2019; Mosaliganti et al., 2019; Ruiz-Herrero et al., 2017), gut elongation (Khalipina et al., 2019) and muscle fiber alignment (Huycke et al., 2019) and organismal elongation in *C. elegans* embryos (Lardennois et al., 2019; Zhang et al., 2011). The findings presented here show that the combination of muscle action and associated fluid forces is critical for larva-polyp morphogenesis and suggest a mechanism in which the hydrostatic skeleton facilitates animal behavior, such as motility, cavity inflation and deflation, and (defensive) contractions, on short time scales, while simultaneously generating forces that drive morphogenesis on long time scales. Here, muscle contractions are transmitted through the hydrostatic skeleton, regulating fluid pressure and distribution, and thereby act as long-range forces that drive morphogenesis by coordinating cellular dynamics across the entire animal. Since hydrostatic skeletons are ubiquitous in marine invertebrates (Kier, 2012), and cnidarians know a wide range of polyp sizes and shapes (Leclère and Röttinger, 2017; Leclère et al., 2016b), it would be interesting to compare muscle organization, body movements, and cellular morphogenetic motifs during polyp morphogenesis across different species. This could help identify if muscular hydraulic forces combined with differential contractility or stiffness in the azimuthal and axial direction are

commonly used across cnidarian species, and if variations in the use of muscular hydraulics correlate with different size-shape relationships observed across Cnidaria. Furthermore, since tubes form the basis for many organs in bilaterians, and the body column of *Nematostella* shares some similarities with the bilaterian heart and gut in terms of gene expression and muscle organization, elucidating principles that apply in *Nematostella* may also help gain further understanding of organ morphogenesis and function.





## 10. Materials and Methods

The sections 10.4, 10.7-10.9, 10.11, 10.13 and 10.15 are included as Materials and Methods sections in a pre-publication of the manuscript on BioRxiv (Stokkermans et al., 2021) and are reproduced here for completeness of the thesis. These sections are entirely my own words and have been written solely by myself. I have made small modifications or additions to parts of the sections here. Sections 10.1-10.3, 10.6, and 10.10 are adapted versions from the sections in the Materials and Methods in (Stokkermans et al., 2021), and are also entirely my own words.

### 10.1. Animal husbandry

Adult *Nematostella* were maintained at 17 °C in the dark in 12 ppt ASW (sea salt; instant ocean) in a circulating system. Spawning was induced every three weeks, by exposing the animals to light for six hours, using a light box with a temperature of 28 °C and a light intensity of 250–300 lumen per square foot (Genikhovich and Technau, 2009). Spawning followed within three to four hours after a cold-water (17 °C) change.

### 10.2. High-throughput live imaging

Mid-stage larvae (typically at 3 days post fertilization) were individually placed in the wells of a 384 well plate (Corning, 3540) containing 25 µl 12 ppt ASW using a glass mouth pipet. Imaging was performed using an Acqifer screening microscope with a 4x magnification objective, with brightfield channel (20% intensity), at 27 °C for three to seven days. Per experiment, 200 animals could be imaged at a time resolution of five minutes. To record short-lived contraction behavior, individual animals were imaged at a time interval of five seconds.

### 10.3. Data analysis of live animals

All image analyses were performed using FIJI (<https://imagej.net/software/fiji/>) (Schindelin et al., 2012). The FIJI Jython script described in Chapter 5 makes use of several FIJI plugins, including 'AnalyzeSkeleton' (Arganda-Carreras et al., 2010), MorphoLibJ (Legland et al., 2016) and the BioFormats plugin (Linkert et al., 2010).

The windowed sinc filter function from the pyBOAT package (Mönke et al., 2020) was used to calculate smoothed curves from the raw measurements of circularity, body length, average body width, and estimated body column volume. This function can be used to filter out components in the frequency domain that have a frequency above a given threshold. By varying the threshold, the data can be smoothed to different extents. Empirically, a cut-off frequency of 500 minutes was found to

give a good general smoothing for five-minute time resolution data. For determining animal stage, a cut-off frequency of 1000 minutes was used, because this relies on the global trend only.

To estimate body column volume, the body column is subdivided into cylinders with a height of 1 pixel, and a radius depending on the local body column width. The volumes of these cylinders are summed up, and the volumes of two half spheres at the two extremities are added, such that the total estimated volume is given by:

$$V = 0.5 * \left(\frac{4}{3}\pi * r_1\right)^3 + 0.5 * \left(\frac{4}{3}\pi * r_n\right)^3 + \sum_{i=1}^n \pi * r_i^2 * pixel\ size,$$

where  $r_1$  is the radius at the oral pole and  $r_n$  is the radius at the aboral pole, and  $n$  indicates the number of pixels belonging to the body column skeleton (**Figure 14**).

To define different morphodynamics, the time differences of smoothed aspect ratio and estimated body column volume (cut-off period of 500 minutes) were used. The values were truncated at the 5<sup>th</sup> and 95<sup>th</sup> percentiles and normalized to fall between -1 and 1, where 0 means no change and 1 corresponds to the value of the 95<sup>th</sup> percentile. Negative scores indicate a decrease in aspect ratio or volume. To define the different morphodynamics, a cut-off value of +0.2 was used, such that 'stretching' is defined by a normalized aspect ratio change  $\geq 0.2$  and body column volume change  $< 0.2$ , 'inflating' is defined by normalized aspect ratio change  $< 0.2$  and body column volume change  $\geq 0.2$ , and 'combined stretching and inflating' is defined by normalized aspect ratio change and body column volume change  $\geq 0.2$ . If none of these criteria are met, the morphodynamics at that given time point is labeled 'no elongation' to indicate that the animal either decreased or did not substantially increase in aspect ratio and/or volume.

Cut-off periods of 83 minutes, 167 minutes, and 500 minutes were used to calculate morphodynamics in five-second time resolution data. It is important to note that morphodynamics are calculated based on the differentiation of the smoothed animal body column volume and aspect ratio, and are therefore directly dependent on the level of smoothing. Light smoothing preserves behavioral changes, but complicates interpretation on the long time scale. In contrast, heavy smoothing removes all behavioral fluctuations and only leaves the trend intact. Therefore, an animal can appear to undergo different morphogenetic changes, depending on the level of smoothing and how far one zooms in on the data.

To detect contractions in five-second time resolution data, I subtracted the global trend of circularity (smoothing with 167-minute cut-off period) from the original circularity measurements that contain short-lived fluctuations (smoothed with 40-second cut-off period to reduce noise). I took the absolute value of this detrended 'behavioral' circularity, and applied a rolling sum kernel with a

window size of 50 seconds to further reduce noise and detect peaks in short-lived changes of circularity. Since the change in circularity is dependent on absolute circularity (larvae have a rounder shape in general, and they undergo smaller changes in circularity, in absolute sense), I multiplied the raw contraction score by the long time scale (developmental) circularity. The resulting contraction score is a semi-quantitative feature that gives an idea about the intensity of shape change at short time intervals. However, it is important to keep in mind that it will detect any kind of circularity change, and is thus sensitive to artifacts resulting from animal swimming behavior (rotations and tumbling in early larvae) or measurement errors.

Body column diameter kymographs were generated by plotting the body column diameter for every pixel along the body column, over time. Since diagonally positioned pixels have a different distance than vertically or horizontally aligned pixels, the exact body column position in  $\mu\text{m}$  for each pixel is unknown. Therefore, these plots show the non-calibrated oral-aboral axis in pixels. The body column length estimates take curvature of the body column into account and therefore show the calibrated body column length in  $\mu\text{m}$ .

#### **10.4. Optical coherence microscopy and data processing**

Microscopy setup and data acquisition were performed by Ling Wang and Kaushikaram Subramanian (Ikmi and Prevedel labs, EMBL Heidelberg). For methods description, please refer to (Stokkermans et al., 2021). Data analysis was performed by me with input from Kaushikaram Subramanian.

The raw OCM images were post-processed by applying a median filter with 2-pixel width, followed by rescaling in order to correct axial and lateral voxel dimensions. Alignment was performed using FijiYama (automatic registration, block matching, default settings) (Fernandez and Moisy, 2020). The two views were combined into a single volume and segmented into tissue and cavity using the trainable WEKA segmentation FIJI plugin (Arganda-Carreras et al., 2017). Tissue volume and cavity were calculated from the segmented masks using the `IntrinsicVolumes3D` function from the `MorpholibJ` package (Legland et al., 2016). 3D views were created with VolumeViewer (2.01) (Barthel, 2012) (<https://imagej.nih.gov/ij/plugins/volume-viewer.html>).

#### **10.5. Pressure measurements**

This work has been performed and described by Prachiti Moghe (Hiragi lab, EMBL Heidelberg). For description, please refer to (Stokkermans et al., 2021).

#### **10.6. Pharmacological treatments**

To test the role of cell proliferation, I treated budded larvae with 5 mM HU (Sigma, h8627) in ASW, while control animals were incubated in 12 ppt ASW. For high-throughput imaging, animals were transferred to a 384 well-plate containing either 25  $\mu$ l 5 mM HU or 25  $\mu$ l 12 ppt ASW. Animal development was recorded following the imaging strategy on the Acquirer microscope. For immunostaining, animals were kept in glass dishes at 27 °C and were fixed after 3 or 24 hours of incubation.

To test the role of muscle contraction, animals were incubated in glass dishes for three days with one of the following muscle inhibiting drugs: 1 mM linalool (Goel et al., 2019) (Sigma, L2602) with 0.03% DMSO, 400  $\mu$ M menthol (Abrams et al., 2015; Batham and Pantin, 1950a) (Sigma, M2772), with 0.1% DMSO, 0.5% MgCl<sub>2</sub>, or 0.5 mM rocuronium bromide (Khuenl-Brady and Sparr, 1996) with 0.2% DMSO (Sigma, R5155). As a control, animals were incubated in either 12 ppt ASW or 12 ppt ASW with 0.2% DMSO. All dishes were sealed with parafilm to prevent evaporation of the volatile drugs. Drug solutions were not refreshed. Body length was measured by drawing a segmented line from the oral to the aboral pole in the mid-section plane of the animal. Area of body cavity and internal tissues in the mid-section plane was measured manually in FIJI.

For the *BMP2/4* KD experiment in combination with inhibition of muscle contraction, I injected fertilized eggs with *BMP2/4* shRNA (550 ng/ $\mu$ l) and fixed them either after two days ( $t_0$ ) or first incubated them in 0.1% DMSO (control), 400  $\mu$ M menthol with 0.1% DMSO, or 1 mM linalool with 0.03% DMSO, for four days prior to fixation.

## **10.7. Fixation and immunostaining**

“Animals were anesthetized in 7% MgCl<sub>2</sub> prior to fixation. Fixation was performed for one hour at room temperature with either 4% paraformaldehyde (EMS, E15710) in PBS with 0.1% Tween (PTw 0.1%, Sigma, P1379) for phosphorylated histone 3 antibody staining (Chen et al., 2020) (pH3, Sigma # 05-806, 1:100), or with Lavdovsky’s fixative (3.7% formaldehyde, 50% ethanol, 4% acetic acid) for Cadherin3 antibody detection (gift from Technau lab (Pukhlyakova et al., 2019), 1:500). Animals were permeabilized in 10% DMSO (Thermo Fisher, 85190) in PBS for 20 minutes and washed with PBS with 0.2% Triton (Sigma, T8787) (PTx 0.2%), followed by one-hour incubation in blocking buffer (PTx 0.1%, 0.1% DMSO, 1% BSA (Sigma, A2153), and 5% Goat serum (Sigma, G9023)). Samples were incubated with the primary antibody in blocking solution overnight at 4 °C. After washing with PTw 0.1%, animals were incubated with the secondary antibody goat-anti-mouse Alexa-488 (Thermo Fisher, A-11001, 1:500) or donkey-anti-mouse Alexa-488 (Thermo Fisher A21202, 1:500) in PTx 0.1% overnight at 4 °C. For (additional) staining for F-actin and nuclei, phalloidin Alexa Fluor 546 (Thermo Fisher, A22283, 1:100) and Hoechst 34580 (Sigma, 63493,

1:1000) were used, in PTx 0.1% overnight at 4 °C. Finally, animals were washed in PTw 0.1% and cleared in 80% glycerol (Merck).” From (Stokkermans et al., 2021).

### **10.8. Confocal imaging**

“Samples were imaged using a Zeiss LSM 780 confocal inverted microscope with Plan-Apochromat 20x/0.8 objective, or using a Zeiss LSM 880 point scanning confocal microscope controlled with the Zeiss Zen 2.3 (black edition) software, with Plan-Apochromat 20x/0.8 air objective. To image ectodermal cells, I used a Plan-Apochromat 40x/1.4 Oil DIC objective, AiryFast mode and tile scans, at 0.5 µm z-resolution. Depending on the staining, the laser lines diode 405 nm, argon multi-line 458/488/514 nm and/or HeNe 561 nm were used.” From (Stokkermans et al., 2021).

### **10.9. Quantification of cellular properties**

“The number of pH3 positive-mitotic cells was counted manually in FIJI and normalized to the imaged tissue volume. Epidermal thickness was measured manually in images of the mid-section plane of the animal at multiple locations along the body axis. For average epidermal thickness, measurements were taken in the mid-body region between 30% and 70% of the total length of the oral-aboral axis. Quantifications of the cell apical surface area and angle with respect to the body axis were based on images of samples stained with phalloidin or with Cdh3 antibody. These images were captured using the LSM880 confocal microscope with a 40x magnification objective. To correct for the typical uneven surface of the animals and the body column deflation upon addition of glycerol, the Minimum cost Z surface projection FIJI plugin (Li et al., 2006; Lombardot, 2017, available at [https://imagej.net/Minimum\\_Cost\\_Z\\_surface\\_Projection](https://imagej.net/Minimum_Cost_Z_surface_Projection)) was used to obtain separate, flattened layers for the ectoderm tissue and the underlying muscular tissue. Next, one or more flattened slices showing cell boundaries were selected and used as input for detection of cells using Cellpose (Stringer et al., 2021) (2D mode, model-type cytoplasm). The mask produced by Cellpose was converted to a label image and was manually corrected. For phalloidin staining in polyps, correctly segmented cells were manually selected. Cell area, ellipse elongation and orientation were obtained using the MorphoLibJ package (Legland et al., 2016). To calculate the cell angles with respect to the body axis, a line was drawn from the oral to the aboral pole along the midline of the animal. Angles for each location on this line were calculated for 10-pixel segments. For each cell, the nearest position on the line was determined, and the angle of the oral-aboral line at this point was used as a reference angle to compare to the cell’s angle.” From (Stokkermans et al., 2021).

Muscle fiber number, thickness, and coverage were measured from the binarized muscle layer images, which were segmented using Weka segmentation. The Directionality FIJI plugin was used to measure fiber orientation.

## 10.10. shRNA design and synthesis

Performed together with Aissam Ikmi and Omar Matar (EMBL Heidelberg)

shRNAs were designed based on (He et al., 2018) and using the siRNA Wizard from Invivogen (available at [https://www.invivogen.com/sirnazard/design\\_advanced.php](https://www.invivogen.com/sirnazard/design_advanced.php)). Additionally, I wrote an R script to facilitate primer motif searches in the cDNA to meet more specific requirements: 19-20 bp length, starting with at least 2 Gs (important for transcription with T7 polymerase), a GC content between 40-55%, an A or T at the 3' end of the sense strand, no stretches of 4+ T, or 6+ G/C, or palindromes, present as single copy in the entire transcriptome.

Primers were synthesized by Sigma and IDT. Primers were annealed at 98 °C for 5 min in the PCR machine or heat block and allowed to cool down to room temperature. shRNA was synthesized using the T7 MegaShortScript kit (Invitrogen, AM1354) with an incubation time of six hours, followed by a purification step using magnetic SPRISelect beads (Beckman Coulter B23319) in the presence of 46% isopropanol (Fishman et al., 2018). Samples were incubated for 15 minutes at room temperature, and were subsequently placed in magnetic stands for five minutes, until the solution appeared clear. The samples were washed twice using 80% freshly prepared ethanol, after which they were shortly dried and resuspended in RNase free water. The solution was aliquoted and stored at -80 °C.

Used primers:

### **GFP shRNA**

(forward) TAATACGACTCACTATAGGGGCACAAGCTGGAGTACAATTCAAGAGATTGTACTCCAGCTTGTGCCCTT

(reverse) AAGGGCACAAGCTGGAGTACAATCTCTTGAATTGTACTCCAGCTTGTGCCCTATAGTGAGTCGTATTA

### **Tbx20 shRNA**

(forward) TAATACGACTCACTATAGGGAACAGCTGCTTAAACATTCAAGAGATGTTTAAGCAGCTGTTCCCTT

(reverse) AAGGGAACAGCTGCTTAAACATCTCTTGAATGTTTAAGCAGCTGTTCCCTATAGTGAGTCGTATTA

### **BMP2/4 shRNA**

(forward) TAATACGACTCACTATAGGACTGGATATTCAAGTGATTCAAGAGATCACTTGAATATCCAGTCCTT

(reverse) AAGGACTGGATATTCAAGTGATCTCTTGAATCACTTGAATATCCAGTCCTATAGTGAGTCGTATTA

### **Nkx2.5 shRNA**

(forward) TAATACGACTCACTATAGGGTATGGAGTCGTGGTATTTCAAGAGAATACCACGACTCCATACCCTT

(Reverse) AAGGGTATGGAGTCGTGGTATTCTCTTGAATACCACGACTCCATACCCTATAGTGAGTCGTATTA

#### **Isl-1 shRNA**

(forward) TAATACGACTCACTATAGGGCCGATCACGAAATTGTATTCAAGAGATACAATTTTCGTGATCGGCCTT

(reverse) AAGGCCGATCACGAAATTGTATCTCTTGAATACAATTTTCGTGATCGGCCCTATAGTGAGTCGTATTA

### **10.11. Microinjection of shRNAs**

“Unfertilized eggs were dejellied in 4% cysteine solution (Sigma, 168149) in ASW for nine minutes and washed with ASW. Eggs were then fertilized and injected with shRNA using a Femtojet Express (Eppendorf). shRNA (500 and 1500 ng/μl), targeting GFP, *Tbx20*, or *BMP2/4* mRNA, was mixed with Texas Red-labelled Dextran (ThermoFisher, D3328) to label injected eggs. Embryos were kept at room temperature and transferred to 27 °C the following day.” From (Stokkermans et al., 2021).

### **10.12. CRISPR/Cas9**

This work has been performed and described by Aissam Ikmi (EMBL Heidelberg). For description, please refer to (Stokkermans et al., 2021).

### **10.13. Photo-conversion of Kaede**

Kaede mRNA synthesis was performed by Stephanie Cheung (Ikmi lab, EMBL Heidelberg)

mRNA was synthesized using the HiScribe™ T7 ARCA mRNA Kit (with tailing) (NEB, E2060S) and a PCR product amplified from the Kaede-NLS plasmid (addgene, 57319). Following mRNA purification with magnetic SPRIselect beads (Beckman Coulter B23319), fertilized eggs were co-injected with a solution mix containing Kaede-NLS mRNA (200 ng/μl), shRNA targeting *BMP2/4* (430 ng/μl) or *Tbx20* (560 ng/μl), and FITC (ThermoFisher, 46425). Control embryos were only injected with Kaede-NLS mRNA and FITC. Photo-conversion of Kaede (Ando et al., 2002) was performed on anesthetized larvae (using MgCl<sub>2</sub>) on a Zeiss LSM 780 microscope with Plan-Apochromat 20x/0.8 objective, using the ‘bleaching’ and ‘regions’ option, and using the 405 nm laser at 0.6% laser power, with 80 iterations. Imaging of developed animals after photo-conversion was performed on a Zeiss LSM 780 or 880, with Plan-Apochromat 20x/0.8 objective. Stripe aspect ratios and animal body column aspect ratios were manually measured using FIJI. Description adapted from (Stokkermans et al., 2021).

## **Biophysical manipulation**

This experiment was performed by Aissam Ikmi (EMBL Heidelberg). For description, please refer to (Stokkermans et al., 2021).

### **10.14. Data analysis**

All image analysis was performed using FIJI (Schindelin et al., 2012). Data analysis and generation of plots was performed in RStudio version 1.1.442 (R Core Team, 2019; RStudio Team, 2015), making use of the tidyverse (Wickham et al., 2019), ggplot2 (Wickham, 2009), ggpubr (Kassambara, 2020), gtable (Wickham and Pedersen, 2019), and ggrastr (Petukhov et al., 2020) packages and Prism 8. Wilcoxon rank sum tests were used for significance testing, unless mentioned otherwise. The forecast package (Hyndman et al., 2008, 2020) was used to remove outliers in time sequence data and the zoo package (Zeileis and Grothendieck, 2005) was used to calculate the rolling sum in time series data. Description adapted from (Stokkermans et al., 2021).

### **10.15. Biophysical model and balloon experiments**

This work was performed by Aditi Chakrabarti and L. Mahadevan (Harvard). For description please refer to (Stokkermans et al., 2021).

### **10.16. Studying environmental impact on larva-polyp transition**

To study the effect of increased and decreased salinity, larvae were incubated in 4, 8, 12, or 36 ppt ASW in glass dishes or in a 384-well plate. To study the effect of increased seawater viscosity, larvae were incubated in dishes containing 1% methylcellulose solution (Sigma, 9004-67-5\_M0387), or in 384-well plates containing 25  $\mu$ l 1% MC or 12 ppt seawater, and development was recorded at 27 °C in the Acquirer microscope. To perturb settlement, larvae were kept in dishes on the heat block shaker, or were mounted upside down on glass slides and sealed with grease to minimize evaporation. Images were taken daily using a stereo microscope with camera. To study the effect of light exposure, developing animals were recorded before, during and after exposure to 470 nm LED light (100% intensity, for approximately 12 seconds) in the Acquirer microscope.



# 11. Appendix

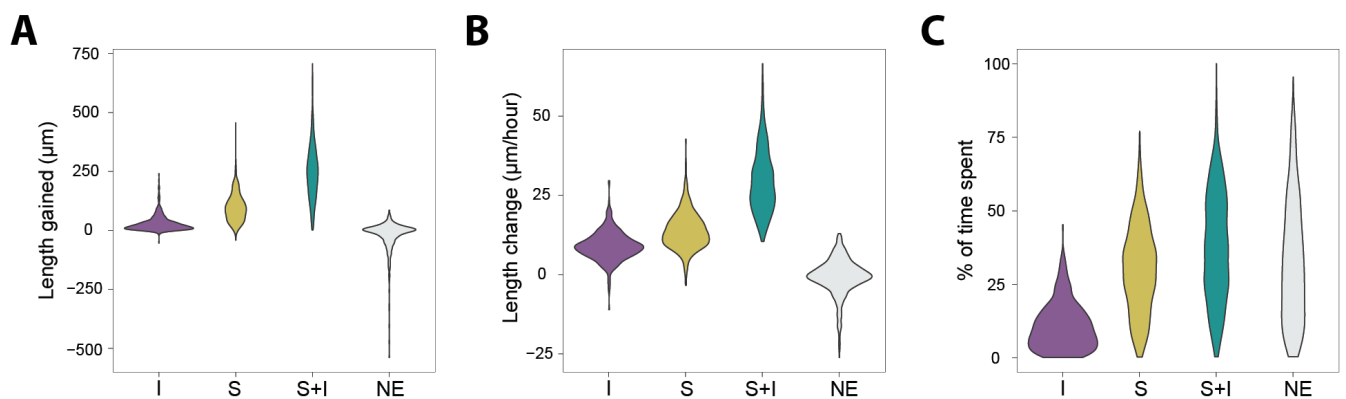
## 11.1. Dynamics of larva-polyp transition in *Nematostella*

**Appendix Table 1. Summary statistics of animal body column length, aspect ratio, and volume at polyp stage.**

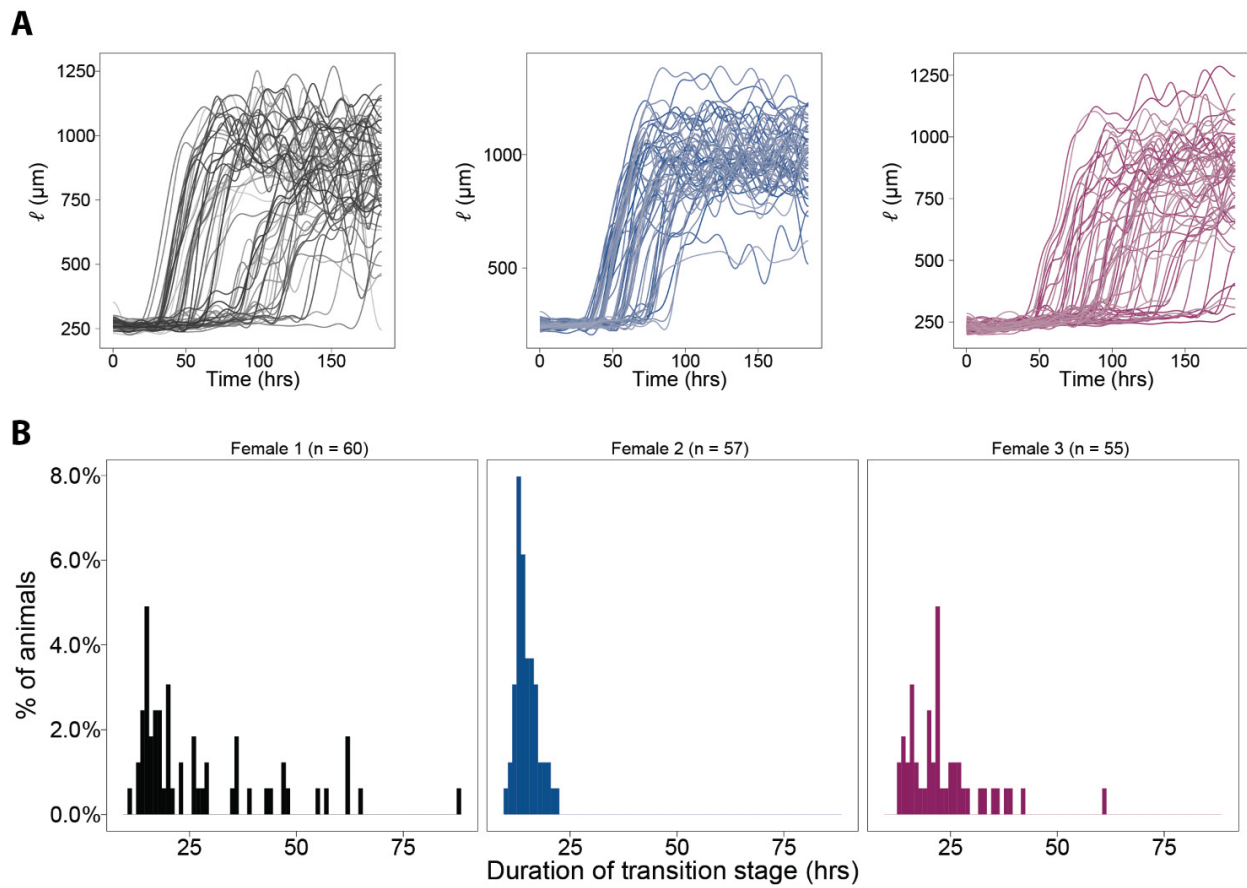
	Mean	Standard deviation	Fold change (w.r.t. larva)
Body column length ( $\mu\text{m}$ )	808.3	166.5	3.2
Aspect ratio	5.3	1.2	4.0
Body column volume ( $\mu\text{m}^3$ )	1.3E7	3.3E6	2.4

**Appendix Table 2. Summary statistics of different morphodynamics during larva-polyp transition**

Morphobehavior	Inflating	Stretching	Combined stretching and inflating	No elongation
Average volume gained ( $\mu\text{m}^3$ )	1.31E+06	-3.96E+05	4.71E+06	-7.85E+05
St. dev volume gained ( $\mu\text{m}^3$ )	1.42E+06	9.05E+05	2.61E+06	1.60E+06
Average aspect ratio gained	0.02	1.00	1.53	-0.06
St. dev aspect ratio gained	0.14	0.57	0.71	0.42
Average length gained ( $\mu\text{m}$ )	29.75	96.76	245.89	-19.95
St. dev. length gained ( $\mu\text{m}$ )	33.58	57.88	112.75	61.14
Average relative time spent	10.84	30.15	37.73	32.71
St. dev. relative time spent	7.94	14.67	18.36	20.55
Average body length change ( $\mu\text{m}/\text{hour}$ )	9.03	13.81	29.56	-0.65
St. dev. body length change ( $\mu\text{m}/\text{hour}$ )	4.48	5.71	9.98	5.72



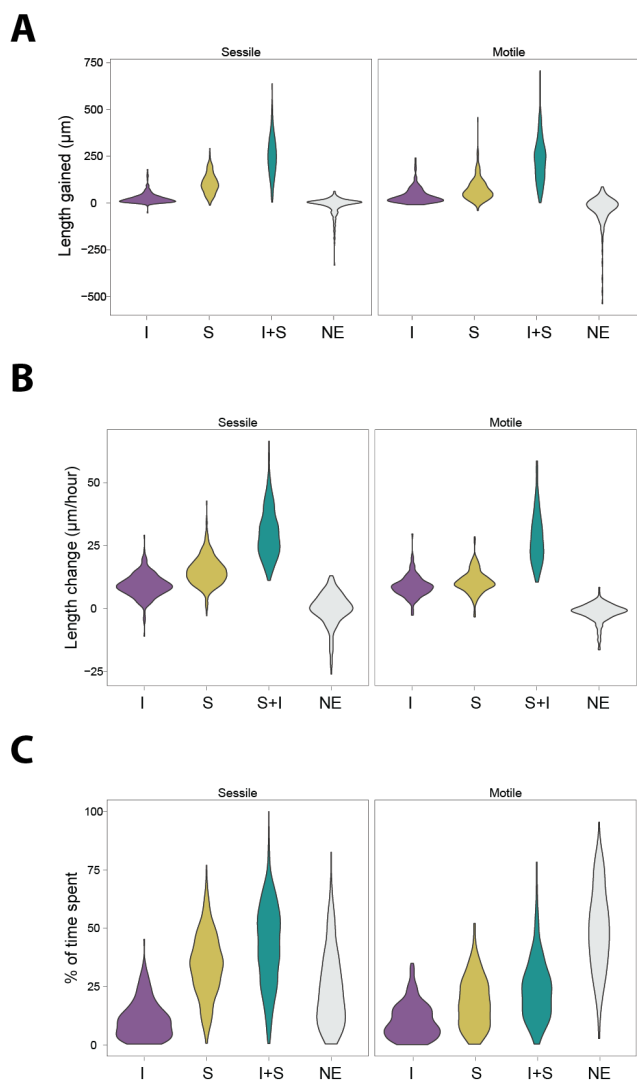
**Appendix Figure 1. Summary statistics for different morphodynamics during the transition stage. A. Total body column length gained. B. Body length change per hour. C. Relative time spent.**



**Appendix Figure 2. Variability in animal length and duration of the transition stage in animals from the same parents. A-B.** Animal length (A) and duration of transition stage (B) in animals developed from eggs from three different females, fertilized with sperm from the same male (female 1: n = 60, female 2: n = 57, female 3: n = 55).

**Appendix Table 3. Morphodynamics in sessile and motile animals.**

Morphodynamics	Inflating		Stretching		Combined stretching and inflating		No elongation	
	Sessile	Motile	Sessile	Motile	Sessile	Motile	Sessile	Motile
Settlement								
Average volume gained ( $\mu\text{m}^3$ )	1.09E+06	1.72E+06	-4.20E+05	-3.28E+05	4.67E+06	4.81E+06	-5.05E+05	-1.34E+06
St. dev volume gained ( $\mu\text{m}^3$ )	1.04E+06	1.89E+06	9.10E+05	8.89E+05	2.51E+06	2.88E+06	1.04E+06	2.26E+06
Average aspect ratio gained	0.02	0.02	1.07	0.82	1.58	1.39	-0.05	-0.10
St. dev aspect ratio gained	0.12	0.17	0.52	0.67	0.69	0.75	0.31	0.56
Average length gained ( $\mu\text{m}$ )	25.29	38.33	104.82	74.17	249.93	234.23	-12.71	-34.26
St. dev. length gained ( $\mu\text{m}$ )	27.77	41.34	54.09	62.17	107.84	125.49	45.33	82.38
Average relative time spent	11.07	10.41	34.31	18.47	42.47	24.05	24.31	49.33
St. dev. relative time spent	8.15	7.55	13.58	10.85	17.44	13.46	16.17	18.06
Average body length change ( $\mu\text{m}/\text{hour}$ )	9.13	8.84	14.95	10.62	30.06	28.11	-0.16	-1.62
St. dev. body length change ( $\mu\text{m}/\text{hour}$ )	4.60	4.24	5.66	4.52	9.90	10.09	6.45	3.72

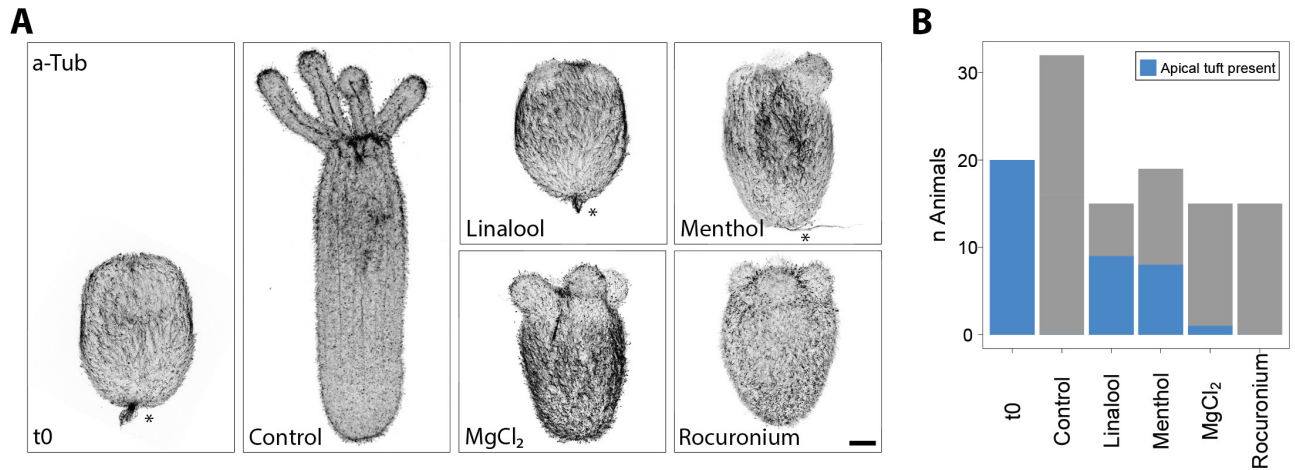


**Appendix Figure 3. Summary statistics for the different morphodynamics for sessile and motile animals during the transition stage. A.** Total body column length gained. **B.** Body column length change per hour. **C.** Relative amount of time spent.

**Appendix Table 4. Morphodynamics and animal behavior measured at 5-second time resolution.**

Morphodynamics	Cut-off period	Aspect ratio change (per hour)	Volume change ( $\mu\text{m}^3$ per hour)	Contraction score (per hour)	Displacement ( $\mu\text{m}$ per hour)
Inflating	167 min	-0.06	754831.96	14.96	6699.57
Stretching	167 min	0.28	-126256.47	10.96	3971.17
Combined stretching and inflating	167 min	0.33	901881.35	13.64	3813.76
No elongation	167 min	-0.09	-196218.79	12.50	6481.85

## 11.2. Effect of pharmacological inhibition of muscle function on loss of apical tuft



**Appendix Figure 4. Presence of apical tuft in drug-treated animals and controls.** **A.** Confocal maximum intensity images of animals stained with an antibody targeting acetylated tubulin, visualizing cilia. At the larval stage, animals possess an apical tuft. This structure is maintained in some of the drug-treated animals. **B.** Quantification of the presence of the apical tuft in drug-treated animals and controls. Scale bar: 50  $\mu$ m.

### **11.3. shRNA knockdown screening experiments**

shRNA KD screening results are summarized in Appendix Table 5. In some cases, phenotypes were unclear or were inconsistent, for example for shRNA targeting *NvRax* and *NvHand1* which potentially lead to an increased occurrence of misdevelopment of the tentacles and sometimes body column. In such cases, the phenotype is indicated as 'maybe' in Appendix Table 5. In other cases, the phenotype was more stereotypic, for example for knockdown of *NvDsh*, which resulted in animals with a flat, wide appearance with tiny tentacles. Interestingly, the phenotype of *NvDsh* knockdown was clearest during early larva-polyp transition, and many animals recovered during later development, indicating that whether or not a phenotype is found may depend on both the developmental stage and the exposure time of the shRNA until it is degraded.

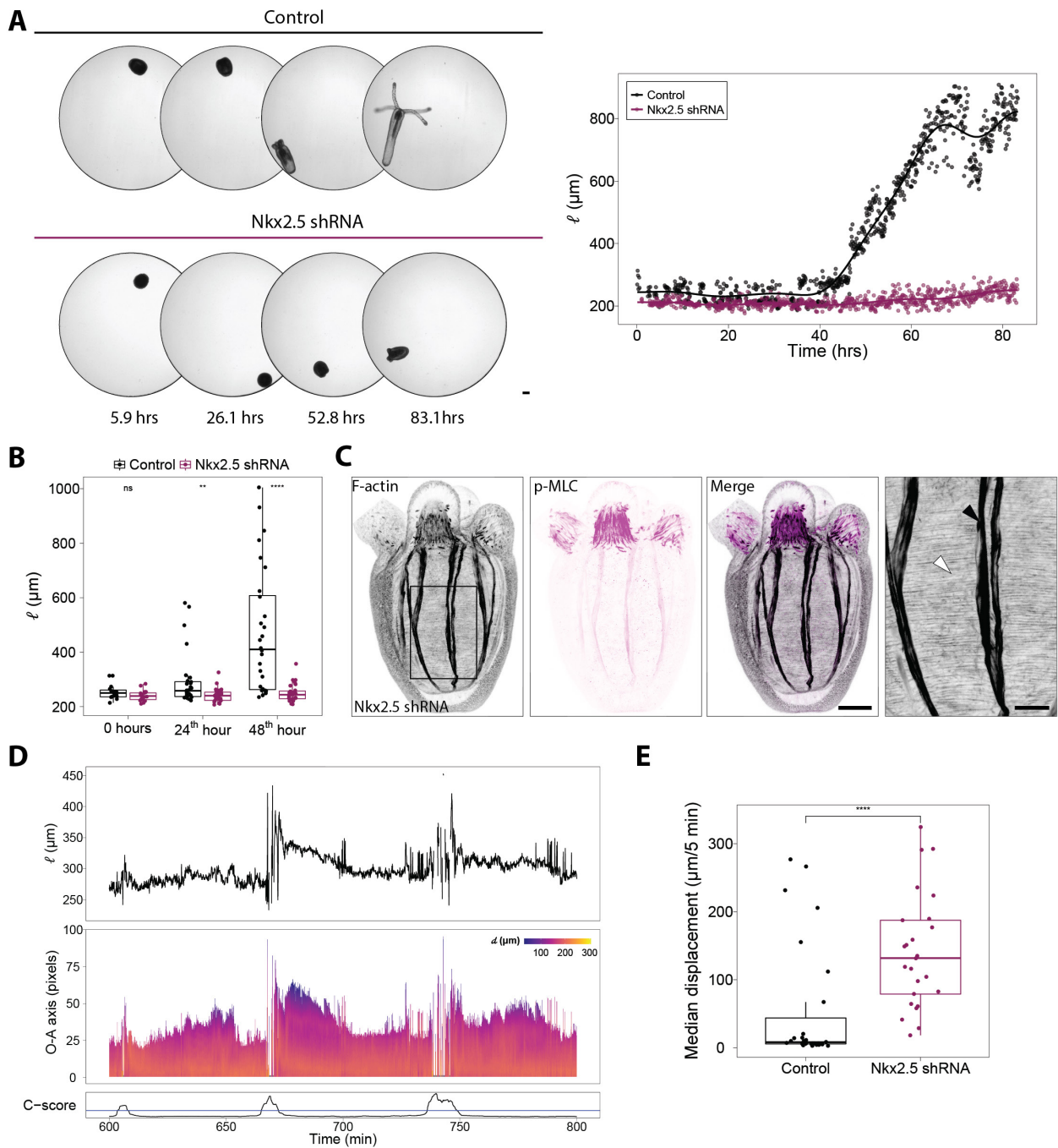
**Appendix Table 5. List of gene targets and phenotypes of shRNA KD.**

Gene	Target	Phenotype	Description
Hlxb9	Neuronal	No	
Islet	Muscle/Neuronal	Yes	Delayed development
SoxB2	Neuronal	No	
Rax	Neuronal	Maybe	Increased occurrence of tentacle and body column defects
Rough	Neuronal	No	
Dlx	Neuronal	No	
HLXb	Neuronal	No	
Elav1	Neuronal	No	
Elav2	Neuronal	No	
Nova1	Neuronal	Yes	Defects in body column and tentacle elongation, wrinkled morphology
anthoRFamide	Neuropeptide	No	
LWamide	Neuropeptide	No	
RFamideI	Neuropeptide	To test	
RFamideII	Neuropeptide	To test	
RWamide	Neuropeptide	To test	
Gata	Muscle	Maybe	Delayed development
Hand2	Muscle	No	
Hand1	Muscle	Maybe	Misdevelopment of tentacles and body column
MuscleLIM	Muscle	No	
Nkx2.2C	Muscle	No	
Nkx2.5	Muscle	Yes	Impaired/delayed elongation
Stmyosin	Muscle	No	
Tbx1.10-1	Muscle	No	
Tbx1.10-2	Muscle	No	
Tbx20	Muscle	Yes	Wide (aboral) body column
Mrlc2	Muscle	No	
Mrlc3	Muscle	No	
Tropomyosin	Muscle	No	
Calponin	Muscle	No	
FoxD.1	Muscle	No	
FoxD.2	Muscle	No	
Sox3	Muscle	Yes	Segmentation defects
SoxE1	Muscle	To test	
Lbx	Muscle	No	
Melc4	Muscle	No	
Klf12	Muscle	No	
SoxE.2	Muscle	To test	
Pkl1	PCP	To test	
Pkl2	PCP	No	
Dsh	PCP	Yes	Flattened, short body column
Vangl	PCP	Maybe	Delayed development
Daaf1	Motile cilia	No	
Dyh9	Motile cilia	To test	
Gas8	Motile cilia	To test	
BMP	Axial patterning	Yes	Loss of directive axis, long and thin body column

### 11.3.1. Knockdown of *Nkx2.5* and *Isl-1* affects elongation dynamics and settlement behavior

*Nkx2.5*, also known as *Nk4* and *tinman*, is an important regulator of cardiomyocyte differentiation and development in bilaterians (Bodmer, 1993; Chen and Fishman, 2000). In *Nematostella*, *Nkx2.5* is expressed in both ectoderm and endoderm of the lower half of the body (Steinmetz et al., 2017). Knockdown of *Nkx2.5* in *Nematostella* appears to arrest animals at late budded larval stage, at which the animals have acquired tentacle buds but have not elongated their body column (**Appendix Figure 5A, B**). In some cases, larva-polyp transition still takes place, but is strongly delayed. Interestingly, although muscle organization appears normal (**Appendix Figure 5C**), knockdown of *Nkx2.5* seems to affect contraction behavior. Whereas normal sporadic longitudinal contractions (**Appendix Figure 5D**) and response to touch can be observed, peristaltic ‘pumping’ contractions produced by the circular muscles seem largely absent or only appeared in a mild form and with a strong delay (7 days post fertilization at 27 °C, compared to wild-type animals that start contracting around 4 days post fertilization). Interestingly, *CnNk-2*, a homolog of *Nkx2.5*, is expressed in the *Hydra* peduncle region, which is associated with body contraction (Shimizu and Fujisawa, 2003). It has therefore been suggested that a common origin may be shared between the peduncle region in *Hydra* and the heart in bilaterians (Shimizu and Fujisawa, 2003). Apart from a delay in development and reduced contractility, *Nkx2.5* knockdown animals also do not show characteristic settlement behavior (**Appendix Figure 5E**).

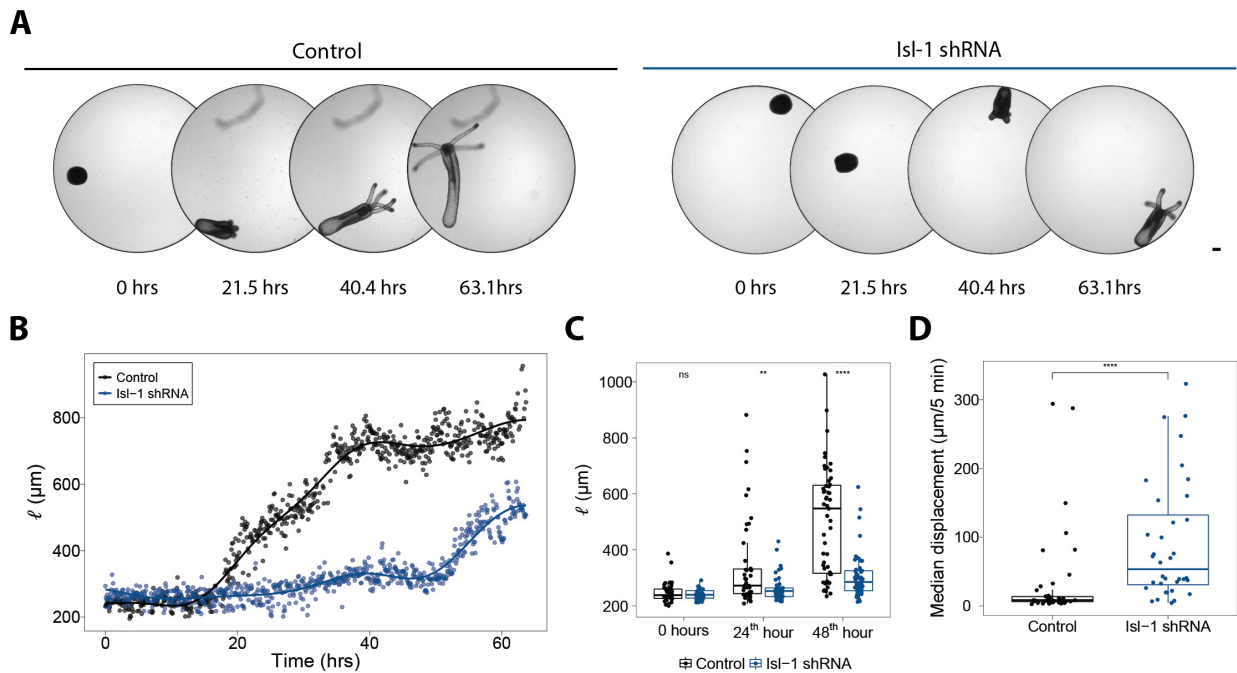




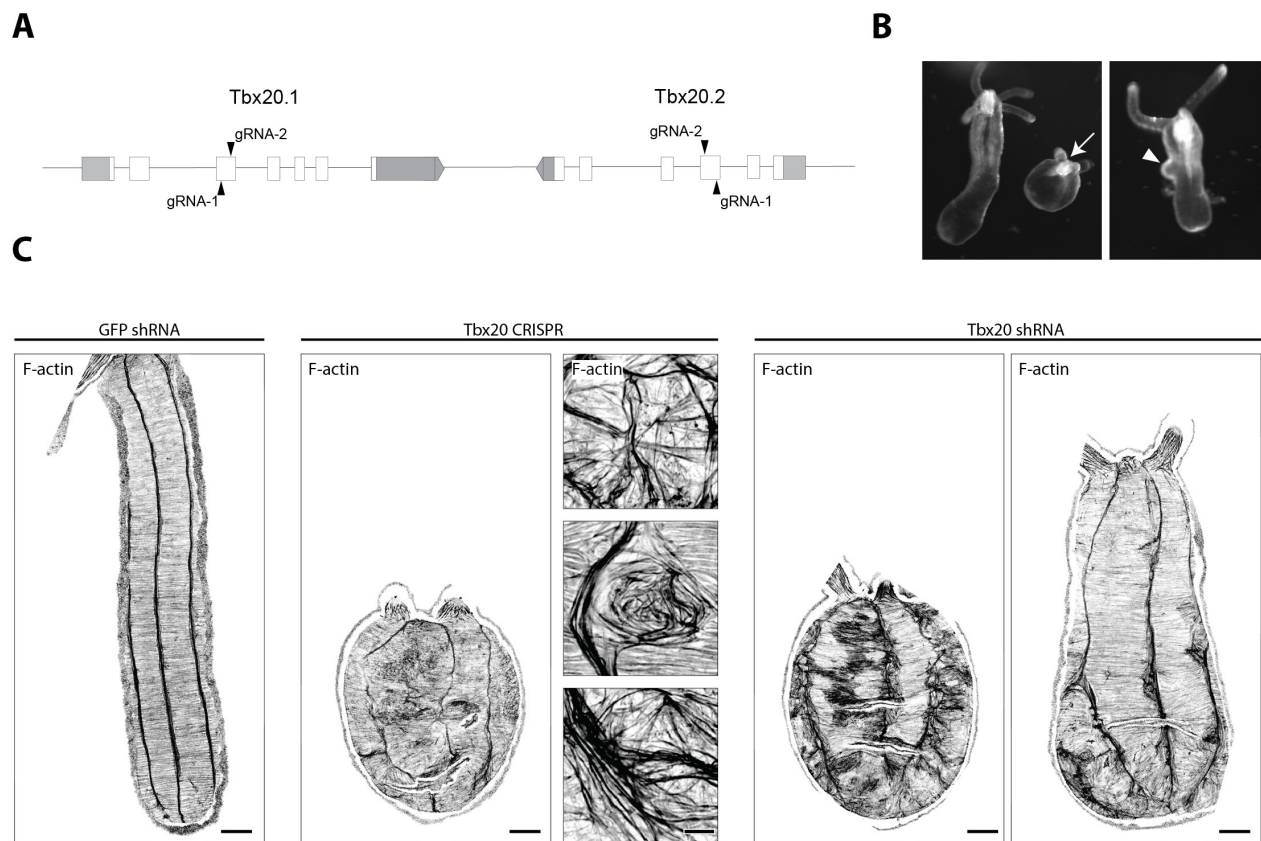
**Appendix Figure 5. Characterization of Nkx2.5 KD phenotype.** **A.** Images and quantification of body length for a control and an *Nkx2.5* KD animal. **B.** Quantification of body length in controls ( $n = 29$  and *Nkx2.5* KD animals ( $n = 30$ ) (two-sided unpaired Wilcoxon rank sum test; \*\*\*\* $p < 0.0001$ , \*\* $p < 0.01$ , n.s.  $p > 0.05$ ). **C.** F-actin and pMLC staining of a *Nkx2.5* KD animal, showing seemingly normal muscle organization. White and black arrowheads indicate circular muscle and longitudinal muscle, respectively. **D.** Quantification of body length, body column diameter along the oral-aboral axis and overall contractility in an *Nkx2.5* KD animal, showing longitudinal but not circular muscle contractions. **E.** Quantification of motility (displacement per 5-minute interval) in control ( $n = 27$ ) and *Nkx2.5* KD ( $n = 25$ ) animals during the transition stage. Scale bars: 100  $\mu\text{m}$  (A), 50  $\mu\text{m}$  (C, overview), and 20  $\mu\text{m}$  (C, zoom).

Interestingly, a similar but milder phenotype was found for knockdown of the LIM homeodomain transcription factor *NvIsl-1* (*Islet*), a gene that is involved in neuron differentiation and is also expressed in cardiac progenitor cells in bilaterians (**Appendix Figure 6A-D**) (Cai et al.,

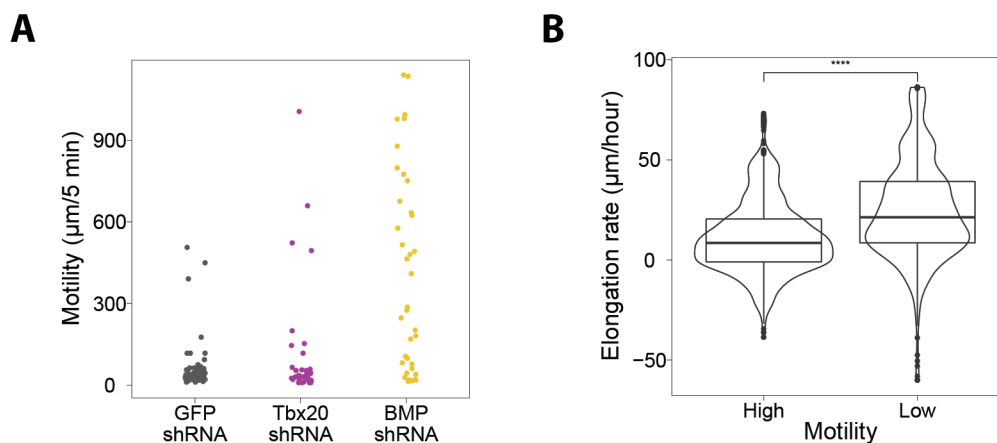
2003; Ericson et al., 1992; Yuan and Schoenwolf, 2000). A direct link between *Nkx2.5* and *Isl-1* may exist, as *Nkx2.5* has been found to repress *Isl-1* transcriptional activity during cardiomyocyte differentiation in *Xenopus* (Dorn et al., 2015). Although the specific functions of *Nkx2.5* and *Isl-1* in *Nematostella* remain to be elucidated, these results suggest that they might be involved in regulation of muscular hydraulics. Therefore, it would be interesting to follow up on analysis of these phenotypes and explore whether there is a potential link to the nervous system.



**Appendix Figure 6. Characterization of the *Isl-1* KD phenotype.** **A.** Images of a control and *Isl-1* KD animal during larva-polyp transition. **B.** Quantification of body length for the animals show in A. **C.** Quantification of body length for control ( $n = 52$ ), and *Isl-1* KD ( $n = 53$ ) animals. **D.** Quantification of motility (displacement per 5-minute interval) in control ( $n = 46$ ) and *Isl-1* KD ( $n = 36$ ) animals during the transition stage. Scale bar: 100  $\mu\text{m}$ .



**Appendix Figure 7. Generation and characterization of *Tbx20* loss of function.** **A.** Schematic showing the gRNA design to generate F0 *Tbx20* CRISPR mutants. **B.** Examples of *Tbx20* CRISPR/Cas9-injected animals showing round morphologies (white arrow) and a bleb-like structure (white arrowhead). **C.** Comparison of muscle organization in a control animal, *Tbx20* CRISPR/Cas9-injected animals, and *Tbx20* shRNA KD animals. Images show maximum intensity projections of stacks that are corrected for curvature using the MinCostZSurface plugin in FIJI. *Tbx20* CRISPR KO animals were generated by Aissam Ikmi. Scale bars: 50  $\mu\text{m}$  (C, overview images) and 10  $\mu\text{m}$  (C, zoom-ins for *Tbx20* CRISPR/Cas9-injected animals). Figure also appears in (Stokkermans et al., 2021).

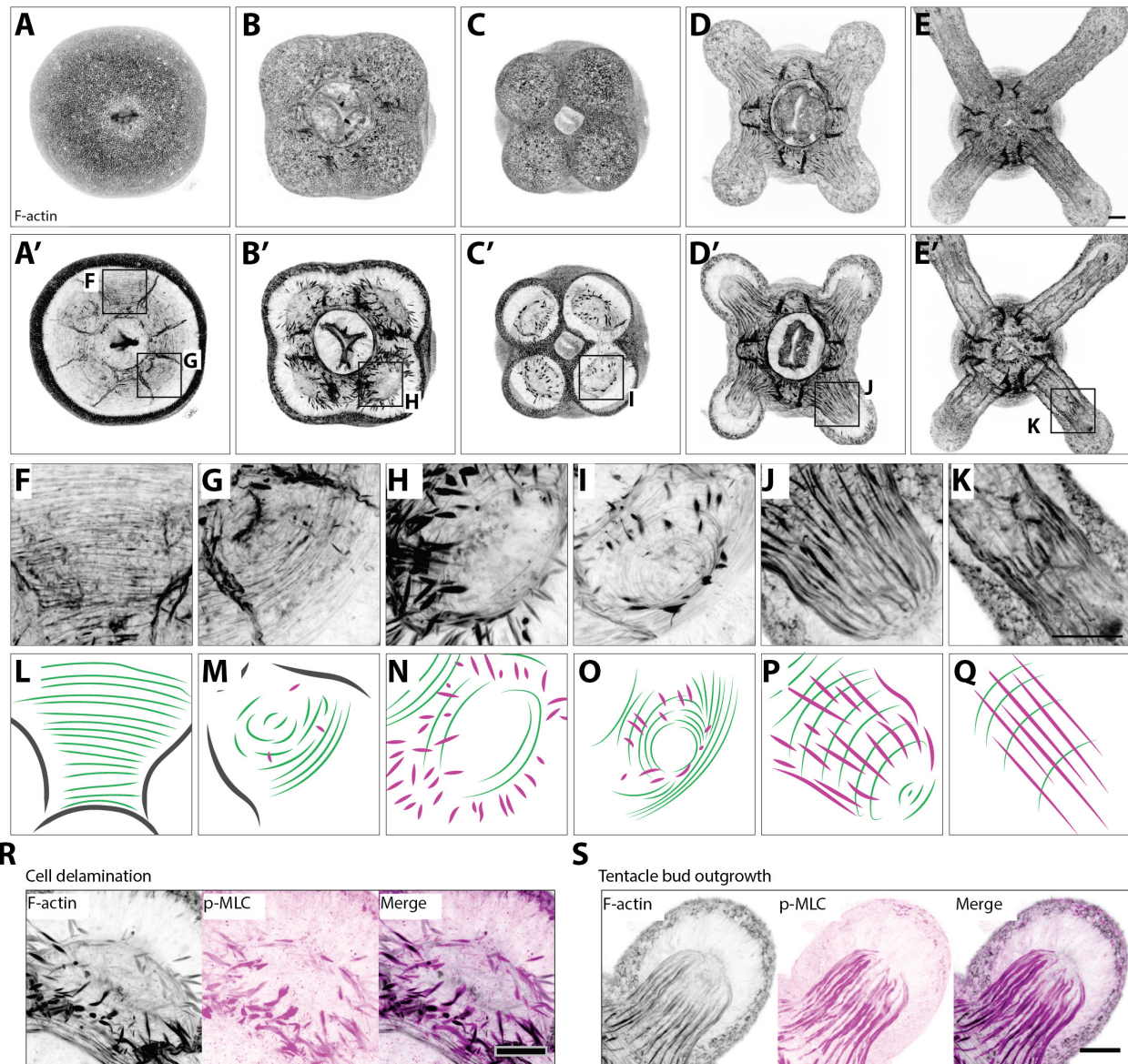


**Appendix Figure 8. Quantification of motility during the transition stage in control, *Tbx20* KD, and *BMP2/4* KD animals.** **A.** Quantification of motility (displacement per 5-minute interval) for GFP shRNA, *Tbx20* KD, and *BMP2/4* KD. **B.** Quantification of elongation rate during transition stage for *BMP2/4* KD animals that show adhesion or motile behavior ( $n = 37$ ) (two-sided unpaired Wilcoxon rank sum test; \*\*\*\* $p < 0.0001$ ).

#### **11.4. Development of tentacle muscles**

The muscle system in the tentacles begins to develop at the start of larva-polyp transition. Unlike the muscles from the body column, longitudinal tentacle muscles develop from the ectoderm. This involves detachment and migration of epithelial longitudinal muscle precursor cells from the ectoderm to the site of tentacle budding. The now mesenchymal cells localize to the base of the epithelium, where they grow and extend into the tentacles (Jahnel et al., 2014). To visualize this process, animals were fixed and stained at different stages for F-actin (phalloidin staining), and phosphorylated myosin light chain (p-MLC), to label muscle cells (**Appendix Figure 9**). Prior to budding, subtle (re)arrangements can be observed in the circular muscles of four of the eight sectors (**Appendix Figure 9A'**, F versus G). Subsequently, newly formed concentric rings of circular muscles form an outgrowth, while individual cells high in actin expression show up in different orientations in a circle around the bud site (**Appendix Figure 9B'**, H). These cells delaminate from the ectoderm (Jahnel et al., 2014), align with the circular muscles and extend into the growing tentacle (**Appendix Figure 9C-D, I-J**). Many of these delaminating cells express p-MLC, suggesting that they are differentiating into muscle cells as they migrate to the bud site (**Appendix Figure 9R-S**). p-MLC staining is maintained in the tentacles and longitudinal muscles of the body column at the polyp stage.





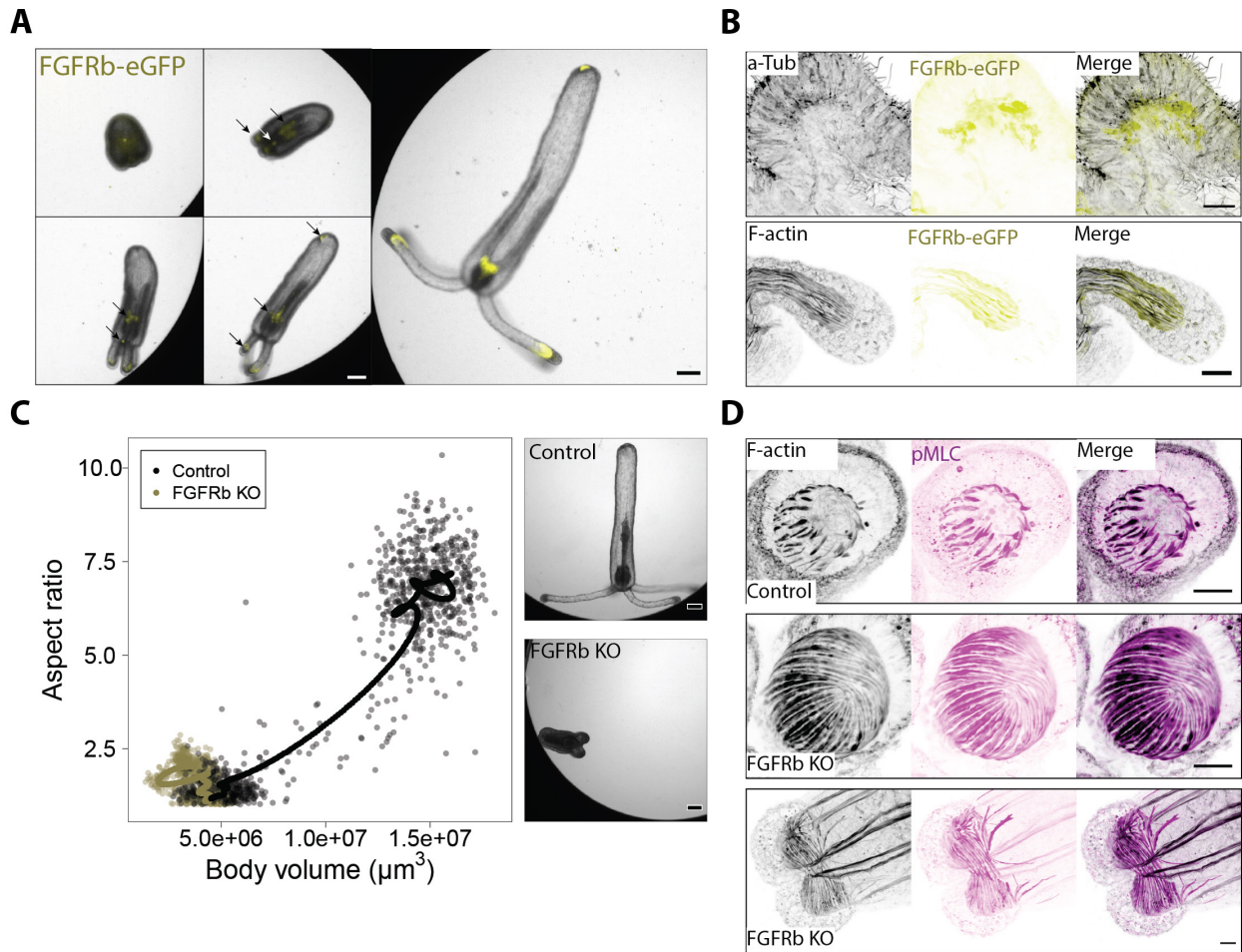
**Appendix Figure 9. Development of tentacle muscles during larva-polyp transition.** A-E. Maximum intensity projection images of animals at different stages, mounted with the oral opening facing upwards, and fixed and stained with fluorescently labeled phalloidin. A'-E'. Maximum intensity projection images of the same animals as shown in A-E, but starting at a lower z-plane. F-K. Zoom-ins of regions marked in A'-E'. L-Q. Schematic drawing of tentacle muscle development, showing longitudinal tentacle muscles (magenta) and circular tentacle muscles (green). R-S. Maximum intensity projection images of early (R) and late tentacle buds (S), showing antibody staining for p-MLC combined with phalloidin. Scale bars: 20  $\mu\text{m}$ .

### 11.5. FGFRb signaling is involved in patterning of longitudinal tentacle muscles

During tentacle budding the individual circular and longitudinal organizations have to be established de novo in the tentacle buds. It is neither well understood how the ectodermal muscle precursors lose their epithelial identity and find their destination, nor what drives the extension of muscle cells into the tentacles, or how new rings of circular muscles are added. *Nematostella* expresses several genes known to be involved in appendage formation in bilaterians, including FGFs

(Edom-Vovard et al., 2001; Eloy-Trinquet et al., 2009; Flanagan-Steet et al., 2000; Matus et al., 2007; Olwin et al., 1994). From previous research, it is known that the fibroblast growth factor receptor B (FGFRb) is expressed in the tentacle tips and in delaminating muscle precursors (Matus et al., 2007) (**Appendix Figure 10A, B**) and that CRISPR/Cas9 mediated knock-out (KO) of FGFRb results in polyps with abnormal tentacle morphology and short body axes (Ikmi et al., 2020) (**Appendix Figure 10C, D**). Also, FGF8b has been found expressed in a small population of cells located at the very tip of the tentacles (Matus et al., 2007).

As it is already known that knocking out FGFRb results in abnormal tentacle morphogenesis, resulting in tentacles with round, 'bubble' like shapes that fail to elongate, muscle organization was studied in this context. In control animals, the longitudinal muscle cells are arranged equally around the circular muscles and roughly parallel with respect to each other, while pointing to the tip of the tentacle (**Appendix Figure 10D**, top). Strikingly, in FGFRb KO animals, the longitudinal muscle cells do not form a straight line from the onset of the tentacle to the tip, but instead bend around the tip and loop back, and cross regularly with other muscle cells (**Appendix Figure 10D**, middle and bottom). The circular muscles are present, but the rings are larger in diameter than in wild type tentacles. In some cases, longitudinal muscle cells were shared between different tentacles (**Appendix Figure 10D**, bottom). The abnormal tentacle muscle morphology suggests that cells lack a signal in absence of FGFRb that is required for guidance to the right location.



**Appendix Figure 10. Tentacle morphology in FGFRb KO animals.** **A.** Brightfield images of the same animal, expressing GFP (yellow) under the control of the FGFRb promoter. **B.** Antibody staining targeting eGFP showing expression of FGFRb-eGFP construct in early and late tentacle muscles. **C.** Developmental trajectory in morphospace of a control animals and an FGFRb KO animal. **D.** Maximum intensity images of tentacles in control (top) or FGFRb KO (bottom) animals, stained with p-MLC antibody and phalloidin. Scale bars: 100  $\mu\text{m}$  (A, C), 20  $\mu\text{m}$  (B, D).

# Bibliography

Abrams, M.J., Basinger, T., Yuan, W., Guo, C.-L., and Goentoro, L. (2015). Self-repairing symmetry in jellyfish through mechanically driven reorganization. *Proc. Natl. Acad. Sci. U. S. A.* *112*, E3365-73.

Adams, D.S., and Koehu, M.A.R. (1990). The mechanics of notochord elongation, straightening and stiffening in the embryo of *Xenopus laevis*. *Development* *110*, 115–130.

Alberts, B., Johnson, A., Lewis, J., Morgan, D., Raff, M., Roberts, K., and Walter, P. (2015). *Molecular biology of the cell* Sixth edition.

Alcorn, D., Adamson, T.M., Lambert, T.F., Maloney, J.E., Ritchie, B.C., and Robinson, P.M. (1977). Morphological effects of chronic tracheal ligation and drainage in the fetal lamb lung. *J. Anat.* *123*, 649–660.

Amiel, A.R., Johnston, H.T., Nedoncelle, K., Warner, J.F., Ferreira, S., and Röttinger, E. (2015). Characterization of morphological and cellular events underlying oral regeneration in the sea anemone, *Nematostella vectensis*. *Int. J. Mol. Sci.* *16*, 28449–28471.

Ando, R., Hama, H., Yamamoto-Hino, M., Mizuno, H., and Miyawaki, A. (2002). An optical marker based on the UV-induced green-to-red photoconversion of a fluorescent protein. *Proc. Natl. Acad. Sci. U. S. A.* *99*, 12651–12656.

Andrés-Delgado, L., and Mercader, N. (2016). Interplay between cardiac function and heart development. *Biochim. Biophys. Acta - Mol. Cell Res.* *1863*, 1707–1716.

Arganda-Carreras, I., Fernández-González, R., Muñoz-Barrutia, A., and Ortiz-De-Solorzano, C. (2010). 3D reconstruction of histological sections: Application to mammary gland tissue. *Microsc. Res. Tech.* *73*, 1019–1029.

Arganda-Carreras, I., Kaynig, V., Rueden, C., Eliceiri, K.W., Schindelin, J., Cardona, A., and Seung, H.S. (2017). Trainable Weka Segmentation: A machine learning tool for microscopy pixel classification. *Bioinformatics* *33*, 2424–2426.

Aulehla, A., and Pourquié, O. (2010). Signaling gradients during paraxial mesoderm development. *Cold Spring Harb. Perspect. Biol.* *2*, a000869.

Aumann, S., Donner, S., Fischer, J., and Müller, F. (2019). Optical Coherence Tomography (OCT): Principle and Technical Realization. *High Resolut. Imaging Microsc. Ophthalmol.* 59–85.

Barthel, K.U. (2012). *Volume Viewer*.

Batham, E.J., and Pantin, C.F. (1950a). Muscular and hydrostatic action in the sea-anemone *Metridium senile* (L.).

Batham, E.J., and Pantin, C.F. (1950b). Muscular and hydrostatic action in the sea-anemone *Metridium senile* (L.). *J. Exp. Biol.* *27*, 264–289.

Bénazéraf, B. (2019). Dynamics and mechanisms of posterior axis elongation in the vertebrate embryo. *Cell. Mol. Life Sci.* *76*, 89–98.

Bénazéraf, B., Francois, P., Baker, R.E., Denans, N., Little, C.D., and Pourquié, O. (2010). A random cell motility gradient downstream of FGF controls elongation of an amniote embryo. *Nature* *466*, 248–252.

Bénazéraf, B., and Pourquié, O. (2013). Formation and segmentation of the vertebrate body axis. *Annu. Rev. Cell Dev. Biol.* *29*, 1–26.

Bertet, C., Sulak, L., and Lecuit, T. (2004). Myosin-dependent junction remodelling controls planar cell intercalation and axis elongation. *Nature* *429*, 667–671.

Bertossa, R.C. (2011). Morphology and behaviour: Functional links in development and evolution. *Philos. Trans. R. Soc. B Biol. Sci.* *366*, 2056–2068.



Blankenship, J.T., Backovic, S.T., Sanny, J.S.S.P., Weitz, O., and Zallen, J.A. (2006). Multicellular Rosette Formation Links Planar Cell Polarity to Tissue Morphogenesis. *Dev. Cell* *11*, 459–470.

Bodmer, R. (1993). The gene *tinman* is required for specification of the heart and visceral muscles in *Drosophila*. *Development* *118*, 719–729.

Bokka, K.K., Jesudason, E.C., Lozoya, O.A., Guilak, F., Warburton, D., and Lubkin, S.R. (2015). Morphogenetic Implications of Peristalsis-Driven Fluid Flow in the Embryonic Lung. *PLoS One* *10*, e0132015.

Bucher, M., Wolfowicz, I., Voss, P.A., Hambleton, E.A., and Guse, A. (2016). Development and Symbiosis Establishment in the Cnidarian Endosymbiosis Model *Aiptasia* sp. *Sci. Rep.* *6*, 1–11.

Buzgariu, W., Al Haddad, S., Tomczyk, S., Wenger, Y., and Galliot, B. (2015). Multi-functionality and plasticity characterize epithelial cells in *Hydra*. *Tissue Barriers* *3*, e1068908.

Cai, C.L., Liang, X., Shi, Y., Chu, P.H., Pfaff, S.L., Chen, J., and Evans, S. (2003). *Isl1* identifies a cardiac progenitor population that proliferates prior to differentiation and contributes a majority of cells to the heart. *Dev. Cell* *5*, 877–889.

Calhoun, A., and Hady, A. El (2021). What is behavior? No seriously, what is it? *BioRxiv* 2021.07.04.451053.

Cambray, N., and Wilson, V. (2002). Axial progenitors with extensive potency are localised to the mouse chordoneural hinge. *Development* *129*, 4855–4866.

Campbell, R.D. (1987). Organization of the nematocyst battery in the tentacle of *hydra*: Arrangement of the complex anchoring junctions between nematocytes, epithelial cells, and basement membrane. *Cell Tissue Res.* *249*, 647–655.

Catala, M., Teillet, M.A., and Le Douarin, N.M. (1995). Organization and development of the tail bud analyzed with the quail-chick chimaera system. *Mech. Dev.* *51*, 51–65.

Chan, B.G., Rocheleau, S.K., Smit, R.B., and Mains, P.E. (2015). The Rho guanine exchange factor RHGF-2 acts through the Rho-binding kinase LET-502 to mediate embryonic elongation in *C. elegans*. *Dev. Biol.* *405*, 250–259.

Chan, C.J., Costanzo, M., Ruiz-Herrero, T., Mönke, G., Petrie, R.J., Bergert, M., Diz-Muñoz, A., Mahadevan, L., and Hiiragi, T. (2019). Hydraulic control of mammalian embryo size and cell fate. *Nature* *571*, 112–116.

Chen, J.N., and Fishman, M.C. (2000). Genetics of heart development. *Trends Genet.* *16*, 383–388.

Chen, C.Y., McKinney, S.A., Ellington, L.R., and Gibson, M.C. (2020). Hedgehog signaling is required for endomesodermal patterning and germ cell development in the sea anemone *nematostella vectensis*. *Elife* *9*, 1–27.

Chen, Y., Xiao, D., Zhang, L., Cai, C.L., Li, B.Y., and Liu, Y. (2021). The Role of *Tbx20* in Cardiovascular Development and Function. *Front. Cell Dev. Biol.* *9*, 69.

Chourrout, D., Delsuc, F., Chourrout, P., Edvardsen, R.B., Rentzsch, F., Renfer, E., Jensen, M.F., Zhu, B., de Jong, P., Steele, R.E., et al. (2006). Minimal ProtoHox cluster inferred from bilaterian and cnidarian Hox complements. *Nat.* 2006 4427103 *442*, 684–687.

Clément, R., Dehapiot, B., Collinet, C., Lecuit, T., and Lenne, P.F. (2017). Viscoelastic Dissipation Stabilizes Cell Shape Changes during Tissue Morphogenesis. *Curr. Biol.* *27*, 3132–3142.e4.

Collinet, C., and Lecuit, T. (2021). Programmed and self-organized flow of information during morphogenesis. *Nat. Rev. Mol. Cell Biol.* *22*, 245–265.

Collinet, C., Rauzi, M., Lenne, P.-F.F., and Lecuit, T. (2015). Local and tissue-scale forces drive oriented junction growth during tissue extension. *Nat. Cell Biol.* *17*, 1247–1258.

Craig, R., Smith, R., and Kendrick-Jones, J. (1983). Light-chain phosphorylation controls the conformation of vertebrate non-muscle and smooth muscle myosin molecules. *Nat.* 1983 3025907 *302*, 436–439.

- Davies, J. (2013). *Mechanisms of morphogenesis* (Academic Press).
- Desmond, M.E., and Jacobson, A.G. (1977). Embryonic brain enlargement requires cerebrospinal fluid pressure. *Dev. Biol.* *57*, 188–198.
- Devenport, D. (2014). The cell biology of planar cell polarity. *J. Cell Biol.* *207*, 171–179.
- Diogon, M., Wissler, F., Quintin, S., Nagamatsu, Y., Sookhareea, S., Landmann, F., Hutter, H., Vitale, N., and Labouesse, M. (2007). The RhoGAP RGA-2 and LET-502/ROCK achieve a balance of actomyosin-dependent forces in *C. elegans* epidermis to control morphogenesis. *Development* *134*, 2469–2479.
- Dorn, T., Goedel, A., Lam, J.T., Haas, J., Tian, Q., Herrmann, F., Bundschu, K., Dobрева, G., Schiemann, M., Dirschinger, R., et al. (2015). Direct Nkx2-5 transcriptional repression of *isl1* controls cardiomyocyte subtype identity. *Stem Cells* *33*, 1113–1129.
- Dray, N., Lawton, A., Nandi, A., Jülich, D., Emonet, T., and Holley, S.A. (2013). Cell-fibronectin interactions propel vertebrate trunk elongation via tissue mechanics. *Curr. Biol.* *23*, 1335–1341.
- Duckworth, R.A. (2009). The role of behavior in evolution: A search for mechanism. *Evol. Ecol.* *23*, 513–531.
- Edom-Vovard, F., Bonnin, M.-A., and Duprez, D. (2001). *Fgf8* transcripts are located in tendons during embryonic chick limb development. *Mech. Dev.* *108*, 203–206.
- Ellis, K., Bagwell, J., and Bagnat, M. (2013). Notochord vacuoles are lysosome-related organelles that function in axis and spine morphogenesis. *J. Cell Biol.* *200*, 667–679.
- Eloy-Trinquet, S., Wang, H., Edom-Vovard, F., and Duprez, D. (2009). *Fgf* signaling components are associated with muscles and tendons during limb development. *Dev. Dyn.* *238*, 1195–1206.
- Ericson, J., Thor, S., Edlund, T., Jessell, T.M., and Yamada, T. (1992). Early stages of motor neuron differentiation revealed by expression of homeobox gene *Islet-1*. *Science* (80-. ). *256*, 1555–1560.
- Escobedo, R., Lecheval, V., Papaspyros, V., Bonnet, F., Mondada, F., Sire, C., and Theraulaz, G. (2020). A data-driven method for reconstructing and modelling social interactions in moving animal groups: Reconstructing social interactions. *Philos. Trans. R. Soc. B Biol. Sci.* *375*.
- Fernandez, R., and Moisy, C. (2020). FijiYama: a registration tool for 3D multimodal time-lapse imaging. *Bioinformatics*.
- Finnerty, J.R., Pang, K., Burton, P., Paulson, D., and Martindale, M.Q. (2004). Origins of bilateral symmetry: *Hox* and *dpp* expression in a sea anemone. *Science* (80-. ). *304*, 1335–1337.
- Fishman, A., Light, D., and Lamm, A.T. (2018). QsRNA-seq: a method for high-throughput profiling and quantifying small RNAs. *Genome Biol.* *19*, 113.
- Flanagan-Steet, H., Hannon, K., McAvoy, M.J., Hullinger, R., and Olwin, B.B. (2000). Loss of FGF Receptor 1 Signaling Reduces Skeletal Muscle Mass and Disrupts Myofiber Organization in the Developing Limb. *Dev. Biol.* *218*, 21–37.
- Fraune, S., Forêt, S., and Reitzel, A.M. (2016). Using *Nematostella vectensis* to Study the Interactions between Genome, Epigenome, and Bacteria in a Changing Environment. *Front. Mar. Sci.* *3*, 148.
- Fritz, A.E., Ikmi, A., Seidel, C., Paulson, A., and Gibson, M.C. (2013). Mechanisms of tentacle morphogenesis in the sea anemone *Nematostella vectensis*. *Dev.* *140*, 2212–2223.
- Fujimoto, J., and Swanson, E. (2016). The Development, Commercialization, and Impact of Optical Coherence Tomography. *Invest. Ophthalmol. Vis. Sci.* *57*, OCT1.
- Fukui, H., Chow, R.W.-Y., Xie, J., Foo, Y.Y., Yap, C.H., Minc, N., Mochizuki, N., and Vermot, J. (2021). Bioelectric signaling and the control of cardiac cell identity in response to mechanical forces. *Science* (80-. ). *374*, 351–354.

Gajewski, M., Leitz, T., Schloßherr, J., and Plickert, G. (1996). LWamides from Cnidaria constitute a novel family of neuropeptides with morphogenetic activity. *Roux's Arch. Dev. Biol.* *205*, 232–242.

Genikhovich, G., and Technau, U. (2009). Induction of Spawning in the Starlet Sea Anemone *Nematostella vectensis*, In Vitro Fertilization of Gametes, and Dejellying of Zygotes. *Cold Spring Harb. Protoc.* *2009*, pdb.prot5281-pdb.prot5281.

Genikhovich, G., Fried, P., Prünster, M.M., Schinko, J.B., Gilles, A.F., Fredman, D., Meier, K., Iber, D., and Technau, U. (2015). Axis Patterning by BMPs: Cnidarian Network Reveals Evolutionary Constraints. *Cell Rep.* *10*, 1646–1654.

Gilbert, S.F. (2000). *Metamorphosis: The Hormonal Reactivation of Development*.

Gillard, G., Nicolle, O., Brugière, T., Prigent, S., Pinot, M., and Michaux, G. (2019). Force Transmission between Three Tissues Controls Bipolar Planar Polarity Establishment and Morphogenesis. *Curr. Biol.* *29*, 1360-1368.e4.

Goel, T., Wang, R., Martin, S., Lanphear, E., and Collins, E.-M.S. (2019). Linalool acts as a fast and reversible anesthetic in Hydra. *BioRxiv* 584946.

Goto, T., Davidson, L., Asashima, M., and Keller, R. (2005). Planar Cell Polarity Genes Regulate Polarized Extracellular Matrix Deposition during Frog Gastrulation. *Curr. Biol.* *15*, 787–793.

Graner, F., and Riveline, D. (2017). 'The forms of tissues, or cell-aggregates': D'arcy thompson's influence and its limits. *Dev.* *144*, 4226–4237.

Grimmelikhuijzen, C.J.P., and Westfall, J.A. (1995). The nervous systems of Cnidarians. *EXS* *72*, 7–24.

Hague, T., Florini, M., and Andrews, P.L.R. (2013). Preliminary in vitro functional evidence for reflex responses to noxious stimuli in the arms of *Octopus vulgaris*. *J. Exp. Mar. Bio. Ecol.* *447*, 100–105.

Hand, C., and Uhlinger, K.R. (1992). The culture, sexual and asexual reproduction, and growth of the sea anemone *Nematostella vectensis*. *Biol. Bull.* *182*, 169–176.

He, S., Del Viso, F., Chen, C.Y., Ikmi, A., Kroesen, A.E., and Gibson, M.C. (2018). An axial Hox code controls tissue segmentation and body patterning in *Nematostella vectensis*. *Science* (80-. ). *361*, 1377–1380.

Hoffman, B.D., Grashoff, C., and Schwartz, M.A. (2011). Dynamic molecular processes mediate cellular mechanotransduction. *Nature* *475*, 316–323.

Hofmann, D.K., and Brand, U. (1987). Induction of metamorphosis in the symbiotic scyphozoan *Cassiopea andromeda*: role of marine bacteria and of biochemicals. *Symbiosis*.

Honegger, K., and de Bivort, B. (2018). Stochasticity, individuality and behavior. *Curr. Biol.* *28*, R8–R12.

Hubel, D.H., Wiesel, T.N., and LeVay, S. (1976). Functional architecture of area 17 in normal and monocularly deprived macaque monkeys. *Cold Spring Harb. Symp. Quant. Biol.* *40*, 581–589.

Huycke, T.R., Miller, B.M., Gill, H.K., Nerurkar, N.L., Sprinzak, D., Mahadevan, L., and Tabin, C.J. (2019). Genetic and Mechanical Regulation of Intestinal Smooth Muscle Development. *Cell* *179*, 90-105.e21.

Hyndman, R.J., Khandakar, Y., and others (2008). Automatic time series forecasting: the forecast package for R. *J. Stat. Softw.* *27*, 1–22.

Hyndman, R.J., Athanasopoulos, G., Bergmeir, C., Caceres, G., Chhay, L., O'Hara-Wild, M., Petropoulos, F., and Razbash, S. (2020). Package 'forecast.' Online] <https://cran.r-project.org/web/packages/forecast/forecast.pdf>.

Ikmi, A., McKinney, S.A., Delventhal, K.M., Gibson, M.C., and Stuurman, N. (2014). TALEN and CRISPR/Cas9-mediated genome editing in the early-branching metazoan *Nematostella vectensis*. *Nat. Commun.* *5*, 5486.

Ikmi, A., Steenbergen, P.J., Anzo, M., McMullen, M.R., Stokkermans, A., Ellington, L.R., and Gibson, M.C. (2020). Feeding-dependent tentacle development in the sea anemone *Nematostella vectensis*. *Nat. Commun.* *11*, 1–13.

- Irvine, K.D., and Wieschaus, E. (1994). Cell intercalation during *Drosophila* germband extension and its regulation by pair-rule segmentation genes. *Development* *120*, 827–841.
- Iwao, K., Fujisawa, T., and Hatta, M. (2002). A cnidarian neuropeptide of the GLWamide family induces metamorphosis of reef-building corals in the genus *Acropora*. *Coral Reefs* *21*, 127–129.
- Jackson, D., Leys, S.P., Hinman, V.F., Woods, R., Lavin, M.F., and Degnan, B.M. (2002). Ecological regulation of development: induction of marine invertebrate metamorphosis. *Int. J. Dev. Biol.* *46*, 679–686.
- Jahnel, S.M., Walzl, M., and Technau, U. (2014). Development and epithelial organisation of muscle cells in the sea anemone *Nematostella vectensis*. *Front. Zool.* *11*, 1–15.
- Jung, H.S., Komatsu, S., Ikebe, M., and Craig, R. (2008). Head–Head and Head–Tail Interaction: A General Mechanism for Switching Off Myosin II Activity in Cells. *Mol. Biol. Cell* *19*, 3234.
- Kassambara, A. (2020). ggpubr: “ggplot2” Based Publication Ready Plots.
- Keller, R., Cooper, M.S., Danilchik, M., Tibbetts, P., and Wilson, P.A. (1989). Cell intercalation during notochord development in *Xenopus laevis*. *J. Exp. Zool.* *251*, 134–154.
- Khalipina, D., Kaga, Y., Dacher, N., and Chevalier, N.R. (2019). Smooth muscle contractility causes the gut to grow anisotropically. *J. R. Soc. Interface* *16*, 20190484.
- Khuenl-Brady, K.S., and Sparr, H. (1996). Clinical pharmacokinetics of rocuronium bromide. *Clin. Pharmacokinet.* *31*, 174–183.
- Kier, W.M. (2012). The diversity of hydrostatic skeletons. *J. Exp. Biol.* *215*, 1247–1257.
- Kim, H.Y.Y., Pang, M.-F.F., Varner, V.D.D., Kojima, L., Miller, E., Radisky, D.C.C., and Nelson, C.M.M. (2015). Localized Smooth Muscle Differentiation Is Essential for Epithelial Bifurcation during Branching Morphogenesis of the Mammalian Lung. *Dev. Cell* *34*, 719–726.
- Kong, D., Wolf, F., and Großhans, J. (2017). Forces directing germ-band extension in *Drosophila* embryos. *Mech. Dev.* *144*, 11–22.
- Kusserow, A., Pang, K., Sturm, C., Hroudá, M., Lentfer, J., Schmidt, H.A., Technau, U., Von Haeseler, A., Hobmayer, B., Martindale, M.Q., et al. (2005). Unexpected complexity of the Wnt gene family in a sea anemone. *Nature* *433*, 156–160.
- Lardennois, A., Pásti, G., Ferraro, T., Llense, F., Mahou, P., Pontabry, J., Rodriguez, D., Kim, S., Ono, S., Beaurepaire, E., et al. (2019). An actin-based viscoplastic lock ensures progressive body-axis elongation. *Nature* *573*, 266–270.
- Lauschke, V.M., Tsiarris, C.D., François, P., and Aulehla, A. (2013). Scaling of embryonic patterning based on phase-gradient encoding. *Nature* *493*, 101–105.
- Lawson, A., and Schoenwolf, G.C. (2001). New Insights Into Critical Events of Avian Gastrulation.
- Layden, M.J., Rentzsch, F., and Röttinger, E. (2016). The rise of the starlet sea anemone *Nematostella vectensis* as a model system to investigate development and regeneration. *Wiley Interdiscip. Rev. Dev. Biol.* *5*, 408–428.
- Leach, W.B., and Reitzel, A.M. (2020). Decoupling behavioral and transcriptional responses to color in an eyeless cnidarian. *BMC Genomics* *21*, 361.
- Leclère, L., and Rentzsch, F. (2014). RGM Regulates BMP-Mediated Secondary Axis Formation in the Sea Anemone *Nematostella vectensis*. *Cell Rep.* *9*, 1921–1930.
- Leclère, L., and Röttinger, E. (2017). Diversity of Cnidarian Muscles: Function, Anatomy, Development and Regeneration. *Front. Cell Dev. Biol.* *4*, 1–22.
- Leclère, L., Bause, M., Sinigaglia, C., Steger, J., and Rentzsch, F. (2016a). Development of the aboral domain in *Nematostella* requires  $\beta$ -catenin and the opposing activities of Six3/6 and Frizzled5/8. *Dev.* *143*, 1766–1777.

- Leclère, L., Copley, R.R., Momose, T., and Houliston, E. (2016b). Hydrozoan insights in animal development and evolution. *Curr. Opin. Genet. Dev.* *39*, 157–167.
- Legland, D., Arganda-Carreras, I., and Andrey, P. (2016). MorphoLibJ: Integrated library and plugins for mathematical morphology with ImageJ. *Bioinformatics* *32*, 3532–3534.
- Leitz, T. (1997). Induction of settlement and metamorphosis of cnidarian larvae: Signals and signal transduction. *Invertebr. Reprod. Dev.* *31*, 109–122.
- Levitis, D.A., Lidicker, W.Z., and Freund, G. (2009). Behavioural biologists do not agree on what constitutes behaviour. *Anim. Behav.* *78*, 103–110.
- Levy, S., Elek, A., Grau-Bové, X., Menéndez-Bravo, S., Iglesias, M., Tanay, A., Mass, T., and Sebé-Pedrós, A. (2021). A stony coral cell atlas illuminates the molecular and cellular basis of coral symbiosis, calcification, and immunity. *Cell* *184*, 2973–2987.
- Li, J., Wang, Z., Chu, Q., Jiang, K., Li, J., and Tang, N. (2018). The Strength of Mechanical Forces Determines the Differentiation of Alveolar Epithelial Cells. *Dev. Cell* *44*, 297–312.e5.
- Li, K., Wu, X., Chen, D.Z., and Sonka, M. (2006). Optimal surface segmentation in volumetric images - A graph-theoretic approach. *IEEE Trans. Pattern Anal. Mach. Intell.* *28*, 119–134.
- Linkert, M., Rueden, C.T., Allan, C., Burel, J.M., Moore, W., Patterson, A., Loranger, B., Moore, J., Neves, C., MacDonald, D., et al. (2010). Metadata matters: Access to image data in the real world. *J. Cell Biol.* *189*, 777–782.
- Livshits, A., Shani-Zerbib, L., Maroudas-Sacks, Y., Braun, E., and Keren, K. (2017). Structural Inheritance of the Actin Cytoskeletal Organization Determines the Body Axis in Regenerating Hydra. *Cell Rep.* *18*, 1410–1421.
- Lombardot, B. (2017). Minimum Cost Z surface Projection - ImageJ.
- Lucitti, J.L., Jones, E.A.V., Huang, C., Chen, J., Fraser, S.E., and Dickinson, M.E. (2007). Vascular remodeling of the mouse yolk sac requires hemodynamic force. *Development* *134*, 3317–3326.
- Luu, O., David, R., Ninomiya, H., and Winklbauer, R. (2011). Large-scale mechanical properties of *Xenopus* embryonic epithelium. *Proc. Natl. Acad. Sci. U. S. A.* *108*, 4000.
- Lye, C.M., Blanchard, G.B., Naylor, H.W., Muresan, L., Huisken, J., Adams, R.J., and Sanson, B. (2015). Mechanical Coupling between Endoderm Invagination and Axis Extension in *Drosophila*. *PLoS Biol.* *13*, e1002292.
- Magie, C.R., and Martindale, M.Q. (2008). Cell-cell adhesion in the cnidaria: Insights into the evolution of tissue morphogenesis. *Biol. Bull.* *214*, 218–232.
- Mao, Y., Tournier, A.L., Hoppe, A., Kester, L., Thompson, B.J., and Tapon, N. (2013). Differential proliferation rates generate patterns of mechanical tension that orient tissue growth. *EMBO J.* *32*, 2790–2803.
- Marlow, H., Roettinger, E., Boekhout, M., and Martindale, M.Q. (2012). Functional roles of Notch signaling in the cnidarian *Nematostella vectensis*. *Dev. Biol.* *362*, 295–308.
- Marlow, H., Matus, D.Q., and Martindale, M.Q. (2013). Ectopic activation of the canonical wnt signaling pathway affects ectodermal patterning along the primary axis during larval development in the anthozoan *Nematostella vectensis*. *Dev. Biol.* *380*, 324–334.
- Marlow, H.Q., Srivastava, M., Matus, D.Q., Rokhsar, D., and Martindale, M.Q. (2009). Anatomy and development of the nervous system of *Nematostella vectensis*, an anthozoan cnidarian. *Dev. Neurobiol.* *69*, 235–254.
- Martin, A.C. (2010). Pulsation and stabilization: Contractile forces that underlie morphogenesis. *Dev. Biol.* *341*, 114–125.
- Martindale, M.Q., Pang, K., and Finnerty, J.R. (2004). Investigating the origins of triploblasty: “mesodermal” gene expression in a diploblastic animal, the sea anemone *Nematostella vectensis* (phylum, Cnidaria; class, Anthozoa). *Development* *131*, 2463–2474.

- Matus, D.Q., Thomsen, G.H., and Martindale, M.Q. (2007). FGF signaling in gastrulation and neural development in *Nematostella vectensis*, an anthozoan cnidarian. *Dev. Genes Evol.* *217*, 137–148.
- Matus, D.Q., Magie, C.R., Pang, K., Martindale, M.Q., and Thomsen, G.H. (2008). The Hedgehog gene family of the cnidarian, *Nematostella vectensis*, and implications for understanding metazoan Hedgehog pathway evolution. *Dev. Biol.* *313*, 501–518.
- McAuley, P.J., and Smith, D.C. (1982). The Green Hydra Symbiosis. V. Stages in the Intracellular Recognition of Algal Symbionts by Digestive Cells. *Proc. R. Soc. B Biol. Sci.* *216*, 7–23.
- Moiseeva, E., Rabinowitz, C., Paz, G., and Rinkevich, B. (2017). Histological study on maturation, fertilization and the state of gonadal region following spawning in the model sea anemone, *Nematostella vectensis*. *PLoS One* *12*, e0182677.
- Momose, T., Kraus, Y., Houliston, E., and Tsuyoshi Momose Yulia Kraus and Evelyn Houliston (2012). A conserved function for Strabismus in establishing planar cell polarity in the ciliated ectoderm during cnidarian larval development. *Development* *139*, 4374–4382.
- Mongera, A., Rowghanian, P., Gustafson, H.J., Shelton, E., Kealhofer, D.A., Carn, E.K., Serwane, F., Lucio, A.A., Giammona, J., and Campàs, O. (2018). A fluid-to-solid jamming transition underlies vertebrate body axis elongation. *Nature* *561*, 401.
- Mongera, A., Michaut, A., Guillot, C., Xiong, F., and Pourquié, O. (2019). Mechanics of anteroposterior axis formation in vertebrates. *Annu. Rev. Cell Dev. Biol.* *35*, 259–283.
- Mönke, G., Sorgenfrei, F.A., Schmal, C., and Granada, A.E. (2020). Optimal time frequency analysis for biological data - pyBOAT. *BioRxiv* 2020.04.29.067744.
- Mosaliganti, K.R., Swinburne, I.A., Chan, C.U., Obholzer, N.D., Green, A.A., Tanksale, S., Mahadevan, L., and Megason, S.G. (2019). Size control of the inner ear via hydraulic feedback. *Elife* *8*.
- Muller, W.A. (1969). Auslösung der Metamorphose durch Bakterien bei den Larven von *Hydractinia echinata*. *Zool. Jb. Anat.* *86*, 84–95.
- Müller, W.A., and Leitz, T. (2002). Metamorphosis in the Cnidaria. *Can. J. Zool.* *80*, 1755–1771.
- Nakanishi, N., and Martindale, M.Q. (2018). CRISPR knockouts reveal an endogenous role for ancient neuropeptides in regulating developmental timing in a sea anemone. *Elife* *7*.
- Nakanishi, N., Renfer, E., Technau, U., and Rentzsch, F. (2012). Nervous systems of the sea anemone *Nematostella vectensis* are generated by ectoderm and endoderm and shaped by distinct mechanisms. *Development* *139*, 347–357.
- Negri, A.P., Webster, N.S., Hill, R.T., and Heyward, A.J. (2001). Metamorphosis of broadcast spawning corals in response to bacteria isolated from crustose algae. *Mar. Ecol. Prog. Ser.* *223*, 121–131.
- Nonaka, S., Tanaka, Y., Okada, Y., Takeda, S., Harada, A., Kanai, Y., Kido, M., and Hirokawa, N. (1998). Randomization of Left–Right Asymmetry due to Loss of Nodal Cilia Generating Leftward Flow of Extraembryonic Fluid in Mice Lacking KIF3B Motor Protein. *Cell* *95*, 829–837.
- Olwin, B.B., Arthur, K., Hannon, K., Hein, P., Zhou, Z., Zuber, M.E., Kudla, A.J., McFall, A., Rapraeger, A.C., Riley, B., et al. (1994). Role of FGFs in skeletal muscle and limb development. *Mol. Reprod. Dev.* *39*, 90–101.
- Paré, A.C., Vichas, A., Fincher, C.T., Mirman, Z., Farrell, D.L., Mainieri, A., and Zallen, J.A. (2014). A positional Toll receptor code directs convergent extension in *Drosophila*. *Nat.* *2014* 5157528 *515*, 523–527.
- Penn, A.A., and Shatz, C.J. (1999). Brain Waves and Brain Wiring: The Role of Endogenous and Sensory-Driven Neural Activity in Development. *Pediatr. Res.* *1999* 454 *45*, 447–458.
- Petridou, N.I., Spiró, Z., and Heisenberg, C.P. (2017). Multiscale force sensing in development. *Nat. Cell Biol.* *19*, 581–588.

- Petridou, N.I., Corominas-Murtra, B., Heisenberg, C.P., and Hannezo, E. (2021). Rigidity percolation uncovers a structural basis for embryonic tissue phase transitions. *Cell* *184*, 1914–1928.e19.
- Petukhov, V., van den Brand, T., and Biederstedt, E. (2020). ggrastr: Raster Layers for “ggplot2.”
- Planas-Paz, L., Strilić, B., Goedecke, A., Breier, G., Fässler, R., and Lammert, E. (2012). Mechanoinduction of lymph vessel expansion. *EMBO J.* *31*, 788–804.
- Prall, O.W.J., Menon, M.K., Solloway, M.J., Watanabe, Y., Zaffran, S., Bajolle, F., Biben, C., McBride, J.J., Robertson, B.R., Chaulet, H., et al. (2007). An Nkx2-5/Bmp2/Smad1 Negative Feedback Loop Controls Heart Progenitor Specification and Proliferation. *Cell* *128*, 947–959.
- Priess, J.R., and Hirsh, D.I. (1986). *Caenorhabditis elegans* morphogenesis: The role of the cytoskeleton in elongation of the embryo. *Dev. Biol.* *117*, 156–173.
- Pukhlyakova, E.A., Kirillova, A.O., Kraus, Y.A., Zimmermann, B., and Technau, U. (2019). A cadherin switch marks germ layer formation in the diploblastic sea anemone *Nematostella vectensis*. *Development* *146*, dev174623.
- Putnam, N.H., Srivastava, M., Hellsten, U., Dirks, B., Chapman, J., Salamov, A., Terry, A., Shapiro, H., Lindquist, E., Kapitonov, V. V., et al. (2007). Sea anemone genome reveals ancestral eumetazoan gene repertoire and genomic organization. *Science* (80-. ). *317*, 86–94.
- Qian, L., Mohapatra, B., Akasaka, T., Liu, J., Ocorr, K., Towbin, J.A., and Bodmer, R. (2008). Transcription factor neuromancer/TBX20 is required for cardiac function in *Drosophila* with implications for human heart disease. *Proc. Natl. Acad. Sci.* *105*, 19833–19838.
- R Core Team (2019). R: A Language and Environment for Statistical Computing.
- Rauzi, M., Lenne, P.-F., and Lecuit, T. (2010). Planar polarized actomyosin contractile flows control epithelial junction remodelling. *Nat.* *2010* 4687327 *468*, 1110–1114.
- Redman, R.S. (1994). Myoepithelium of salivary glands. *Microsc. Res. Tech.* *27*, 25–45.
- Regev, I., Guevorkian, K., Pourquie, O., and Mahadevan, L. (2017). Motility-gradient induced elongation of the vertebrate embryo. *BioRxiv* 187443.
- Reitzel, A.M., Burton, P.M., Krone, C., and Finnerty, J.R. (2007). Comparison of developmental trajectories in the starlet sea anemone *Nematostella vectensis*: Embryogenesis, regeneration, and two forms of asexual fission. *Invertebr. Biol.* *126*, 99–112.
- Reitzel, A.M., Sullivan, J.C., Traylor-Knowles, N., and Finnerty, J.R. (2008). Genomic survey of candidate stress-response genes in the estuarine anemone *Nematostella vectensis*. *Biol. Bull.* *214*, 233–254.
- Renfer, E., Amon-Hassenzahl, A., Steinmetz, P.R.H., and Technau, U. (2010). A muscle-specific transgenic reporter line of the sea anemone, *Nematostella vectensis*. *Proc. Natl. Acad. Sci. U. S. A.* *107*, 104–108.
- Rentzsch, F., and Technau, U. (2016). Genomics and development of *Nematostella vectensis* and other anthozoans. *Curr. Opin. Genet. Dev.* *39*, 63–70.
- Rentzsch, F., Anton, R., Saina, M., Hammerschmidt, M., Holstein, T.W., and Technau, U. (2006). Asymmetric expression of the BMP antagonists chordin and gremlin in the sea anemone *Nematostella vectensis*: Implications for the evolution of axial patterning. *Dev. Biol.* *296*, 375–387.
- Rentzsch, F., Fritzenwanker, J.H., Scholz, C.B., and Technau, U. (2008). FGF signalling controls formation of the apical sensory organ in the cnidarian *Nematostella vectensis*. *Development* *135*, 1761–1769.
- Resende, T.P., Andrade, R.P., and Palmeirim, I. (2014). Timing embryo segmentation: Dynamics and regulatory mechanisms of the vertebrate segmentation clock. *Biomed Res. Int.* *2014*, 718683.

- Richards, G.S., Rentzsch, F., Sasai, N., Yamazaki, H., Shiota, K., Nakanishi, S., and Sasai, Y. (2014). Transgenic analysis of a SoxB gene reveals neural progenitor cells in the cnidarian *Nematostella vectensis*. *Development* *141*, 4681–4689.
- Röttinger, E., Dahlin, P., and Martindale, M.Q. (2012). A Framework for the Establishment of a Cnidarian Gene Regulatory Network for “Endomesoderm” Specification: The Inputs of  $\beta$ -Catenin/TCF Signaling. *PLoS Genet.* *8*, e1003164.
- RStudio Team (2015). RStudio: Integrated Development Environment for R.
- Ruiz-Herrero, T., Alessandri, K., Gurchenkov, B. V., Nassoy, P., and Mahadevan, L. (2017). Organ size control via hydraulically gated oscillations. *Dev.* *144*, 4422–4427.
- Ryan, J.F., Mazza, M.E., Pang, K., Matus, D.Q., Baxeavanis, A.D., Martindale, M.Q., and Finnerty, J.R. (2007). Pre-bilaterian origins of the hox cluster and the hox code: Evidence from the sea anemone, *Nematostella vectensis*. *PLoS One* *2*, e153.
- Saina, M., Genikhovich, G., Renfer, E., and Technau, U. (2009). BMPs and Chordin regulate patterning of the directive axis in a sea anemone. *106*, 18592–18597.
- Savin, T., Kurpios, N.A., Shyer, A.E., Florescu, P., Liang, H., Mahadevan, L., and Tabin, C.J. (2011). On the growth and form of the gut. *Nat.* *2011* 4767358 *476*, 57–62.
- Schindelin, J., Arganda-Carreras, I., Frise, E., Kaynig, V., Longair, M., Pietzsch, T., Preibisch, S., Rueden, C., Saalfeld, S., Schmid, B., et al. (2012). Fiji: an open-source platform for biological-image analysis. *Nat. Methods* *9*, 676–682.
- Schuett, W., Dall, S.R.X., Kloesener, M.H., Baeumer, J., Beinlich, F., and Eggers, T. (2015). Life-history trade-offs mediate “personality” variation in two colour morphs of the pea aphid, *Acyrtosiphon pisum*. *J. Anim. Ecol.* *84*, 90–101.
- Sebé-Pedrós, A., Saudemont, B., Chomsky, E., Plessier, F., Mailhé, M.P., Renno, J., Loe-Mie, Y., Lifshitz, A., Mukamel, Z., Schmutz, S., et al. (2018). Cnidarian Cell Type Diversity and Regulation Revealed by Whole-Organism Single-Cell RNA-Seq. *Cell* *173*, 1520-1534.e20.
- Sepich, D.S., Calmelet, C., Kiskowski, M., and Solnica-Krezel, L. (2005). Initiation of convergence and extension movements of lateral mesoderm during zebrafish gastrulation. *Dev. Dyn.* *234*, 279–292.
- Shader, M., Suwailem, A.M., and Rowe, G.A. (1997). The anemone, *nematostella vectensis*, in Britain: Considerations for conservation management. *Aquat. Conserv. Mar. Freshw. Ecosyst.* *7*, 13–25.
- Shih, J., and Keller, R. (1992). Cell motility driving mediolateral intercalation in explants of *Xenopus laevis*. *Development* *116*, 901–914.
- Shimizu, H., and Fujisawa, T. (2003). Peduncle of Hydra and the heart of higher organisms share a common ancestral origin. *Genesis* *36*, 182–186.
- Shindo, A. (2018). Models of convergent extension during morphogenesis. *Wiley Interdiscip. Rev. Dev. Biol.* *7*, e293.
- Shyer, A.E., Tallinen, T., Nerurkar, N.L., Wei, Z., Gil, E.S., Kaplan, D.L., Tabin, C.J., and Mahadevan, L. (2013). Villification: How the Gut Gets Its Villi. *Science* *342*, 212.
- Shyer, A.E., Rodrigues, A.R., Schroeder, G.G., Kassianidou, E., Kumar, S., and Harland, R.M. (2017). Emergent cellular self-organization and mechanosensation initiate follicle pattern in the avian skin. *Science* (80-. ). *357*, 811–815.
- da Silva, S.M., and Vincent, J.P. (2007). Oriented cell divisions in the extending germband of *Drosophila*. *Development* *134*, 3049–3054.



- Simões, S. de M., Blankenship, J.T., Weitz, O., Farrell, D.L., Tamada, M., Fernandez-Gonzalez, R., and Zallen, J.A. (2010). Rho-Kinase Directs Bazooka/Par-3 Planar Polarity during *Drosophila* Axis Elongation. *Dev. Cell* *19*, 377–388.
- Sinigaglia, C., Busengdal, H., Leclère, L., Technau, U., and Rentsch, F. (2013). The Bilaterian Head Patterning Gene *six3/6* Controls Aboral Domain Development in a Cnidarian. *PLoS Biol.* *11*, e1001488.
- Sinigaglia, C., Busengdal, H., Lerner, A., Oliveri, P., and Rentsch, F. (2015). Molecular characterization of the apical organ of the anthozoan *Nematostella vectensis*. *Dev. Biol.* *398*, 120–133.
- Slijper, E.J. (1942). Biologic anatomical investigations on the bipedal gait and upright posture in mammals—With special reference to a little goat born without forelegs II. *Proc. K. Ned. Akad. Van Wet.* *45*, 407–415.
- Smutny, M., Ákos, Z., Grigolon, S., Shamipour, S., Ruprecht, V., Čapek, D., Behrndt, M., Papusheva, E., Tada, M., Hof, B., et al. (2017). Friction forces position the neural anlage. *Nat. Cell Biol.* *19*, 306.
- Steinmetz, P.R.H., Kraus, J.E.M., Larroux, C., Hammel, J.U., Amon-Hassenzahl, A., Houlston, E., Wörheide, G., Nickel, M., Degnan, B.M., and Technau, U. (2012). Independent evolution of striated muscles in cnidarians and bilaterians. *Nature* *487*, 231–234.
- Steinmetz, P.R.H.H., Aman, A., Kraus, J.E.M.M., and Technau, U. (2017). Gut-like ectodermal tissue in a sea anemone challenges germ layer homology. *Nat. Ecol. Evol.* *1*, 1535–1542.
- Stennard, F.A., Costa, M.W., Elliott, D.A., Rankin, S., Haast, S.J., Lai, D., McDonald, L.P., Niederreither, K., Dolle, P., Bruneau, B.G., et al. (2003). Cardiac T-box factor *Tbx20* directly interacts with *Nkx2-5*, *GATA4*, and *GATA5* in regulation of gene expression in the developing heart. *Dev. Biol.* *262*, 206–224.
- Steventon, B., Duarte, F., Lagadec, R., Mazan, S., Nicolas, J.F., and Hirsinger, E. (2016). Species-specific contribution of volumetric growth and tissue convergence to posterior body elongation in vertebrates. *Dev.* *143*, 1732–1741.
- Stokkermans, A., Chakrabarti, A., Wang, L., Moghe, P., Subramanian, K., Steenbergen, P., Mönke, G., Hiiragi, T., Prevedel, R., Mahadevan, L., et al. (2021). Ethology of morphogenesis reveals the design principles of cnidarian size and shape development. *BioRxiv* 2021.08.19.456976.
- Stooke-Vaughan, G.A., and Campàs, O. (2018). Physical control of tissue morphogenesis across scales. *Curr. Opin. Genet. Dev.* *51*, 111–119.
- Stringer, C., Wang, T., Michaelos, M., and Pachitariu, M. (2021). Cellpose: a generalist algorithm for cellular segmentation. *Nat. Methods* *18*, 100–106.
- Sulston, J.E., Schierenberg, E., White, J.G., and Thomson, J.N. (1983). The embryonic cell lineage of the nematode *Caenorhabditis elegans*. *Dev. Biol.* *100*, 64–119.
- Susic-Jung, L., Hornbruch-Freitag, C., Kuckwa, J., Rexer, K.-H., Lammel, U., and Renkawitz-Pohl, R. (2012). Multinucleated smooth muscles and mononucleated as well as multinucleated striated muscles develop during establishment of the male reproductive organs of *Drosophila melanogaster*. *Dev. Biol.* *370*, 86–97.
- Tada, M., and Heisenberg, C.P. (2012). Convergent extension: Using collective cell migration and cell intercalation to shape embryos. *Dev.* *139*, 3897–3904.
- Takahashi, T., Muneoka, Y., Lohmann, J., Lopez De Haro, M.S., Solleder, G., Bosch, T.C.G., David, C.N., Bode, H.R., Koizumi, O., Shimizu, H., et al. (1997). Systematic isolation of peptide signal molecules regulating development in hydra: LWamide and PW families. *Proc. Natl. Acad. Sci. U. S. A.* *94*, 1241–1246.
- Thompson, D.W. (1942). *On growth and form* (Cambridge university press Cambridge).
- Tlili, S., Yin, J., Rupprecht, J.-F., Mendieta-Serrano, M.A., Weissbart, G., Verma, N., Teng, X., Toyama, Y., Prost, J., and Saunders, T.E. (2019). Shaping the zebrafish myotome by intertissue friction and active stress. *Proc. Natl. Acad. Sci.* *116*, 25430–25439.

- Tsata, V., and Beis, D. (2020). In Full Force. Mechanotransduction and Morphogenesis during Homeostasis and Tissue Regeneration. *J. Cardiovasc. Dev. Dis.* 2020, Vol. 7, Page 40 7, 40.
- Tzouanacou, E., Wegener, A., Wymeersch, F.J., Wilson, V., and Nicolas, J.-F.F. (2009). Redefining the Progression of Lineage Segregations during Mammalian Embryogenesis by Clonal Analysis. *Dev. Cell* 17, 365–376.
- Vuong-Brender, T.T.K., Ben Amar, M., Pontabry, J., and Labouesse, M. (2017). The interplay of stiffness and force anisotropies drives embryo elongation. *Elife* 6.
- Watanabe, H., Fujisawa, T., and Holstein, T.W. (2009). Cnidarians and the evolutionary origin of the nervous system. *Dev. Growth Differ.* 51, 167–183.
- Werkhoven, Z., Bravin, A., Skutt-Kakaria, K., Reimers, P., Pallares, L.F., Ayroles, J., and de Bivort, B.L. (2021). The structure of behavioral variation within a genotype. *Elife* 10.
- Wickham, H. (2009). *ggplot2* (Springer New York).
- Wickham, H., and Pedersen, T.L. (2019). *gtable: Arrange “Grobs” in Tables*.
- Wickham, H., Averick, M., Bryan, J., Chang, W., McGowan, L.D., François, R., Golemund, G., Hayes, A., Henry, L., Hester, J., et al. (2019). Welcome to the Tidyverse. *J. Open Source Softw.* 4, 1686.
- Wiesel, T.N., and Raviola, E. (1977). Myopia and eye enlargement after neonatal lid fusion in monkeys. *Nature* 266, 66–68.
- Williams, B.D., and Waterston, R.H. (1994). Genes critical for muscle development and function in *Caenorhabditis elegans* identified through lethal mutations. *J. Cell Biol.* 124, 475–490.
- Wittemyer, G., Northrup, J.M., and Bastille-Rousseau, G. (2019). Behavioural valuation of landscapes using movement data. *Philos. Trans. R. Soc. B Biol. Sci.* 374.
- Xiong, F., Ma, W., Bénazéraf, B., Mahadevan, L., and Pourquié, O. (2020). Mechanical Coupling Coordinates the Co-elongation of Axial and Paraxial Tissues in Avian Embryos. *Dev. Cell* 55, 354-366.e5.
- Yamada, A., Pang, K., Martindale, M.Q., and Tochinai, S. (2007). Surprisingly complex T-box gene complement in diploblastic metazoans. *Evol. Dev.* 9, 220–230.
- Yen, W.W., Williams, M., Periasamy, A., Conaway, M., Burdsal, C., Keller, R., Lu, X., and Sutherland, A. (2009). PTK7 is essential for polarized cell motility and convergent extension during mouse gastrulation. *Development* 136, 2039.
- Yin, C., Kiskowski, M., Pouille, P.A., Farge, E., and Solnica-Krezel, L. (2008). Cooperation of polarized cell intercalations drives convergence and extension of presomitic mesoderm during zebrafish gastrulation. *J. Cell Biol.* 180, 221–232.
- Yonemura, S., Wada, Y., Watanabe, T., Nagafuchi, A., and Shibata, M. (2010).  $\alpha$ -Catenin as a tension transducer that induces adherens junction development. *Nat. Cell Biol.* 12, 533–542.
- Yuan, S., and Schoenwolf, G.C. (2000). Islet-1 marks the early heart rudiments and is asymmetrically expressed during early rotation of the foregut in the chick embryo. *Anat. Rec.* 260, 204–207.
- Yum, S., Takahashi, T., Koizumi, O., Ariura, Y., Kobayakawa, Y., Mohri, S., and Fujisawa, T. (1998). A novel neuropeptide, Hym-176, induces contraction of the ectodermal muscle in *Hydra*. *Biochem. Biophys. Res. Commun.* 248, 584–590.
- Zallen, J.A., and Wieschaus, E. (2004). Patterned Gene Expression Directs Bipolar Planar Polarity in *Drosophila*. *Dev. Cell* 6, 343–355.
- Zeileis, A., and Grothendieck, G. (2005). zoo: S3 Infrastructure for Regular and Irregular Time Series. *J. Stat. Softw.* 14, 1–27.

Zhang, H., Landmann, F., Zahreddine, H., Rodriguez, D., Koch, M., and Labouesse, M. (2011). A tension-induced mechanotransduction pathway promotes epithelial morphogenesis. *Nature* 471, 99–103.

Zimmermann, B., Robb, S.M.C., Genikhovich, G., Fropf, W.J., Weilguny, L., He, S., Chen, S., Lovegrove-Walsh, J., Hill, E.M., Ragkousi, K., et al. (2020). Sea anemone genomes reveal ancestral metazoan chromosomal macrosynteny (Cold Spring Harbor Laboratory).